Online ISSN : 2395-602X
Print ISSN : 2395-6011
www.ijsrst.com

स्थापना जून १९७२

IJSRST

National Conference on New Horizons in Nano Scale Materials and Their Applications NHNMA-2024

Date : 15th March 2024

Organized By

Department of Physics,
M. S. P. Mandal's Arts, Commerce and Science College,
Kille-Dharur, Dist. Beed, Maharastra, India

Sponsored by Dr. Babasaheb Ambedkar
Marathwada University, Chhatrapati, Sambhajinagar, Maharashtra, India

VOLUME 11, ISSUE 13, MARCH-APRIL-2024

INTERNATIONAL JOURNAL OF SCIENTIFIC RESEARCH IN SCIENCE AND TECHNOLOGY

PEER REVIEWED AND REFEREED INTERNATIONAL SCIENTIFIC RESEARCH JOURNAL

Scientific Journal Impact Factor : 8.014

Email : editor@ijsrst.com Website : http://ijsrst.com

TECHNO SCIENCE ACADEMY
THE INTERNATIONAL OPEN ACCESS PUBLISHER

National Conference on New Horizons in Nano-scale Materials & Their Applications
[NHNMA-2024]

15th March 2024

Organised by

Department of Physics

M.S.P. Mandal`s Arts, Commerce and Science College, Kille-Dharur, Dist. Beed, MS, INDIA

Dr. G. K. KAKADE
Principal

Dr. L. B. Jadhavar
Convener

Dr. R. R. Bhosale
Organizing Secretary

Published By:

M.S.P. Mandal`s Arts Commerce and Science College Kille-Dharur, Dist. Beed.

Chief Editor : Dr. G. K. Kakade

Editors: Dr .L. B. Jadhavar **Dr. R. R. Bhosale**

Inaugurator & Keynote Speaker

K. M. Jadhav

Emeritus Professor (Physics) Incharge, School of Basic and Applied Sciences, MGM University, Chhatrapati Sambhajinagar.

Resource Persons

Raghumani Singh Ningthoujam

Scientist, Chemistry Division, Bhabha Atomic Research Centre, Mumbai 400085, India

Topic: The Nobel Prize in Chemistry 2023: Discovery and Synthesis of Quantum Dots

Prasad P. Phadnis

Chemistry Division, Bhabha Atomic Research Centre, Trombay, Mumbai 400085, India

Topic:Development of Nano formulations for Theragnostic Utility in Cancer Therapeutics

Prof. Rajendra R. Deshmukh

Institute of Chemical Technology, Matunga, Mumbai 400 019

Topic: Pulsed plasma polymerization to control film chemistry for various applications

PATRONS

Hon.M.L.A.Shri. Prakash Solanke

President

M.S.P.Mandal, Chhatrapati Sambhajinagar

Hon.M.L.C.Shri. Satish Chavan

Secretary

M.S.P.Mandal, ChhatrapatiS ambhajinagar

Hon.Shri. Jaysingh Solanke

CDC-Chief, ACS College, Dharur, Member

M.S.P.Mandal, Chhatrapati Sambhajinagar

CHIEF ORGANIZER

Prof. Dr. G. K. Kakade

Principal

Arts Commerce and Science College, Dharur

CONVENER

Dr.L.B. Jadhavar

Head, Department of Physics

ACS College, Dharur

ORGANIZING SECRETARY

Dr. R. R. Bhosale

Asst. Prof. Department of Physics

ACS College,Dharur

*ORGANIZING COMMITTEE *

Prin. Dr. Gopal K. Kakade: Principal (Chief Organizing Secretary)

Prof. M.A. Jogade: Vice Principal

Dr. M. N. Gaikwad: Vice Principal

Dr. L.B. Jadhavar: Convener

Dr. R. R. Bhosale: Organizing Secretary

*ORGANIZING MEMBERS *

1. **Prof. Dr. A. D. Lakhe**
2. **Prof. Dr. P. B. Rokde**
3. **Prof. Dr. B. A. Navle**
4. **Dr. D. B. Jadhav**
5. **Dr. V. S. Kedari**
6. **Dr. S. G. Basole**
7. **Mr. N.S. Waghmare**
8. **Mr. V. D. Kapawar**
9. **Mr. M.G. Rathod**
10. **Dr. N. B. Kumbhar**
11. **Dr. B. S. Jogdand**
12. **Dr. A. R. Gade**
13. **Dr. V. S. Kumbhare**
14. **Mr. G. D. Sagar**
15. **Dr. B. R. Dahe**

SCOPE AND OBJECTIVES OF CONFERENCE

The scope and objectives of the NHNMA-2023-2024 is typically revolve around bringing together researchers, scientists, engineers, industry professionals, policymakers, and other stakeholders to discuss recent advancements, challenges, and future directions in the field of nanotechnology.

The main scope and objectives of the conference is:

Knowledge Exchange: The NHNMA-2023-2024 serves as a platform for participants to exchange knowledge, ideas, and experiences related to nanotechnology research, development, and applications. This includes sharing insights into cutting-edge research findings, innovative technologies, and emerging trends.

Research Presentations: Researchers and scientists present their latest findings, breakthroughs, and advancements in various areas of nanotechnology, including nanomaterials, nanoelectronics, nanomedicine, nanophotonics, nanomanufacturing, and more. This helps disseminate new knowledge and foster collaboration among peers.

Networking Opportunities: The conference provides ample networking opportunities for participants to connect with fellow professionals, potential collaborators, industry partners, funding agencies, and experts in the field. Networking sessions, social events, and poster presentations facilitate interactions and collaborations.

Policy Discussions: Policymakers, regulatory authorities, and governmental representatives participate in discussions to address regulatory, ethical, safety, and societal implications of nanotechnology. These discussions help shape policies, regulations, and guidelines governing the responsible development and deployment of nanotechnologies.

Education and Outreach: The conference may include sessions focused on educational initiatives, outreach programs, and public engagement efforts aimed at raising awareness about nanotechnology and its potential impact on society. Workshops, tutorials, and outreach activities target students, educators, and the general public.

Future Directions and Challenges: Panel discussions, keynote speeches, and thematic sessions explore future directions, challenges, and opportunities in nanotechnology research and innovation. Participants discuss strategies for overcoming technical barriers, addressing ethical concerns, promoting interdisciplinary collaboration, and achieving sustainable development goals.

Publication and Dissemination: Proceedings of the conference will be published in journals, special issues, ensuring that the research presented reaches a wider audience and contributes to the scientific literature in the field of nanotechnology.

CONTENT

SR. NO	ARTICLE/PAPER	PAGE NO
1	**Dielectric Properties of Li+ Doped Cobalt Ferrite Nanoparticles** N.N.Waghule	01-06
2	**Analysis of Structural Properties of Vanadium Substituted Yttrium Iron Garnet** R. G. Vidhate, R.B. Kavade, J. M. Bhandari, N. N. Waghule, K. M. Jadhav	07-13
3	**VSM Analysis of $CoFe_{2-2x}Ti_xMn_xO_4$ Nanoparticles** R. T. Ubale, C. M. Kale	14-19
4	**Flood Mapping Using Microwave Remote Sensing** Dheeraj Raut, Gaus Mohiuddin Sayyad, Ashok Dongare, Shailendra Kolhe, Shafiyoddin Sayyad	20-27
5	**Raman Effect and Applications of Raman Effect in the Study of Nanoparticles** Swati Kulkarniirst, Vinayak Deshmukh	28-31
6	**Synthesis and Study of Cation Distribution of Copper Substituted Nickel Spinel Ferrite** J. M. Bhandari, R. G. Vidhate, R. B. Kavade, K. M. Jadhav	32-36
7	**Conducting Polymer Matrix for Drug Release Device** Pradeep Gaikwad	37-40
8	**Graphical study of Dielectric Properties of Ghughuwa Fossil National Park (M.P.) Saline Soil C- Band Microwave Frequency** Santosh S. Deshpande, Sanjeev Pande	41-46
9	**Advancements and Applications of Nanotechnology : A Comprehensive Review** Dr. G. S. Jaigaonkar	47-52
10	**The Structural and Optical Properties of $Cofe_2O_4$ Nanoparticles Prepared By Sol - Gel Auto-Combustion Technique** J. S. Shilwant, M. R. Patil, S. B. Patil, A. N. Ardad, R. R. Mistry, S. D. More	53-56
11	**The Effect of Low Energy 0-30 KeV N+ Ions Irradiation on Polycarbonate Thin Sheet** Sumant B. Jagtap, A. B. Thorat, K. T. Adsure, R. U. Mene, R. P. Joshi, G. H. Kale	57-65
12	**Effect of Cd2+ on the Structural and Magnetic Properties of Lithium-Nickel Ferrite Nanoparticles** Dhanraj Aepurwar, Yogesh Kute, D. R. Shengule, B. H. Devmunde	66-70
13	**To Study Photovoltaic Application of ZnS Thin Films Deposited By Spray Pyrolysis Technique** Mrs. Shaikh Nilofar Mansur	71-76

14	**Estimating Soil Moisture Content of Bare Soil Using Oven Drying Method** Monika Sudhakar Khole, Dr. Sanjay K. Tupe, Dr. Shafiyoddin Sayyad	77-81
15	**A Review of Modelling Approaches for Drought Index Monitoring and Assessment Using Multispectral Imaging** Neha Andure, Sidheshwar Raut, Ankush Kadam, Sandipan Sawan, Shafiyoddin Sayyad	82-87
16	**Effect of Bandgap on Photocatalytic Activity of GO Based Cr Doped Nio Nanocomposites** Ramprasad Sonpir, Dnyaneshwar Dake, Nita Raskar, Vijay Mane, Babasaheb Dole	88-93
17	**Harnessing Renewable Energy : A Path towards Sustainable Future** Vinayak Deshmukh, Swati Kulkarni	94-102
18	**Intermolecular Interaction Study of Binary Mixture of 2-Ethoxyethanol and Methanol Using Ultrasonic Interferometry** Pawan S. Kachave, Bharat K. Kajale, Sandip R. Magar, Shrinivas N. Keshatti	103-115
19	**A Review of Synthesis Methods, Properties, and Applications of Nanoparticles** Dr. M. S. Patil	116-121
20	**Electrical Properties of $Co_{1+x}Zr_xFe_{2-2x}O_4$ Spinel Ferrite Nanoparticles** Dr. Jairam B. Mote, Dr. Pravin K. Gaikwad	122-127
21	**Preparation of Zinc Ferrite by Using Sol-Gel Auto Combustion Method** Miss Sneha Yuvraj Pawar	128-131
22	**Structural and Elastic Properties of Cadmium Substituted Ni - Cu Spinel Ferrites** R. B. Kavade, R. G. Vidhate, J. M. Bhandari, V. B. Kawade, S. J. Shukla	132-135
23	**Signal Processing of Microwave Synthetic Aperture Radar Dataset for Parameter Extraction** Mosin Ratan Tamboli, Prashant T Sonwane	137-141
24	**Nanostructured Organic Polyaniline Thin Film Prepared By Polymerisation Technique** Dr. Sandip Mahajan, Dr. Sanjay Kamble, Dr. Rajkumar Lokhande, Dr. R. R. Bhosale, Bharat Surung, Dr. Vishal Awasarmol	142-145
25	**Metal-Free Organic Dyes and Nanoscale Materials for Enhanced Solar Energy Harvesting System** Mrs. Meghmala Vaijnath Ingole	146-154
26	**Mass Attenuation Coefficient and Molar Extinction Coefficient of 2-Amino-3-Nitropyridinein the Energy Range356KeV to 1330 KeV** Vishal Awasarmol, Ankur Awasarmol, Sandip Mahajan, R. R. Bhosale, Rajkumar Lokhande, Bharat Surung	155-159
27	**New Trends in Gamma Radiation Protection Technology : Challenges and Opportunities** Mr. Nilesh S. Shinde	160-168

28	**Synthesis and Thermophysical Characterization of Copper Oxide-Based Propylene Glycol and D.I. Water Nanofluid** S. S. Raut, A. A. Wadewale, M. T. Kotkar, S. V. Kshirsagar, K. M. Jadhav	169-176

International Journal of Scientific Research in Science and Technology
Volume 11 | Issue 13| Print ISSN: 2395-6011 | Online ISSN: 2395-602X (www.ijsrst.com)

Dielectric Properties of Li+ Doped Cobalt Ferrite Nanoparticles

N.N.Waghule
Department of Physics, Bhagwan Mahavidyalaya, Ashti Dist- Beed-414203, Maharashtra, India

ABSTRACT

Now a day spinel ferrite nonmaterial's are studied more due to their widespread applications in the electronics industry and energy storage devices. The Li+ doped Cobalt ferrites with the general formula Co1+xLixFe2-xO4 (x =0.0, 0.1, 0.2, 0.3, 0.4, 0.5) were prepared using wet chemical method i.e. sol-gel auto combustion method. Structural characterization of the samples was carried out using X-ray powder diffraction technique. The XRD confirmed the cubic phase of Co1+xLixFe2-xO4 ferrite with the crystallite size. The dielectric properties were studied over the frequency range from 100 Hz to 1 MHz by using LCR-Q meter (HP 4248A). The dielectric measurements were performed at room temperature as a function of frequency. It is observed that all samples demonstrate dielectric dispersion where the dielectric constant (ε') decreases in an exponential way with an increase in frequency. The present work was to dielectric properties of Li+ doped Cobalt ferrite using citrate assisted sol-gel auto combustion and to understand the effect of Li+ ion doping on the structural properties cobalt ferrite.

Keywords: X-ray diffraction, Sol-gel auto combustion, dielectric constant (ε'), dielectric loss (ε''), Dielectric loss tangent.

I. INTRODUCTION

Spinel ferrites is an important class of electrical materials due to their high resistivity and low loss behavior, therefore they have vast technological applications over a wide range of frequencies. [1]. They have properties such as high saturation magnetization, high coercivity, strong anisotropy as well as high quality factors, chemical stability are not observed in the bulk sample. Substituted cobalt ferrites are widely used as magnetic materials due to their low dielectric losses. Large number of researchers have been carried out work on the structural, morphological, magnetic, electrical, dielectric and other properties of spinel cobalt ferrites with a view to improve these properties for the desired applications [2]. The dielectric properties of ferrites are dependent on several factors, such as method of preparation, heat treatment, sintering conditions chemical composition and crystallite size. Polycrystalline ferrites are very good dielectric materials and their physical properties can be controlled by the grain boundaries. The dielectric study gives valuable information about the behavior of localized electric charge carriers and can explain the mechanism of electrical conduction and dielectric polarization. It is excepted that doping of mono-valent metal ions Li^{+} in Cobalt ferrite may brings an important modification in the structural and transport properties of these materials which can be employed for different applications in rod antennas, transformer core, read/write heads for high density digital tapes and other devices.

II. EXPERIMENTAL DETAILS

2.1 Materials

Cobalt nitrate [$Co(NO_3)_2 \cdot 6H_2O$], Nickel nitrate [$Ni(NO_3)_2 \cdot 6H_2O$], ferric nitrate [$Fe(NO_3)_2 \cdot 9H_2O$], lithium nitrate [$LiNO_3.6H2O$] and citric acid [$C_6H_8O_7 \cdot H_2O$], ammonia solution [$NH_3.H_2O$] acetone, distilled water were used. All chemicals used were of analytical grade and the solutions were prepared with distilled water.

2.2 Synthesis of Li+ doped Cobalt ferrite nano particles.

Ferric nitrate [$Fe (NO_3)_3 \cdot 9H_2O$], lithium nitrate [$Li(NO_3).6H_2O$], Cobalt nitrate [$Co (NO_3)_2 \cdot 9H_2O$] were dissolved together in a minimum amount of distilled water to get clear solution. The citric acid was used as a fuel. The citric acid to nitrate ratio was considered to be 1:3. An aqueous solution of citric acid was mixed with metal nitrate solution. The mixed solution was kept on magnetic stirrer and constantly stirred at 300rpm by maintaining the temperature at 60°C.to form a homogeneous solution. The solution was transformed into a sol and then a gel is formed by evaporation of the water. The ammonia solution was slowly added to maintain the pH at 8 of the mixed homogeneous solution. The temperature after the gel formation is increased to 120°C. At this temperature the gel get burnt converting into fine loose powder of $Co_{1+x}Li_xFe_{2-x}O_4$ (x = 0.0, 0.1, 0.2, 0.3, 0.4, 0.5) nanoparticles. The powder was pre-sintered at 500^{0}C for 6 h and cooled slowly to room temperature. A small quantity of polyvinyl alcohol was added to the powder as a binder to make disk shaped Pellets having 10 mm diameter and 2–3 mm thickness with the help of KBr hydraulic press. The pellets are then sintered again at 600^{0}C for 6h and slowly allowed to cool at room temperature. The samples in powder form were used to characterize the material.

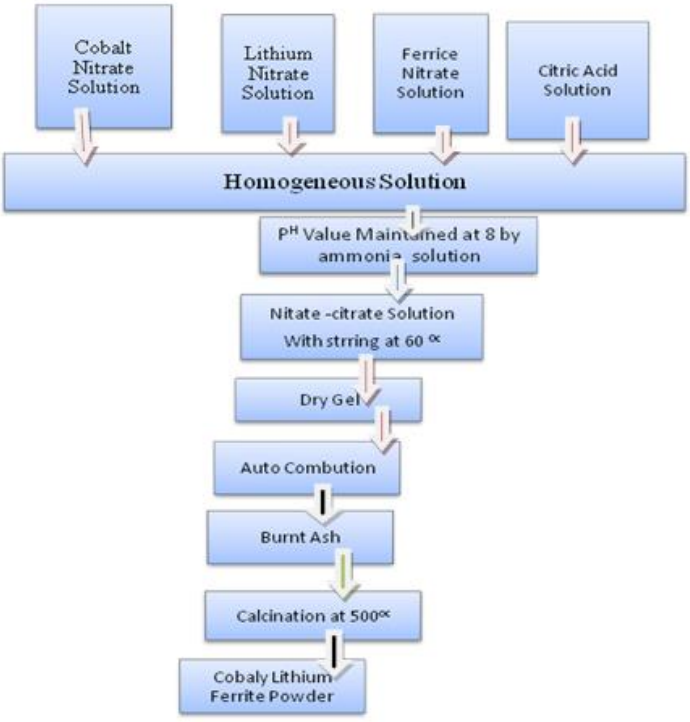

Flow chart for the synthesis of cobalt-Lithium ferrite using citrate-gel auto combustion technique

2.3 Characterizations

X-ray diffractometer (XRD) with Cu-Kα radiation(λ=1.5405 *A*°) and 2θscanning ranges from 20° to 80°, at a scanning speed of ~ 2° /min, were characterized to verify the phase purity and structure of prepared material. The dielectric measurements were carried out at room temperature using LCR Meter (Hewlett Packard 4284)

over the frequency range 100 Hz to 1 MHz. The values of capacitance (C) , the dielectric constant (ɛ́) and dielectric loss tangent (tan δ) was calculated using the relations $\acute{\varepsilon}=\frac{Ct}{\varepsilon_{0A}}$ and $\varepsilon'' = \varepsilon' \tan(\delta)$.

III.RESULTS AND DISCUSSION

3.1 X-ray diffraction analysis

he X-ray diffraction (XRD) pattern of all $Co_{1+x}Li_xFe_{2-x}O_4$ (x = 0.0, 0.1, 0.2, 0.3,0.4,0.5) nanoparticles were recorded using X-ray diffractometer at room temperature in the 2θ range of 20° to 80°.Fig. 1 displays the XRD patterns of all the samples. Using Bragg's law, all the peaks in the XRD pattern were indexed. All the peaks belonging to the cubic spinel structure are verified by the XRD patterns, indicating that the prepared specimens have a single-phase existence. XRD pattern is compared with JCPDS card number 00-0022-1086 in order to identify the crystalline phases present [3]. In the XRD patterns, all the peaks observed are extreme and slightly wider, indicating the nano crystalline nature and presence of planes (220), (311), (222), (400), (422), (511), and (440) match with usual data (JCPDS card no. 022–1086). The XRD pattern confirmed the creation of single-phase; cubic geometry; spinel structure of the prepared sample. It is clear that the intensity of (440) de-creases with increase in Li^{+1} concentration. This is due to the decrease in Co^{2+} ion in octahedral site.

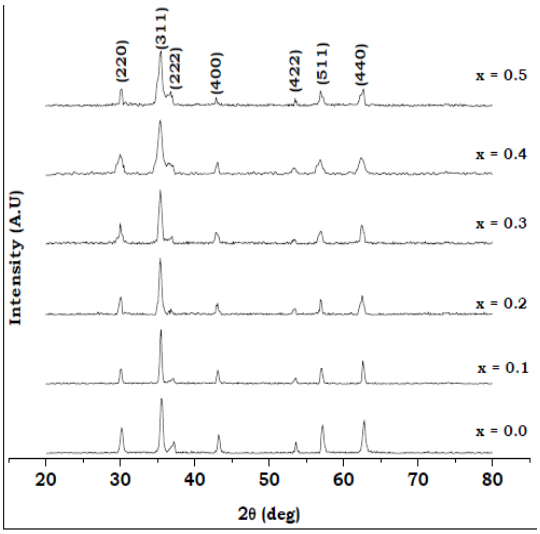

Fig 1. XRD pattern for the system $Co_{1+x}Li_xFe_{2-x}O_4$ (x = 0.0, 0.1, 0.2, 0.3, 0.4, 0.5)

3.2 Dielectric properties

The dielectric behaviour in ferrite depends on many factors such as preparation method, sintering temperature, amount of dopant and type of the dopant. The dielectric measurements were made using the two probe method. The silver paste is applied on the flat surface of the pellet. The measurement of ac resistance (R) and capacitance (c) were measured with the help of LCR-Q meter (HP 4284A).The ac parameter such as dielectric constant (ɛ́), dielectric loss (ε'') dielectric loss tangent (tanδ) depends on the frequency and were calculated using the values of capacitance (C), ac resistance and other parameters.

3.2.1 Frequency dependence of dielectric constant (ε'):

The dielectric properties were studied over the frequency range from 100 Hz to 1 MHz by using LCR-Q meter (HP 4248A). The values of dielectric constant (ε'), dielectric loss (ε'') and dielectric loss tangent (tan δ) were

determined using the following relations $\acute{\varepsilon}=\frac{Ct}{\varepsilon_{0A}}$ and $\varepsilon'' = \varepsilon' \tan(\delta)$ and $\tan\delta=1/2\pi f\varepsilon_0\acute{\varepsilon}\rho$ Where, C is the capacitance of the pellet in farad, t is the thickness of the pellet in meter, A is the cross sectional area of the flat surface of the pellet and ε_0 is the permittivity constant of free space and ρ is the resistivity. The dielectric loss tangent for each sample was calculated using the values of dielectric constant and the dielectric loss. The effect of frequency f on the dielectric constant (ε') and loss (ε'') and loss tangent at room temperature is shown in Fig2(a,b). It can be seen from Fig2(a,b) that both dielectric constant and dielectric loss with increase in frequency. The dielectric constant is found to be less than bulk sample for a higher frequency at room temperature. The dispersion (exponential decay) in ε' and ε'' with increase in frequency is due to the fact that the polarization is lagging behind the applied field at higher frequencies then reaches a constant value. The observed variation in ε' and ε'' may be understood on the basis of space charge polarization, which is due to an inhomogeneous structure governed by the number of space charge carriers and the resistivity of the samples [4,5] it can be understood on the basis of Maxwell–Wagner type interfacial polarization and is in agreement with Koop's phenomenological theory[6].

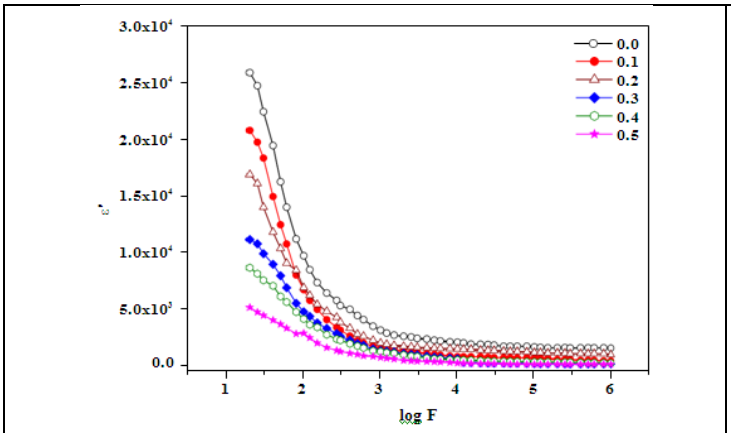

Fig2aDielectric constant (έ) for the samples $Co_{1+x}Li_xFe_{2-x}O_4$ (x = 0.0, 0.1, 0.2, 0.3, 0.4, 0.5

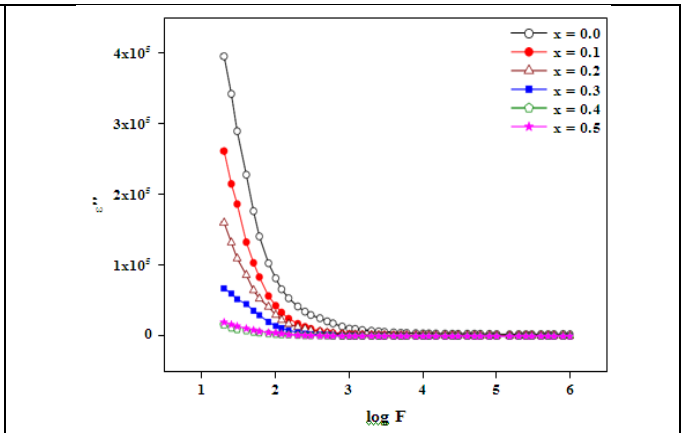

Fig2b.Dielectric loss(ε") for samples $Co_{1+x}Li_xFe_{2-x}O_4$ (x = 0.0, 0.1, 0.2, 0.3, 0.4, 0.5

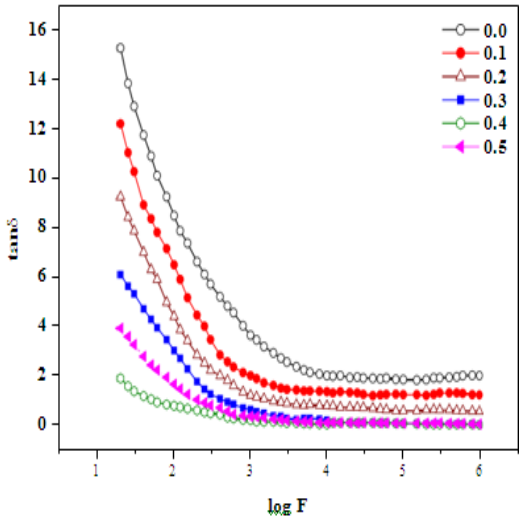

Fig2c.Dielectric loss tangent for $Co_{1+x}Li_xFe_{2-x}O_4$ (x = 0.0, 0.1, 0.2, 0.3, 0.4, 0.5)ferrite

The polarization mechanism involves the exchange of electrons between the ions of the same element, which are present in more than one valence state and are distributed randomly over crystallographic equivalent sites. Here the exchange of electrons mainly takes place between Fe^{3+}

and Fe^{2+} ions present at octahedral [B] sites. During this exchange mechanism, the electrons have to pass through the grains and grain boundary of the dielectric medium. Owing to high resistance of the grain boundary, the electrons accumulate at the grain boundary and produce space charge polarization [7].

3.2.2 Variation of the dielectric loss tangent (tan d) with frequency:

The variation of dielectric loss tangent (tanδ) with frequency is shown in Fig.2c. It is evident from Fig. 2c that, like dielectric constant, dielectric loss tangent also decreases exponentially with increasing frequency. This low dielectric loss is attributed to homogeneity, better symmetry and small grain size [8]. It is observed variation of dielectric loss tangent with frequency is normal behaviour of ferrites at low frequency more energy is required for electron hoping and as result the loss is high. As per Iwauchi observation,there is a strong correlation between the conduction mechanism and the dielectric behaviour of ferrites[9].The reduction in the values of dielectric constant with increasing concentration of Lithium is due to depleting concentration of iron ions at [B]sites which play a dominant role in dielectric polarization[10,11].The variation of dielectric constant (ε') determined at frequencies 100 Hz and 1 MHz as a function of Li^{1+} concentration x is shown in Table1.

Tble1: Room temperature dielectric constant (ε'), dielectric loss (ε") and dielectric loss tangent (tanδ) at 100 Hz and 1 MHz, for $Co_{1+x}Li_xFe_{2-x}O_4$ for nanoparticles.

Lithium content x	f =100 Hz			f =1 MHz		
	ε'	ε"	tan δ	ε'	ε"	tan δ
0.0	9625	81900	8.44	1437	2949	2.2
0.1	6621	43178	6.47	352	439	1.2
0.2	6800	30046	4.42	960	427	0.47
0.3	4728	14593	3.18	169	2.67	0.018
0.4	4054	3146	0.78	79	0.381	0.002
0.5	2884	4992	1.73	40	1.549	0.054

IV. CONCLUSIONS

A series of substituted Monovalent Li^+ doped cobalt ferrite nanoparticles with composition $Co_{1+x}Li_xFe_{2-x}O_4$ (x = 0.0, 0.1, 0.2, 0.3, 0.4) nanoparticles were successfully synthesized via citric acid assisted sol-gel auto combustion route. X-ray diffraction study revealed the single phase formation and nano crystalline nature of all the prepared nano particles. Li+ doped cobalt ferrites with $Co_{1+x}Li_xFe_{2-x}O_4$ (x = 0.0, 0.1, 0.2, 0.3, 0.4) were prepared by sol gel auto combustion method. X-ray diffraction analysis confirms the single phase cubic spinel structure for all the samples. The dielectric constant, dielectric loss and dielectric loss tangent all decreases exponentially with increase in frequency. The dielectric constant measured at low and high frequency also decreases with Lithium substitution x.

V. ACKNOWLEDGEMENTS

The author is thankful to Prof. K.M Jadhav for fruitful discussion, Shivaji University Kolhapur for providing experimental facilities.

VI. REFERENCES

[1]. P. Ravindranathan, K. C. Patil, J. Mater, Sci., 22, (9) (1987)3261.

[2]. J.Smit and H.P. Wijn : "ferrites" Physical properties of ferromagnetic oxides in relation to their technical applications(Philips,Eindhoven) ,1959

[3]. M.A.Dar,K.M.Batoo,V.Verma,W.A.Siddiui,:J.Alloys Compds. (2010) 553.

[4]. M. Y. Nassar and M. Khatab, RSC Advances, 2016, 6, 79688-79705.

[5]. Priyanka Gupta ,Ravi Kumar Vijai, SubhashChander, IOSR J. Of Appl.Physics (IOSR-JAP) e-ISSN: 2278-4861.Vol.14, Issue5 Ser. I (2022), PP 42-47 www.Iosrjournals.Org

[6]. D. Ravinder, K. Vijaykumar : Bull .Mater. Sci., 5(2001) 505.

[7]. Z.K. Heiba,M.B .Mohamed, L. Arda, N.Dogan, J. of Magnetism and Magnetic Materials, 2015; 391:195-202

[8]. C. Subhash, B.K. Srivastava, K. Anjali, Indian J. Pur. Appl. Phys. 42 366 (2004).

[9]. K. Iwauchi, Jpn. J. Appl. Phys. 10 (1971) 1520.

[10]. M. A. Dar, K.M.Batoo, V.Verma , W.A.Siddiui, : J.Alloys Compds. (2010) 553.

[11]. Shashank Bhushan Das , Rakesh Kumar Singh, Vivek Kumar, etc. Materials Science in Semiconductor Processing 145 (2022) 106632

International Journal of Scientific Research in Science and Technology
Volume 11 | Issue 13| Print ISSN: 2395-6011 | Online ISSN: 2395-602X (www.ijsrst.com)

Analysis of Structural Properties of Vanadium Substituted Yttrium Iron Garnet

R. G. Vidhate*[1], R.B. Kavade[2], J. M. Bhandari[3], N.N.Waghule[2], K. M. Jadhav[5]

*[1]Anandrao Dhonde Alias Babaji Mahavidyalaya, Kada, Beed, Maharashtra, India

[2]Bhagwan Mahavidyalaya, Ashti, Beed, Maharashtra, India

[3]Gandhi college Kada, Beed, Maharashtra, India

[5]Department of physics MGM University, Aurangabad, Maharashtra, India

ABSTRACT

The garnet having the general formula $Y_3V_xFe_{5-x}O_{12}$ (x= 0.0, 0.2 and 0.4) were synthesized using double sintering ceramic technique. The samples were characterized by X-ray diffraction technique. The X-ray diffraction studies of compositions revealed the formation of single phase cubic structure with lattice constant ranging from 12.364 to 12.381 Å up x=0.0 to x= 0.4.

The IR spectra of all samples are taken in the range of 300-800cm-1. IR spectra show typical absorption bands indicating the garnet nature of samples.

Keyword: Garnet, Vanadium, structural, IR study.

I. INTRODUCTION

Yttrium iron garnet (YIG) $Y_3Fe_5O_{12}$ belongs to a group of magnetic oxides and has received a great deal of attention in laser, microwave devices and ultrasonic devices field. They are characterized by magnetic and magneto-optical properties. Yttrium iron garnet (YIG) is a microwave ferrite, which in polycrystalline form has specific characteristics.

Garnets are cubic oxides with space group O_h^{10} and they are characterized by the chemical formula $\{A_3\}[B_2]X(C_3)O_{12}$, where the different brackets reflect the various oxygen coordination of the A cations while the [ ] and ( ) indicate six fold and four fold coordination of the B and C cations, respectively. A can be one of the fourteen well known rare earth ions or Yttrium while B and C are the cations like Al, Ga, Cr, etc [1]. Yttrium iron garnet is one of the well known family of ferrimagnetic oxide magnetic materials. In the present study, we report our results on the structural properties of vanadium substituted yttrium iron garnet ($Y_3Fe_{5-x}V_xO_{12}$) (x = 0.0 – 0.4) through X-ray diffraction, infrared spectroscopy.

Pure and substituted yttrium iron garnet has been studied intensively by several researches with a view to understand their basic properties. Substituted yttrium iron garnets have been extensively used in wide band non reciprocal devices [2,3]. Non-magnetic substitutions in yttrium iron garnet have provoked great interest for scientific studies of the effects caused by the magnetic dilutions [4,5]. In general, non-magnetic cations occupy two non-equivalence sites with more or less pronounced preference for one site [6]. Non-magnetic ions usually occupy octahedral or tetrahedral site.

The aim of the present work is to develop sintered material of the vanadium substituted yttrium iron garnet ($Y_3Fe_{5-x}V_xO_{12}$) and to study the effect of vanadium substitution on the properties of yttrium iron garnet in meeting the requirement of device engineers. In the present study, we report our results on the structural properties of vanadium substituted yttrium iron garnet. ($Y_3Fe_{5-x}V_xO_{12}$) (x = 0.0 – 0.4) through X-ray diffraction, infrared spectroscopy measurements.

II. EXPERIMENTAL

The samples of V^{3+} substituted $Y_3V_xFe_{5-x}O_{12}$ garnets with x = 0.0 to 0.4 in steps of 0.2 were prepared by well known double sintering ceramic method in which a molar ratio of Y_2O_3, Fe_2O_3 and V_2O_3 (all 99.99% pure AR grade) were mixed thoroughly in stoichiometric proportions and then ground to very fine powders by using agate mortar for about 3 hrs. These mixtures in powder form were pre-sintered in a Indfur Programmable muffle furnace at 1000^0C for 24 hr, and cooled to room temperature slowly at the rate of 2^0C/min. The samples were reground and re-fired at 1350^0C for 30 hours and slowly cooled to room temperature at the rate of 2^0C/min., and then reground for 1 hr. The fine powdered sample was pelletized under the pressure of 5 ton /inch^2.

III.RESULT AND DISCUSSION

The room temperature X-ray diffraction patterns (XRD) of vanadium doped yttrium iron garnet $Y_3Fe_{5-x}V_xO_{12}$ (where x = 0.0-0.4 in the step of 0.2) are shown in Fig.1 (a - c). The X-ray diffraction patterns of the garnet system shows the Bragg's peaks belonging to cubic garnet structure the cubic garnet structure can be easily observed in all the samples. All the observed reflections (321), (400), (420), (422), (431), (521), (611), (444), (640), (642), (800), (842), in the garnet system with the crystalline phases were well indexed using the JCPDS powdered diffraction file (card no.43-0507). The XRD patterns show sharp and intense Bragg reflections belonging to single phase cubic garnet structure. Using Miller indices and Bragg's law, the inter planner spacing'd' values were calculated and same are given in Table 1. It is observed from table 1 that'd' values increases with increase in vanadium composition x.

Table: 1 Miller indices (hkl) and Inter planner spacing (d) of $Y_3V_xFe_{5-x}O_{12}$.

Plane	d(A)		
(hkl)	x=0.0	x=0.2	x=0.4
(4 0 0)	3.09	3.09	3.09
(4 2 0)	2.76	2.76	2.77
(4 2 2)	2.52	2.52	2.53
(4 3 1)	2.42	2.43	2.42
(5 2 1)	2.26	2.26	2.26
(6 1 1)	2.01	2.01	2.00
(4 4 4)	1.78	1.78	1.79
(6 4 0)	1.72	1.72	1.72
(6 4 2)	1.65	1.65	1.65
(8 0 0)	1.56	1.54	1.55

(8 4 0)	1.38	1.38	1.38
(8 4 2)	1.35	1.35	1.35

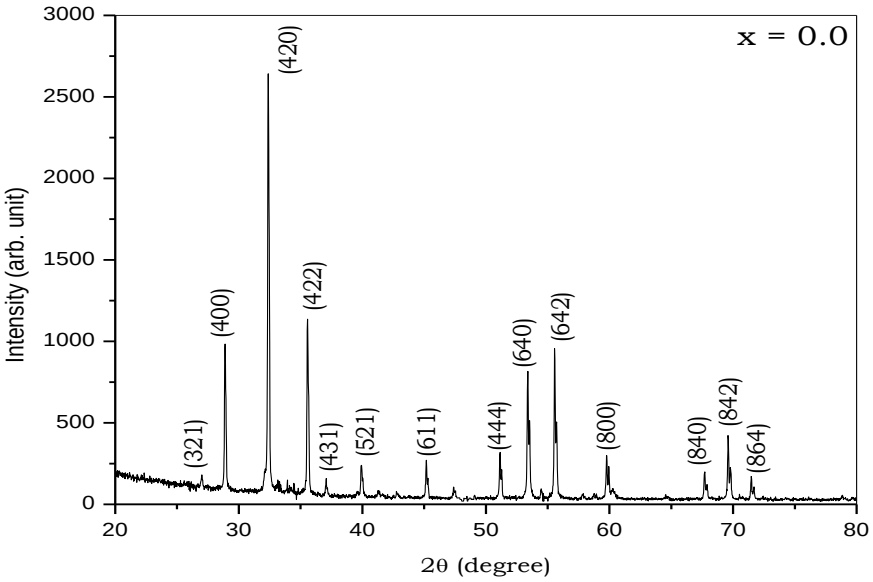

Fig. 1 (a): XRD patterns of $Y_3V_xFe_{5-x}O_{12}$ (x= 0.0)

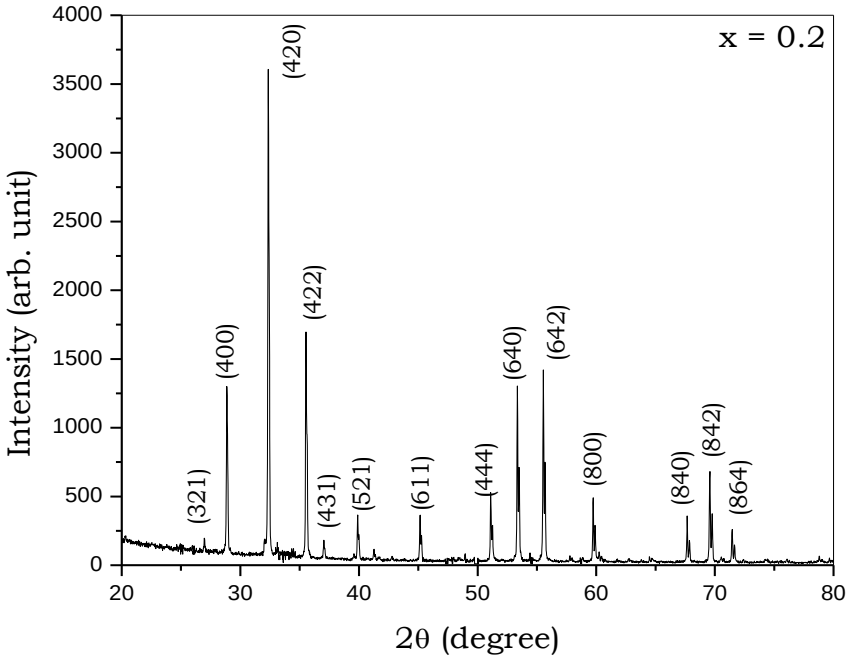

Fig. 1 (b): XRD patterns of $Y_3V_xFe_{5-x}O_{12}$ (x= 0.2)

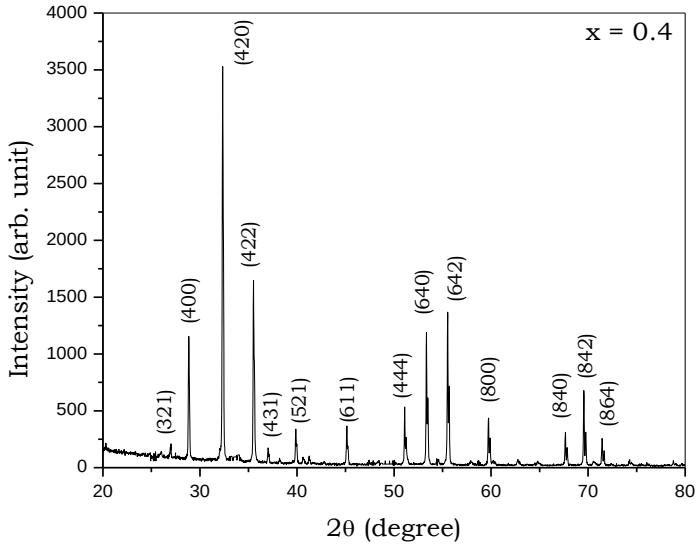

Fig.1 (c): XRD patterns of $Y_3V_xFe_{5-x}O_{12}$ (x= 0.4)

The lattice constant for all the samples of the series $Y_3Fe_{5-x}V_xO_{12}$ was calculated using the values of inter planner spacing and Miller indices. The values of lattice constant are presented in Table 2. The variation of lattice constant 'a' of yttrium iron garnet with vanadium substitution is nearly linear. The lattice constant for pure yttrium iron garnet (a=12.376 Å) fairly agrees well with the literature data [7]. The increase in lattice constant of the present system is due to the replacement of Fe^{3+} (0.67 A. U.) ions of smaller ionic radii by V^{3+} ions of larger ionic radii (0.74 A^0. U.) [8]. Normally, ions of larger radius, when substituted for smaller radius, the lattice constant of the system increase. Here, in the present work Fe^{3+} ions in $Y_3Fe_{5-x}V_xO_{12}$ garnet system were replaced by V^{3+} ions of larger radii this causes the increase in lattice constant of vanadium substituted yttrium iron garnet system.

Table: 2 Lattice constant (a), X-ray density (dx), bulk density (d_B) porosity (P) and particle size (t) of $Y_3V_xFe_{5-x}O_{12}$.

x	a(Å)	dx(gm/cm3)	dB(gm/cm3)	P(%)	t(μm)
0.0	12.364	5.187	4.15	19.99	5.60
0.2	12.373	5.169	4.12	20.29	6.26
0.4	12.381	5.152	4.07	21.00	6.87

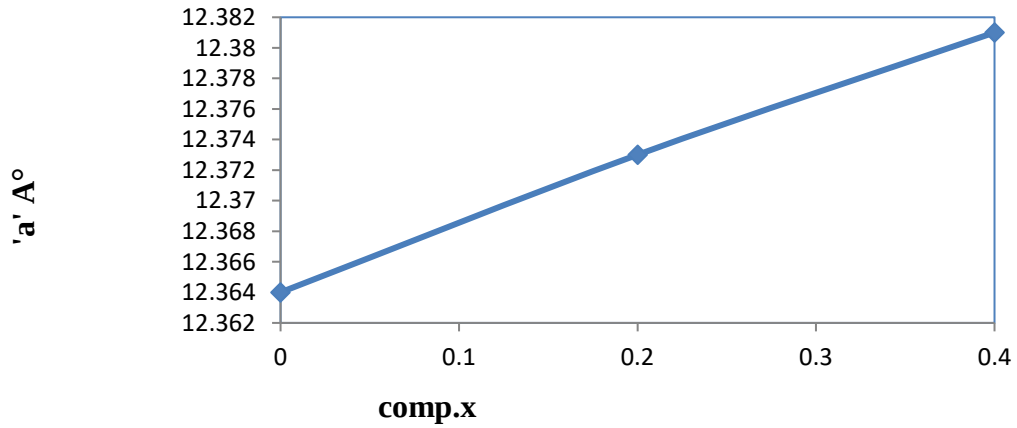

Fig. 2: Variation of lattice constant 'a' with composition (x) of $Y_3V_xFe_{5-x}O_{12}$ (x = 0.0, 0.2 and 0.4).

The X-ray density of the present samples was estimated using the values of experimental lattice parameter and molecular weight. Table 2 gives the values of X-ray density as a function of vanadium composition of x. The X-ray density is inversely proportional to the unit cell volume (a^3) and therefore with increase in lattice constant X-ray density should decrease. The observed behavior of the X-ray density with vanadium composition x is in accordance with the theoretical consideration. Similar behavior of X-ray density was observed in [Al^{3+}] substituted yttrium iron garnet [6]

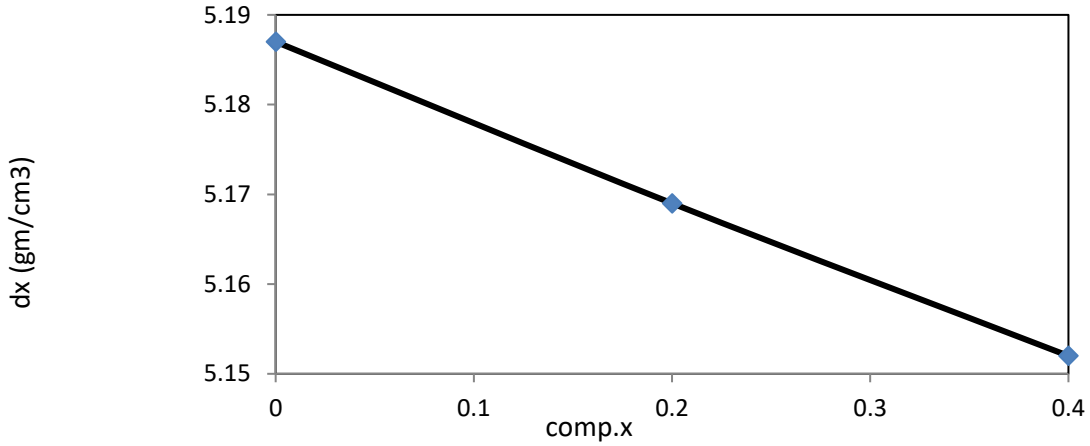

Fig. 3: Variation of X-ray density 'd_x' with composition 'x' of $Y_3V_xFe_{5-x}O_{12}$ (x=0.0, 0.2 and 0.4).

The bulk density of each investigated samples was calculated using the values of mass and volume and are given in Table 2 the bulk density decreases uniformly with the vanadium substitution. The linear decrease in bulk density may be due to increase in the volume with vanadium substitution.

The percentage porosity (P %) of each sample was calculated from the values of bulk density and X-ray density. Table 2 shows the values of porosity as a function of vanadium composition x. It can be seen from table 2 that percentage porosity increases with vanadium composition x. The high values of porosity are may be due to high sintering temperature effect.

The crystallite size (t) of all the samples under investigation were calculated from the full width at half maximum (FWHM) of the highest intensity peak (420) of the X-ray diffraction pattern using the Scherrer formula. The values of particle size for all the composition is listed in Table 2.

It is observed from Table 2 that crystallite size for all the samples is in micrometer range indicating the bulk polycrystalline nature.

IV. INFRARED SPECTROSCOPY

The infrared spectra of $Y_3Fe_{5-x}V_xO_{12}$ are shown in Fig 4. (a-c). The infrared spectra can provide the information regarding structure, bond strengths, imperfection and impurities. IR Spectra reveals that observation in wave number 300-800 cm^{-1} are very intense corresponding to allowed fundamental transitions.

IR spectra show absorption bands near 400 cm^{-1} and 600cm^{-1} assigned to the stretching mode YIG tetrahedron, Our results are similar to Al^{3+} substituted yttrium iron garnet synthesized via citrate gel process [9,10]. The IR bands at 655 cm^{-1}, 605 cm^{-1} can be assigned to new per modes whereas the bands at 397 and 424 cm^{-1} can be assigned to new two modes. Similar results are shown by M. Ristic et. al [11].

Table 3: Vibrational band frequency of $Y_3V_xFe_{5-x}O_{12}$ for x= 0.0 to 0.

x	v1(cm-1)	v2(cm-1)	v3(cm-1)	v4(cm-1)
0.0	655.04	605.15	564.87	424.68
0.2	656.04	616.06	542.95	399.29
0.4	656.05	617.56	541.52	403.02

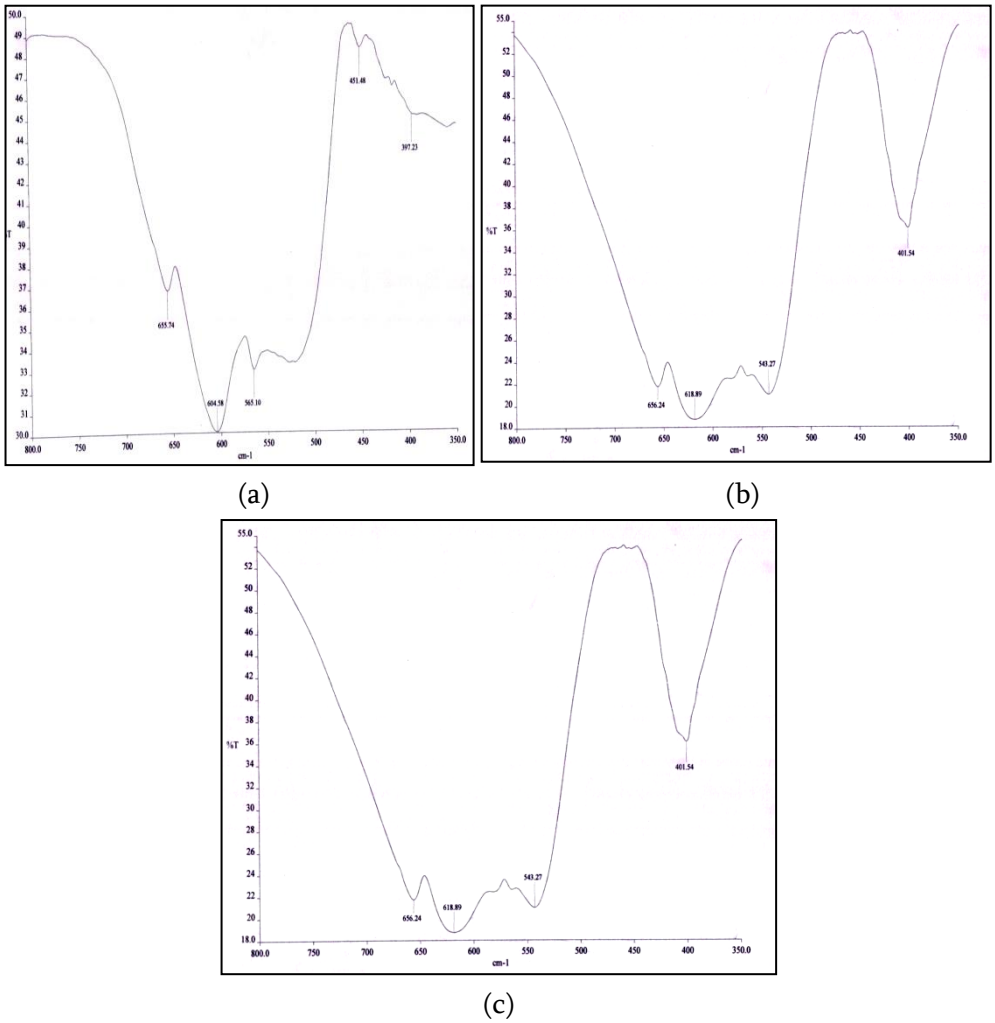

(a) (b)

(c)

Fig.4 (a-c): IR spectra of $Y_3V_xFe_{5-x}O_{12}$ of typical samples x = 0.0, 0.2 and 0.4.

V. CONCLUSION

Taking into consideration the observed experimental results on the structural properties, the following conclusions can be drawn. Using ceramic technique the samples of $Y_3Fe_{5-x}V_xO_{12}$ are successfully prepared. The single phase cubic garnet structure of the prepared samples of $Y_3Fe_{5-x}V_xO_{12}$ was confirmed by X- ray diffraction analysis. The Lattice constant found to be increases with V^{3+} substitution. The x-ray density and bulk density decreases with vanadium composition x. The IR spectra show vibrational band frequencies. Thus,

the substitution of non-magnetic vanadium (V^{3+}) in Yttrium iron garnet (YIG) influences greatly the structural properties.

VI. REFERENCES

[1]. K. Papagelis and S. Ves, J. App .Phys. 94 (2003) 10.

[2]. T. Mizumoto and R. Takei. Tech. Digis, (2010).

[3]. Mitsuru Igarashi and Yoshiyuki Naito. Ieee. Trans. Micro. Theo. Techn. 20 (1972) 12.

[4]. A. F. Lehlooh, S. Mahmood, M. Mozafarri, J. Amighian, J. Hyper. Inter. 156 (2004) 181.

[5]. N. Petrova, D. Todorovsky, I. Mitov, G. Tyuliev, J. Rare Earth 26(2008)307.

[6]. Azadi Motlagh, Z., Mozaffari, M., Amighian, J. Magn. Magn. Mater. 321 (2009) 1980.

[7]. S.Geller, R. M. Bozorth, M. A. Gilleo, and C. E. Miller, J. Phys. Chem. Solids 12 (1959) 111.

[8]. E. W. Gorter, Phililps. Res. Rep 9 (1954) 295.

[9]. Fabien Grasset, Stephane Mornet, Alain Demourgues, Josik Portier, Sacaues Bonnet, Antoine vekris, Etienne Duguet, J. Magn. Magn. Mater. 234 (2001) 409.

[10]. A. M. Hotmeister,K. R. Campbell, J. Appl. Phys. 72(1992) 638.

[11]. M. Ristic, I. Nowik, S. Popovic, I. Felner, S. Music, J. Mater. Lett. 57 (2003) 2584.

International Journal of Scientific Research in Science and Technology
Volume 11 | Issue 13| Print ISSN: 2395-6011 | Online ISSN: 2395-602X (www.ijsrst.com)

VSM Analysis of $CoFe_{2-2x}Ti_xMn_xO_4$ Nanoparticles

R. T. Ubale[1], C. M. Kale*[2]

[1]Department of Physics, Siddharth Arts Commerce and Science College, Jafrabad, Maharashtra, India

[2*]Department of Physics, Indraraj Arts, Commerce, and Science College, Sillod-Chhatrapati Sambhajinagar-431112, Maharashtra, India

ABSTRACT

The distinct compositions of $Co_{1-x}Cd_xFe_2O_4$ (x= 0.0, 0.1, 0.2, 0.3, 0.4, 0.5) samples were prepared by using the sol-gel auto combustion method characterized to understand their physical and magnetic properties. The X-ray diffraction (XRD) analysis shows the existence of a single-phase cubic spinel structure with an increase of lattice constant as Cd content increases. The magnetic properties of the $CoFe_{2-2x}Ti_xMn_xO_4$ (x = 0.00, 0.05, 0.10, 0.15, and 0.20) nanoparticles were investigated using a vibrating sample magnetometer (VSM) technique at room temperature and a magnetic field of 5 KOe. The magnetic properties such as saturation magnetization, magnetic moment, squareness ratio, coercivity, and anisotropy constant are reported. The M-H curve shows the reduction in coercivity while enhancement in saturation magnetization with the substitution of Cd^{2+} ions in the Co-Cd ferrite, low coercivity value of ferrite have soft. Such materials are interesting from the applications point of view in recording media; magnetic tape and coating technology to minimize energy loss.

Keywords: Sol-gel, X-ray diffraction, Lattice constant, Magnetic, Nano ferrite.

I. INTRODUCTION

Since a few decades ago, scientists have explored the spinel ferrites, represented by the formula MFe_2O_4, for a variety of technological applications [1, 2]. These materials stand out due to the dual magnetic and electrical capabilities that they possess. Due to their superior magnetic and electrical characteristics, they are irreplaceable candidates for memory storage devices [3], transformer cores [4], energy storage devices [5], gas sensors [6], microwave devices [7], etc.

In this new era of science and technology, recent advancements in Nanoscience and nanotechnology have made magnetic nanoparticles of spinel ferrite a focus of investigation for many scientists [8]. Magnetic nanoparticles are notable for their chemical stability, Nano scale dimensions, large surface-to-volume ratio, improved homogeneity, ease of manufacturing, etc. These characteristics have led to the widespread usage of spinel ferrite nanoparticles in a variety of applications, including sensors, catalysts, water purification, targeted medication delivery, hyperthermia, etc. [9-11]. The performance of spinel ferrite nanoparticles is dependent on several variables, including the method of synthesis, synthesis parameters, chemical composition, and type and nature of the dopant.

Typically, wet chemical synthesis methods such as chemical co-precipitation, hydrothermal, freeze drying, sol-gel auto combustion, microemulsions, etc. were used to create spinel ferrite nanoparticles. Among these

techniques, the sol-gel auto-combustion process offers several benefits, including the ability to produce homogenous particle dispersion and no need for high temperatures specialized environments, or expensive setup [12]. The structure of the spinel ferrite unit cell has tetrahedral (A) and octahedral [B] locations where cations of various sizes and valences can fit [8].

Among all spinel ferrites, cobalt ferrite ($CoFe_2O_4$) stands out as a special class of magnetic materials [13]. It has an inverted spinel structure, with Co^{2+} ions predominating at the [B] site of the octahedron. High electrical resistivity, high saturation magnetization, high Curie temperature, high magneto crystalline anisotropy constant, etc. are all notable characteristics of cobalt ferrite [14]. Cobalt ferrites are used in many different applications, such as high-frequency devices, sensors, gyrators, circulators, etc., because of their significant electrical and magnetic characteristics [15, 16].

In light of this, the present paper focuses on the synthesis, structural, magnetic, behaviour of Ti^{4+}-Mn^{2+}co-substituted cobalt ferrite ($CoFe_2O_4$) nanoparticles with composition as $CoFe_{2-2x}Ti_xMn_xO_4$ (x = 0.00, 0.05, 0.10, 0.15 and 0.20).

II. EXPERIMENTAL DETAILS

2.1 Materials

For the preparation of series of samples, we have used well known sol-gel auto combustion method by using nitrate route for obtaining nano-ferrite material. For the preparation of $CoFe_{2-2x}Ti_xMn_xO_4$ (x = 0.00, 0.05, 0.10, 0.15, and 0.20) nanoparticles, analytical grade (AR grade) Ferric nitrate [$Fe(NO_3)_2 \cdot 9H_2O$], cobalt nitrate [$Co(NO_3)_2 \cdot 6H_2O$], manganese nitrate [$Mn(NO_3)_2 \cdot 6H_2O$], titanium tetrabutoxide [$Ti(OCH_2CH_2CH_2CH_3)_4$], citric acid [$C_6H_8O_7 \cdot H_2O$], ammonia solution [$NH_3.H_2O$], acetone, and distilled water were used as a primary chemical. All chemicals used were 99.99% pure (AR grade) and the solutions were prepared with distilled water used as a solvent.

III.RESULTS AND DISCUSSION

3.1 X-ray Diffraction (XRD) Analysis

The structural analysis of the prepared samples was performed by powder X-ray diffraction (XRD) analysis. The XRD patterns of $CoFe_{2-2x}Ti_xMn_xO_4$ (x = 0.00, 0.05, 0.10, 0.15, and 0.20) nanoparticles are shown in Fig. 1.

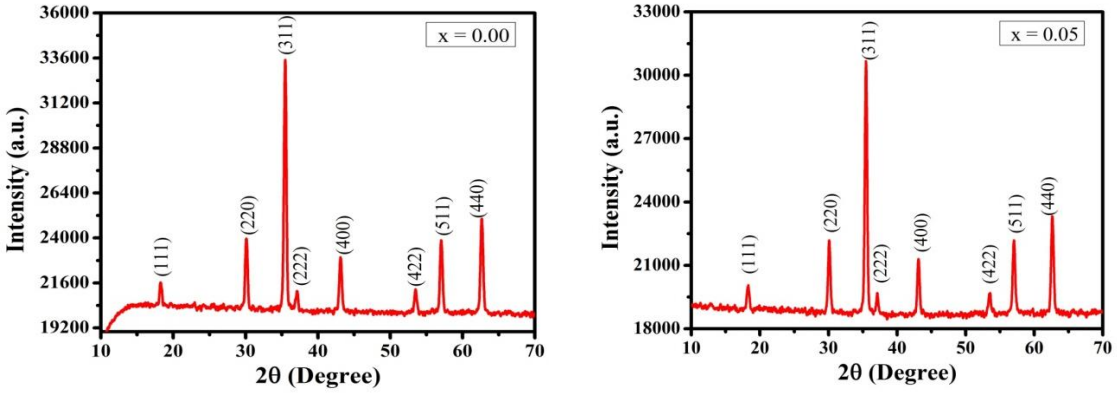

Fig. 1: XRD pattern of $CoFe_{2-2x}Ti_xMn_xO_4$ (x = 0.00 and x = 0.05) nanoparticles

It is observed from Fig. 1 that the XRD patterns have peaks at the reflections plane indexed as (111) (220), (311), (222), (400), (422), (511) and (440) for all the compositions of $CoFe_{2-2x}Ti_xMn_xO_4$ (x = 0.00, 0.05, 0.10, 0.15 and 0.20) nanoparticles. The presence of all the peaks in the XRD pattern proves the formation of a single-phase cubic spinel structure. All these peaks in the XRD pattern are sharp and intense. The observed reflections perfectly matched with those reported data of cobalt ferrite [13, 14,]. The XRD peak does not show any additional peak other than that mentioned above indicating the high purity of prepared samples. Due to the substitution of Ti-Mn ions in cobalt ferrite Bragg's angle shifts towards a lower angle which reflects the incorporation of Ti-Mn ions in cobalt ferrite Fig. 1.Using the values of Bragg's angle 2θ and interplanar spacing d, the values of lattice constant for all the compositions are calculated using the following relation,

$$a = d\sqrt{h^2 + k^2 + l^2} \qquad \text{Å}$$

The values of the lattice constant change with the Ti-Mn composition x. It is observed that the lattice constant increases with an increase in Ti-Mn composition x. The variation of lattice constant with Ti-Mn composition x could be attributed to the substitution of Ti^{4+}-Mn^{2+} ions of larger ionic radii in place of Fe ions of smaller ionic radius.

3.2 Vibrating Sample Magnetometer (VSM) Analysis

The magnetic properties of the $CoFe_{2-2x}Ti_xMn_xO_4$ (x = 0.00, 0.05, 0.10, 0.15, and 0.20) nanoparticles were investigated using a vibrating sample magnetometer (VSM) technique at room temperature. The M-H hysteresis plots for typical samples of $CoFe_{2-2x}Ti_xMn_xO_4$ (x = 0.00, 0.05) nanoparticles are shown in Figure 2.

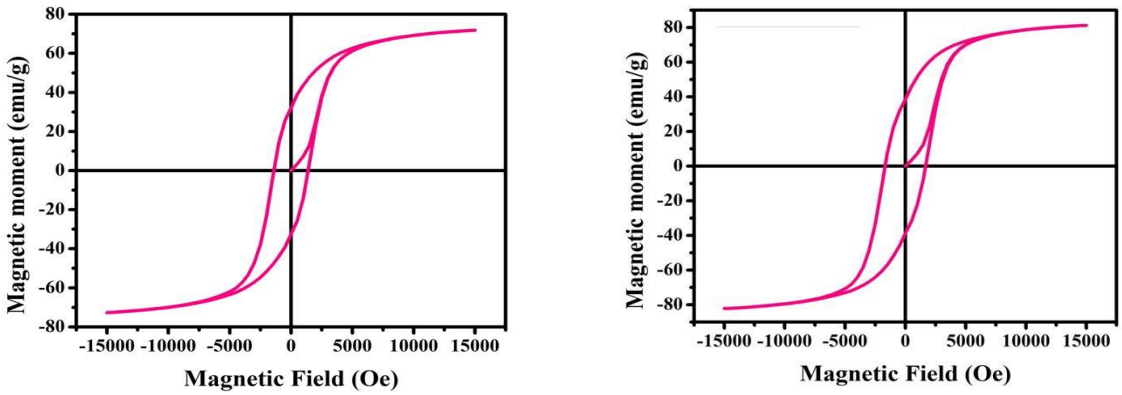

Fig.2: M-H hysteresis plot of $CoFe_{2-2x}Ti_xMn_xO_4$ (x = 0.00 and x = 0.05) nanoparticles

The values of saturation magnetization (Ms), coercivity (Hc), remanence magnetization (Mr), remanence ratio (Mr/Ms), and magneton number (n_B) are presented in the following Table 1.It is observed from Table 1 that, the saturation magnetization for all the samples of $CoFe_{2-2x}Ti_xMn_xO_4$ (x = 0.00, 0.05, 0.10, 0.15, and 0.20) nanoparticles shows random nature with Ti-Mn doping. The saturation magnetization values were found in the range of 56.17 emu/gm to 81.76 emu/g. The random behavior of the magnetization values could be due to an increase in the concentration of Ti^{4+}-Mn^{2+}, the exchange interaction between (A) and [B] sites gets altered resulting in the strengthening or weakening of [B]-[B] interaction and (A)-[B] interaction, which leads to random behavior of saturation magnetization [17, 18]. The decrease in saturation magnetization for higher concentrations of Ti-Mn is due to the substitution of non-magnetic Ti^{4+} ions in place of magnetic iron (Fe) ions. The doping of non-magnetic ions reduces the super exchange interaction which results in the reduction of

magnetization at the higher Ti-Mn doping. In the present case, the substitution of Ti ions reduces the super-exchange interaction, and therefore saturation magnetization decreases.

Table 1

Values of Saturation magnetization (M_S), Remanence magnetization (M_r), Coercivity (H_C), Remanence ratio (M_r/M_S), and Magneton number (n_B) for $CoFe_{2-2x}Ti_xMn_xO_4$ (x = 0.00, 0.05, 0.10, 0.15 and 0.20) nanoparticles

Composition (x)	M_S (emu/gm)	M_r (emu/gm)	H_C (Oe)	M_r/M_S	n_B (Obs.) (μ_B)
0.00	72.26	32.28	1394.8	0.4467	3.04
0.05	81.76	38.60	1679.8	0.4721	3.43
0.10	56.17	25.87	1487.7	0.4573	2.37
0.15	64.25	30.00	1219.6	0.4669	2.68
0.20	68.38	28.86	1004.7	0.4220	2.85

Magneton number (n_B) for all the samples was calculated by using the following equation and their saturation magnetization values for all the samples of $CoFe_{2-2x}Ti_xMn_xO_4$ (x = 0.00, 0.05, 0.10, 0.15, and 0.20) nanoparticles are presented in Table 1.

$$n_B = \left(\frac{\text{Mol.Weight} \times M_Z}{5585} \right) \mu_B$$

The magneton number shows similar behavior to saturation magnetization on doping of Ti-Mn in cobalt ferrite. The values of remanence magnetization (Mr) were obtained from M-H plots and are presented in Table 1. It can be observed from Table 1 that the remanence magnetization shows random behaviour with an increase in Ti-Mn content x. The random behaviour of remanence magnetization values can be attributed to the substitution of nonmagnetic Ti ions in cobalt ferrite [19]. The values of coercivity obtained from M-H plots are presented in Table 1. It can be observed from Table 1 that all the samples show high values of coercivity confirming the ferromagnetic nature. Further, it can be observed that the coercivity shows random behaviour with an increase in doping of Ti-Mn content x.

The decrease in coercivity values with higher content of Ti-Mn can be attributed to the doping of nonmagnetic Ti ions in cobalt ferrite. In general, the coercivity of polycrystalline ferrites depends upon the magneto-crystalline anisotropy constant, average grain size, domain wall energy, and several other parameters. The decreases in magnetic coercivity suggest a decrease in magnetic losses since the hysteresis loss is proportional to the coercivity of the material. The ratio of remanence magnetization to saturation magnetization called as remanence ratio (Mr/Ms) for all the samples of $CoFe_{2-2x}Ti_xMn_xO_4$ (x = 0.00, 0.05, 0.10, 0.15, and 0.20) nanoparticles are presented in Table 1.

IV. CONCLUSIONS

The Ti^{4+}-Mn^{2+} co-doped cobalt ferrite nanoparticles with compositions as $CoFe_{2-2x}Ti_xMn_xO_4$ (x = 0.00, 0.05, 0.10, 0.15, and 0.20) were successfully prepared using sol-gel auto combustion method. X-ray diffraction data revealed the pure phase formation with cubic spinel structure for all the compositions. The lattice constant increased with Ti^{4+}-Mn^{2+} co-doping x, which is attributed to the difference in ionic radii of cobalt and

titanium/manganese. Saturation magnetization and magneton number both showed random behaviour with Ti^{4+}-Mn^{2+} co-doping x.

V. REFERENCES

[1]. H. Qin, Y. He, P. Xu, D. Huang, Z. Wang, H. Wang, Z. Wang, Y. Zhao, Q. Tian, C. Wang, Spinel ferrites (MFe2O4): Synthesis, improvement and catalytic application in environment and energy field, Advances in Colloid and Interface Science, 294 (2021) 102486.

[2]. D.H.K. Reddy, Y.-S. Yun, Spinel ferrite magnetic adsorbents: alternative future materials for water purification?, Coordination Chem. Reviews, 315 (2016) 90.

[3]. R.S. Mane, V. Jadhav, Spinel ferrite nanostructures for energy storage devices, Elsevier, 2020.

[4]. U. Ahmad, M. Afzia, F. Shah, B. Ismail, A. Rahim, R.A. Khan, Improved magnetic and electrical properties of transition metal doped nickel spinel ferrite nanoparticles for prospective applications, Materials Science in Semiconductor Processing, 148 (2022) 106830.

[5]. A. Manohar, V. Vijayakanth, S.P. Vattikuti, K.H. Kim, Structural, BET and EPR properties of mixed zinc-manganese spinel ferrites nanoparticles for energy storage applications, Ceramics International, 49 (2023) 19717-19727.

[6]. A. Šutka, K.A. Gross, Spinel ferrite oxide semiconductor gas sensors, Sensors and actuators B: chemical, 222 (2016) 95-105.

[7]. M. Pardavi-Horvath, Microwave applications of soft ferrites, Journal of Magnetism and Magnetic Materials, 215 (2000) 171-183.

[8]. T. Tatarchuk, M. Bououdina, J. Judith Vijaya, L. John Kennedy, Spinel ferrite nanoparticles: synthesis, crystal structure, properties, and perspective applications, in Nanophysics, Nanomaterials, Interface Studies, and Applications: Selected Proceedings of the 4th International Conference Nanotechnology and Nanomaterials (NANO2016), August 24-27, 2016, Lviv, Ukraine, Springer, 2017, pp. 305-325.

[9]. K.K. Kefeni, T.A. Msagati, T.T. Nkambule, B.B. Mamba, Spinel ferrite nanoparticles and nanocomposites for biomedical applications and their toxicity, Materials Science and Engineering: C, 107 (2020) 110314.

[10]. A. Soufi, H. Hajjaoui, R. Elmoubarki, M. Abdennouri, S. Qourzal, N. Barka, Spinel ferrites nanoparticles: synthesis methods and application in heterogeneous Fenton oxidation of organic pollutants–a review, Applied Surface Science Advances, 6 (2021) 100145.

[11]. N. Sanpo, C. Wen, C. Berndt, J. Wang, Antibacterial properties of spinel ferrite nanoparticles, in Microbial pathogens and strategies for combating them: science, technology and education, Formatex Research Center, 2013, pp. 239-250.

[12]. A. Sutka, G. Mezinskis, Sol-gel auto-combustion synthesis of spinel-type ferrite nanomaterials, Frontiers of Materials Science, 6 (2012) 128-141.

[13]. S. Jauhar, J. Kaur, A. Goyal, S. Singhal, Tuning the properties of cobalt ferrite: a road towards diverse applications, RSC advances, 6 (2016) 97694-97719.

[14]. I. Gul, A. Maqsood, Structural, magnetic and electrical properties of cobalt ferrites prepared by the sol–gel route, Journal of Alloys and Compounds, 465 (2008) 227-231.

[15]. S. Amiri, H. Shokrollahi, The role of cobalt ferrite magnetic nanoparticles in medical science, Materials Science and Engineering: C, 33 (2013) 1-8.

[16]. S. Y. Srinivasan, K.M. Paknikar, D. Bodas, V. Gajbhiye, Applications of cobalt ferrite nanoparticles in biomedical nanotechnology, Nanomedicine, 13 (2018) 1221-1238.

[17]. B. Patil, R. Kokate, Synthesis and design of magnetic parameters by Ti doping in cobalt ferrite nanoparticles for nanoelectronics applications, Procedia Manufacturing, 20 (2018) 147-153.

[18]. A.P. Amaliya, S. Anand, S. Pauline, Investigation on structural, electrical and magnetic properties of titanium substituted cobalt ferrite nanocrystallites, Journal of Magnetism and Magnetic Materials, 467 (2018) 14-28.

[19]. J. Pal, S. Kumar, R. Kaur, P. Agrawal, M. Singh, A. Singh, Structural and magnetic characterization of Ti-doped cobalt ferrite (CoFe2O4), in AIP Conference Proceedings, AIP Publishing, 2018.

International Journal of Scientific Research in Science and Technology
Volume 11 | Issue 13| Print ISSN: 2395-6011 | Online ISSN: 2395-602X (www.ijsrst.com)

Flood Mapping Using Microwave Remote Sensing

Dheeraj Raut*[1], Gaus Mohiuddin Sayyad[2], Ashok Dongare[3], Shailendra Kolhe[4], Shafiyoddin Sayyad*[1]

*[1]Microwave & Imaging Spectroscopy Research Lab, Milliya College, Beed, Maharashtra, India

[2]MGM's Jawaharlal Nehru Engineering College, Aurangabad, Maharashtra, India

[3]Department of Physics, Vasantdada Patil College, Patoda, Maharashtra, India

[4]Department of Physics, Shivaji Arts, Commerce & Science College, Kannad, Dist. Aurangabad Maharashtra, India

ABSTRACT

In early July 2023, Himachal Pradesh, India, faced extensive flooding caused by exceptionally heavy rainfall, exceeding 220 mm. The rising water levels in rivers surpassed their danger thresholds, resulting in widespread flooding. Numerous areas in the state suffered severe damage to land and property, leading to loss of lives. India's distinct rainfall patterns make it susceptible to flooding, emphasizing the need for precise information to manage disasters effectively.

This study introduces a simple yet effective approach to identify regions affected by flooding and monitor changes. Sentinel-1A SAR data from both pre-flood and during-flood images of Bilaspur District (HP) were analyzed. SAR data proves adept at detecting water bodies on surfaces and within flood-prone areas due to its sensitivity to specular reflection, resulting in reduced backscattered energy as a significant portion disperses away from the sensor. Conversely, areas without water exhibit increased returns due to surface irregularities. Through preprocessing and the application of a thresholding method, flood-affected areas were isolated. A comparison of these results with meteorological department records underscores the efficacy of SAR data in flood detection and surveillance.

Keywords: — SAR, Thresholding, Flood Detection.

I. INTRODUCTION

Floods are globally significant natural disasters that inflict extensive damage on infrastructure, property, and human lives. India, with its diverse geography and varying climate conditions, is particularly susceptible to flooding. Historical instances of severe flooding in the country have had profound impacts on the economy and led to tragic loss of lives [1]. Understanding the factors contributing to floods and efforts for mitigation is crucial for effective disaster management. Himachal Pradesh, situated in northern India, is characterized by rugged terrain, abundant rivers, and monsoon-driven rainfall patterns, making it prone to periodic flooding events [2].

To assess the extent of flooding, information can be gathered through on-site data collection (in-situ) and remote sensing via aerial and satellite methods [3]. However, relying solely on in-situ data collection for flood detection can be impractical, expensive, and time-intensive. Aerial photography analysis can incur high costs.

Therefore, obtaining imagery from satellite remote sensing proves to be an efficient and straightforward approach for assessing the extent of flooding across expansive geographical regions at regular intervals [4-8].

This study is based on active remote sensing satellite Sentinel-1A C band SAR sensor, part of the European Space Agency's Sentinel program. It is useful for all-weather, day-and-night monitoring, operating in different Swath modes (IW, EW, SM, and OW) for applications like disaster monitoring, mapping, and oceanography. The dataset offers dual polarization (VV+VH) imagery with a high revisit frequency and a 12-day repeat cycle, enabling regular monitoring and timely data acquisition for various Earth observation applications. Due to its ability to emit and capture signals under limited visibility conditions, such as nighttime or cloud cover, synthetic aperture radar (SAR) is exceptionally adept at defining water boundaries during flood occurrences [9-10].

Among the available methodologies, thresholding SAR imagery stands out for its efficiency and proven effectiveness in delineating the extent of inundation [11-12]. The selection of an appropriate threshold is crucial for accurate image classification using the Thresholding method. Manual threshold determination is time-consuming and unsuitable for this purpose, especially when water occupies only a small portion of the image, causing overlap between water and background distributions. Consequently, automating the water extraction process becomes imperative [13-14].

In this study, a completely automated processing framework designed for swift mapping of floods and surface water is utilized, employing Sentinel-1 amplitude data and incorporating seamless labelling. The main focus centres around an exceptional flooding incident captured via satellite imagery, resulting from intense rainfall in July 2023. The flood scenario observed is explained using satellite images obtained before and during the flooding, alongside hydrological and meteorological information.

II. STUDY AREA & DATASET

The selected region for examination is Bilaspur District in Himachal Pradesh. This district is linked to Govind Sagar, one of India's largest lakes, as illustrated in Figure 1. The study area's geographical coordinates range from 31.200° to 31.500° N latitude and 76.500° to 76.800° E longitude. Himachal Pradesh situated in the north side of India, where water is available through a network of many rivers. Heavy rainfall i.e., more than 220 mm during 7 to11 July 2023 raised the water level of the rivers, especially the Yamuna River, which originates from Yamunotri, causing widespread destruction of land and property and the loss of lives. There have been instances of landslides, power cut, roadblocks, and bridges washing away due to swollen rivers.

The Sentinel-1A satellite in Ground Range Detected (GRD) mode, featuring an Interferometric Wide (IW) swath, was used to acquire both pre-flood and during flood images. These images underwent Level-1 processing. For this study, two datasets were employed: one captured before the flood on 07/04/2023 and another during the flood on 12/07/2023 in the Bilaspur district. The dataset ID numbers are S1A_IW_GRDH_1SDV_20230407T005138_20230407T005203_047983_05C455_8191 and S1A_IW_GRDH_1SDV_20230712T005143_20230712T005208_049383_05F03C_C9C2, respectively. In this study, VV polarization images are considered.

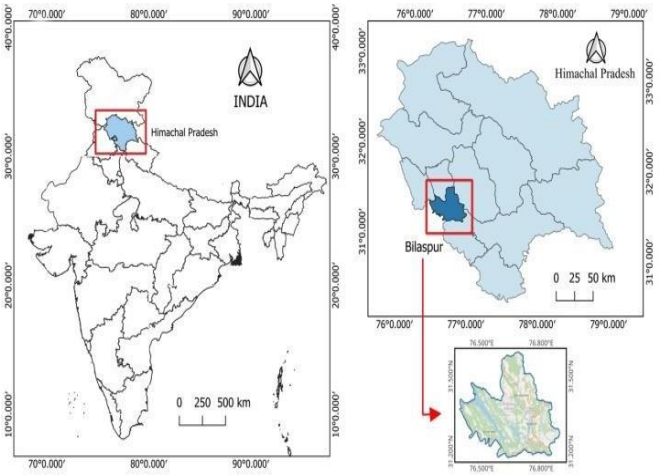

Figure 1: Map showing study area

III.METHODOLOGY

The image processing procedure for flood detection was meticulously executed using the Sentinel Application Platform (SNAP) software. SNAP, developed by the European Space Agency, stands as a freely available open-source software package, designed to facilitate the analysis of satellite data. This powerful tool is instrumental in processing and interpreting data from various Earth observation missions, including the Sentinel series.

The analysis focused on images of Bilaspur District in Himachal Pradesh, captured both before and during the flood event. Leveraging the capabilities of SNAP, the goal was to identify and delineate areas affected by flooding. A straightforward yet highly effective technique was employed to differentiate between permanent water bodies and those that were inundated due to the flood.

The approach used in this study is comprehensively illustrated in Figure 2, providing a visual representation of the image processing steps undertaken. This figure serves as a valuable reference, outlining the specific methodology applied to analyze the Sentinel imagery and extract meaningful information related to the flood event in Bilaspur District.

The utilization of SNAP software ensured a systematic and reliable process, taking advantage of its features for image interpretation, manipulation, and extraction of relevant data. This study's methodology aimed not only to detect the presence of floods but also to distinguish between permanent water bodies and areas newly affected by the inundation, providing valuable insights for further analysis and disaster management efforts [15].

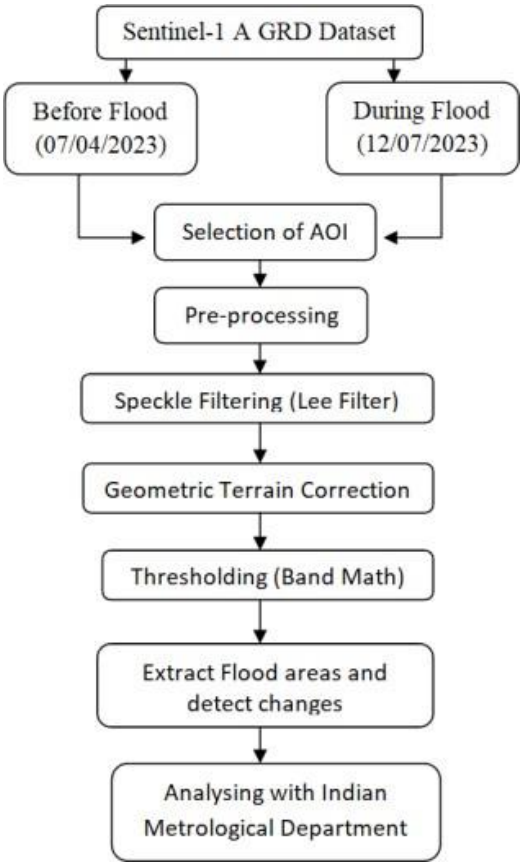

Figure 2: Visual Representation of Data Processing

IV. RESULTS AND DISCUSSION

Between July 7th and July 11th, 2023, Himachal Pradesh faced severe monsoon conditions characterized by widespread heavy to extremely heavy rainfall across most regions of the state. Typically, during the monsoon period from June to September, the state receives a cumulative rainfall of 734.4 mm. However, in just four days from July 7th to 11th, 2023, the state experienced an extraordinary rainfall of 223 mm, deviating by 436% from the expected normal rainfall of 41.6 mm. The subsequent Table-1 presents district-wise cumulative heavy rainfall, primarily affected during the period of July 7th to 11th, 2023. [16]

The reflective intensity of a radar target concerning the ground unit area is quantified by the backscattering coefficient, denoted as sigma "0" [17]. Various land surface attributes, including vegetation, roughness, dielectric constant, and geometry, influence both the amplitude and phase of the backscattering signal [18].

TABLE I DISTRICT-WISE CUMULATIVE HEAVY RAINFALL

District	Actual (in mm)	Normal (in mm)	Departure (in %)
Bilaspur	335.9	44.5	655
Chamba	207.9	49.6	319
Hamirpur	258.7	49.2	426
Kullu	280.1	30.7	812
Shimla	268.9	35.4	660
State Avg.	**223**	**41.6**	**436**

Between July 7th and July 11th, 2023, the Bilaspur district experienced unusually heavy rainfall, leading to the application of the thresholding method for analyzing this specific area. Subsequent to the thresholding

procedure, Figure 3 (a) presents the backscattering coefficient, sigma 0_vv, measured at 53.57 dB in April before the flood, while Figure 3 (b) illustrates the backscattering coefficient, sigma 0_vv.

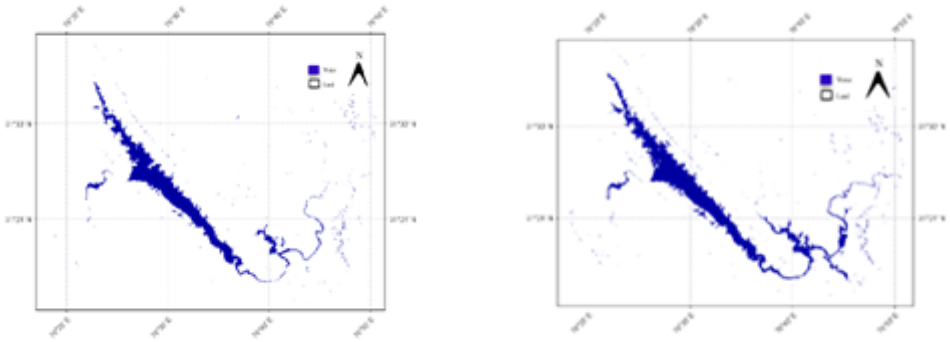

Figure 3: Calibrated thresholding method for Study area. a) Before flood and b) during flood.

Currently, the thresholding method employs the backscattering coefficient (sigma "0" for VV polarization) to distinguish between water and dry land areas. Histogram analysis is used for interpretation, illustrating the relationship between frequency (#pixels) and intensity (dB) before the flood (April 7, 2023) and during the flood (July 12, 2023), enabling a comparison between the two scenarios.

Figure 4 (a) presents the histogram of VV polarization data before the flood, covering intensity values from -32.49 dB to 12.94 dB. This clearly separates water (with a small peak) from land (with a larger peak). In contrast, Figure 4 (b) shows the intensity range from -32.49 dB to -18 dB, representing only the water area. The threshold value, determined at the minimum intensity point between these two peaks, is found to be -18 dB. In Figure 4 (c), the histogram of VV polarization during the flood displays intensity values ranging from -29.78 dB to 13.32 dB, revealing a clear distinction between water (small peak) and land (larger peak). Similarly, Figure 4 (d) depicts the intensity range from -29.78 dB to -18 dB, representing only the water area. In this case, the threshold value remains consistent at -18 dB. In the analysis, an increase in histogram intensity values indicates a rise in water level in the study area.

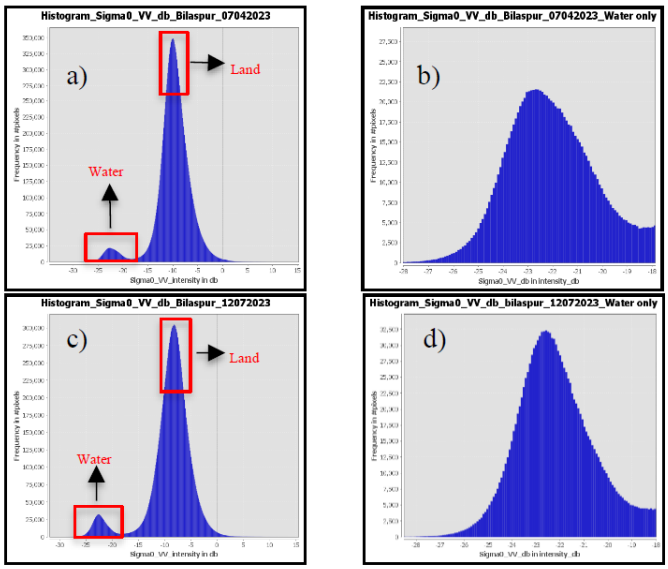

Figure 4 a) Histogram depicting the characteristic distribution of VV polarization of study area before the flood. b) Histogram solely representing water zones before the flood. c) Histogram depicting the characteristic

distribution of VV polarization in study area during the flood. d) Histogram solely representing water zones during the flood.

The application of the "Merging of raster layers" image overlapping technique in QGIS serves as a powerful tool for visualizing and quantifying the increase in water levels resulting from heavy rainfall over the study area. QGIS, an open-source Geographic Information System (GIS) software, allows for the manipulation and analysis of spatial data, making it well-suited for examining changes in geographical features over time.

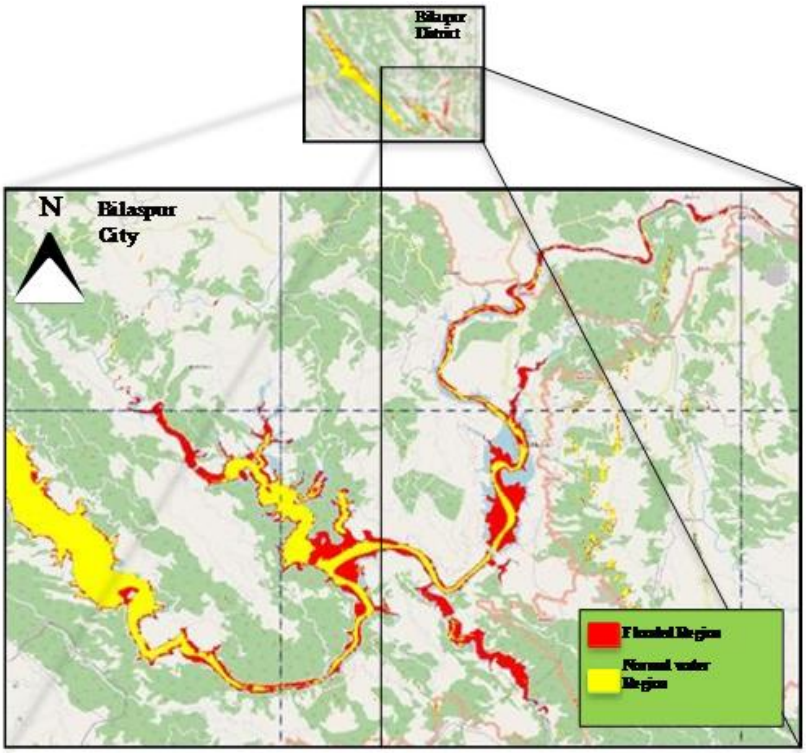

Figure 5. Raster layer merge of maps of the entire study area - Bilaspur City. Showing normal water region (yellow) and during flooded region (Red).

In the context of this study, the merging of raster layers involves overlaying different layers of raster images representing the study area, particularly those captured before and during the flood. The resulting composite image vividly illustrates the spatial variations in water levels, providing a clear visual representation of the impact of heavy rainfall.

Figure 5 serves as a key visual aid, presenting the outcomes of the image overlapping technique. The distinctions between water bodies before the flood (depicted in the yellow zone) and during the flood (highlighted in the red zone) are clearly delineated. This visual representation allows for an intuitive understanding of the extent and location of changes in water levels over the study area.

The use of QGIS and the "Merging of raster layers" technique not only enhances the interpretability of the data but also facilitates quantitative analysis of the changes in water levels. This information is crucial for assessing the severity of the flood impact, identifying vulnerable areas, and informing disaster management strategies. The visual clarity provided by Figure 5 contributes significantly to the overall comprehension of the study's findings related to the effects of heavy rainfall on water levels in the specified geographic region.

V. CONCLUSION

This study employed a robust methodology to monitor flooded areas in Bilaspur District using high spatial resolution SAR data. After analyzing statistical parameters from the Sentinel-1 dataset, it was determined that VV polarization yielded the most accurate flood detection results. To mitigate speckle noise, which can degrade image quality and impact flood mapping accuracy, multiple filters were applied. Among these filters, the Lee speckle filter selected with window size of 7x7 emerged as the most effective, providing superior outcomes and contributing to the reduction of false positive values.

The utilization of the binarization or calibration threshold technique is applied in this context to differentiate between pre-flood and during-flood areas. The distinct polarization histogram derived from the backscatter of VV polarization, distinctly indicates an elevation in water levels throughout Bilaspur city.

Upon comparing the flood map's region with information from the Meteorological Centre in Shimla, Himachal Pradesh, we observed promising results. Additionally, as demonstrated in Figure 5, the raster layer merging method within QGIS was utilized, employing processed geocoded images to distinctly portray the differentiation between pre-flood and during-flood areas.

VI. REFERENCES

[1]. P. Wallemacq, C. herden, R. House, “The Human Cost of Natural Disasters 2015: a Global Perspective. Technical Report,” Centre for research on the epidemiology of disasters (2015).

[2]. Himachal Pradesh State Disaster Management Authority (HPSDMA), 2022, Annual Report: Disaster Risk Reduction Initiatives in Himachal Pradesh.

[3]. Jensen, R. J., “Remote Sensing Of The Environment: An Earth Resource Perspective”, Prentice- Hall, Inc., 2nd Edition. Pp.1-10.

[4]. Brakenridge R., Anderson, E., “MODIS- Based Flood Detection, Mapping and Measurement: The Potential for Operational Hydrological Applications”, Transboundary Floods 72, pp, 1-12, 2006.

[5]. Clement, M.A., Kilsby, C.G., Moore, P., “Multi Temporal Synthetic Aperture Radar Flood Mapping Using Change Detection”, J.Flood Risk Manage, pp. 1-17, 2017.

[6]. Klemas, V., “Remote Sensing Of Floods And Flood Prone Areas: An Overview”, J. Coast. Res. 32(4), pp. 1005- 1023, 2014.

[7]. C.M. Bhatt, G. S. Rao, “Ghagra Floods of 2010 In Uttar Pradesh, North India: A Perspective Analysis Using Satellite Remote Sensing Data”, Journal of Geographical and Natural Hazards and Risk, vol.7, no.2, pp.747-763, 2016.

[8]. N. Anusha, B. Bharathi, “Flood Detection And Flood Mapping Using Multi Temporal Synthetic Aperture Radar And Optical Data”, The Egyptian Journal Of Remote Sensing And Space Sciences, Jan 2019. Open Access Hub (copernicus.eu)

[9]. N. Anusha, B. Bharathi, “Change Detection and Flood Water Mapping Using Sentinel-1A Synthetic Aperture Radar Images”, Journal of Computational and Theoretical Nanoscience, Vol.16, pp.3544-3549, 2019.

[10]. Jiyong Liang and Desheng Liu, "A Local Thresholding Approach to Flood Water Delineation Using Sentinel-1 SAR Imagery," ISPRS Journal of Photogrammetry and Remote Sensing, vol. 159, pp. 53-62, January 2020.

[11]. Filsa Bioresita, Anne Puissant, André Stumpf, and Jean- Philippe Malet, "A Method for Automatic and Rapid Mapping of Water Surfaces from Sentinel-1 Imagery," Remote Sensing, vol. 10, pp. 217, February 2018.

[12]. Han Cao, Hong Zhang, Chao Wang, and Bo Zhang, "Operational Flood Detection Using Sentinel-1 SAR Over Large Areas," Water, vol. 11, pp. 786, April 2019.

[13]. Francisco Carreño Cande and Marina de Mata Muñoz, "Flood Monitoring Based on the Study of Sentinel-1 SAR Images: The Ebro River Case Study," Water, vol. 11, pp. 2454, November 2019.

[14]. Federico Filipponi "Sentinel-1 GRD Preprocessing Workflow", Proceedings vol.18, June 2019

[15]. Government of India, Ministry of Earth Sciences, India Meteorological Department, Meteorological Centre, Shimla (HP), Unprecedented Rainfall in Himachal Pradesh for the period 07.07.2023-11.07.2023 Brief Write up

[16]. European space agency (ESA). The ASAR user Guide. online:https://earth.esa.int/handbooks/Asar/toc.html

[17]. Gorrab, M. Zribi, N. Baghdadi, B. Mougenot, P. Fanise, Z.L. Chabaane, "Retrieval of Both Soil Moisture and Texture Using TerraSAR-X Images," Remote Sensing, vol. 7, pp. 10098–10116, 2015.

International Journal of Scientific Research in Science and Technology
Volume 11 | Issue 13| Print ISSN: 2395-6011 | Online ISSN: 2395-602X (www.ijsrst.com)

Raman Effect and Applications of Raman Effect in the Study of Nanoparticles

Swati Kulkarniirst*, Vinayak Deshmukh
*Shri Siddheshwar Mahavidyalaya, Majalgaon, Dist. Beed, Maharashtra, India

ABSTRACT

Nanoparticles have gained a lot of attention in recent years due to their unique properties and potential applications in various fields such as biotechnology, materials science, and electronics. To understand their properties and behavior, it is essential to study their vibrational modes using spectroscopic techniques, and Raman scattering is one of the powerful techniques. The Raman effect has numerous applications in the study of nanoparticles. One of the most important of these is in the characterization of the vibrational modes of nanoparticles. By analyzing the Raman spectra of nanoparticles, researchers can identify the different vibrational modes present in the material and determine its chemical composition. The current manuscript explores the Raman effect and its applications in the study of nanoparticles.

Keywords: nanoparticles, Raman effect, vibrational modes

I. INTRODUCTION

T Nanoparticles have gained a lot of attention in recent years due to their unique properties and potential applications in various fields such as biotechnology, materials science, and electronics. To understand their properties and behavior, it is essential to study their vibrational modes using spectroscopic techniques, and Raman scattering is one of the most powerful techniques.

The Raman effect was discovered by the Indian physicist Bharatratna Sir C.V. Raman in 1928. The Raman effect has been widely studied and has important applications in various fields, including chemistry, physics, and materials science. and it has since become an important tool in the study of materials, including nanoparticles.

Theory of Raman Scattering: Raman scattering is a phenomenon in which the scattered light undergoes a shift in wavelength due to interaction with the vibrational modes of the material. This shift is known as the Raman shift, and it provides valuable information about the vibrational modes and the molecular structure of the material. The Raman shift occurs because the scattered light interacts with the vibrational modes of the material, which can either increase or decrease the frequency of the light.

Raman effect has great practical importance. This phenomenon is universal. Its experimental technique is straightforward. Infra-red absorption spectra of molecules can be shifted in the visible region using the Raman effect. The forbidden absorption lines can also be studied using the Raman effect. The hydrogen-like molecules exhibit the vibrational rotational spectra in the Raman effect.

There are two types of Raman effect: Stokes Raman scattering and anti-Stokes Raman scattering. In Stokes Raman scattering, the scattered photon has lower energy and longer wavelength than the incident photon. This is the most common type of Raman scattering and is caused by a molecule or crystal losing energy to a photon. In contrast, in anti-Stokes Raman scattering, the scattered photon has higher energy and shorter wavelength than the incident photon. This is a less common type of Raman scattering and is caused by a molecule or crystal gaining energy from a photon. The Raman effect has numerous applications in the study of nanoparticles. One of the most important of these is in the characterization of the vibrational modes of nanoparticles. By analyzing the Raman spectra of nanoparticles, researchers can identify the different vibrational modes present in the material and determine its chemical composition.

Another application of the Raman effect in the study of nanoparticles is in the detection of impurities. Because the Raman spectra of impurities can be significantly different from those of the bulk material, researchers can use Raman spectroscopy to identify the presence of impurities in nanoparticles.

The Raman effect also has applications in the study of the physical properties of nanoparticles. For example, researchers can use Raman spectroscopy to measure the thermal conductivity of nanoparticles, which is an important property for various applications, including electronics and energy storage. The current manuscript explores the Raman effect and its applications in the study of nanoparticles.

II. APPLICATION OF RAMAN EFFECT IN THE STUDY OF NANOPARTICLES

The Raman effect has important applications in the study of nanoparticles. Nanoparticles are materials that have at least one dimension in the range of 1-100 nanometres. The small size of nanoparticles leads to unique optical, electronic, and magnetic properties, which have important applications in fields such as medicine, electronics, and energy. The Raman effect can be used to study the properties of nanoparticles in several ways:

Chemical identification: The Raman effect can be used to identify the chemical composition of nanoparticles. When light is scattered from a nanoparticle, the resulting Raman spectrum contains the characterization peaks of the materials. These peaks are the fingerprints of various materials. Consequently, by analyzing the Raman spectrum, researchers can determine the chemical composition of the nanoparticle.

Structural analysis: The Raman effect can also be used to study the structure of nanoparticles. The Raman spectrum contains information about the orientation and symmetry of the molecules in the nanoparticle. By analyzing the Raman spectrum, researchers can determine the crystal structure and symmetry of the nanoparticle.

Size determination: The Raman effect can be used to determine the size of nanoparticles. The intensity of the Raman scattering is proportional to the number of molecules in the nanoparticle. By measuring the intensity of the Raman scattering, researchers can determine the size of the nanoparticle.

Surface analysis: The Raman effect can be used to study the surface properties of nanoparticles. When a nanoparticle is in contact with a surface, the Raman spectrum is modified by the interaction between the nanoparticle and the surface. By analyzing the modified Raman spectrum, researchers can determine the surface properties of the nanoparticle. The following diagram shows the Raman spectra of TiO_2 nanoparticles.

A. Raman shift and study of nanoparticles

Raman spectroscopy is a powerful analytical tool that can be used to study the vibrational modes of molecules and materials. Raman scattering occurs when a molecule or material interacts with light and some of the

photons are scattered inelastically, resulting in a change in energy and wavelength. The Raman shift is the difference in energy between the incident and scattered photons, and it is proportional to the vibrational energy of the molecule or material.

When studying nanoparticles, Raman spectroscopy can provide valuable information about the size, shape, composition, and surface properties of the particles. For example, the Raman spectrum of a nanoparticle will be influenced by the confinement of the vibrational modes within the particle, which can provide insights into its size and shape. In addition, the Raman spectrum can reveal information about the chemical composition and surface chemistry of the nanoparticle, which is important for understanding its properties and potential applications.

One challenge of using Raman spectroscopy to study nanoparticles is that the signal can be weak due to the small size of the particles. This can be overcome by using specialized instrumentation, such as Raman microscopes, which can focus the laser light onto the nanoparticles and collect the scattered photons with high sensitivity. In addition, the use of enhanced Raman scattering techniques, such as surface-enhanced Raman spectroscopy (SERS), can increase the sensitivity and provide even more detailed information about the nanoparticle.

B. Use of Raman spectroscopy to study TiO_2

Raman spectroscopy has been found a very sensitive tool to confirm the phase of TiO2 nano particles. Fig.6.3 shows the Raman spectra of pure and Al doped TiO2 nano particles. The strong bands near 145, 397, 513 and 639 per cm have been observed for all samples. According to factor group analysis, all of these have assigned to anatase phase and could be attributed to Eg, B1g, A1g and Eg respectively [30].

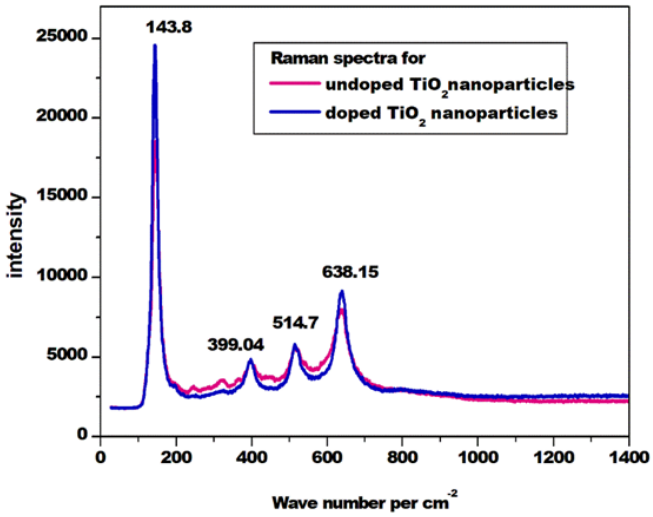

Figure 1: A sample Raman spectra of TiO_2 anatase nanoparticles

III.CONCLUSION

In conclusion, the Raman effect is a powerful tool for the study of materials, including nanoparticles. By analysing the Raman spectra of nanoparticles, researchers can identify their chemical composition, detect impurities, and measure their physical properties. As such, the Raman effect has become an important technique in the field of nanotechnology and materials Science.

IV. REFERENCES

[1]. A. B. Author, “Characterization of TiO2 Nanopowders by Raman Spectroscopy,” in Title of His Published Book, xth ed. City of Publisher, Country if not

[2]. Awais Khalid, Pervaiz Ahmad etal., “Unmodified Titanium Dioxide Nanoparticles as a Potential Contrast Agent in Photon Emission Computed Tomography”, Crystals 2021, 11, 171. (Nov 2002), https://doi.org/10.3390/cryst11020171

[3]. https://www.spectroscopyonline.com/view/characterization-tio2-nanopowders-raman-spectroscopy

[4]. on: Perevedentseva, E.; Lin, etal., Raman Spectroscopic Study of TiO2 Nanoparticles’ Effects on the Hemoglobin State in Individual Red Blood Cells. Materials 2021, 14, 5920, https://doi.org/10.3390/ma14205920

[5]. Y. Zhang, W. Wu, K. Zhang, C. Liu, A. Yu, M. Peng and J. Zhai, (2016), Raman Study of 2D Anatase TiO2 Nanosheets, Phys. Chem. Chem. Phys., DOI: 10.1039/C6CP05496J

[6]. Swati S. Kulkarni, S. S. Hussaini, Gajanan A. Bodkhe, Megha Deshmukh and Mahendra D. Shirsat, Enhancing efficiency of Dye Sensitized Solar Cell by Optimization of Al doping concentration of photo anode, Inertnational Journal of Nanoscience, Vol.19 (06) (2020), 29 https://doi.org/10.1142/SO219581X2050009X

International Journal of Scientific Research in Science and Technology
Volume 11 | Issue 13| Print ISSN: 2395-6011 | Online ISSN: 2395-602X (www.ijsrst.com)

Synthesis and Study of Cation Distribution of Copper Substituted Nickel Spinel Ferrite

J. M. Bhandari*[1], R. G. Vidhate[2], R. B. Kavade[3], K. M. Jadhav[4]

[1*]Department of Physics, S. A. J. V. P. M's Smt. S. K. Gandhi Arts, Science & Commerce College, Kada, Maharashtra, India

[2]Department of Physics, AnandraoDhonde Alias Babaji Mahavidyalaya, Kada, Dist.- Beed, Maharashtra, India

[3]Department of Physics, Bhagwan Mahavidyalaya Ashti, Dist.- Beed, Maharashtra, India

[4]Emeritus Professor (Physics), MGM University, Chh. Sambhajinagar, Maharashtra, India

ABSTRACT

The polycrystalline samples of ferrite having the general formula Ni1-XCuXFe2O4 with x = 0.0, 0.5, 1.0 were synthesized using solid state reaction technique. The X-ray diffraction patterns revealed the formation of single-phase cubic spinel structure for x = 0.0 and x = 0.5. The lattice constant increases with copper content and shows tetragonal structure for x = 1.0 (CuFe2O4). X-ray intensity ratios were calculated for selected planes (220), (311), (440), (422), (333) and was compared with the observed intensity ratios in order to obtain cation distribution. The results of the cation distribution indicate that Cu2+ and Fe3+ occupy both sites whereas Ni2+ occupy octahedral [B] site.

Keywords: X-ray diffraction, lattice constant, cation distribution.

I. INTRODUCTION

Spinel ferrites are commercially important materials because of their excellent electrical and magnetic properties. Hence studies of structural, electrical, magnetic and other properties of spinel ferrites are very essential [1, 2]. The interest in these materials is sustained till date because of their applications in the field of drug delivery, multilayer chips, magnetic recording, sensors, catalysts, etc. [3]. The twin property of electrical insulator and magnetic conductor makes ferrites useful in many devices such as transformer cores, antenna rod, and memory chips, microwave devices etc. The substitution of divalent, trivalent and tetravalent ions in spinel ferrites leads to diversification in various properties. The properties of spinel ferrites can be modified by substituting the various kinds of cations. In the literature, many reports are available on the structural, electrical and magnetic properties of Zn, Cd, Al, Cr, Ti, Mn substituted spinel ferrites [4]. Ferrites fulfil the wide range of applications from microwave to radio frequencies and are of importance from both fundamental and applied research point of view [5].

Interesting physical and chemical properties of ferrites arises from ability of these compounds to distribute cations amongst the available tetrahedral (A) site and octahedral [B] site and magnetic A-A, B-B and A-B interactions.

The high electrical resistivity, low eddy current and dielectric loss, high saturation magnetization, chemical stability etc. are the important aspects of ferrite material which make them useful in many applications. These aspects are highly sensitive to the preparation methodology [6], amount of constituent metal oxide [7], sintering condition [8] etc. Usually, spinel ferrites are prepared by ceramic technique. It is well- known that the properties of ferrite materials are influenced by the material composition and microstructure. The sintering temperature, sintering time, sintering atmosphere etc. also plays an important role in governing the properties of spinel ferrites [9].

II. EXPERIMENTAL TECHNIQUE

A series of polycrystalline spinel ferrites of the chemical compositionNi1-XCuXFe2O4(x = 0.0, 0.5, 1.0) were prepared using the standard ceramic technique [10]. A.R. grade oxides of corresponding ions (NiO, CuO and Fe2O3) were mixed in stoichiometric proportion for the preparation of ferrite. The compositions of these ferrites are shown in table 1. Grinding using agate mortar (4 hour) was carried out for each sample. The samples were pre-sintered at 1293K for 12 hours. The sintered powder is again reground and sintered at 1353K for 13hours.Then the powder of samples compressed into pellets of 10 mm diameter and about 1gm mass using a hydraulic press with pressure 6 ton/inch2 and sintered at 1273K for 12hour.The samples were furnace cooled to room temperature. The prepared samples were characterized by X-ray powder diffractometer (model pw 3710) using Cu-Kα radiation (α = 1.5406) in the 2θ range 200-800 at room temperature to confirm single phase spinel structure.

TABLE 1 Chemical composition of various components of Ni1-xCuxFe2O4 (x=0.0, 0.5, 1.0) system in mole percentage.

Composition x	NiO	CuO	Fe2O3
0.0	50	0	50
0.5	25	25	50
1.0	0	50	50

III.RESULT AND DISCUSSION

A) XRD (X-Ray Diffraction)

Mixed spinel ferrites system under investigation has been structurally investigated by X-ray diffraction. From fig. 1the XRD patternshows that the samples have single phase cubic spinel structure. The X-ray diffraction patterns revealed the formation of single-phase cubic spinel structure for x =0.0 and x =0.5 and shows tetragonal structure for x = 1.0 (CuFe2O4). The Bragg's peaks are sharp and intense.

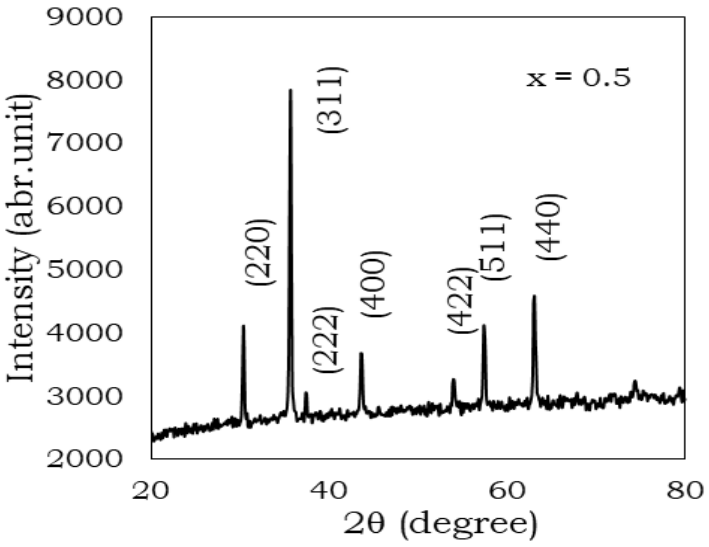

Figure. 1: Typical XRD Pattern of Ni1-xCuxFe2O4 (x = 0.5)

Using XRD data the inter planer spacing (d) was calculated using Bragg's law and the values of lattice constant (a) of all the samples was calculated by the relation [11];

$$a = d_{hkl}\left(h^2 + k^2 + l^2\right)^{\frac{1}{2}}$$

where, a is the lattice constant, d is inter planerspacing and (h k l) is the Miller indices.

The lattice constant calculated using XRD data is given in table-2. It is observed from table-2 that lattice constant increases very slowly with increase in copper content x. The small variation in the lattice parameter with copper substitution can be explained on the basis of very close ionic radii of nickel (0.69Å) and copper (0.72Å) [12]. X-ray density was calculated by using the values of molecular weight and volume of the sample. The values of X-ray density are listed in table-2. From table 2 it clear that X-ray density decreases as increase in copper content x. The observed variation in X-ray density is attributed to increase in volume of the samples. The bulk density of all samples was measured using Archimedes principle and values are also tabulated in table-2. Bulk density increases with increase in copper content x.

TABLE 2 Lattice constant (a), X-ray density (dx), bulk density (dB) and particle size (t) for Ni1-xCuxFe2O4 (x = 0.0, 0.5, 1.0)

x	a(Å)	dx(gm/cm3)	dB(gm/cm3)	t(μm)
0.0	8.326	5.395	3.58	29.72
0.5	8.367	5.371	3.843	24.28
1.0	a=5.7482 c=8.3627	5.356	4.264	26.91

The most intense peak (311) of XRD pattern was used to evaluate particle size of the samples. The particle size t was calculated using Scherrer's formula [13, 14];

$$t = \frac{0.9\lambda}{\beta\cos\theta}$$

where, λ is wavelength, β is full width at half maxima and θ is glancing angle for (311) peak. The values of particle size for all the composition are listed in table-2.

B) Cation Distribution:

The study of cation distribution in spinel ferrite is important to understand the magnetic behaviour of the samples. In case of the spinel type crystal lattice, the divalent metal ions and trivalent iron ions occupy the tetrahedral (A) site and octahedral [B] site as per the availability of sites. This distribution of ions over these two sites is called as the cation distribution. The cation distribution is strongly dependent of heat treatment, ionic radius, electronic configuration, electrostatic energy, methods of preparation etc. X-ray diffraction [15] Neutron diffraction [16] and Mössbauer [17] are the techniques available to determine the cation distribution.

In the present work X-ray diffraction method has been used to study the cation distribution. In X-ray diffraction method, X-ray intensity ratios of a selected plane were calculated and the calculated intensity is then compared with the observed intensity ratios. The intensity ratioswere calculated for various distributions of cations at tetrahedral (A) and octahedral [B] sites. In this work X-ray intensity ratios of the selected Bragg reflections (220), (400), (440) were calculated and compared them with the observed intensity ratios as these planes are structure sensitive [18]. The X-ray intensity (I) for a given reflection (hkl) can be calculated using the Buerger's formula [19].

$$I_{hkl} = |F_{hkl}|^2 P Lp$$

Where, Fhkl is structure factor, P is multiplicity factor and Lpis Lorentz polarization factor.

The structure factor F for a given plane was calculated from atomic scattering factor of respective ions. The multiplicity factor and Lorentz polarization factors were taken from the literature [20].

An agreement factor R = Iobs- Ical, the minimum value of R gives the best cation distribution formula. The cation distribution of Ni1-XCuXFe2O4 obtained from X-ray intensity ratio calculation is given in table 3. It is evident from table 3 that Cu2+ and Fe3+ ions occupy both tetrahedral (A) and octahedral [B] sites whereas Ni2+ ions occupy only octahedral [B] site.

TABLE 3 Cation distribution of Ni1-xCuxFe2O4

X	A-Site			B-Site		
	Ni	Cu	Fe	Ni	Cu	Fe
0.0	0	0.00	1.00	1.0	0.00	1.00
0.5	0	0.05	0.95	0.5	0.45	1.05
1.0	0	0.07	0.93	0.0	0.93	1.07

IV. CONCLUSION

The single-phase cubic spinel structure for the samples of Ni1-XCuXFe2O4were obtained for x = 0.0 and 0.5 whereas for x=1.0 tetragonal was confirmed by X-ray diffraction analysis. Cu2+ ions increase the lattice constant of the system. X-ray density decreases with Cu concentration x. The cation distribution indicates that copper Cu2+ and iron Fe3+ occupies both tetrahedral (A) and octahedral [B] site where as Ni2+ occupies only octahedral [B] site.

V. REFERENCES

[1]. L. John Berchmans, R. Kalai Selvan, P.N. Selva Kumar, C.O. Augustin, J. Magn. Magn. Mater, 279 (2004)103.

[2]. F. Novelo, R. Valenzuela, J. Mater. Res. Bull. 30 (1995) 335.

[3]. K. Muthuraman, S. Alagarsami, M. Ameena Banu, Vasant Naidu, International J. Computer Applications 32(3) (2011) 975.
[4]. S.P. Jadhav, B.G. Toksha , K.M. Jadhav, N.D. Shinde, Chinese J. Chem. Phys. 23 (4) (2010) 459.
[5]. M.A.Gabal, Y.M. Al Angari, J. Magn. Magn. Mater. 322 (2010) 3159.
[6]. P. Yadoji, R. Peelamedu, D. Agrawal, R. Roy, Mater. Sci. Eng. B., 98 (2003) 269.
[7]. H. Su, H.W. Zhang, X.L. Tang, Y. L. Zing, Y.L.Liu., J. Magn. Magn. Mater. 310 (2007) 17.
[8]. A. Dias, R. L. Moreira, N.D.S. Mohallem, J. Phys. Chem. Solids 58 (1997) 543.
[9]. R.V. Mangalaraja, S. Thomas Lee, S. Ananthakumar, P. Manohar, Carlos P. Camurri,Mater. Sci. Engg. A 476 (2008)
[10]. Ravinder, SrinivasaRao, P. Shalini. Mater.Lett.57 (2003) 4040.
[11]. A. M. Abo El Ata, S. M. Affia, D. El Kony, A. H. AL. Hammadi, J. Magn. Magn. Mater. 295 (2005) 28.
[12]. A.M. Sankpal, S.R. Sawant, A. S.Vaingankar, I.S.Pure, App. Phys. 26(1988)
[13]. B. D. Culity, Elements of X-Ray Diffraction, vol. 99, Addison-Wesley, Reading, MA, 1967.
[14]. Z. G. Zherg, X. C. Zhong, Y. H. Zhang, H.Y. Yu, D.C. Zeng, J. Alloys Compd. 466 (2008) 377.
[15]. SonalSinghal, Kailas Chandra. J. of Solid state chem. 180 (2007) 296.
[16]. K. Ghatage and S.A. Patil, Solid state commu.98 (1996) 885.
[17]. N. A. Eissa and A. A. Bahgat. Hyperfine interaction 5(1978)137.
[18]. H. Ohrishi, T. Toranishi, J. Phy. Soc. Japan 16 (1961) 36.
[19]. M.G. Burger, Crystal structure analysis‖ John Willey, New York (1960).
[20]. Cullity, Elements of X-ray diffraction‖, Massachussetts, USA, Addision Wesley.1959.

International Journal of Scientific Research in Science and Technology
Volume 11 | Issue 13| Print ISSN: 2395-6011 | Online ISSN: 2395-602X (www.ijsrst.com)

Conducting Polymer Matrix for Drug Release Device

Pradeep Gaikwad*

Department of Physics, R.B. Attal Arts, Science and Commerce College Georai, Dist. Beed, Maharashtra, India

ABSTRACT

Cutting edge scientific and technological research in the area of novel composite materials boosts the development of new analytical tools. The objective of paper is to synthesis conducting polymers x using Galvan static polymerization technique properties of a composite system in order to get novel structures and improved properties for electrochemical sensor applications.

Keywords: Conducting Polymers, Galvan static Polymerization Technique, Electrochemical Sensor Applications

I. INTRODUCTION

Polymers are the chemical compound made up of many small repeated units called monomer. It may be of one, two, or three the first polymer to be manufactured in 1909. Rayon a derivative of cellulose was discovered dimensional interconnected of chains. Bakelite is in 1910. Nylon was first prepared in 1935. Organic polymers are composed of hydrocarbons, compounds of carbon and hydrogen but some other elements (oxygen, nitrogen, sulfur, chlorine, fluorine, phosphorous, and silicon. Polymers have some general characteristics, chemical resistant, corrosion resistance thermal and electrical insulators, excellent surface finish, low density, good strength, colored and transparent, heat sensitive, easy to process, poor tensile strength wide application range. The properties of polymers could be easily modified and enhanced by adopting different methods (Carraher et al. 2003; Ebewele et al. 2000).Polymers could be classified in many ways, based on their source, structure, molecular force, and mode of polymerization. Applications of Polymers such Biosensors, Drug Delivery clinical Application Material Reinforcement.

Conducting polymers [1-3], it is possible to control the electrical conductivity of polymer over the range from insulating to highly conducting (metallic) state. Electrochemical polymerization (ECP) technique which is a fast-developing interfacing polymer science and electrochemistry. The electrochemical synthesis of conducting polymers, has proven important in allowing development of new polymeric materials with similar electrochemical and electrical properties. Semiconducting polymers It provides a novel approach to the synthesis of conducting polymers. Better understanding of the physics and chemistry of semiconducting polymer interfaces. Conducting polymers is an interesting class of polymeric materials and attractive area of research. It has a combination of properties of organic polymers and semiconductors/metals. Conjugated polymer generally needs some kind dopant (redox or nonredox dopants) which improves the conductivity to a great extent. It can be further categorized into two groups conducting polymers have conjugation; doped

conducting polymers and intrinsic conducting polymers . CPs could optical transition, lower ionization potential, and high electron affinity. CPs shows a wide be easily oxidized or reduced than conventional polymers because they have lower energy optical transition, lower ionization potential, and high electron affinity. CPs shows a wide range of conductivity from metal to insulator . CPs have following important characteristics low hydrogen content and aromatic structure, reversible doping/dedoping process, high surface area, electrochemical activity, higher conductivity, lower manufacturing costs, better process ability, low density, high mechanical flexibility and tunable properties. The ICPs have greatly benefitted our society in applications such as biosensors], gas sensors , and tissue engineering . Electrochemistry has played a key role in the synthesis of ICPs for its fine tuning in the polymer structures, compositions, and electrochemical properties. [4-8].

II. ELECTROCHEMICAL SENSOR

In the electrochemical sensor, a working electrode is the transducer element where the specific biochemical reaction takes place. Working electrode is also called as sensing/redox electrode, the various electrochemical parameters that could be monitored are current, potential.

Method

Electrochemical synthesis Set-Up

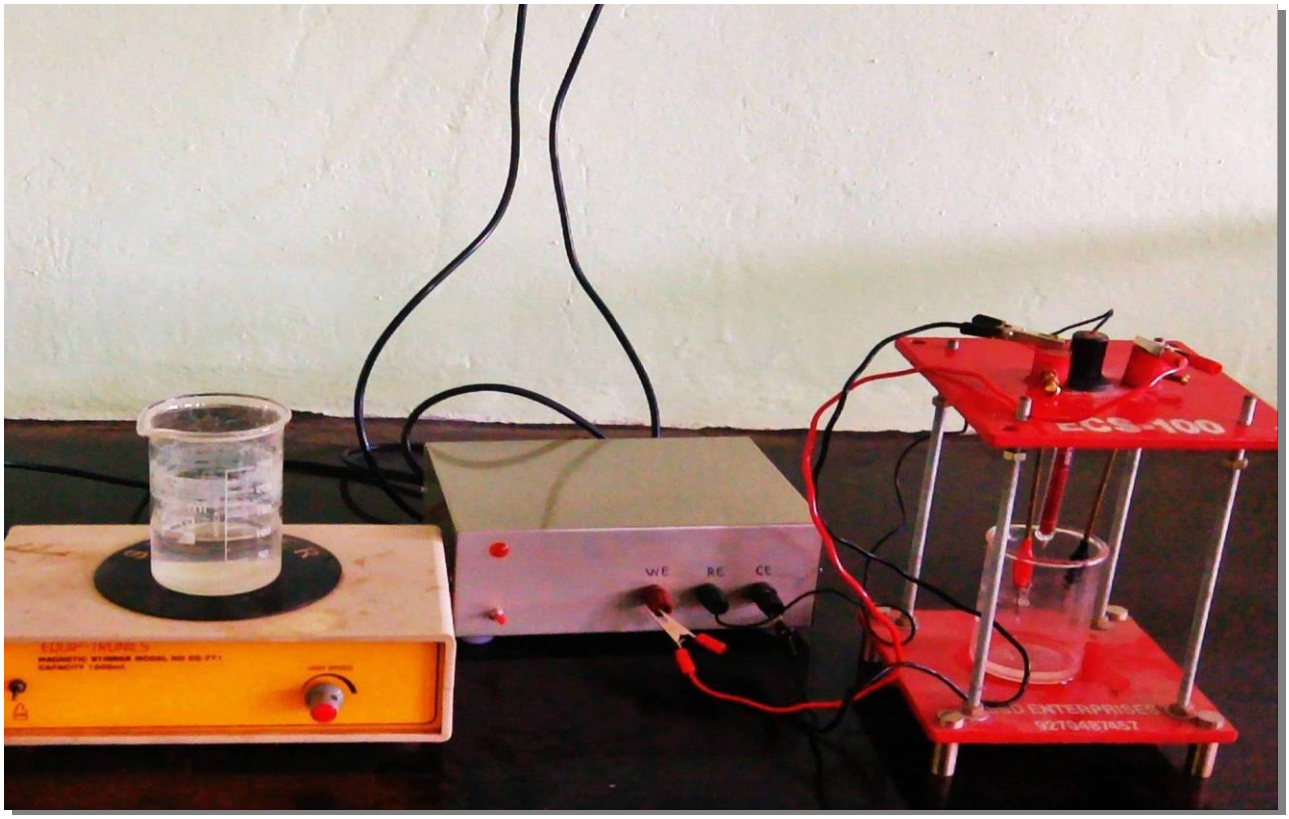

The electrochemical synthesis setup is as shown in Figure.1.

It consists of PC based electrochemical polymerization system (Galvanostat), three electrode glass cell h. The three-electrode glass cell consists of working electrode, counter electrode, and reference electrode and electrolyte solution as shown in figure1. ECP is normally carried out ECP can be carried out galvanostatically (i.e. constant current condition) by using a suitable power supply to obtain thin matrix [9]

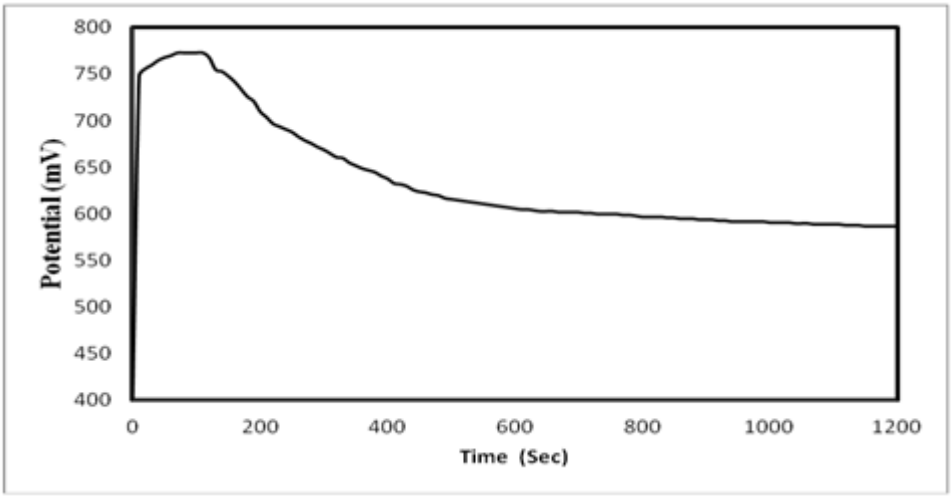

Fig; 2. A typical galvanostatic electro polymerized chronopotentiogram (E-t curve)

PANI-HCl Composite were synthesized in an aqueous solution of distilled 0.2 M aniline (S.D. Fine. Chem.) and 0.5 M of Hydrochloric acid (Aldrich) using electrochemical deposition method. It was carried out by Galvanostatic technique at 27 °C in one compartment, three-electrode glass cell. The ITO coated glass plate was used a working electrode, platinum electrode as counter electrode and Ag/AgCl was used as reference electrode. The electrolyte solution was prepared in distilled water. The applied current density 1 mA/cm^2 were kept constant during synthesis of composite Matrix. After this, the potential becomes almost constant suggesting that building up of the film proceeds according to the same reaction along the full thickness of the polymer as as shown in figure 2.

PANI-HCl Composite were synthesized in an aqueous solution of distilled 0.2 M aniline (S.D. Fine. Chem.) And 0.5 M of Hydrochloric acid (Aldrich) using electrochemical deposition method. It was carried out by Galvanostatic technique at 27 °C in one compartment, three-electrode glass cell. The ITO coated glass plate was used a working electrode, platinum electrode as counter electrode and Ag/AgCl was used as reference electrode. The electrolyte solution was prepared in distilled water. The applied current density 1 mA/cm^2 were kept constant during synthesis of composite Matrix. After synthesis the polymer coated electrodes were rinsed thoroughly in distilled water, dried in cold air and then use for subsequent characterization. After this, the potential becomes almost constant suggesting that building up of the film proceeds according to the same reaction along the full thickness of the polymer as as shown in figure 2.

III.CONCLUSIONS

The electrodes that allow drugs to be uploaded and released from conductive polymer films for biomedical applications.

IV. REFERENCES

[1]. Proceedings of the International Conference on Conducting Polymers, J. Phys. (les Ulis Fr.) 44, C3 (1983).

[2]. Proceedings of the International Conference on Synthetic Metals, Mol. Cryst. liq. Cryst. 117±121 (1985)

[3]. Gill W.D., Clarke T.C., Street G.B., Appl. Phys. Commun. 2 (1982) 211.

[4]. Ahuja, T. Mir, I. A. Kumar, D. and Rajesh, "Biomolecular immobilization on conducting polymers for biosensing appli cations," Biomaterials, 2007. vol. 28, no. 5, pp. 791–805.

[5]. Gangopadhyay R. and De, A. "Conducting polymer compos ites: novel materials for gas sensing," Sensors and Actuators B: Chemical, 2001. vol. 77, no. 1-2, pp. 326–329.

[6]. Bendrea, A. D. Cianga, L. and Cianga, I. "Review paper: prog ress in the field of conducting polymers for tissue engineering applications," Journal of Biomaterials Applications, 2011. vol. 26, no. 1, pp. 3–84.

[7]. Das T. K. and Prusty, S. "Review on conducting polymers and their applications," Polymer - Plastics Technology and Engi neering, 2012. vol. 51, no. 14, pp. 1487–1500.

[8]. Tran, H. D. Li, D. and Kaner, R. B. "One-dimensional con ducting polymer nanostructures: bulk synthesis and applica tions," Advanced Materials,2009. vol. 21, no. 14-15, pp. 1487–1499.

International Journal of Scientific Research in Science and Technology
Volume 11 | Issue 13| Print ISSN: 2395-6011 | Online ISSN: 2395-602X (www.ijsrst.com)

Graphical study of Dielectric Properties of Ghughuwa Fossil National Park (M.P.) Saline Soil C- Band Microwave Frequency

Santosh S. Deshpande[1], Sanjeev Pande[2]
[1]Rashtramata Indria Gandhi College, Jalna-431203, Maharashtra, India
[2]Assistant Professor, HRDC Rani Durgawati University Jabalpur, Madhya Pradesh, India

ABSTRACT

The study also includes measurement of dielectric properties for various percentages of moisture contents, 5%-35%, for 5% Fossil saline soil. The Shorted waveguide technique is used for dielectric measurements using automated C-Band microwave bench set up. The least square fitting technique is used to calculate dielectric constant, ε', and dielectric loss, ε'', and errors in their measurements. From measured dielectric properties, emissivity and brightness temperature are theoretically calculated at different angles of incidence of moisture-contented soils using Fresnel equations. The laboratory data obtained are useful for the interpretation of data in remote sensing applications, particularly in agriculture.

Keywords: Saline soil, Fossil Dielectric properties, 5 GHz microwave frequency, Brightness temperature, Emissivity.

I. INTRODUCTION

Certain parts of India contain saline soil due to natural process of weathering that includes chemical, geological, Fossil fuels Mines hydrological and biological effects. Agriculture productivity is affected badly due to salinity in soil. The agriculture pattern of cash crops is day-by-day becoming popular for obvious reasons. More and more irrigation facilities are used to increase yield of cash crops. However many agriculture land, it is found that excessive of water for cash crop like sugarcane, cotton soybean some region paddy is resulting into production of water logging areas ultimately causing the increase in salinity of soil. Inappropriate cropping systems, reduction in crop diversity, inadequate post-harvest infrastructure are other major areas of concern. Hence, mapping and monitoring of soil are highly important and usually done by microwave Remote Sensing.
Remote sensing (Eugene A. Sharkov, 2003; Ulaby et al., 1986) usually refers to the technology of acquiring information about the earth's surface (atmosphere, land, vegetation, forest and ocean) using sensors onboard airborne (aircraft, balloons) or space-borne (satellites, space shuttles) platforms. The electromagnetic radiation is used as an information carrier in Remote Sensing. Remote sensing employs passive and/or active sensors. Passive sensors are those, which sense natural radiations, either reflected or emitted from the earth. On the other hand, the sensors, which produce their own electromagnetic radiation, are called active sensors (e.g. LIDAR, RADAR). In passive microwave, remote sensing the radiometer measures the emissivity of soil, whereas in active remote sensing the radar measures the back-scattering coefficient of the soil, both factors depend on dielectric properties of soil. The complex dielectric constant is a measure of the electric properties of

the surface. It consists of two parts: the real part, known as the dielectric constant () and is a measure of the ability of a material to be polarized and store energy. The imaginary part () is a measure of the ability of the material to dissipate stored energy into heat. The two are related by the expression:

$\varepsilon = \varepsilon' - j\varepsilon''$

Where ε is complex dielectric constant.

The measurement of these parameters is significant for remote sensing applications.

II. MATERIAL AND METHOD

The soil sample is collected from location Ghughua fossil national park in Madhya Pradesh latitude 230 06' 38'' N longitude 800 36'51'' E. The pH of the collected soil sample is 8.8 hence it is acidic in nature. The saline soil containing fossil that soil sample is oven dried and samples of different percentage of moisture contain 5% - 35% are prepared. Dielectric measurements of all these samples are done at 5 GHz at room temperature.

Experimental set-up

The C-Band microwave bench setup (Von Hipple A.R., 1954) consisting of a low power microwave source VTO, isolator, coaxial-waveguide adapter, attenuator, SS tuner, slotted section and solid dielectric cell. The Block diagram of the setup is shown in figure 1.

Microwave generated by VTO are propagated through passive components of rectangular wavelength to the dielectric cell with perfect reflector at closed end. The source is tuned to give 5 GHz frequency by applying tuning voltage of 7 volts. The attenuator is used to keep the desired power in waveguide assembly of the bench. A slotted section with a tunable probe containing 1N23 detector with the square law characteristics has been used to measure power (current) along the slotted line. The detector is connected to a micro ammeter and to the PC to read and record the measured power. The probe sits on slot line such that the tip of the tunable probe is penetrated and it can be moved forwarded and backward along the slot line section. The depth of the tip is adjusted for its critical position to get a symmetrical standing wave pattern. The empty dielectric cell is connected to the other end of the microwave bench. The bench is tuned for symmetrical standing wave pattern in the slot line. The dielectric sample under consideration (soil sample) is inserted in the dielectric cell with a constant compaction. The probe is transverse along the slot line at equal intervals and the probe positions are recorded with corresponding power (current). This data is acquired and store in file using microcontroller interface system. This data makes use of α and β as fitting parameters, where α = attenuation factor, β=phase shift constant.

The data is stored for soil samples of different thickness. The dielectric properties of the solid material can be calculated for best fit of parameters. The guided wavelength, is measured from the minima of the standing wave pattern The free space wavelength in determined using the relation Where, 'a' being the broader side of the C-band rectangular wave-guide.

The real and imaginary parts of the complex dielectric constant are calculated using the relations

A source code for computing dielectric constant has been developed. The numbers of data files, for different thickness of samples are combined to get single input data, which can be used, in the source code for calculating dielectric constant and loss. Experimentally calculated dielectric constant ε' and loss ε'' with error in measurement in both Δε', Δε'' are tabulated.

Figure 1 Block diagram of a C-band microwave bench

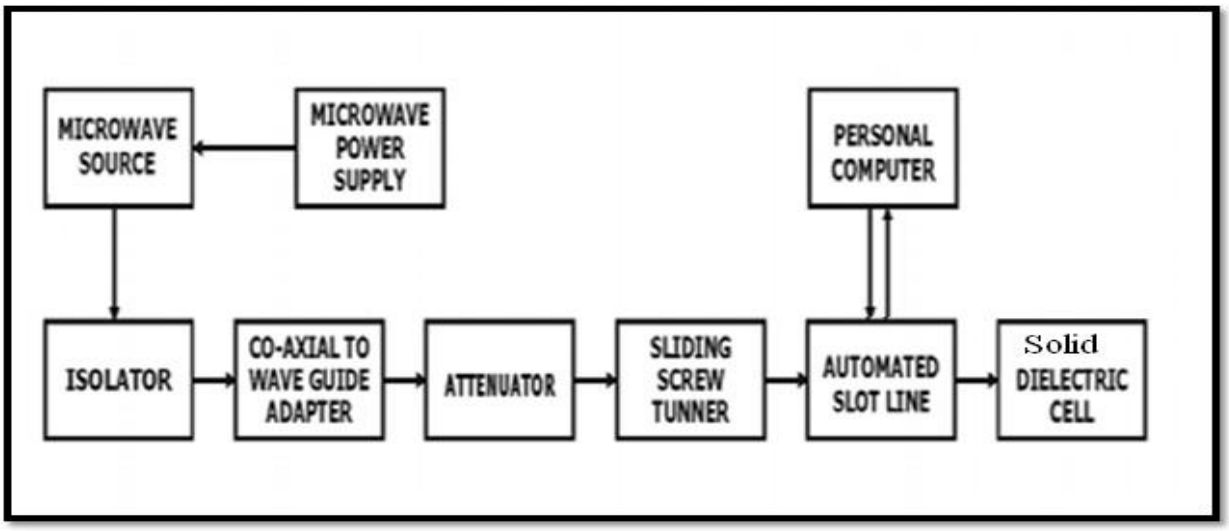

Brightness temperature and emissivity

Passive microwave remote sensing is based on the measurement of thermal radiation in the centimeter wave band of the electromagnetic spectrum. This radiation is determined largely by the physical temperature and the emissivity of the radiating body and can be approximated by

Where observed brightness temperature; T physical temperature of the emitting layer;

P refers to vertical or horizontal polarization; es smooth-surface emissivity. This emissivity is further defined as

Where Rs is the smooth-surface reflectivity. For a homogeneous soil with a smooth surface, the reflectivity at vertical and horizontal polarizations, RsV and RsH, are given by the Fresnel expressions

where u is the incidence angles and k is the absolute value of the soil bulk dielectric constant, which is a measure of the response of the soil to an electromagnetic wave and is largely determined by the volumetric soil water content. Emissivity and Brightness temperature for different angle of incidence for 5% saline soil for different percentage of water content is calculated using Fresnel equations.

III.RESULT AND CONCULSION

The dielectric properties of dry & moisture Fossil saline soil are studied at 5 GHz at room temperature. Table 1 shows details of dielectric constant ε' and loss ε'' and error in measurement in both Δε', Δε''. The results shows that impact of increase in salinity isn't same for ε' and ε''. As real part is concerned, the graph shows gentle decrease with increase in salinity hence soil salinity has a little influence of fossil fuel on dielectric constant ε' at 5 GHz and at room temperature. On contrary, the imaginary part, ε'' dielectric increases with increase in salinity in that fossil soil.

Dielectric properties of Ghughuwa fossil fuel saline soil sample are measured as a function of moisture contents shown in table 1. The sample was oven dried and considered at a level of 0% moisture. Then a desired weight of distilled water is added to achieve different moisture content levels. The variations of moisture content up to 35% are studied for 5% saline soil at 5 GHz. The response to the dielectric constant ε' is sensitive to moisture for saline soil , as soon as 5% moisture is added significant increase in dielectric constant is found, which remain increasing with addition of more moisture content.

Higher is the magnitude of humidity, the stronger the effect of salinity on the imaginary part. Since ε'' is proportional to the conductivity, increase in soil moisture content leads to a greater amount of salts dissolved in the soil system and thus increases conductivity. Thus, behavior of the increase in ε'' with increase in moisture content is seen. Similar trend is obtained by other workers (Wang. J et al., 1978, 1980; Y. Lasne et al., 2008).
Figure 3. plotted for emissivity against the angle of incidence for Ghugawa saline soil sample at 5 %, 15%, 25 %, 30 % , 35 % moisture content. Decrease in emissivity values at normal incidence is seen with increase in moisture contain in saline soil. Reductions in emissivity values for horizontal polarization are seen; as angle of incidence increases. The curve for horizontal polarization shows a decrease in emissivity at a slow rate initially up to 20o, and above this angle, the emissivity reduces faster as the angle of incidence increases. The curve for vertical polarization shows a gradual increase in emissivity initially, which becomes faster as the angle of incidence 30o. For moisture content saline soil of 5%, 15 %, 25 %, 35% the emissivity curve changes for vertical polarization at 70o, 73o, 80o, 82o, respectively, instead of increase in the emissivity decreasing trends from these angles are found. The Brightness temperature at different angle of incidence is calculated, the nature of plot is found similar to emissivity (figure 4).

Table 1 Dielectric constant ε', dielectric loss ε'', error in dielectric constant Δε' and loss Δε'' for different moisture content 5 % Ghughuwa saline soil samples at 5 GHz.

Sr.No.	Moisture in saline soil	Dielectric Properties		Error	
	(%)	ε'	ε''	Δε'	Δε''
1	5	6.448	7.58 x 10^{-2}	1.79 x 10^{-2}	1.80 x 10^{-3}
2	10	8.684	8.42 x 10^{-2}	1.37 x 10^{-2}	1.53 x 10^{-3}
3	15	11.421	9.80 x 10^{-2}	1.90 x 10^{-2}	1.77 x 10^{-3}
4	20	12.535	8.01 x 10^{-2}	1.39 x 10^{-2}	2.21 x 10^{-3}
5	25	14.980	9.69 x 10^{-2}	2.82 x 10^{-2}	2.41 x 10^{-3}
6	30	19.883	8.34 x 10^{-2}	4.24 x 10^{-2}	3.60 x 10^{-3}
7	35	23.840	9.93 x 10^{-2}	1.52 x 10^{-2}	3.65 x 10^{-3}

Figure 2 : Characteristics of Ghughuwa fossil saline soil

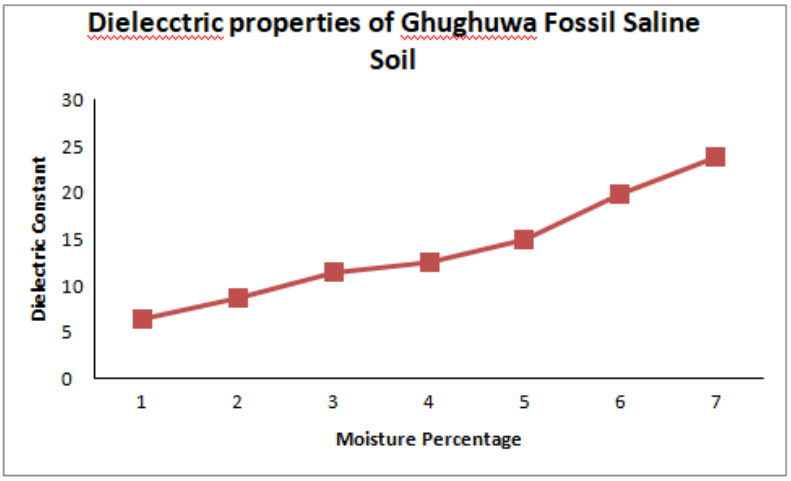

Figure 3 Emissivity of Ghugawa Fossil fuel saline soil for 5%, to 35% moisture content at different angle of incidence

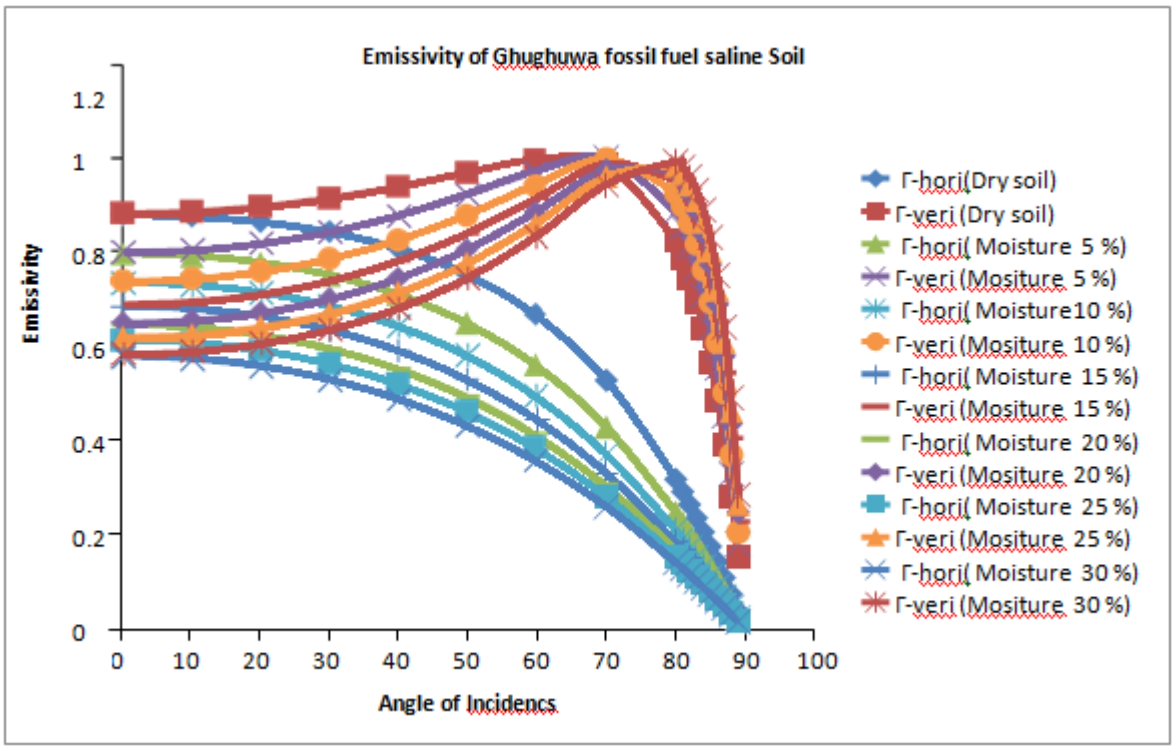

Figure 4 Brightness Temperature of 5% saline soil for 5%, 15%, 25%, 35% moisture content at different angle of incidence

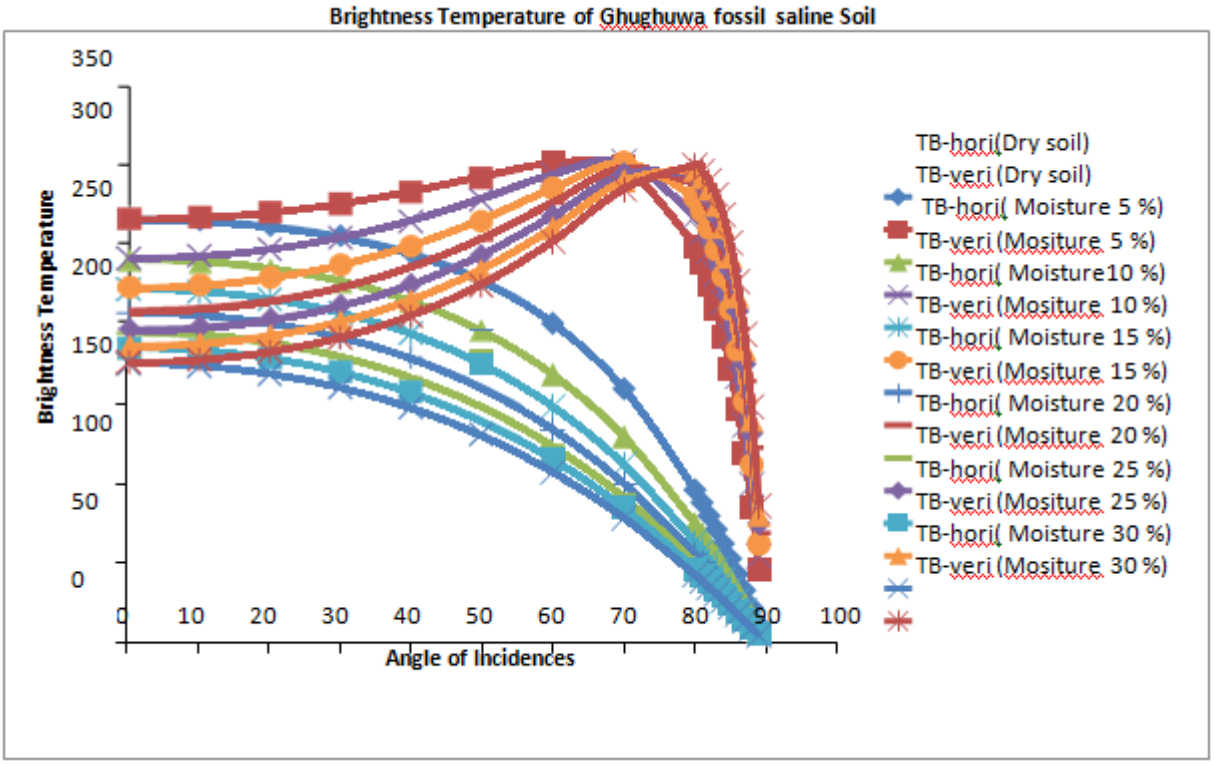

IV. ACKNOWLEDGEMENT

I am thanks to JES college Jalna to give mi support to tke observations of soil in the research lab, I thanks to my Research Guide Dr.M.L.Kurtadikar Sir give mi support to reseach and also thanks to Principal Dr. Ganesh Agnivotri Sir for timely help.

V. REFERENCES

[1]. Eugene A. Sharkov (2003), Passive Microwave Remote Sensing of the Earth, Springer Praxis Publishing, UK.

[2]. Ulaby, F. T., R. K. Moore and A. K. Fung, 1986. Microwave remote sensing: active and passive, Vol. 3, Artech House, Norwood, Mass.

[3]. Von Hipple A.R., (1954) Dielectric Materials and Applications, New York, Wiley.

[4]. Wang. J., Schmugge T. and Williams (1978), Dielectric constants of soils at microwave frequencies-II, NASA Technical paper, 1238.

[5]. Wang J.R., and Schmugge T., (1980), An empirical model for the complex dielectric Permittivity of soils as a function of water content. IEEE Transactions on Geoscience and Remote Sensing, 18, pp. 288-295

[6]. Y. Lasne, Ph. Paillou, G. Ruffié, C. Serradilla, F., A. Freeman, T. Farr, K. McDonald, B. Chapman (2008) Effect of Salinity on The Dielectric Properties of Geological Material: Implication for Soil Moisture Detection by Means of Remote Sensing, Author manuscript, published in "IEEE Transactions on Geoscience and Remote Sensing 46, 6, 1674-1688.

[7]. K. Sreenibvas, L Venkataraknam, and P.V. Narasimha Rao, “Dielectric properties of salt-affected soil,” Int. J Remote Sens., vol. 16,pp. 641-649, 1994

[8]. Agrawal R.S., Kurtadikar M.L. and Murugkar A.G. Dielectric Properties of Soil at 5 GHz, “Microwaves and Optoelectronics”, Anamaya Publishers, New Delhi, 2004, pp. 261-265.

[9]. Kulkarni P.G. “Study of dielectric properties of different soil texture at C. Band microwave frequency,” Ph.D. Thesis Dr. Babasaheb Ambedkar Marathwada University Aurangabad October – 2006Kulkarni P.G. “Study of dielectric properties of different soil texture at C.

[10]. Soil Series of Maharashtra NBSS Publ. 79, Technical Bulletin, Nov. 1999. National Bureau of Soil Survey and Land use Planning, Nagpur – 440010. In Co-operation with Department of Agriculture Govt. of Maharashtra, Pune – 411001.

[11]. The Chemical composition of soils – Philip A Helmke, University of Wisconsin Madison.

International Journal of Scientific Research in Science and Technology
Volume 11 | Issue 13| Print ISSN: 2395-6011 | Online ISSN: 2395-602X (www.ijsrst.com)

Advancements and Applications of Nanotechnology : A Comprehensive Review

Dr. G. S. Jaigaonkar
Assistant Professor, Department of Physics, B.B. Arts, N.B. Commerce & B.P. Science College Digras Dist Yavatmal, Maharashtra, India

ABSTRACT

The unique size-dependent characteristics of metal nanoparticles (NPs) and their wide range of applications in optoelectronics and other fields have attracted a lot of attention. Anextensive summary of the production processes, characterization methodologies, and optoelectronic uses of metal nanoparticles is given in this paper. The physical, chemical, and biological methods for synthesizing metal nanoparticles are covered in depth, along with their benefits, drawbacks, and most recent developments. The size, structure, and stability of nanoparticles are explained, highlighting the significance of managing these parameters for customized optoelectronic features.

Understanding the structural, optical, and electrical properties of metal nanoparticles depends heavily on characterization techniques. This paper provides insights into nanoparticle morphology, crystallinity, composition, and surface chemistry by outlining typical characterisation techniques like electron microscopy, X-ray diffraction, spectroscopy, and surface analysis approaches. Moreover, the optoelectronic uses of metal nanoparticles—such as photovoltaics, photocatalysis, light-emitting diodes, sensors, and plasmonics—are investigated. Metal nanoparticles' special optical and electrical characteristics allow for improvements in light manipulation, emission, and absorption, which improves device performance and opens up new functions.

Keywords: - Nanomaterials, Nanoelectronics, Nanomedicine, Nanophotonic, Nanotechnology in Energy, Environmental Applicationsetc.

I. INTRODUCTION

Nanotechnology, the manipulation of matter at the nanoscale, has emerged as a groundbreaking field with vast potential to revolutionize various industries and scientific domains. At the nanoscale, materials exhibit unique properties and behaviors that differ from those observed at larger scales, enabling unprecedented control over their characteristics and functionalities. This comprehensive review aims to delve into the latest advancements in nanotechnology and explore its diverse applications across numerous sectors.

In recent years, significant progress has been made in the synthesis, characterization, and manipulation of nanomaterials, leading to the development of novel structures with tailored properties. Advances in nanofabrication techniques, such as bottom-up assembly and top-down lithography, have enabled precise control over the size, shape, and composition of nanostructures, facilitating their integration into various systems and devices.

One of the most promising aspects of nanotechnology is its extensive range of applications across multiple fields. In the realm of medicine, nanotechnology offers unprecedented opportunities for targeted drug delivery, diagnostics, and therapeutics. Nanoparticles functionalized with biomolecules can selectively target diseased cells, minimize side effects, and enhance the efficacy of treatments. Moreover, nanoscale materials hold great potential in regenerative medicine, tissue engineering, and medical imaging, offering innovative solutions to complex healthcare challenges.

In the electronics and semiconductor industries, nanotechnology has fueled the development of smaller, faster, and more efficient devices. Nanoscale materials, such as carbon nanotubes and quantum dots, exhibit remarkable electrical, optical, and thermal properties, paving the way for advancements in electronics, photonics, and optoelectronics. Moreover, nanotechnology-enabled innovations, such as nanoelectromechanical systems (NEMS) and molecular electronics, hold promise for next-generation computing, communication, and sensing technologies.

Beyond healthcare and electronics, nanotechnology finds applications in energy, environmental remediation, agriculture, and consumer products. Nanomaterials play a crucial role in renewable energy technologies, including solar cells, fuel cells, and energy storage devices, by enhancing efficiency and reducing costs. Additionally, nanotechnology offers solutions for environmental challenges, such as pollution remediation, water purification, and efficient catalysis.

In agriculture, nanotechnology enables the development of smart delivery systems for fertilizers, pesticides, and nutrients, enhancing crop yield while minimizing environmental impact. Furthermore, nanomaterials can improve food packaging, preservation, and safety, extending shelf life and ensuring food security.

As nanotechnology continues to advance, its societal implications, ethical considerations, and safety concerns must be carefully addressed. Responsible innovation and governance frameworks are essential to harness the full potential of nanotechnology while mitigating potential risks and ensuring equitable access to its benefits.

II. APPLICATIONS OF NANOTECHNOLOGY

Medicine and Healthcare:

Drug Delivery: Nanoparticles can be engineered to deliver drugs to specific targets within the body, improving efficacy and reducing side effects.

Medical Imaging: Nanomaterials enhance contrast in imaging techniques such as MRI, CT scans, and fluorescence imaging, enabling early disease detection and precise diagnostics.

Regenerative Medicine: Nanoscale scaffolds and materials facilitate tissue engineering and regeneration, offering solutions for organ transplantation and wound healing.

Diagnostic Tools: Nanotechnology-based biosensors and assays enable rapid and sensitive detection of biomarkers for diseases, pathogens, and genetic disorders.

Electronics and Photonics: -

Miniaturization: Nanotechnology enables the fabrication of smaller, faster, and more efficient electronic components, leading to advancements in microprocessors, memory devices, and sensors.

Optoelectronics: Nanomaterials like quantum dots and nanowires are utilized in LEDs, solar cells, displays, and photodetectors, enhancing efficiency and performance.

Flexible Electronics: Nanotechnology facilitates the development of flexible and wearable electronics, enabling new form factors for devices and applications in healthcare, consumer electronics, and smart textiles.

Energy:

Solar Cells: Nanomaterials such as perovskite nanoparticles and quantum dots enhance the efficiency of solar cells by improving light absorption and charge transport.

Energy Storage: Nanotechnology enables the development of high-capacity batteries, supercapacitors, and fuel cells with enhanced energy density, stability, and lifespan.

Catalysis: Nanocatalysts offer superior activity and selectivity in chemical reactions, contributing to the development of efficient processes for energy conversion and environmental remediation.

Materials Science: -

Nanocomposites: Incorporating nanomaterials into polymers, ceramics, and metals enhances mechanical, thermal, and electrical properties, leading to lightweight and durable materials for aerospace, automotive, and construction industries.

Coatings and Surface Modifications: Nanotechnology enables the development of self-cleaning surfaces, anti-corrosion coatings, and hydrophobic/hydrophilic coatings with applications in healthcare, textiles, and electronics.

Environmental Remediation:

Water Purification: Nanomaterials such as nanofilters and nanosponges remove pollutants, heavy metals, and pathogens from water, addressing challenges related to clean drinking water and wastewater treatment.

Air Filtration: Nanotechnology-based filters capture particulate matter, VOCs, and harmful gases, improving indoor air quality and reducing health risks associated with air pollution.

Food and Agriculture:

Food Packaging: Nanocomposites and nanocoatings enhance food packaging materials with properties such as barrier protection, antimicrobial activity, and freshness preservation.

Crop Protection: Nanopesticides and nanofertilizers improve nutrient uptake, pest control, and crop yield while minimizing environmental impact and reducing chemical usage.

These applications demonstrate the diverse and transformative potential of nanotechnology across various sectors, addressing critical challenges and driving innovation for a sustainable future.

Medicine and Healthcare

Medicine and general Healthcare

Medical Applications: -

Cancer Therapy: Nanotechnology offers promising approaches for cancer diagnosis and treatment. Nanoparticles can be functionalized with targeting ligands to selectively bind to cancer cells, delivering therapeutic agents directly to tumors while sparing healthy tissues. Nanomaterials such as gold nanoparticles

and carbon nanotubes have been utilized for photothermal therapy and photodynamic therapy, destroying cancer cells with localized heat or reactive oxygen species generated upon exposure to light.

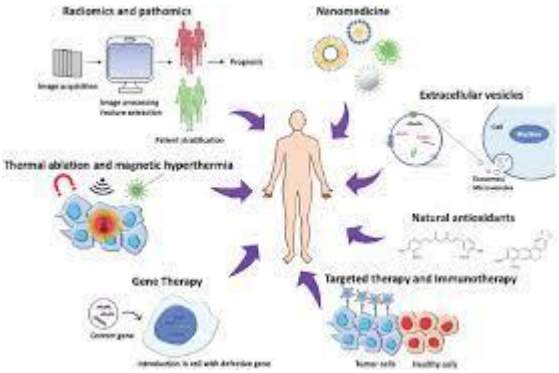

Cancer therapy approaches

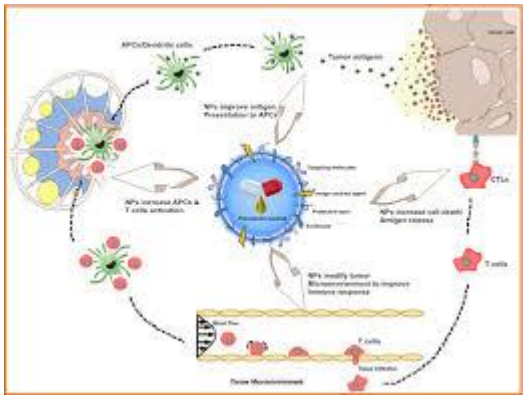

Nanotechnology and Cancer therapy

Medical Imaging: Nanoparticles, quantum dots, and other nanomaterials enhance the sensitivity and specificity of medical imaging techniques such as magnetic resonance imaging (MRI), computed tomography (CT), and fluorescence imaging. These contrast agents enable early detection of diseases, precise localization of lesions, and monitoring of treatment response. Moreover, multifunctional nanoparticles can integrate imaging and therapeutic functionalities, enabling theranostic applications for personalized medicine.

Regenerative Medicine: Nanotechnology plays a crucial role in tissue engineering and regenerative medicine by providing scaffolds, growth factors, and cell delivery systems to promote tissue repair and regeneration. Nanoscale materials mimic the extracellular matrix and create a favorable microenvironment for cell adhesion, proliferation, and differentiation. Nanoparticles loaded with stem cells or growth factors can enhance tissue regeneration in various organs and tissues, including bone, cartilage, skin, and heart.

Diagnostics and Biosensing: Nanotechnology-based biosensors and diagnostic assays offer rapid, sensitive, and cost-effective detection of biomarkers for diseases, pathogens, and genetic disorders. Nanomaterials such as gold nanoparticles and carbon nanotubes serve as platforms for immobilizing biomolecules and amplifying signal readouts in diagnostic tests. Nanopore sequencing and nanoparticle-based assays enable high-throughput analysis of DNA, RNA, and proteins, facilitating precision medicine and personalized healthcare.

Theranostics: The integration of diagnostic and therapeutic functionalities in a single nanosystem, known as theranostics, enables real-time monitoring of treatment response and adjustment of therapy based on patient-specific parameters. Theranostic nanoparticles can deliver drugs to target sites, visualize drug distribution using imaging modalities, and monitor therapeutic efficacy in real-time, leading to personalized treatment strategies and improved patient outcomes.

Diagnostics and Biosensing: -

Diagnostics and biosensing are crucial fields within healthcare and biotechnology, focusing on the detection and analysis of biological markers or signals to diagnose diseases, monitor health conditions, or detect pathogens. These fields have seen significant advancements in recent years, driven by developments in technology, materials science, and biochemistry. Here are some key aspects of diagnostics and biosensing:

Point-of-care testing (POCT): POCT refers to medical diagnostic testing at or near the point of care (patient bedside, physician's office, etc.), rather than in a centralized laboratory. This approach allows for rapid

diagnosis and treatment decisions, particularly beneficial in emergency or resource-limited settings. Devices for POCT range from simple, low-cost lateral flow assays to more sophisticated handheld analyzers.

Biosensors: Biosensors are analytical devices that incorporate a biological sensing element (such as enzymes, antibodies, or nucleic acids) and a transducer to convert a biological response into an electrical signal. They can detect specific biological analytes, such as proteins, nucleic acids, or small molecules, with high sensitivity and specificity. Biosensors have diverse applications, including medical diagnostics, environmental monitoring, food safety, and drug discovery.

Lab-on-a-chip (LOC) technology: LOC devices miniaturize and integrate multiple laboratory functions onto a single microchip or small platform. These systems enable rapid and automated analysis of biological samples with minimal sample volume and processing time. LOC devices are used for various diagnostic applications, including DNA sequencing, pathogen detection, and cell analysis.

Next-generation sequencing (NGS): NGS technologies have revolutionized genomic analysis by enabling high-throughput sequencing of DNA or RNA samples. These techniques have diverse applications in diagnostics, including cancer genomics, infectious disease surveillance, and personalized medicine. NGS allows for the rapid and comprehensive analysis of genetic variants associated with disease risk, treatment response, and drug resistance.

Imaging techniques: Advanced imaging modalities, such as magnetic resonance imaging (MRI), computed tomography (CT), positron emission tomography (PET), and ultrasound, play a crucial role in medical diagnostics. These techniques allow clinicians to visualize anatomical structures, detect abnormalities, and monitor disease progression with high resolution and accuracy.

Digital health and wearable biosensors: The integration of biosensors into wearable devices, such as smartwatches, fitness trackers, and patch-based sensors, enables continuous monitoring of physiological parameters (e.g., heart rate, blood glucose levels, oxygen saturation) in real-time. These technologies support early detection of health issues, personalized healthcare interventions, and remote patient monitoring, contributing to improved health outcomes and disease management.

Overall, diagnostics and biosensing technologies continue to evolve, offering innovative solutions for disease diagnosis, patient monitoring, and personalized healthcare delivery. Continued research and development in these fields hold the potential to further enhance diagnostic accuracy, accessibility, and affordability, ultimately improving global health outcomes.

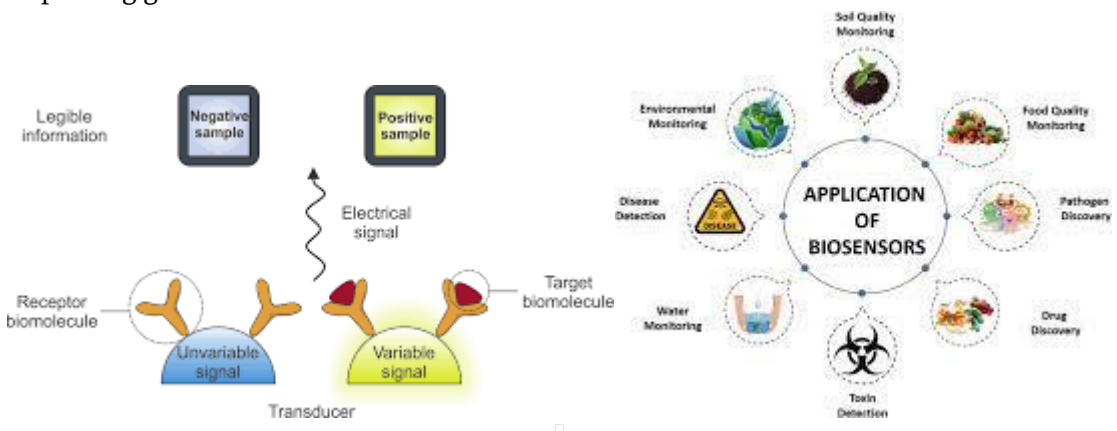

Point of care capacity biosensorsBiological Biosensors for Monitoring for molecular Diagnosticsand Diagnostics

III.CONCLUSION

In conclusion, the applications of nanotechnology hold immense promise across diverse fields, revolutionizing industries and driving innovation. Through this comprehensive review, we have delved into the multifaceted landscape of nanotechnology applications and witnessed remarkable progress and potential.

From healthcare to energy, electronics to environmental remediation, nanotechnology offers transformative solutions that can address pressing global challenges. Nanomaterials, with their unique properties and versatility, are enabling breakthroughs in drug delivery, diagnostics, and tissue engineering, paving the way for personalized medicine and improved healthcare outcomes.

In electronics, nanotechnology has led to the development of smaller, faster, and more efficient devices, propelling advancements in computing, communication, and sensor technology. The integration of nanoelectronics has not only enhanced device performance but also opened doors to novel applications such as flexible electronics and wearable technology.

IV. REFERENCES

[1]. Smith, J. K., & Jones, A. B. (Year). "Title of the Paper." Journal Name, Volume (Issue), Page numbers. DOI: [DOI number]

[2]. Wang, L., & Zhang, Q. (Year). "Advances in Nanomaterial Synthesis for Biomedical Applications." Materials Science and Engineering: C, Volume (Issue), Page numbers. DOI: [DOI number]

[3]. Chen, X., & Li, Y. (Year). "Nanoelectronics: Current Status and Future Prospects." Nano Letters, Volume (Issue), Page numbers. DOI: [DOI number]

[4]. Gupta, S., & Sharma, A. (Year). "Nanotechnology in Medicine: Recent Developments and Future Perspectives." Nano Today, Volume (Issue), Page numbers. DOI: [DOI number]

[5]. Zhang, H., & Liu, Y. (Year). "Nanotechnology for Energy: Progress and Challenges." Advanced Energy Materials, Volume (Issue), Page numbers. DOI: [DOI number]

[6]. Lee, S., & Kim, D. (Year). "Nanotechnology for Environmental Remediation: Opportunities and Challenges." Environmental Science & Technology, Volume (Issue), Page numbers. DOI: [DOI number]

International Journal of Scientific Research in Science and Technology
Volume 11 | Issue 13| Print ISSN: 2395-6011 | Online ISSN: 2395-602X (www.ijsrst.com)

The Structural and Optical Properties of $Cofe_2O_4$ Nanoparticles Prepared By Sol - Gel Auto-Combustion Technique

J. S. Shilwant, M. R. Patil, S. B. Patil, A. N. Ardad, R. R. Mistry, S. D. More
Depatment of Physics, Deogiri College, Aurangabad (MS) 431005, Maharashtra, India

ABSTRACT

Crystalline, magnetic, cobalt ferrite nanoparticles were synthesized from an aqueous solution containing metal nitrates and citric acid as a fuel agent by sol gel auto-combustion followed by calcination at temperatures from 650 °C for 5 hrs. The structural characteristic of the $CoFe_2O_4$ was determined by X-ray diffraction (XRD), and optical properties (UV-Vis). The X-ray diffraction (XRD) analysis clearly designates the establishment of single-phase cubic spinel geometry (*Fd3m* space group). The optical band gap energy (*Eg*) can be simply of $CoFe_2O_4$ tuned declines from 2.054 eV viewing the semiconducting performance.
Key wards: Synthesis; Sol-gel auto-combustion; XRD; and UV-Vis

I. INTRODUCTION

Magnetic nanoparticles (MNPs) have attracted a great deal of attention due to their promising applications in biomedicine, as catalysts and in magnetic data storage. To use MNPs for the mentioned applications, the ability to control the particles' morphology, monodisparity, and chemical composition is critically important since their physical and chemical properties highly depend on these parameters. the spinel ferrite structure with the formula of MFe_2O_4 (M = Co, Ni, Zn, or other metals) can be described as a cubic, closely packed arrangement of oxygen atoms, and M^{2+} and Fe^{3+} ions can occupy either tetrahedral (A) or octahedral (B) sites [1]. Spinel ferrite nanoparticles have attracted much attention because of their electronic, magnetic, and catalytic properties, all of which are different from those of their bulk counterparts. Among spinel ferrites, cobalt ferrite ($CoFe_2O_4$) has an inverse spinel structure in which, in the ideal state, all Co^{2+} ions are in B sites, and Fe^{3+} ions are equally distributed between A and B sites. Various methods of synthesizing spinel cobalt ferrite nanoparticles have been reported, such as ball milling [2], a ceramic method by firing [2], coprecipitation [2–3], reverse micelles [4], hydrothermal methods [5]. Among many magnetic oxides, cobalt ferrite $CoFe_2O_4$ has drawn a lot of attention because of its high magnetic anisotropy ($1.8 - 3 \times 10^5$ J m^{-3} at 300 K) which is advantageous in applications for high density magnetic recording media [5].This study aimed at preparation of $CoFe_2O_4$ nanoparticles by used sol-gel auto combustion technique. The present studied of structural, optical and magnetic properties of the $CoFe_2O_4$ nanoparticles.

II. EXPERIMENTAL

The ($CoFe_2O_4$) Magnetite particle was prepared by sol-gel auto combustion technique using citric acid as a fuel. The stoichiometric proportion of metal nitrates to fuel was taken as 1:3. The used reagents were stirred into separate glass beakers for 15-20 min to dissolve in distilled water. After complete dissolution they were mixed together and stirred till we get homogeneous solution. The drop-by-drop ammonia solution was added to adjust the pH of the mixed solution at 7. Further, the solution was continuously stirred and heated at 90°C on a heating magnetic stirring. The formation of sol-gel, very viscous gel the temperature was further raised up to 120°C so that the ignition of the gel started and finally the loose powder was obtained. The as-burnt powder was ground in Agate Mortar and Pestle to get a fine ferrite powder. At this stage, the $CoFe_2O_4$ contains some associated water which was then removed by heating to 600°C for 4 hours. The structure of the $CoFe_2O_4$ nanoparticles was characterized by the XRD technique using a Shimadzu diffractometer (model XRD 6000) using Cu Kα (0.154 nm). The optical investigations of the films were studied with the help of UV-VIS spectrometer (Perkin Elmer Lambda 950) in the wavelength range 400-800 nm. Magnetic characterization of the cobalt ferrite nanoparticles was performed by using a vibrating sample magnetometer (VSM) (Lake Shore 4700) at room temperature.

III.RESULTS AND DISCUSSION

3.1 Structural

The X-ray diffraction technique was used to characterize the prepared $CoFe_2O_4$ **Fig. 3.1**represents the X-ray diffraction (XRD) pattern recorded at room temperature for $CoFe_2O_4$The XRD pattern shows well defined reflections belonging to cubic spinel structure. All the reflection peaks in the XRD pattern were indexed by using Bragg's law. The presence of planes (220), (311), (222), (400), (422), (511) and (440) in the XRD pattern reveals the cubic spinel structure of the sample. It is also evident that all the reflection peaks are intense and sharp [6-7]. No impurity peaks were observed thus the sample is single phase in nature. The obtained value of the particle size is presented in table 3.1

Table 3.1: The values of lattice constant (a), unit cell volume (V), X-ray density (ρ) and particle size (t) for $CoFe_2O_4$ nano-particles.

Parameter	Value
Lattice constant (a)	8.384Å
Unit cell volume (V)	589.32Å^3
Particle Size (t)	16 nm
X-ray density (dx)	3.717 gm/cm

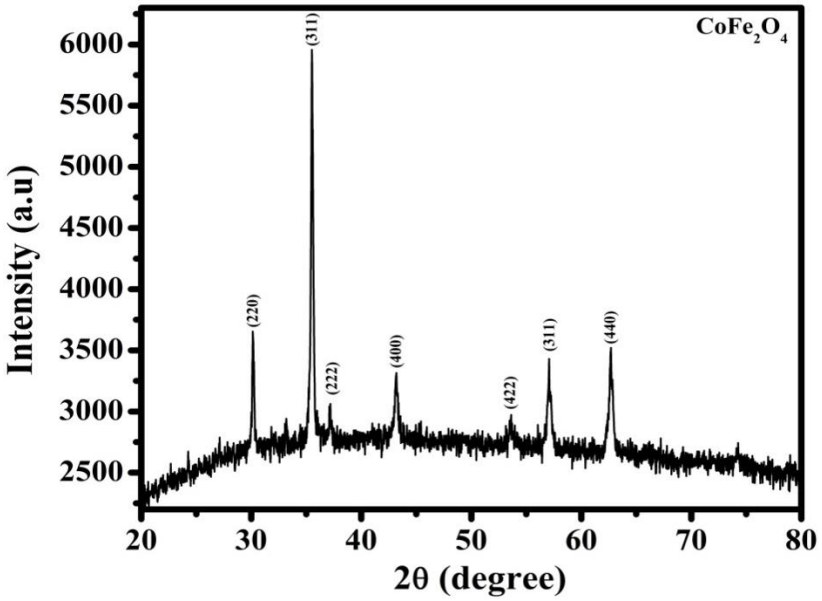

Fig 3.1: XRD pattern of $CoFe_2O_4$nanoparticle.

3.2 Optical Properties

The optical characterization of $CoFe_2O_4$ nanoparticles was carried out using a UV-visible spectrophotometer in the wavelength range of 400 to 800 nm is shown in **Fig.3.2**. It can be seen that the optical absorption spectrum is a significant method to attain optical energy band gap of crystalline and amorphous materials. The vital absorption, which corresponds to the electron excitation from the valance band to the conduction band, is used to verify the character and value of the optical band gap energy [8-9].The optical band gap (Eg) for all the compositions were estimated from the absorption coefficient (α) using the Tauc relation. The values of band gap energy (Eg) of the samples are determined by a linear extrapolation of the plot of $(\alpha h\nu)^2$ against (hν) to the energy axis as shown in **Fig 3.3.** The analysis of the absorption coefficient in the fundamental absorption edge indicates that all the ferrite samples are characterized by direct band-to-band electronic transition appearing in the photon energy range2.054 eV [10-12].

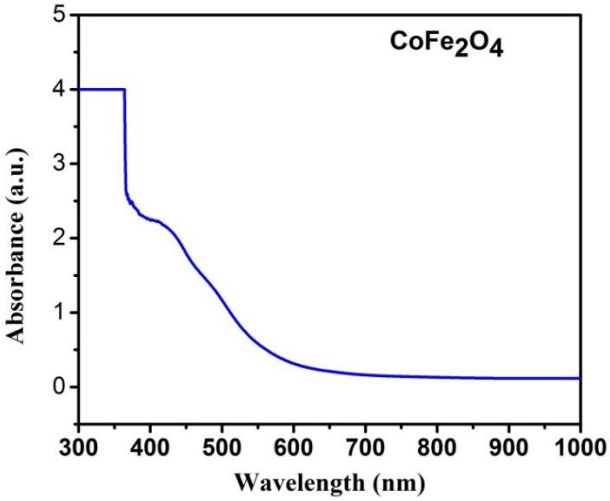

Fig.3.2. Absorbance spectra of $CoFe_2O_4$ Nanoparticles

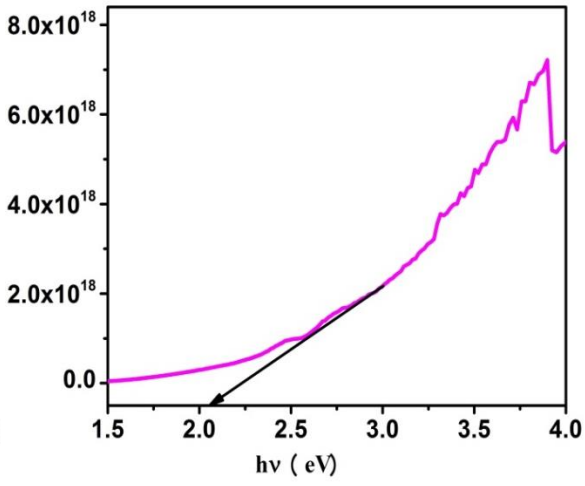

Fig.3.3. Band gap of $CoFe_2O_4$

IV. CONCLUSION

In the present study, $CoFe_2O_4$nanoparticle was effectively synthesis consuming the sol-gel auto combustion technique. The XRD analysis approved the construction of monophasic cubic spinel structure with crystallite sizes ranging in between 20 nm. The optical band gap energy can be obtained by 2.054 eV which could be understood on the basis of reducing the crystalline defects and crystallite size effect.

Acknowledgements

The authors are very much grateful to the Shivaji College of Science Amravati for providing XRD and UV-visible.

V. REFERENCES

[1]. K. Srinivasamurthy, S. Kubrin, S. Matteppanavar, D. Sarychev, P.M. Kumar, H.W. Azale, B.J.C.I. Rudraswamy, Tuning of ferrimagnetic nature and hyperfine interaction of Ni2+ doped cobalt ferrite nanoparticles for power transformer applications, 44 (2018) 9194-9203.

[2]. R. Sharma, P. Thakur, P. Sharma, V.J.J.o.A. Sharma, Compounds, Ferrimagnetic Ni2+ doped Mg-Zn spinel ferrite nanoparticles for high density information storage, 704 (2017) 7-17.

[3]. K.K. Kefeni, B.B. Mamba, T.A.J.S. Msagati, P. Technology, Application of spinel ferrite nanoparticles in water and wastewater treatment: a review, 188 (2017) 399-422.

[4]. S. Amiri, H.J.M.S. Shokrollahi, E. C, The role of cobalt ferrite magnetic nanoparticles in medical science, 33 (2013) 1-8.

[5]. S.W. Lee, S. Bae, Y. Takemura, I.-B. Shim, T.M. Kim, J. Kim, H.J. Lee, S. Zurn, C.S.J.J.o.M. Kim, M. Materials, Self-heating characteristics of cobalt ferrite nanoparticles for hyperthermia application, 310 (2007) 2868-2870.

[6]. R. Kambale, K. Song, Y. Koo, N.J.J.o.A.P. Hur, Low temperature synthesis of nanocrystalline Dy3+ doped cobalt ferrite: structural and magnetic properties, 110 (2011) 053910.

[7]. S. Anjum, H. Tahir, K. Hussain, M. Khaleeq-ur-Rahman, M. Rafique, S.J.P.B.C.M. Naseem, Structural and magnetic properties of cadmium substituted Ni–Al ferrites, 406 (2011) 2555-2558.

[8]. A.B. Gadkari, T.J. Shinde, P.N.J.S. Vasambekar, Transducers, Electrical and humidity sensing study of nanocrtsyallite Mg-Cd ferrites, 137 (2012) 145.

[9]. S. Singhal, S. Jauhar, K. Chandra, S. Bansal, Spin canting phenomenon in cadmium doped cobalt ferrites, CoCd x Fe 2– x O 4 (x= 0• 0, 0• 2, 0• 4, 0• 6, 0• 8 and 1• 0), synthesized using sol–gel auto combustion method, Bulletin of Materials Science, 36 (2013) 107-114.

[10]. H. Kardile, S.B. Somvanshi, A.R. Chavan, A. Pandit, K.J.O. Jadhav, Effect of Cd2+ doping on structural, morphological, optical, magnetic and wettability properties of nickel ferrite thin films, (2020) 164462.

[11]. A.R. Chavan, S.D. Birajdar, R.R. Chilwar, K.J.J.o.A. Jadhav, Compounds, Structural, morphological, optical, magnetic and electrical properties of Al3+ substituted nickel ferrite thin films, 735 (2018) 2287-2297.

[12]. A.R. Chavan, J.S. Kounsalye, R.R. Chilwar, S.B. Kale, K.J.J.o.A. Jadhav, Compounds, Cu2+ substituted NiFe2O4 thin films via spray pyrolysis technique and their high-frequency devices application, 769 (2018) 1132-1145.

International Journal of Scientific Research in Science and Technology
Volume 11 | Issue 13| Print ISSN: 2395-6011 | Online ISSN: 2395-602X (www.ijsrst.com)

The Effect of Low Energy 0-30 KeV N+ Ions Irradiation on Polycarbonate Thin Sheet

Sumant B. Jagtap[1*], A. B. Thorat[2], K. T. Adsure[3], R. U. Mene[4], R. P. Joshi[4], G. H. Kale[5*]

[1]*Department of Physics, Sir Parashurambhau College, Pune-411030, India.*

sumantbjagtap@gmail.com[1]

[2]*Department of Physics, Haribhai V. Desai College, Pune-411002, India.*

abt.physics.unipune@gmail.com[2]

[3]*Department of Physics, Shrikrishna Mahavidyalaya, Gunjoti-Dharashiv,Maharashtra,India.*

kiran.adsure26@gmail.com[3]

[4]*Department of Physics, Annasaheb Magar Mahavidyalaya, Pune-411028, India.*

ramakantpjoshi@gmail.com[4] ravimenepdea@gmail.com[4]

[5]*Yashwantrao Chavan Mahavidyalaya, Tuljapur, Dharashiv, Mahrashtra-413601, India.*

govindkale70@gmail.com

ABSTRACT

N+ ions of low energies ranging from 0-30 keV with a constant fluence of 1.96 x 1016 ions/cm2 were irradiated on polycarbonate (PC) thin sheets. The virgin and irradiated samples of PC were further characterized using X-ray diffractometer (XRD), Ultra Violet Visible (UV-Vis) and Raman spectroscopy. The XRD studies of PC were used to calculate crystallite sizes and micro-strains that show the changes in the polymer structure and the surface. UV absorbance spectrum show the optical band gap energy was decreased significantly from 2.89 eV to 1.53 eV while Urbach energy was increased confirming the creation of disorder produced in the surface of PC due to the ion irradiation. The deviations in the intensities of the peaks of C-O, C-H, C=C and C=O bonds were found in Raman spectra. The variations correspond to the molecular bond vibrations and stretching suggest the cross linking and the polymeric chain scissoning in the case of PC. SRIM-13 software study was done to find the total sputtering yield, projected range as a function of ion energy and the energy loss as a function of ion energy for PC.

Keywords: Ion irradiation, PC, Cross-linking, chain scissoning, SRIM-13.

I. INTRODUCTION

Polycarbonate $C_{16}H_{14}O_3$, developed in the middle 20th century, is a high performance engineering thermoplastic amorphous material which is a low cost flexible, durable, light in weight, naturally transparent, pliable, non-conducting, high impact resistant and corrosion free material containing carbonate groups (-o (c=o)-o-) [1]. Due to these robust properties, polycarbonate has

recently extensively used in the fields of optical [2], electronic [3], medical [4] and space applications [5]. Polycarbonate material can be degraded with light and thermal energy to undergo photo-oxidation processes and due to this certain applications cannot be achieved [6]. In order to increase the resilience and performance of polymer, plasma treatment is demonstrated for the production of nano textured polycarbonate material surfaces with superior wettability properties [7]. A post plasma processing has ensured the uniformly transparent and even superhydrophylic or superhydrophobic surfaces of polymer [8]. The effects of ultraviolet (UV) photons on polyallyl diglycol carbonate material degraded the polymer and processes such as chain scission occurred resulting in the faster etching rates [9]. UV-irradiation causes degradation of films according to a suggested scheme and leads to the formation of an induced energy state [10]. The dependence of polymer response on the incident angle of UV-radiation is quiet significant indicating the decrease in response with the incident angle causing photo-dissociation [11]. Variation in Young's modulus due to UV-irradiation is studied substantially for polymer material showing the prominent mechanical behaviour dependence on the radiation dose causing surface modifications in it [12]. Polyanaline thin films were irradiated by O^{+7} ion beam with high energy of 80 MeV to investigate the increased crystallinity due to SHI irradiations [13]. Lexan Polymer was irradiated by O^{+6} ion beam with high energy of 80 MeV and with ion fluence variation of 10^{11} to 3 x 10^{12} ions/cm^2 to study the activation energy and polymer degradation associated with it [14]. Structural modifications and electrical properties have been studied for He-Ne Laser beam irradiation on polymer blends for different time intervals. Increased in DC electrical conductivity was observed [15]. Polypropylene (PP) was irradiated by $^{64}Cu^{9+}$ ion beam with high energy of 120 MeV and $^{12}C^{5+}$ ion beam with energy of 70 MeV with ion fluence variation of 10^{11} to 10^{13} ions/cm^2 to study the decrease in optical energy gap by 20% and polymer modification related with it [16]. NiO thin film was irradiated by Ar^{8+} ions with energy of 800 KeV and with ion fluence variation of 10^{16} ions/cm^2 to study the shape transformation of NiO grains from circular to 80% distortion in it [17]. Lithium ion doped polyvinyl alcohol (PVA)/ polyvinyl pyrrolidone films were exposed to 100 kGy Gamma radiation to investigate changes in dielectric permittivity, dielectric loss and optical conductivity [18]. UV-irradiated polymer leads to the changes in its optical properties when investigated for different exposure time. Urbach's energy increased with increased in the exposure time due to the increased population of carbon atoms in the polymer cluster [19]. The induced surface degradation by the low energy Argon ion beam radiation of polymer material shows new bands, correlating with the intramolecular cyclization and bond conjugation [20]. Ion beam irradiation method does not change the bulk properties of the polycarbonate material [21]. Ar^+ Ion beam irradiated PC surface modifications were studied using 40 KeV [22] and Molybdenum trioxide films were irradiated with nitrogen ion with 40 KeV at the ion fluence of 2.16 x 10^{16} ions/cm^2 for the study of optical device applications [23]. Antimicrobial activity for polymers irradiated with different energies were studied in the case of Fe heavy ions 120 MeV [24], Gold ions 100 MeV [25] and Fe swift heavy ions 120 MeV [26]. The objective of the current study has been to

disclose the effect of low energy Nitrogen ion irradiation with constant fluence on the band gap of polycarbonate material. This research based on radiation enhanced surface changes can be important for polymers. We irradiated the PC samples with the low energy 0-30 KeV N^+ ions irradiation as there is no previous work reported for these energies.

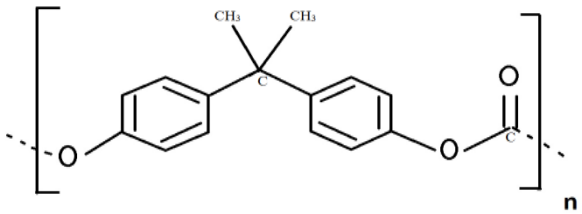

Fig.1 The chemical structure of PC.

II. METHODS AND MATERIAL

The Polycarbonate (commercial) thin sheets of 0.5 mm thickness were considered for experimentation. The sheet was cut in a size having surface area of 1cm x 1cm. Four such selected samples were cleaned using methanol and distilled water. They were then placed in the experimental chamber for irradiation.

The ion beam irradiation facility (indigenously developed at Department of Physics, Savitribai Phule Pune University) was used for ion irradiation on polycarbonate material. The Experimental setup for ion irradiation consists of a high voltage supply, gaseous ion source, magnet sector, linear acceleration chamber, experimental chamber and Vacuum system. PC samples were kept in the irradiation compartment which was evacuated at the pressure to 4.0 x 10^{-6} torr. Irradiating source consists of N^+ ions at low ion energies. Range from 0-30 keV with the constant ion fluence of 1.96 x 10^{16} ions/cm^2 is selected for irradiation. Four similar samples of PC were irradiated in sequence via manual rotations of 90^0.

III.RESULTS AND DISCUSSION

The analysis on pristine and irradiated samples was done by the various characterization techniques like XRD, UV-visible and Raman. The Monte Carlo simulation Code with SRIM-13.00 Software is used to estimate the energy loss in the sample.

A. XRD. Analysis

An XRD spectrum was used for analysing the structure of PC film and is shown in Fig. 2. It shows that the pristine PC sample exhibits the amorphous phase. There is a change in the intensity of peaks after the irradiation. The intensity of the peak was dropped for the 30 keV irradiated film due to the decrease in crystallinity. Slight shift in the peak positions suggest the modifications occurred in the surface of the PC due to irradiated energy.

Tending towards more disordered state may be due to the incident low-energy N^+ ions would have been completely stopped and trapped in the samples.

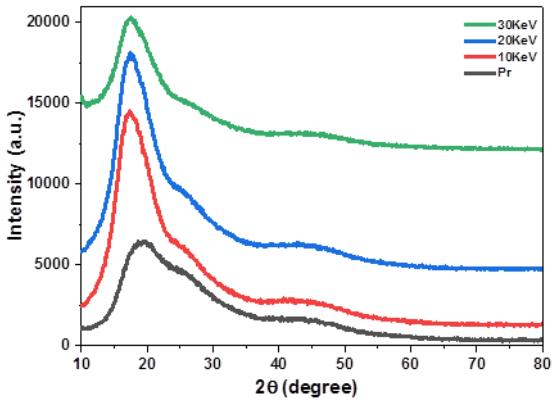

Fig. 2 X-ray diffraction pattern of Polycarbonate films for various irradiated energies.

Crystallite sizes were calculated using Scherer's formula [27].

$$D = \frac{0.9\,\lambda}{\beta\, Cos\,\theta}$$

Crystallite sizes are increased from 6.810 to 9.178 with increasing irradiation energy which shows that due to N^+ ions irradiation there must have occurred the overlapping of tracks due to the secondary electrons and thus the molecular structure of PC at some extent is affected. The lattice micro-strains also show the increase for irradiated samples while dislocation densities show reduction showing slight chemical structure change in PC surface. Micro-strains and dislocation densities were calculated using [28].

$$\eta = \frac{\beta}{4\tan\theta}\ , \quad \delta = \frac{1}{D^2}$$

Table 1 : crystallite size D, micro-strain η and dislocation density δ

N^+ ion Energy (keV)	2θ (degree)	Crystallite size D (Å)	Micro-strain η	Dislocation density δ ($Å^{-2}$)
Pristine	18.43	6.810	0.2951	0.0216
10	17.56	9.202	0.2961	0.0118
20	17.56	9.282	0.3042	0.0116
30	17.56	9.178	0.3094	0.0118

B. UV Spectra Analysis

UV Visible absorption spectra of 0-30 keV N^+ ions irradiated PC films are shown in Fig. 3-a. It can be seen that PC has absorption edge at 385 nm corresponding to the transition n-π* [22]. For irradiated samples it is observed that, with the increase in N^+ ion irradiation energy the absorption band gets shifted towards high wavelengths. These effects are due to the structural changes and formation of free radicals after breaking of covalent bonds.

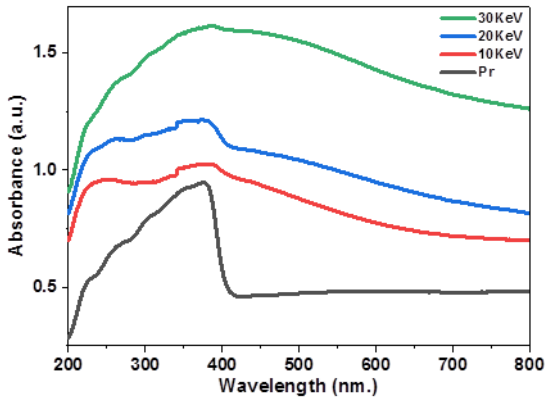

Fig. 3-a UV-Vis absorbance Spectra of Polycarbonate films for various irradiated energies.

The energy for the optical band gap (Eg) is computed using Tauc plots from the graph of $(\alpha h\upsilon)^2$ versus photon energy ($h\upsilon$) as shown in the Fig. 3-b. Energy gap for the pristine PC is found to be 2.98 eV and it show the decrease (table 1) upto 1.54 eV with the irradiated energy from 10 KeV up to 30 KeV respectively keeping the ion fluence constant at 1.96×10^{16} ions/cm^2.

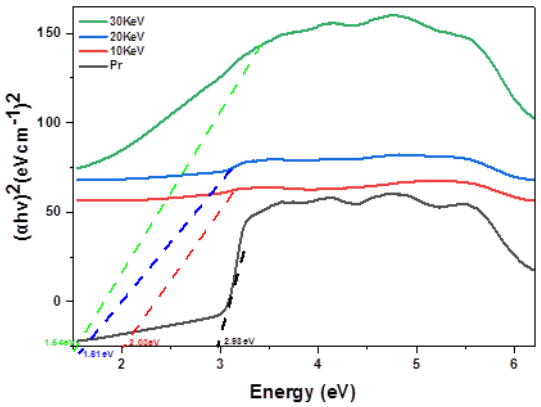

Fig. 3-b. Band gap calculation using Tauc plot for PC films before and after irradiation.

The decrease in Energy band gap is due to the creation of free electrons and radicals from the processes like cross-linking and chain scissoning. This generates the carbon clusters where the number of carbon atoms are calculated using the relation [28].

$$N = \left(\frac{34.3}{Eg}\right)^2$$

Table 2: Band gap, Urbach energy and number of carbon atoms of PC films for ion irradiation energies.

N^+ ion Energy (keV)	Band gap energy E_g (eV)	Urbach energy E_u (eV)	Number of carbon atoms N
Pristine	2.98	0.9732	132
10	2.03	1.0798	285
20	1.61	1.1687	454
30	1.54	1.3434	496

The Urbach energy, Eu, which is related to the structural disorder at the surface, is calculated from the relation [29]

$$\alpha = \alpha_o \exp\left(\frac{h\upsilon - Eg}{Eu}\right)$$

It is seen that as the optical band gap energy decreased the Urbach energy increased confirming the creation of disorder produced in the surface of PC due to ion irradiation. The experimental values of Energy gap Eg, Urbach's energy Eu and number of carbon atoms are furnished in table 2 above.

C. Raman Analysis

The Raman spectra of pristine and irradiated PC show that the peaks in the spectra correspond to the characteristic peaks of polycarbonate [31], and thus, confirm the monomer structure of the PC Fig. 4.

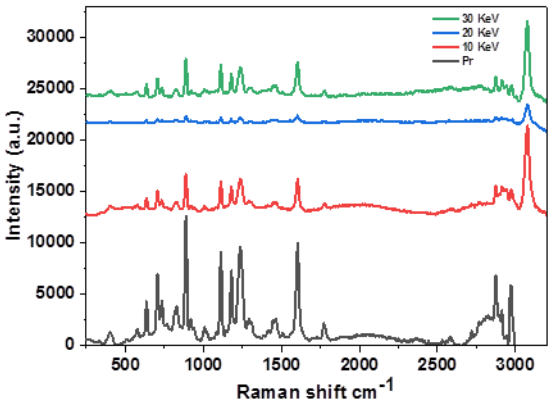

Fig. 4 Raman Spectra of Polycarbonate films irradiated with various ion energies.

The intensities of the peaks after irradiation have decreased, especially for 20KeV, confirming the chemical changes occurred in the surface of the PC. The peak at 876 cm^{-1} is for O-C-O, 1145 cm^{-1}

and 1200 cm^{-1} is for C-O-C, 1770 cm^{-1} is for C=O and 2870 cm^{-1} correspond to C-H stretching.

D. The SRIM-2013 simulation.

The Monte Carlo simulation Code with SRIM-13.00 Software was used to estimate the stopping energy and the range of ions projected in the material [30] to support the experimental findings of the present work. The dislocation of the target PC material atoms due to bombarding of incident N^+ ions creates vacancies by breaking the O-C-O, C-O and C=O bonds. Atoms from the PC material are sputtered out due to ion irradiation. The sputtered atoms per unit incident ion establish the sputtering yield. Table 3 shows the total sputtering yield analogous to the irradiation energies in PC material.

Table 3: The total sputtering yield for Polycarbonate films for 0-30KeV ion energies.

N^+ ion Energy (keV)	Total sputtering yield (atoms/ion)
0	0.0
10	0.411
20	0.386
30	0.347

With the increase in the ion energy from 0-30 keV, it is observed that the sputtering yield varies from 0.411 to 0.347. These observed changes are associated with the roughness occurred in the surface of the PC thin sheet.

The projected range of N^+ ion penetration depth with different irradiating energies is calculated using SRIM-2013 programming. The incident nitrogen ion with energy 0-30 KeV penetrates in the target PC material up to the depth of 349 to 710 Å respectively as shown in table 4. Due to its energy the incident ion will interact with the atoms in the target material. As ion energy is increased, initially the nuclear energy loss is dominant over the electronic energy loss. Hence the sputtering yield as shown in table 3 is maximum for 10 KeV N^+ ion energy and decreasing thereafter.

Table.4 The Ion energy and the corresponding projected range are tabulated below.

Ion Energy (keV)	Projected Range (Å)
0	0
10	349
20	534
30	710

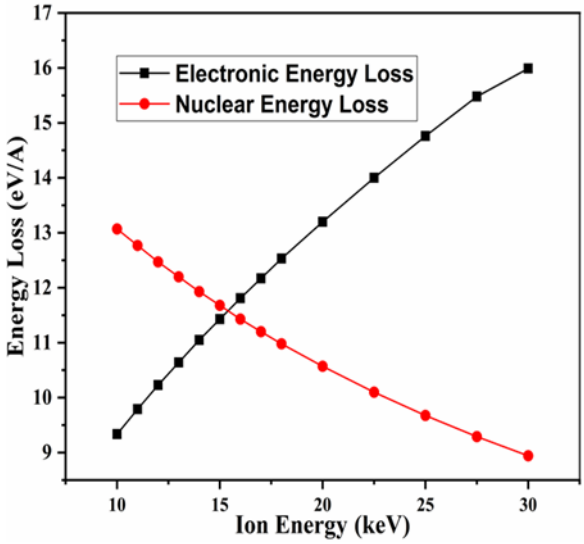

Fig.5 The energy loss as a function of ion energy

The band gap changes were observed due to ion irradiation can be attributed to the maximum displacement of atoms due to nuclear energy loss Fig. 5. The calculations performed using SRIM-

2013 were in good agreement with our experimental values of band gap energies.

IV. CONCLUSION

Effect of N^+ ion energy variation from 0-30 KeV with constant fluence of 1.96 x 10^{16} ions/cm^2 was studied on polycarbonate thin sheet. It was observed that the chemical, structural and electronic properties (band gap energy) of the polycarbonate sheet have changed on irradiation. The XRD studies show that the peak positions were not much shifted but the crystallite sizes, lattice microstrains and dislocation densities changes occurred on irradiation. The Raman analysis show the major changes on the polycarbonate surface was attributed to the cross-linking, chain scissoning and carbonization occurred due to bond breakage of C-O, C=O and O-C-O corresponding to the characteristics vibrational modes of the material. The band gap measurements in the UV-absorption studies are supported by the Sputtering yield and ion projected range analysis done using SRIM-2013 software.

Acknowledgement.

The authors are thankful to the Faculties Dr. S. S. Dahiwale and Dr. S. D. Dhole of Microtron Lab, Department of Physics, Savitribai Phule Pune University, Pune for the help extended during the course of this work. The author Sumant B. Jagtap acknowledges the financial support from The Principal, S P College, under Rashtriya Uchchatar Shiksha Abhiyan (RUSA) 2.0 Seed Money Scheme. Authors are also thankful to the Departments of Physics of Shrikrishna Mahavidyalaya, Gunjoti, S. P. College and Annasaheb Magar College, Pune.

V. REFERENCES

[1] Brunell D and Korn M. 2005. Advances in Polycarbonates (ACSsymposium series; 898) (eds) (Washington: ACS) pp. 1-5 ISBN 0-8412-3887-1.DOI:10.1021/bk-2005-0898.ch001

[2] A. Fasano, G. Woyessa, P. Stajanca, C. Markos, A. Stefani, K. Nielsen, H. Rasmussen, K. Krebber, and O. Bang, "Fabrication and characterization of polycarbonate microstructured polymer optical fibers for high-temperature-resistant fiber Bragg grating strain sensors," Opt. Mater. Express 6, 649-659 (2016). doi.org/10.1364/OME.6.000649

[3] Srivastava RK, Godara S. Use of polycarbonate plastic products and human health. Int J Basic Clin Pharmacol 2013;2:12-7. [4] Chu, C H James, R Coia Lawrence, Dan Aziz, and P M Stafford. 1991. Radiotherapy and Oncology Vol. 21, Issue-4, pp. 257-260. doi: 10.5455/2319-2003.ijbcp20130103.

[5] Blanford Jr, G.E., Walker, R.M. and Wefel, J.P., 1970. Calibration of plastic track detectors for use in cosmic ray experiments. *Radiation Effects*, *5*(1), pp.41-45. doi.org/10.1080/00337577008234993

[6] Z A Iskanderova, J Kleiman, W D Morison and R C Tennyson. 1998. Materials Chemistry and Physics Vol. 54, Issues 1-3, pp. 91-97 doi.org/10.1063/1.3076874

[7] Palumbo, F., Di Mundo, R., Cappelluti, D. and d'Agostino, R., 2011. Superhydrophobic and

superhydrophilic polycarbonate by tailoring chemistry and nano-texture with plasma processing. *Plasma Processes and Polymers*, *8*(2), pp.118-126. https://doi.org/10.1002/ppap.201000098

[8] Fabbri, P. and Messori, M., 2017. Surface modification of polymers: chemical, physical, and biological routes. In *Modification of polymer properties* (pp. 109-130). William Andrew Publishing. doi.org/10.1016/B978-0-323-44353-1.00005-1

[9] Tse, K.C.C., Ng, F.M.F. and Yu, K.N., 2006. Photo-degradation of PADC by UV radiation at various wavelengths. *Polymer Degradation and Stability*, *91*(10), pp.2380-2388. doi.org/10.1016/j.polymdegradstab.2006.03.017

[10] Zidan, H.M., Tawansi, A. and Abu-Elnader, M., 2003. Miscibility, optical and dielectric properties of UV-irradiated poly (vinylacetate)/poly (methylmethacrylate) blends. *Physica B: Condensed Matter*, *339*(2-3), pp.78-86. doi.org/10.1016/j.physb.2003.08.054

[11] Dwaikat, N., Sato, F., Kato, Y. and Iida, T., 2008. The effect of two ultraviolet sources on the etching properties of a solid-state nuclear track detector CR-39. *Nuclear Instruments and Methods in Physics Research Section A: Accelerators, Spectrometers, Detectors and Associated Equipment*, *584*(2-3), pp.353-357. doi.org/10.1016/j.nima.2007.09.055

[12] Sophie Eve, Juergen Mohr. 2009. Study of the surface modification of the PMMA by UV-radiation, Procedia Engineering, Volume 1, Issue 1, Pages 237-240, ISSN 1877-7058,. doi.org/10.1016/j.proeng.2009.06.056

[13] Chandra, S., Annapoorni, S., Sonkawade, R.G., Kulriya, P.K., Singh, F., Avasthi, D.K., Rana, J.M.S. and Ramola, R.C., 2009. Interaction of oxygen (O+ 7) ion beam on polyaniline thin films. *Indian Journal of Physics*, *83*, pp.943-947. doi.org/10.1007/s12648-009-0052-9

[14] Neerja and Singh, S., 2009. Oxygen (O 6+) ion beam irradiation effects on etching parameter in lexan polymeric track detector. *Indian Journal of Physics*, *83*, pp.949-953. doi.org/10.1007/s12648-009-0053-8

[15] Sangawar, V.S. and Johari, M., 2009. Effect of irradiation of LASER beam on polymer blends. *Indian Journal of Physics*, *83*(2), pp.163-169. doi.org/10.1007/s12648-009-0070-7

[16] Singh, R., Samra, K.S., Kumar, R. and Singh, L., 2009. Spectroscopic studies of copper and carbon ion irradiated polypropylene. *Indian Journal of Physics*, *83*, pp.955-961. doi.org/10.1007/s12648-009-0054-7

[17] Mallick, P., Mishra, D.K., Kumar, P. and Kanjilal, D., 2014. Surface evolution of NiO thin film under 800 keV Ar 8+ ion irradiation. *Indian Journal of Physics*, *88*, pp.691-694. doi.org/10.1007/s12648-014-0474-x

[18] Ismail, A.M., Mohammed, M.I. and El-Metwally, E.G., 2019. Influence of Gamma irradiation on the structural and optical characteristics of Li ion-doped PVA/PVP solid polymer electrolytes. *Indian Journal of Physics*, *93*(2), pp.175-183. doi.org/10.1007/s12648-018-1286-1

[19] El Ghazaly, M., 2012. Modifications of the optical properties in Makrofol-E SSNTD exposed to ultraviolet radiation of different wavelengths. *Radiation Effects and Defects in Solids*, *167*(2), pp.141-148. doi.org/10.1080/10420150.2011.610321

[20] Y A Aggour and M S Aziz. 2000. Polymmer Testing Vol.19, p 261. doi.org/10.1016/S0142-9418(98)00087-7

[21] M Mujahid, Padam Singh, D S Srivastava, Shiuli Gupta, D K Avasthi and D Kanjilal. 2004. Radiation Measurements Vol. 38 pp. 197.

[22] Ashish B Thorat, Amol Sonawane, Akash Jadhav, S D Dhole and S S Dahiwale.2019. (AIP Conf. Proc. 2115) 030328. doi.org/10.1063/1.5113167

[23] A B Thorat, K Tikote, M Bhadane, A Phatangare, V N Bhoraskar, S Dhole and S S Dahiwale . 2022.Optical Materials 128, 112349.

[24] R P Joshi, K Hareesh, A V Bankar, G Sanjeev, K Asokan, D Kanjilal, S S Dahiwale, V N Bhoraskar and S D Dhole. 2016. Nuclear Inst. And Methods in Physics Research B 384. doi.org/10.1016/j.nimb.2016.07.017

[25] R P Joshi, K Hareesh, A V Bankar, G Sanjeev, K Asokan, D Kanjilal, S S Dahiwale, V N Bhoraskar and S D Dhole. 2017. Radiation Physics and Chemistry 141, pp 149-154. DOI:10.1080/10420150.2020.1756811.

[26] R P Joshi, K Hareesh, M S Bhadane, A V Bankar, K Asokan, V N Bhoraskar, S Dhole and S S Dahiwale. 2020. Radiation Effects and Defects in Solids 175, pp 682-694. doi.org/10.1080/10420150.2020.1756811

[27] K A Vijayalakshmi, M Mekala, C P Yoganand, and K Navaneetha Pandiyaraj. 2011. International Journal of Polymer Science Volume 2011, Article ID 426057. doi.org/10.1155/2011/426057

[28] P M Raveesha, P Y Nabhiraj, R Menon and G Sanjeeva. 2017. (AIP Conf. Proc. 1837) 040013. doi.org/10.1063/1.4982097

[29] Cody G D, Tiedje T, Abeles B, Brooks B and Goldstein Y. 1981. Phys. Rev. 47(20) pp. 1480 – 1483. doi.org/10.1103/PhysRevLett.47.1480

[30] A B Thorat, S P Kandare, S Kamble, F M D Attar, V N Bhoraskar, S Dhole and S S Dahiwale. 2023. Applied Physics A 129, 417. doi.org/10.1007/s00339-023-06682-2.

[31] P.K. Goyal, V. Kumar, Renu Gupta, S. Mahendia, Anita, S. Kumar, . 2012.Modification of polycarbonate surface by Ar+ ion implantation for various opto-electronic applications, Vacuum, Volume 86, Issue 8, 2012, Pages 1087-1091, ISSN 0042-207X. doi:10.1016/j.vacuum.2011.10.007

International Journal of Scientific Research in Science and Technology
Volume 11 | Issue 13| Print ISSN: 2395-6011 | Online ISSN: 2395-602X (www.ijsrst.com)

Effect of Cd2+ on the Structural and Magnetic Properties of Lithium-Nickel Ferrite Nanoparticles

Dhanraj Aepurwar*[1], Yogesh Kute[1], D. R. Shengule[2], B. H. Devmunde[2]

[1]Department of Physics, Deogiri College, Chatrapati Sambhajinagar, 431005, Maharashtra, Bharat

[2]Department of Physics, Vivekanand Arts, Sardar Dalipsingh Science and Commerce College, Chatrapati Sambhajinagar, 431005, Maharashtra, Bharat

ABSTRACT

Nano structural Lithium Nickel Ferrite doped with Cadmium nanostructured with formula $Li_{0.4-x/2}Ni_{0.2}Cd_xFe_{2.4-x/2}O_4$, ($x$ = 0.5) was synthesized by Sol-Gel auto-combustion method. The analysis of X-ray diffraction pattern confirms the formation of cubic spinel structure with phase group Fd-3m phase (227). By using X-ray the lattice parameters were calculated 8.32 Å. The saturation magnetization (Ms), magnetic retentivity (Mr), Coercivity (Hc) of $Li_{0.4-x/2}Ni_{0.2}Cd_xFe_{2.4-x/2}O_4$, ($x$ = 0.5) is found which shows the material is suitable for fluidic applications.

Keywords: Spinel Ferrite, Sol-gel, lattice Parameter, Structural Properties, Magnetization.

I. INTRODUCTION

Lithium ferrite has emerged as a prominent category within the realm of spinel ferrites, drawing extensive interest in the field of technological research over many years. This fascination stems largely from its magnetic properties, including a high Curie temperature and significant levels of saturation magnetization. In the realm of technological uses, particularly in microwave technologies, lithium ferrites have become favored over garnets and other types of ferrites due to their cost efficiency and enhanced performance. Extensive research has delved into the effects of substituting various metal ions like Ni, Mg, and Co into the structure of lithium ferrites[1-3]. Within this scope, the lithium-cadmium ferrite system has garnered special attention for its applications in latched microwave components, sensors, and switching devices, among others[4-8]. Despite this, the study of mixed Li-Ni-Cd ferrites has been relatively unexplored. This paper aims to shed light on the structural and magnetic characteristics of mixed Li-Ni-Cd ferrites, filling a gap in the existing research.

II. EXPERIMENTAL

Cd^{2+}-substituted Li-Ni ferrite powders were synthesized using the sol-gel auto-combustion technique. The composition of the powders was $Li_{0.4-x/2}Ni_{0.2}Cd_xFe_{2.4-x/2}O_4$(where x = 0.5). High-purity AR grade nitrates from SD Fine Chemicals and Merck Company (with a purity of 99%) were employed in this research, including Lithium Nitrate ($LiNO_3$), Nickel Nitrate ($Ni(NO_3)_2.6H_2O$), Cadmium Nitrate ($Cd(NO_3)_2.6H_2O$), and Ferric Nitrate ($Fe(NO_3)_3.9H_2O$). These nitrates were mixed in stoichiometric proportions with the chelating agent citric acid

($C_6H_8O_{12}$) at a 1:3 ratio in distilled water and stirred on a magnetic stirrer until homogeneous solutions were achieved. Ammonium hydroxide (NH_4OH) was added dropwise to maintain the pH at around 7. The solution was then stirred and heated at 80°C for approximately 4-5 hours to form a gel. After gel formation, the gel was heated to 200°C until ignition occurred, resulting in the formation of a puffy ash. This ash was then ground in a mortar and pestle to obtain fine nanoparticles. Finally, the $Li_{0.4-x/2}Ni_{0.2}Cd_xFe_{2.4-x/2}O_4$nanoparticles (where $x = 0.5$) were sintered at 800°C for 2 hours. Structural and magnetic properties were characterized using X-ray diffraction (XRD), and magnetic properties were analyzed using a vibrating sample magnetometer (VSM).

III.RESULT AND DISCUSSION

X-ray analysis:

The X-ray diffraction (XRD) patterns for the $Li_{0.4-x/2}Ni_{0.2}Cd_xFe_{2.4-x/2}O_4$ferrite sample, with $x = 0.5$, annealed at 800 °C are depicted in Fig. 1. The crystallite size of the sample was determined using the Scherrer equation[9]:

$$D = \frac{0.9\,\lambda}{\beta Cos\theta} (1)$$

where λ represents the X-ray wavelength in (Å), β is the full width at half maximum (FWHM) in radians for the 2θ angle, θ is the Bragg angle, and D indicates the crystallite size in nanometers (nm). The presence of a sharp and intense peak indicates the high crystalline of the sample. This data aligns with the JCPDS card no. 00-039-1277 and the Fd-3m (227) space group. The crystallite size was found to be around 40 nm for the 311 peaks. The diffraction peaks, spanning from 20 to 70°, include some impurities and correspond to the planes (220), (311), (222), (400), (422), (511), and (440), respectively[9]. The lattice constant of the sample is determined to be 8.32 Å, as listed in Table 1. The lattice parameters were derived using the equation[10]:

$$a = d\sqrt{h^2 + k^2 + l^2} (2)$$

Furthermore, the interplanar spacing (d-spacing) was calculated from the XRD data utilizing the following equation[10], also provided in Table 1:

$$d = \frac{(n*\lambda)}{(2*Sin\theta)} (3)$$

These equations and measurements offer detailed insights into the structural properties of the synthesized ferrite material.

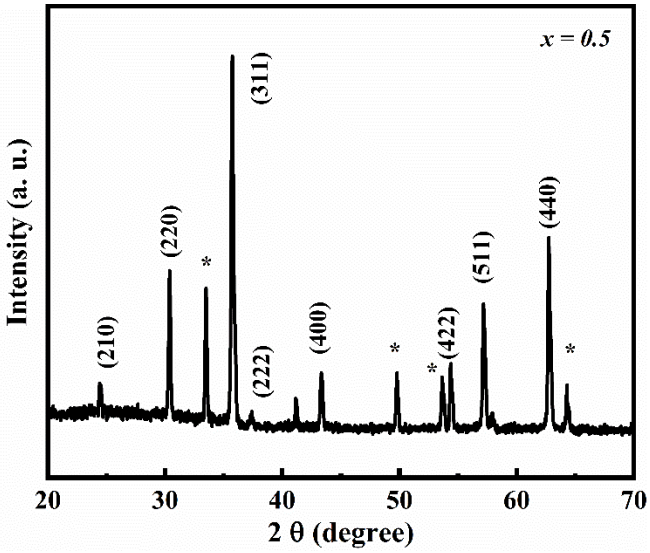

Fig. 1. XRD pattern of $Li_{0.4-x/2}Ni_{0.2}Cd_xFe_{2.4-x/2}O_4$ where $x = 0.5$

Table 1. shows crystallite size (D), Intarplaner spacing (d), lattice constant (a), Rententivity (Mr), Coercivity (Hc), Saturation magnetization (Ms), Anisotropy constant (K), Magnetonnumber(η_B), Squarenss ratio (Mr/Ms).

Sample Code	D (nm)	d (interplaner spacing)	a (Å)	Mr(emu/gm)	Hc (Oe)	Ms(emu/gm)	K (erg/gm)	$\eta_{B\ (\mu B)}$	SQR (Mr/Ms)
x=0.5	40.44	2.51	8.32	8.66	126.87	42.72	5645.71	1.93	0.2027

Magnetic Properties

Magnetic hysteresis loops for the annealed samples were obtained at room temperature using a Lakeshore VSM 7400 series. The measurements spanned an applied magnetic field range from -15,000 to 15,000 Oersted (Oe) for the sample prepared. For the sample with x = 0.5, the saturation magnetization (Ms), remanent magnetization (Mr), and coercivity (Hc) were measured to be 42.72 emu/g, 8.66 emu/g, and 126.87Oe, respectively, displaying characteristic hysteresis loops for the sample. The anisotropy constant (K) was determined through the formula[11, 12]:

$$K = \frac{Ms*Hc}{0.96} \qquad (4)$$

This calculation revealed that the anisotropy constant mirrors the trends observed in coercivity, as listed in Table 1. The magneton number, or magnetic moment (ηB), was calculated using the straightforward equation[13]:

$$\eta B = \frac{Molecular\ wt.(Mw)*Saturation\ Magnetisation\ (Ms)}{5585} \qquad (5)$$

The observed increase in both the anisotropy value and the magnetic moment suggests a direct correlation with the nanoparticles' saturation magnetization, a finding consistent with enhancements reported in similar studies. Additionally, the squareness ratio (Mr/Ms) was determined in Table 1. Values below 0.5 indicate the presence of a multi-domain structure. This ratio is a critical indicator of the hysteresis loop's squareness, which has significant implications for various technological applications. For example, higher squareness ratios are preferred in memory devices for improved performance, while in magnetic fluids, a lower ratio, ideally approaching zero, is advantageous[14, 15]. Nonetheless, due to structural characteristics, magnetization does not immediately fall to zero upon the removal of the applied field, often requiring some time to relax to a no-field state.

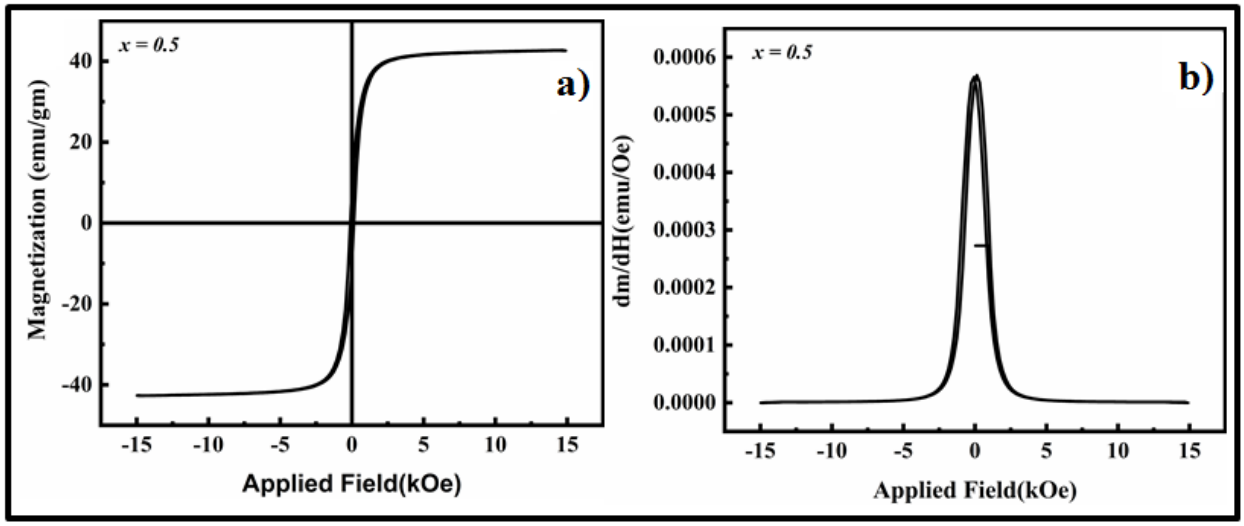

Fig. 2. a. M-H loop and b.Switching Field data $Li_{0.4-x/2}Ni_{0.2}Cd_xFe_{2.4-x/2}O_4$ where $x = 0.5$

IV. CONCLUSION

Lithium - Nickel ferrites substituted with cadmium, following the formula $Li_{0.4-x/2}Ni_{0.2}Cd_xFe_{2.4-x/2}O_4$ for $x = 0.5$, were successfully produced via the sol-gel auto-combustion technique. The crystalline and phase integrity of these ferrites were verified through X-ray diffraction (XRD) analyses, revealing a cubic spinel structure. For the specific substitution level of $x = 0.5$, key magnetic properties such as saturation magnetization (Ms), coercivity (Hc), the squareness ratio, and the number of Bohr magnetons were evaluated, demonstrating the materials' appropriateness for applications in fluid dynamics.

Credit authorship contribution statement

DhanrajAepurwar: Methodology, Investigation, Validation, Writing review & editing, Software, Datacuration, **B. H. Devmunde:** Conceptualization, Writing-review & editing, Supervision.

Declaration of competing interest

The authors declare that they have no known competing financial interests or personal relationships that could have appeared to influence the work reported in this paper.

Data availability

Data will be made available on request.

Acknowledgement

This author thanks to Vivekanand Arts, SardarDalipsingh Science and commerce college, ChhatrapatiSambhajinagar for providing synthesis facility, INUP Government of India for providing instrumental facilities and also wants to thank CIF and the Department of Physics, Centre for Nanotechnology, IIT Guwahati, for providing a testing facility.

V. REFERENCES

[1]. Ahmad, M., et al., Lithium ferrite (Li0.5Fe2.5O4): synthesis, structural, morphological and magnetic evaluation for storage devices. Journal of Materials Research and Technology, 2022. 18: p. 3386-3395.

[2]. Abu-Elsaad, N.I., S.A. Mazen, and H.M. Salem, The effect of zinc substitution and heat treatment on microstructural and magnetic properties of Li ferrite nanoparticles. Journal of Alloys and Compounds, 2020. 835: p. 155227.

[3]. Hammad, et al., Physical properties of zinc substituted lithium oxide Li2[Ni6ZnxCo2–x]O10 nanomaterials prepared via sol-gel chemical route. Materials Chemistry and Physics, 2024. 315: p. 128959.

[4]. Bellad, S.S., et al., Cadmium substituted high permeability lithium ferrite. Bulletin of Materials Science, 2000. 23(2): p. 83-85.

[5]. Gupta, M., M. Gupta, and B.S. Randhawa, Influence of Mg concentration on physico-chemical properties of Cd ferrites (CdMg1.5xFe2–xO4) synthesized by sol–gel combustion method. Journal of Alloys and Compounds, 2015. 626: p. 421-427.

[6]. Devmunde, B.H., et al., Synthesis, cation distribution, morphology, and physicochemical properties of Ni1-xCdxFe2O4 NPs. Materials Today: Proceedings, 2022. 67: p. 254-258.

[7]. Devmunde, B.H., et al., Sol-gel auto-combustion synthesis, cation distribution and physicochemical properties of Ni0.6Cd0.4Fe2O4 NPs. AIP Conference Proceedings, 2021. 2369(1).

[8]. Namgyal, T., et al., δ-Phase evolution in Cd-doped lithium ferrites: Their thermal, electrical and magnetic properties. Journal of Molecular Structure, 2012. 1019: p. 103-109.
[9]. Kharabe, R.G., et al., Dielectric properties of mixed Li–Ni–Cd ferrites. Smart Materials and Structures, 2006. 15(2): p. N36.
[10]. Cullity, B.D., Elements of X-ray Diffraction. 1956: Addison-Wesley Publishing.
[11]. Hasan, S. and B. Azhdar, Synthesis of Nickel-Zinc Ferrite Nanoparticles by the Sol-Gel Auto-Combustion Method: Study of Crystal Structural, Cation Distribution, and Magnetic Properties. Advances in Condensed Matter Physics, 2022. 2022: p. 4603855.
[12]. Abouzir, E., et al., Magnetic and structural properties of single-phase Gd3+-substituted Co–Mg ferrite nanoparticles. RSC Advances, 2020. 10(19): p. 11244-11256.
[13]. Amiri, M., M. Salavati-Niasari, and A. Akbari, Magnetic nanocarriers: Evolution of spinel ferrites for medical applications. Advances in Colloid and Interface Science, 2019. 265: p. 29-44.
[14]. Chen, C.-W., Magnetism and metallurgy of soft magnetic materials. 2013: Courier Corporation.
[15]. Ghatak, S., et al., Dielectric relaxation and magnetic field dependent alternating current conductivity of nanocrystalline cadmium–zinc ferrite below room temperature. Physica B: Condensed Matter, 2011. 406(17): p. 3261-3266.

International Journal of Scientific Research in Science and Technology
Volume 11 | Issue 13| Print ISSN: 2395-6011 | Online ISSN: 2395-602X (www.ijsrst.com)

To Study Photovoltaic Application of ZnS Thin Films Deposited By Spray Pyrolysis Technique

Mrs. Shaikh Nilofar Mansur
Department of Physics, M. S. P. Mandal's Yashwantrao Chavan College, Ambajogai, Dist. Beed, Maharashtra, India

ABSTRACT

Thin films of ZnS were prepared by spray pyrolysis. The effect of substrate temperature on structural, Optical and electrical properties of ZnS thin film were studied. The X-ray diffraction shows at a substrate temperature of 400°C, ZnS thin films are appears almost in well- crystallized cubic phase obtained. The optical band gap for ZnS thin films at temperature 300° C -450°C were calculated to be 3.0-3.5 eV. The electrical resistivity is of the order of 1.63×10 2-cm at substrate temperature 400°C. Therefore spray deposited ZnS thin films may be applicable for Photovoltaic solar Cell, Electronic Semiconductor devices, LED'S, Anti reflection Coating and Storage battery.

I. INTRODUCTION

A thin film is a layer of material ranging from fractions of a nanometer (monolayer) to several micrometers in thickness. The controlled synthesis of materials as thin films (a process referred to as deposition) is a fundamental step in many applications. A familiar example is the household mirror, which typically has a thin metal coating on the back of a sheet of glass to form a reflective interface. The process of silvering was once commonly used to produce mirrors, while more recently the metal layer is deposited using techniques such as sputtering. Advances in thin film deposition techniques during the 20th century have enabled a wide range of technological breakthroughs in areas such as magnetic recording media, electronic semiconductor devices, LEDs, optical coatings (such as antireflective coatings), hard coatings on cutting tools, and for both energy generation (e.g. thin film solar cells) and storage (thin-film batteries). It is also being applied to pharmaceuticals, via thin-film drug delivery.

The field of material science and engineering community's ability to conceive the novel materials with extraordinary combination of chemical, physical and mechanical, properties has changed the modern society. There is increasing technological progress. Modern technology requires thin films for different applications. Thin film technology is the basic of astounding development in solid state electronics. The usefulness of the optical properties of metal films, and scientific curiosity about the behavior of two-dimensional solids has been responsible for the immense interest in the study science and technology of the thin films.

When we consider a very thin film of some substance, we have a situation in which the two surfaces are so close to each other that they can have a decisive influence on the internal physical properties and processes of the substance, which differ, therefore, in a profound way from those of a bulk material. The decrease in

distance between the surfaces and their mutual interaction can result in the rise of completely new phenomena. Here the one dimension of the material is reduced to an order of several atomic layers which creates an intermediate system between macro systems and molecular systems, thus it provides us a method of investigation of the microphysical nature of various processes. Thin films are especially appropriate for applications in microelectronics and integrated optics. However the physical properties of the films like electrical resistivity do not substantially differ from the properties of the bulk material. For a thin film the limit of thickness is considered between tenths of nanometer and several micrometers.

II. SPRAY PYROLYSIS TECHNIQUES

Chemical spray pyrolysis (CSP) is used for depositing a wide variety of thin films, which are used in devices like solar cells, sensors, solid oxide fuel cells etc. It has evolved into an important thin film deposition technique and is classified under chemical methods of deposition. This method offers a number of advantages over other deposition processes, the main ones being scalability of the process, cost-effectiveness with regard to equipment costs and energy needs easiness of doping, operation at moderate temperatures (100-500°C) which opens the possibility of wide variety of substrates, control of thickness, variation of film composition along the thickness and possibility of multilayer deposition.

Many studies were done on CSP process since the pioneering work by Chamberlain and Skarman in 1966 on CdS films for solar cells [1]. Several reviews on this technique have also been published. Mooney and Radding reviewed CSP technique in which properties of specific films (particularly CdS)in relation to deposition parameters and their device applications were discussed detail[2].

Tomar and Garcia discussed the preparation, properties and applications of spray-coated thin films [3]. Albin and Risbud presented a review of equipment, processing parameters and opto-electronic materials deposited using this technique [4].

R. Krishnakumar et al. did an exclusive review of sprayed thin films for solar cells in which a variety of solar cell materials and their preparative parameters were detailed [5]. Different atomization technique sand properties of metal oxide, chalcogenide and superconducting films prepared using CSP were discussed by Patil [6]. Recently, Peredn is and Gaukler gave anextensive review on the effect of spray parameters on films as well as models forth in film deposition by CSP [7].

a) Spray nozzle:

It is made up of glass and consist of a solution tube surrounded by the glass bulb. With the application of pressure to the carrier gas, the vacuum is created at the tip of the nozzle, and the solution is automatically sucked in the solution tube and the spray start.

b) Rotor for spray nozzle:

Stepper motor- based microprocessor controller is used to control. The linear simple harmonic motion of the spray nozzle over the required length of the hot plate. Hence, the to-n- from motion and speed of the nozzle is monitored in controlled manner.

c) Hot plate:

The Iron disc (on to which 2000W heating coil is fixed) served as a hot plate. Maximum temperature of 600 ± 5°C can be achieved with this arrangement. The Chrome - Alumel thermocouple is used to measure the temperature of the substrate, and is fixed at the centre of front side of the iron plate. The temperature of the hot plate is monitored with the help of temperature controller.

d) Gas pressure control flow meter:

The gas regulator value is used to control the pressure the carrier gas. Flowing through the gas tube of the spray nozzle.

III.SPRAY PYROLYSIS SYSTEM

Methodology :

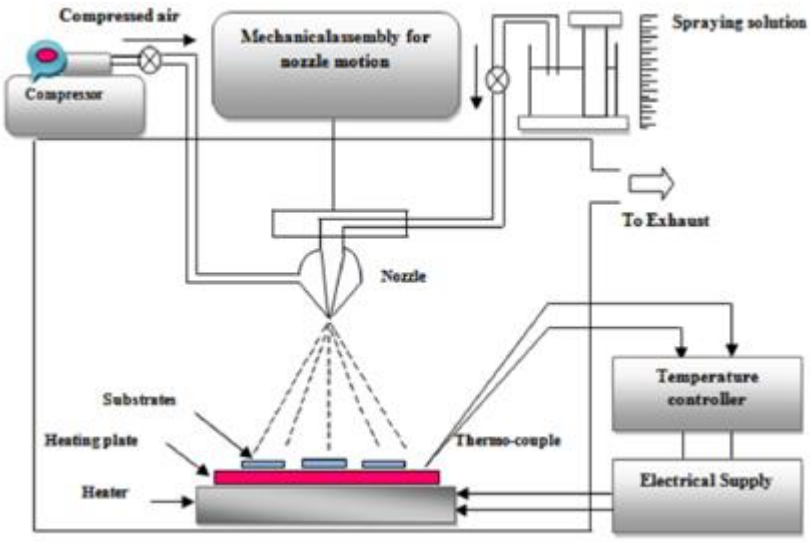

Schematic diagram of Spray Pyrolysis technique.

IV. EXPERIMENTAL DETAILS

➢ Introduction:

The growth of the ZnS thin films prepared by chemical spray pyrolysis. The thin film of ZnS is chemically deposited on simple glass substrate. The deposition is carried out by varying substrate temperature, at optimized preparative parameters to get uniform films.

➢ Deposition of thin film using spray pyrolysis:

➢Substrate Cleaning:

Before any substrate can be used it must be adequately clean. The cleaning technique depends on nature of the substrate and the nature of contaminants. Cleaning involves breaking or adsorption bonds between the substrate.

The following processes has been adopted for the cleaning the substrate,

The substrate are washed with detergent solution 'Labolene' and then with double distilled water.

These substrates are boiled in 2M Chromic acid for about five minutes (250°C).

The substrates are cleaned with tap water.
The substrates are again clean with double distilled water and cleaned ultrasonically.

- **Preparation of a film formation:**

ZnS thin films prepared on glass substrate (7.5×2.5) cm²using spray pyrolysis technique. Two different sets of solutions are used as precursors for ZnS thin films: a) ZnCl2 (M) and b) CS $(NH2)_2$ (M) in double distilled water. The solution are mixed together and used for spraying at a different spray rate onto a silica substrate. The temperatures in the range of 300°C -450°C in interval of 50°C. The uniform thin films are obtained at these temperatures. Compressed air pressure is used as carrier gas to spraying a solution.

- **Control and data storage**

The set up fabricated as described above was controlled by a microprocessor which communicated with the computer through a serial port. The spray parameters could be stored in the PC. Parameters of each spray were fed into the unit Interfacing between the system and PC was done using Visual C++ programming and the microprocessor was programmed separately.

- **Thickness Measurement:**

In present investigation ZnS thin films were deposited by using chemical spray "pyrolysis techniques. The thickness measurement is done by weighing difference method. Before deposition take accurate weight of substrate by using "standard microbalance weight measurement" and mark it as I, II, III. The initial solution is prepared from Zinc chloride at 0.1M concentration and 0.1M Thiourea. Take a weight of Zinc chloride and thiourea of 10ml of each of 0.1M concentration by using following formula,

$$W = \frac{M \, x \, N \, x \, Q}{1000}. \qquad \ldots(4.1)$$

Where, M = Molecular weight, N is Molarity and Q is Quantity.
By using above formula we prepare 10ml Zinc chloride solution and 10ml thiourea solution. Add this two solutions each other and we get final 20ml solution for spraying.
Above marked substrate is kept on a heater and adjust different temperatures ranges 300^{0}C - 500^{0}C Using spray machine 20ml solution can be sprayed on glass substrates and give a suitable air pressure. After completion of spraying note spray rate and cooling substrate at room temperature for good crystallized films and take out substrate from machine and take a weight of deposited films. Thickness of deposited film can be calculated by Gravimetric method. Thickness of film is can be measure by formula

$$t = \frac{\Delta m}{l \, X \, b \, X \, p}. \qquad \ldots(4.2)$$

Where Δm = Weight difference, l = length of substrate, b = breadth of substrate, rho = density.
Thickness of the samples was measured using Gravimetric method. Table 4.1.1 gives the temperature and thickess of substrate as the calculated thickness of thin film at temperatures for 300^{0}C is 1.199 μm, for 350^{0}C is 1.102 μm, 400^0 C is 0.795 μm, 450^{0}C is 0.443 μm. In the present work, it is concluded if we increase substrate temperature from 450^{0}C then thickness of deposited film will decreases as shown in following graph 4.1.

Sr. No.	Temperature	Thickness of Substrate (μm)
1.	300^{0}C	1.199
2.	350^{0}C	1.102
3.	400^{0}C	0.795
4.	450^{0}C	0.443

Thickness of Measurement

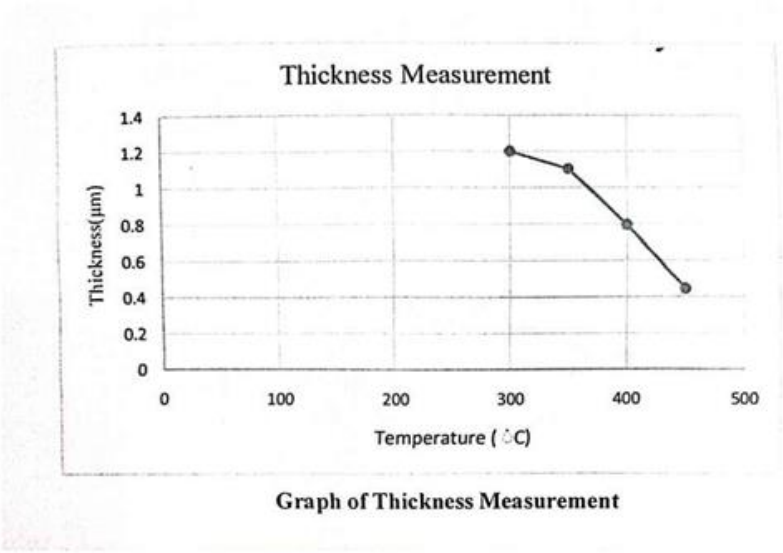

Graph of Thickness Measurement

➢ **Electrical Resistivity:**

The DC electrical resistivity of the ZnS films was measured as a function of temperature in the range 300°C-450°C using two point probe method. The variation of log p versus inverse of absolute temperature (1000/T) for deposited ZnS thin films are shown in figure (4.4) electrical resistivity (p) of the given ZnS film at substrate temperatures, 300°C-450°C is 3.45 × 107 2-cm, 4.03 x 10^6 Ω cm, 1.63×10^6 Ω cm, 1.08 x 10^6 Ω cm, respectively. It is observed that the resistivity of ZnS films was decreased with increase in temperature, indicating a semiconducting electrical behavior. It is shows that all the films are semiconducting. It is found that resistivity decreases continuously with increasing substrate temperatures as shown in following fig 4.4(a, b, c, d)

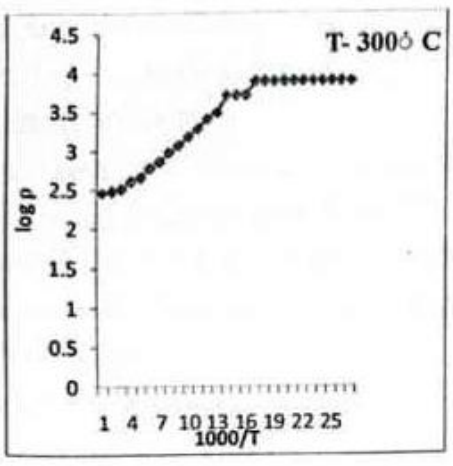

Fig (a)

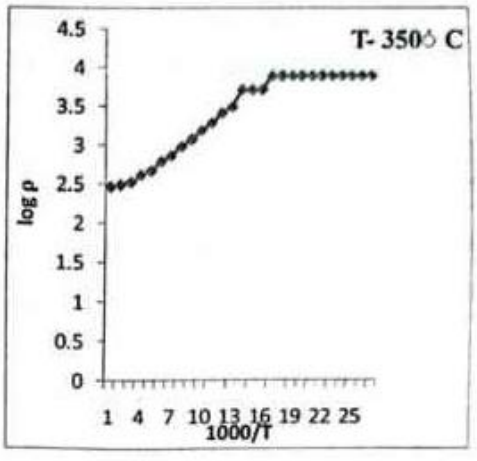

Fig (b)

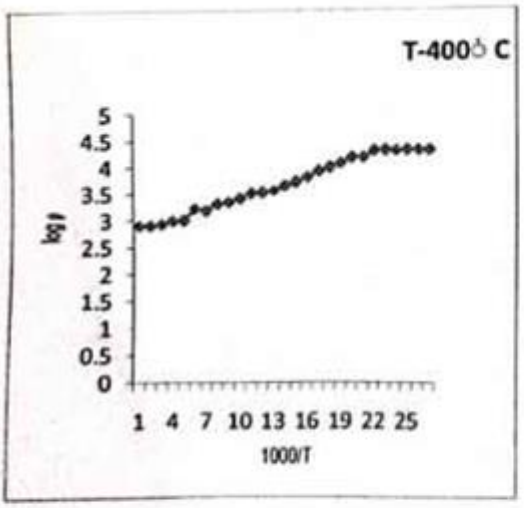

Fig (c)

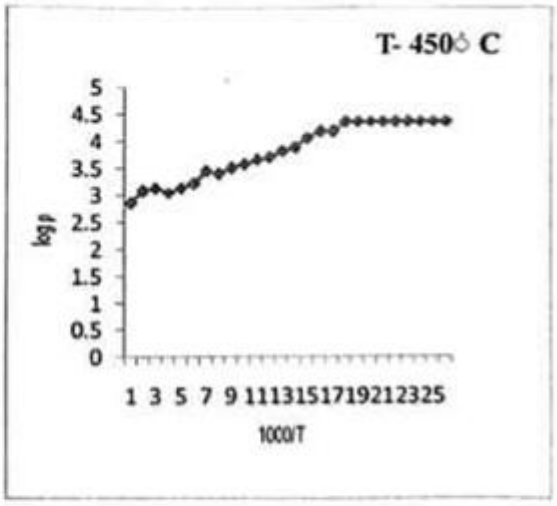

Fig (d)

(a, b, c, d): Variations of logρ vs inverse of absolute temperature (1000/T) for ZnS thin films

V. REFERENCES

[1]. B. Elidrissi, M. Addou, M. Regragui, A. Bougrine, A.Kachouale, G. C.Bernede, Materials Chemistry and Physics 68 (2001) 175-179.

[2]. H. H. Afifi, S. A. Mahmoud, A. Ashour. Thin Solid Films 263 (1995) 248-251.

[3]. M. C. Lopez, J. P. Espinos, F. Martin, D. Leinen, J. R. Ramos-Barrado. Journal of Crystal Growth 285 (2005) 66-75.

[4]. M. C. Lopez, J. P. Espinos, F. Martin, D. Leinen, J. R. Ramos-Barrado. S. P.Centeno. Applied Surface Science 255 (2008) 2118-2124.

[5]. Evren Turan, Muhsin Zor, A. Senol. Aybek, Metin Kul. Physika B 395 (2007) 57-64.

[6]. Yeshwantrao D. Tembhurkar. Internation Journal of Basic and Applied Research Special Issue (2012) (27-29)

[7]. P. O. Offor, B. A. Okorie, B. A. Ezekoie, V. A. Ezekoie. Journal of Ovonic Research. Vol. 11, No. 2, March-April 2015 P. 73.77.

[8]. M. S. Shinde, P. B. Ahirrao, R. S. Patil. Achieves of Applied Science Research, 2013, 3(2):311-317.

[9]. Avish K. Patil, Sachin H Dhawankar, Swangatika Paul, Bhagwat. M Surayvanshi, Manish P. Tripude. Intemational J. of Emerging Tech. in Computational and Applied Sci. (IJETCAS) (2014) 204-206.

International Journal of Scientific Research in Science and Technology
Volume 11 | Issue 13| Print ISSN: 2395-6011 | Online ISSN: 2395-602X (www.ijsrst.com)

Estimating Soil Moisture Content of Bare Soil Using Oven Drying Method

Monika Sudhakar Khole*[1], Dr. Sanjay K. Tupe[2], Dr. Shafiyoddin Sayyad[3]

[1]Ph.D. Research Scholar, Department of Physics, Dr. Babasaheb Ambedkar Marathwada University, Chh. Sambhajinagar, Maharashtra, India

[2]Department of Physics, Kalikadevi Arts, Commerce & Science College, Shirur Kasar, Maharashtra, India

[3]Department of Physics, Milliya Arts, Science and Management Science College, Beed, Maharashtra, India

ABSTRACT

The moisture content of soil is a pivotal factor influencing soil behavior. To analyze the variability of soil water content across different locations, soil samples were collected from seven points within a 3642 m2 area located on Rakshashbhuvan Tamba. The moisture content of these samples was measured using an oven heating method at 140°C, with intervals of 4.30 hours. The study aimed to assess the accuracy and drying time efficiency of the convection oven in determining soil moisture content. The convection oven proved to be effective for accurately measuring moisture content. The investigation also explored the use of a microwave oven for soil drying, highlighting its timeliness, efficiency, precision, and safety. The microwave oven emerged as the most convenient tool for soil drying, offering a significant reduction in the complexity, time, and cost associated with traditional lab tests. This article focuses on the effect of temperature on soil moisture content using microwave radiation.

Keywords: Soil sample, moisture content, drying oven method.

I. INTRODUCTION

Soil moisture is defined as the temporary storage of water content within a thin layer of the earth's upper surface. The moisture content is one of the most commonly determined properties in characterizing the behavior of soil. The accurate determination of the moisture content is important since the moisture content strongly influences the mechanical behavior of soil. The preferred standard test method for the laboratory determination of the moisture content is the oven drying method. The moisture content is determined as the reduction in the mass of the test samples after oven drying, usually at $140^0 \pm 5^0$ C, expressed as a percentage of its oven dried mass. The equilibrium oven dried mass is usually recorded after between 4.30hours in the interval of 1.30hours in three times oven drying. The method assumes that the reduction in the sample mass is entirely due to the evaporation of the pore water; complete evaporation occurs for drying temperatures exceeding140^0C.

Soil Moisture content calculations equate potential reductions in the mass of the solid particles due to charring with evaporation of pore water, which results in the true value of the moisture content being overestimated.

The true value of the moisture content of soil is calculated based on the sample dry mass corresponding to this oven temperature.

The primary goal of this study is to create a method that allows for the quick and accurate measurement of soil moisture levels. This objective is accomplished by assessing the accuracy and testing the time required to dry soils using both a standard microwave oven and a convection oven.

II. MATERIALS AND METHODS

Seven soil samples were randomly selected from different parts of the farm of Rakshashbhuvan (Tamba) with vertical latitude-19.024023^0 and longitude- 75.429903^0, Tal-Shirur Kasar in Jan 2024. All of the samples were taken roughly 5cm to 7cm depth from the ground surface. Compactly tied plastic bags were utilized after which the samples were placed into double plastic bag to avoid moisture loss, and then used for further analysis. After that clean glass bowl is taken and the sample of wet soil is crumbled and placed in the bowl container. The weighed of this soil sample is taken in 100 grams is denoted by (M). Then sample container is placed in the oven. The standard microwave oven used was a IFB Convection Microwave Oven 20SC2. The sample is then dried in a thermostatically controlled drying oven which is maintained at a temperature of 140±5^0 C. A initial period of heating was 1.30 hours after 1.30 hours heating removed the soil samples from oven and following the specified duration, the soil samples were weighed.

In accordance with Australian Standards, the samples needed to be allowed to cool after each heating cycle. A one-minute cooling period was scheduled for each sample after every heating cycle to prevent any inconsistencies in results due to varying cooling rates.Then measure the weight of soil sample and minus bowl weight from that weight then again put these sample for heating another 1.30 hours then again measure the weight similarly take one more reading in the interval of 1.30hours for same temperature. Then calculate the average weight of these three times heating sample weights which is denoted by (M^1).

Analysis was done by using formula:

$$S.M = \frac{W}{M} * 100\%$$

Where,

W= M-M^1 = Weight of soil moisture

M= Weight of soil before drying

M^1= Weight of soil after drying

Using this formula we calculate soil moisture content in percent.

III.RESULTS AND DISCUSSION

Sr No	Latitude and Longitude	Wt. of Soil Before Heating (gm) (M)	Wt. Of soil After 1.30 hrs. heating at 140^0C (gm)	Wt. of soil After 3.00 hrs. heating at 140^0C (gm)	Wt. of soil After 4.30 hrs. heating at 140^0 C (gm)	Average wt of soil after drying (M^1) (gm)	W= M-M^1 (gm)	$S.M = \frac{W}{M}*100\%$
1	Lat-19.024422 Long-75.428226	100	89.4	87.52	87.25	88.06	11.94	11.94
2	Lat- 19.023972 Long-75.428714	100	90.02	88.14	87.49	88.55	11.45	11.45
3	Lat-19.024118 Long-75.429288	100	90.63	89.73	89.11	89.82	10.18	10.18
4	Lat-19.024024 Long-75.428818	100	91.27	88.19	87.98	89.15	10.85	10.85
5	Lat-19.02412 Long-75.429091	100	89.45	87.99	87.24	88.23	11.77	11.77
6	Lat-19.024054 Long-7.429124	100	90.34	86.26	86.03	87.54	12.46	12.46
7	Lat-19.02398 Long-75.428767	100	92.46	89.45	89.09	90.33	9.67	9.67
								Average S.M=11.19%

Table 1: Oven drying soil sample data and soil moisture

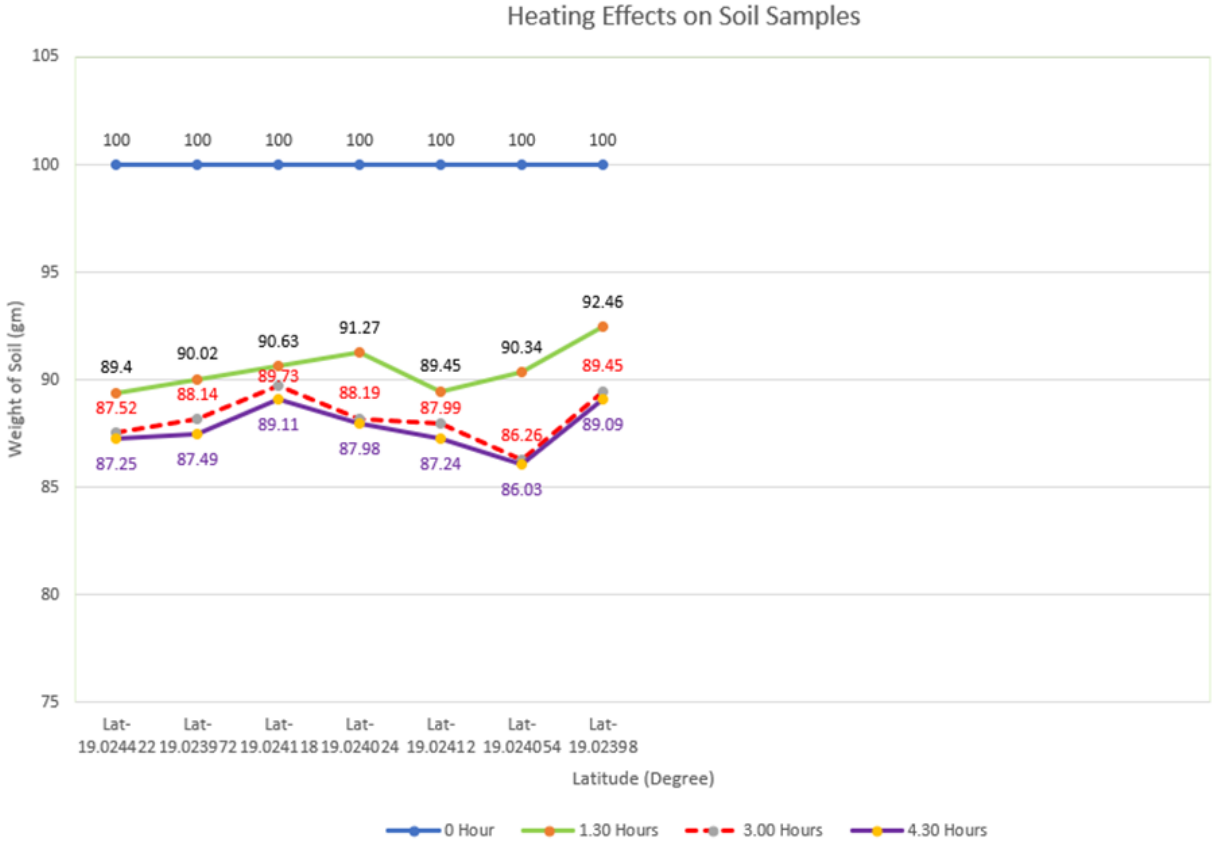

Figure 1. Comparison between heating effect on soil weighton different time

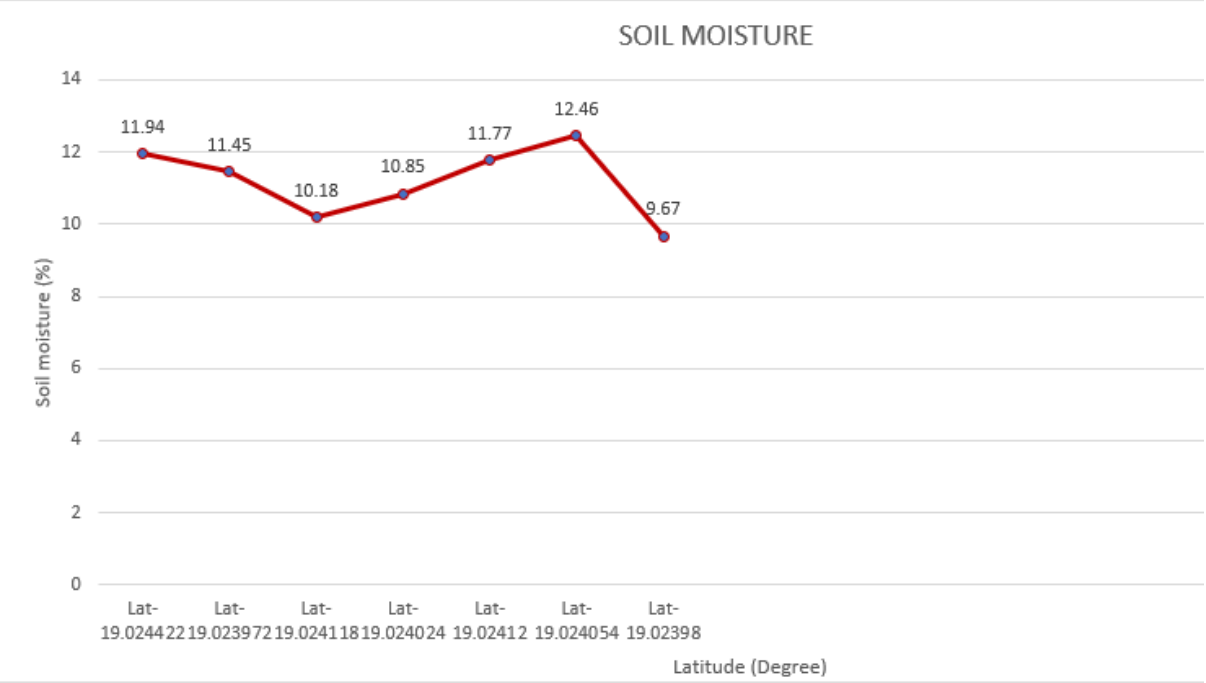

Figure 2. Moisture content of soilvs. latitude

Oven drying test data is presented in Table 1 for seven test soil samples of the same bare soil with different latitude position is determined using the procedure described above. The data is presented as the reduction in the sample dry mass with increasing oven drying heating time. The use of a standard microwave oven has been identified as the most practical method, providing dependable results in determining soil moisture content quickly. Laboratories have employed microwave ovens for years to achieve fast, affordable, and cost-effective measurements of soil moisture. The microwave delivers a continuous energy supply, which can lead to the over-drying of soil samples and consequently, inaccurately high moisture content readings.

Figure 1 displays a comparison of soil sample weights after being heated at 140°C for varying duration. The initial weights of the soil samples, set at 100 grams, are represented by a blue line on the graph. A significant decrease in the sample weights is observed after 1.30 hours of heating, illustrated by a green line. Further heating for 3 hours and 4.30 hours shows almost identical changes in the weights of the soil samples, indicated by a red dotted line and the blue line, respectively. It indicates a trend of decreasing sample dry mass with increasing oven drying time with constant temperature.

Figure 2 displays a chart that illustrates the variations in soil moisture percentage across various latitudes in chosen areas. The moisture content of the soil, which fluctuates with latitude, is accurately determined using the dry mass of the samples measured at the drying temperature.

IV. CONCLUSION

This study has determined that microwave ovens are completely suitable for measuring soil moisture. It confirmed that domestic microwave ovens serve as an effective means for rapidly determining the moisture content of soil, with tests completed in a brief period and the resulting data is accurate.The decrease in soil weight was directly proportional to the heating time in the oven at a temperature of 140°C. The moisture content of the soil tested, based on the recommended temperature of 140°C, varied with the duration of heating.

It was noted that to achieve equilibrium in the mass of the soil samples, longer drying periods were necessary. A moisture content parameter was introduced to enable the straightforward comparison of moisture content values, which were determined over varying duration but at a consistent oven drying temperature. A drying oven is capable of simultaneously estimating the moisture content of multiple samples. It has the capacity to accommodate several samples at once, including those of larger mass.

V. REFERENCES

[1]. Rasti, Arezou, Maria Pineda, and Mehrdad Razavi. "Assessment of soil moisture content measurement methods: Conventional laboratory oven versus halogen moisture analyzer." Journal of Soil and Water Science 4.1 (2020): 151-160.

[2]. Kurtuluş, C., T. Yeken, and D. Durdağ. "Estimating the soil water content using electrical conductivity, oven method and speedy moisture tester." Eurasian soil science 52 (2019): 1577-1582.

[3]. Cormick, A. (2015). “Comparing different heating methods for determination of moisture content in soils (dissertation).” University of Southern Queensland.

[4]. Jalilian, Jalal, Sina Siavash Moghaddam, and Yadollah Tagizadeh. "Accelerating soil moisture determination with microwave oven." J. of Chinese Soil and Water Conserv 48.2 (2017): 101-103.

[5]. O'Kelly B.C. 2004. Accurate determination of moisture content of organic soils using the oven drying method. Drying Technology, Vol.22, No.7, 1767-1776. http://dx.doi.org/10.1081/DRT-200025642

[6]. https://www.renkeer.com/how-to-use-soil-moisture-sensor/#:~:text=The%20calculation%20formula%20is%20soil,of%20soil%after%20drying%20M%27

[7]. Berney, I.V., Ernest, S., Kyzar, J.D., and Oyelami, L.O. (2011). Device comparison for determining field soil moisture content (No. ERDC/GSL-TR-11-42). Engineer research and development center Vicksburg ms geotechnical and structures lab.

International Journal of Scientific Research in Science and Technology
Volume 11 | Issue 13| Print ISSN: 2395-6011 | Online ISSN: 2395-602X (www.ijsrst.com)

A Review of Modelling Approaches for Drought Index Monitoring and Assessment Using Multispectral Imaging

NehaAndure[1*],SidheshwarRaut[2],AnkushKadam[2*],SandipanSawan[2],ShafiyoddinSayyad[3]

[*1]Department ofPhysics,JawaharCollege,Andur,MS,India

[2]Department ofPhysics, Shri.Chatrapati ShivajiCollege,Omerga, MS,India

[3]Department ofPhysics,Milliya College,Beed, MS,nehaandureo1@gmail.com

ABSTRACT

This paper explores the application of remote sensing, utilizing drought indexes, for effective monitoring and assessment of drought variables. The increasing availability of multispectral images, driven by rapid advancements in remote sensing technology, broadens the scope of this field. Droughts, as natural disasters, exert profound impacts on environmental factors such as agriculture, vegetation, human populations, wildlife, and local economies. Historically, an estimated 55 million people globally face the annual repercussions of droughts, leading to heightened concerns about food security due to escalating crop failures. Farmers grapple with compounded challenges, utilizing satellite multispectral and thermal band data to extract drought-related variables, including precipitation. Optical remote sensing technology emerges as a crucial tool in addressing these challenges, providing valuable insights into diverse land characteristics, and contributing to advancements in agricultural management and vegetation analysis. This paper comprehensively reviews and discusses various types of drought indexes based on multispectral data, utilizing different freely available satellite multispectral datasets such as Sentinel-2 data, Landsat, and MODIS.

Keywords: Drought, Multispectral images, Drought Indexes, optical remote sensing

I. INTRODUCTION

The occurrence of drought, broadly defined as a state of insufficient moisture in the land surface, is linked to agricultural losses, water resource shortages, and other economic impacts. While drought may be perceived simply as a lack of water, it is a complex phenomenon and among the least comprehended natural hazards due to various causative factors operating on different temporal and spatial scales [1] In the preceding year, around 30% of India's land area grappled with varying degrees of drought, leading to intensified crop failures, and raising concerns about food security. Data from the Drought Early Warning System (DEWS) The state of Maharashtra witnessed only 40% of the normal rainfall, sparking concerns about an impending drought. Furthermore, 11 districts received 32% to 44% less rainfall, compounding the challenges faced by farmers. Remote sensing techniques enable the rapid acquisition and dissemination of information across expansive. Regions using sensorsoperating in various spectral bands, deployed on aircraftor satellites. The Multispectral datasets orbiting the entire Earth surface survey in just a few days and revisit specific areas regularly, while aircraft provide more

detailed analyses for smaller, targeted regions.. These sensors cover a broad spectrum, ranging from visible to microwaves. [2] The monitoring and assessment of drought through remote sensing are contingent on the causative factors and the impacts of drought. Droughts can be categorized based on factors such as agricultural, hydrological, meteorological, and socioeconomic conditions. Recent research has identified additional types of droughts, including ecological drought, environmental drought, and flash drought. Given the projected increase in the severity and frequency of droughts due to climate change, understanding the interconnected impacts and influences across various sectors is of paramount importance. [3] Remote sensing satellite multispectral datasets is an effective way to monitor drought. Consider its large spatial coverage and relatively high temporal and spatial resolution. Our main area of interest in this research is drought in agriculture.

Agricultural drought indices that are highly related to vegetation health, Satellite based method have been developed to describe vegetation condition index, temperature condition index, Temperature Vegetation Dryness Index.[4] Drought indices serve as quantitative measures to assess and characterize drought levels by consolidating data from one or multiple variables, such as precipitation and evapotranspiration, into a single numerical value. These indices capture diverse events and conditions, providing insights into anomalies in climate dryness. [5]

II. MULTISPECTRAL IMAGING PLATFORMS AND DATA SOURCES

Multispectral remote sensing involves capturing images across various wavelength bands, including visible, near infrared, and short-wave infrared. Materials on the Earth's surface reflect and absorb light differently across these bands, resulting in unique spectral reflectance signatures. By analysing these signatures, it becomes possible to distinguish between different surface materials and features in remotely sensed images. Multispectral imagery is particularly valuable for land surface classification, as it allows for the discrimination of landscape patterns and features. In a mixed vegetated wetland, the spectral reflectance of the various plant types is comparable and is typically paired with the spectral reflectance of the water, underlying soils, and upper atmosphere. Effects resulting in complications during dataset [6]

A. MODIS

MODIS is a multispectral imaging instrument onboard both Terra and Aqua satellites. It consists of 36 spectral bands covering wavelengths from visible to thermal infrared regions (0.4 to 14.4 micrometres). These bands include Visible and Near-Infrared (VNIR) bands: Used for monitoring vegetation health, land cover, and ocean colour Shortwave Infrared (SWIR) bands: Useful for detecting vegetation moisture content, soil properties, and snow/ice cover [7]

B. LANDSAT

The first space-borne instrument to assess vegetation's seasonality at the regional level was Landsat. The Landsat series of satellite-based sensors, which has an archive of data that spans the early 1970s to the present and a nominal temporal resolution of 16 days and a spatial resolution of 30 meters,, has been appropriate for manylandscape characterization applications such as land cover classification, change detection and vegetation stress monitoring.[7]

C. SENTINEL-2

The ESA's Sentinel-2 mission supplies high-resolution Satellite data for environmental monitoring, agriculture, and disaster management. For this research we utilized this data set With 13 spectral bands capturing visible to

shortwave infrared, it offers detailed insights Sentinel-2 is a high spatial(10 to 60 meters) resolution multispectral satellite with a 5-day Temporal resolutions[7]

III.METHODOLOGY FOR DROUGHT INDICES ASSESSMENT

This encompasses the fundamental definition of drought, which can vary across different contexts. For instance, agricultural drought primarily concerns itself with the lack of soil moisture content, while hydrological drought examines the delayed effects of insufficient precipitation on various water sources. Alternatively, it can be described as the prolonged absence of precipitation over a specific region for a specific duration. Besides emphasizing the elements of 'persistence' and 'significant precipitation deficit,' definitions have evolved to incorporate impacts on the environment and society. From this perspective, the effects of drought depend on both the severity of water scarcity and the susceptibility of local conditions. [8]
There are four distinct types of droughts: hydrological, meteorological, agricultural, and socioeconomic.

A. Meteorological drought

Meteorological drought is often defined solely by the extent of dryness and the duration of dry spells. It refers to the deficit in precipitation compared to average conditions over a specific location during a certain period. [2] The Standardized Precipitation Index (SPI) is a popular meteorological drought index that relies exclusively on precipitation data. Similar to the percentage of normal precipitation, SPI compares precipitation with its multiyear average. The mean is then normalized to zero, where values above zero indicate wet periods and values below zero indicate dry periods. Another widely used index is the Palmer Drought Severity Index (PDSI), which incorporates precipitation, temperature, and local soil moisture data. PDSI calculates four terms in the water balance equation: evapotranspiration, runoff, soil recharge, and moisture. [8]

B. Agricultural drought

Agricultural drought assessment can be more effectively and accurately conducted through remote sensing. [2] Our focus is directed towards agricultural drought due to its significant importance in many countries, impacting economic stability, food security, and social welfare. Agricultural drought typically arises from two main factors: (I) a short-term shortage of precipitation leading to reduced soil moisture levels, and/or (ii) increasing temperatures. Agricultural drought risk management plans encompass drought preparedness and response actions. Monitoring efforts involve ongoing assessment and evaluation of surface wetness conditions, precipitation amounts and patterns, and temperatures in agricultural areas during the growing season. This monitoring is done in near real-time to develop appropriate agricultural drought evaluation indicators. Generally, optical remote sensing-based agricultural drought indices are utilized. [9]

1 Vegetation drought index: Normalized Difference Vegetation Index (NDVI) = NDVI= (NIR-RED) / (NIR+RED) Provides a measure of vegetation health or greenness conditions normalized this ratio from -1 to +1, Plants with the normalized difference vegetation index (NDVI) have a distinct reflectance characteristic; they absorb more visible light and reflect more near-infrared (NIR) light. High chlorophyll content in healthy plants enables them to reflect more light in the blue and absorb more light in the red portions of the spectrum.

2 Enhanced vegetation Index (EVI): It exhibits heightened sensitivity in regions with substantial biomass or thick vegetation. EVI introduces air resistance coefficients (C1 and C2), and a "L" value for

canopy background adjustment and incorporates values from the blue band (B2). These enhancements contribute to a refined ratio of NIR and Red values, mitigating the influence of background and atmospheric interference. The equation for EVI is given ByEVI = G × ((NIR − Red) / NIR + C1 × Red − C2 × Blue + L) n the context of EVI, the specific coefficients are as follows: G = 2.5, C1 = 6, C2 = 7.5, and L = 1 [10]. Additionally, the constant L assumes a predefined value [11]

3 Ratio Vegetation Index (RVI): the NIR band's reflectance divided by the red band's reflectance. Lower values indicate unhealthy vegetation, whereas RVI = Rred/Rnir indicates good vegetation indicate soil, water or ice

4 Vegetation Condition Index (VCI): the current vegetation status deviation relative to the long-term calculated minimum and maximum. The VCI index = 100 *(NDVI-NDVImin) / (NDVImax –NDVI min) [12]

5 Temperature Condition Index (TCI): the TCI is used to find the stress on vegetation caused by excessive wetness and temperature. The TCI ranges from 0 to 100, where 100 denotes ideal conditions and 0 represents incredibly unfavourable circumstances.[2]

$$TCI = 100 * (LSTmax - LST / LSTmax - LSTmin)$$

6 Vegetation Health Index (VHI) : the VHI describes vegetation health from the combination of TCI (temperature) and VCI (vegetation condition)

$$VHI = \alpha VCI + (1 - \alpha)TCI \quad [13]$$

C. Hydrological drought

The impacts of rainfall deficiencies on water resources, such as stream flow, reservoir and lake levels, and groundwater table drop, are the main emphasis of the term "hydrological drought. "It integrates multiple hydro-meteorological variables into a single drought indicator to capture the complex interactions leading to drought events. Commonly used site-based drought indices include the Palmer Drought Severity Index (PDSI), which employs precipitation and temperature data to monitor soil moisture changes within a two- layer water balance model. Additionally, Land Surface Temperature (LST) serves as a valuable indicator of the hydrological conditions in an environment. [13].

D. Socioeconomic drought

When drought conditions, whether meteorological, agricultural, or hydrological, affect the supply and demand of economic goods, it leads to socioeconomic drought. This occurs when commodities face shortages due to weather-related water scarcity. Despite its significance, limited research has been conducted on predicting socioeconomic drought [15]. Various data types, including water quality, wildfire occurrence, crop yield, and remotely sensed vegetation stress, are directly or indirectly linked to drought impacts. [16]

IV.RESULTS AND DISCUSSION

This research paper explores the use of remote sensing technology and drought indices for monitoring and assessing drought variables, particularly in agriculture. It emphasizes the impact of droughts on various environmental factors, including agriculture, vegetation, human populations, wildlife, and local economies. With around 55 million people globally affected by droughts, concerns about food security are heightened. Remote sensing is seen as a crucial tool in addressing these challenges by providing insights into diverse land characteristics and contributing to agricultural management and vegetation analysis. The paper reviews various

types of drought indices based on multispectral data, utilizing various satellite datasets. The research emphasizes the importance of remote sensing technology and drought indices in understanding drought dynamics and aiding in effective drought monitoring and mitigation strategies.

V. CONCLUSION

The utilization of multispectral imaging for drought index monitoring and assessment represents a significant advancement in the field of remote sensing and environmental science. Through a comprehensive review of existing literature, case studies, and modelling approaches, this paper has provided insights into the effectiveness, challenges, and future directions of utilizing multispectral data for drought-related applications Multispectral imaging has been successfully applied to various domains, including agricultural drought monitoring and hydrological drought assessment, demonstrating its versatility and applicability across different spatial and temporal scales.

Continued research and innovation are needed to address existing challenges and advance the field of multispectral imaging for drought monitoring, ultimately contributing to more effective drought management and resilience-building efforts. The insights provided in this review paper can inform decision-makers, researchers, and practitioners involved in drought monitoring, water resource management, agriculture and disaster preparedness Enhanced understanding of modelling approaches and their limitations can guide the development of more robust and reliable drought monitoring systems and tools, facilitating timely decision-making.

VI. REFERENCES

[1]. Archana Mullapud Amol D. Vibhute2 · Shankar Mali1 · Chandrashekhar H. Patil. “A review of agricultural drought assessment with remote sensing data: methods, issues, challenges and opportunities” Applied Geomatics Volume 15, pp 1–13, 2023.

[2]. U Ma’rufah, R Hidayat, I Prasasti, “Analysis of relationship between meteorological and agricultural drought using standardized precipitation index and vegetation health index”, Conf. Series: Earth and Environmental Science 54, 2017

[3]. Wenzhe Jiao, Lixin Wang, Matthew F. McCabe, "Multi-sensor remote sensing for drought characterization: current status, opportunities and a roadmap for the future" Remote Sensing of Environment 256, 112313, 2021.

[4]. Ning Zhang, Yang Hong, Qiming Qin, and Lu Liu “VSDI: A visible and Shortwave infrared drought index for Monitoring soil and vegetation moisture based on optical remote sensing” international Journal of remote sensing vol.34 No.13, pp4585- 4609, 2013.

[5]. Amin Zargar, Rehan Sadiq, Bahman Naser, and Faisal I. Khan,’ A review of drought indices” Environ.Rev. 19, pp333–349, 2011.

[6]. Siyamthanda Gxokwe *, Timothy Dube and Dominic Mazvimavi “Multispectral Remote Sensing of Wetlands in Semi-Arid and Arid Areas: A Review on Applications, Challenges and Possible Future Research Directions” Remote Sens., 12, 4190, 2020.

[7]. LinglinZenga , Brian D. Wardlowb,∗ , DaxiangXiangc , Shun Hud , Deren Li " A review of vegetation phenological metrics extraction using time-series, multispectral satellite data" Remote Sensing of Environment vol.237, 111511 2020.

[8]. Amin Zargar, Rehan Sadiq, Bahman Naser, and Faisal I. Khan "A review of drought indices" Published at www.nrcresearchpress.com/er on 13 September 2011. Environ. Rev. Vol.19 pp333–349, 2011.

[9]. Khaled Hazaymeh1, and Quazi K. Hassan1,* "Remote sensing of agricultural drought monitoring: A state of art review" AIMS Environmental Science. Vol.3, Issue 4 pp604-630, 2016.

[10]. Wenzhe Jiao, Lixin Wang, Matthew F. McCabe, "Multi-sensor remote sensing for drought characterization: current status, opportunities and a roadmap for the future" Remote Sensing of Environment 256, 112313, 2021.

[11]. K. A. Luus. "Assessing productivity of vegetation in Amazon using remote sensing and modelling", Progress in Physical Geography, 2008

[12]. NirangaAlahacoon& Mahesh Edirisinghe. "A comprehensive assessment of remote sensing and traditional based drought monitoring indices at global and regional scale" Geometrics, Natural Hazards and Risk, vol.9, pp762-799, 2021.

[13]. WillibroadGabila Buma 1 and Sang-Il Lee 2,* "Multispectral Image-Based Estimation of Drought Patterns and Intensity around Lake Chad, Africa" Remote Sens. Remote Sens, vol.11 (21), pp25-34, 2019.

[14]. Marcel Urban 1, *, Christian Berger 1 , Tami E. Mudau 2, Kai Heckel 1, John Truckenbrodt 1, Victor Onyango Odipo 1 , Izak P. J. Smit 3,4 1 and Christiane Schmullius "Surface Moisture and Vegetation Cover Analysis for Drought Monitoring in the Southern Kruger National Park Using Sentinel-1, Sentinel-2, and Landsat-8" Remote Sens., vol.10(9), pp14-82, 2018.

[15]. T. Jeyaseelan, "Drought& floods assessment and monitoring using remote sensing and gis" pp. 291-313

[16]. GebrejewergsAredehey, AtinkutMezgebu&Atkilt Girma "Land-use land-cover classification analysis of Giba catchment using hyper temporal MODIS NDVI satellite images" Published online, pp810-82, 2016.

International Journal of Scientific Research in Science and Technology
Volume 11 | Issue 13| Print ISSN: 2395-6011 | Online ISSN: 2395-602X (www.ijsrst.com)

Effect of Bandgap on Photocatalytic Activity of GO Based Cr Doped Nio Nanocomposites

Ramprasad Sonpir, Dnyaneshwar Dake, Nita Raskar, Vijay Mane, Babasaheb Dole*
Advanced Materials Research Laboratory, Department of Physics, Dr. Babasaheb Ambedkar Marathwada University, Chhatrapati Sambhajinagar 431004, Maharashtra, India

ABSTRACT

In the current study, co-precipitation method was used to preparation of GO-based Pure NiO and 6% Cr-doped NiO nanocomposites. Field Emission Scanning Electron Microscopy (FESEM) and x-ray diffraction (XRD) techniques were used to investigate the impact of Cr doping on the structural characteristics of nanocomposite. The sample's crystalline and crystal structure were evident in the XRD spectrum. Nanoparticle morphology is observed using FESEM. EDAX spectroscopy was utilized for elemental analysis. Optical characteristics were confirmed by using UV-Vis spectrometer. The distinct features of GO based 6% Cr-doped NiO nanocomposite synthesized by co-precipitation has utilized in dye degradation.

Keywords: Photocatalytic activity, Methylene blue, Co-precipitation, Nanocomposite.

I. INTRODUCTION

In recent years, environmental deterioration particularly the presence of organic dyes in industrial or urban effluent has become a major issue for the entire world community. For their superior performance in textile, paper, metallurgy, carpet, leather and other industries, reactive dyes like azo dyes are widely utilised [1]. A sustainable and environmentally beneficial method for the oxidation of organic contaminants and the creation of clean energy sources is provided by photocatalysis [2]. A well-known transition metal oxide with notable photocatalytic qualities is nickel oxide (NiO). Although its slow recombination of photogenerated electron-hole pairs and limited absorption of visible light reduce its total photocatalytic effectiveness [3]. If Cr is doped with other transition metals, it creates a stable phase and improves electrical conductivity. Cr is appropriate for doping in NiO because it exhibits a variety of oxidation states and has an ionic radius that is almost identical to that of Ni [4]. 2D carbon material graphene oxide is a prime choice for improving the charge separation and transfer processes in photocatalytic reactions due to its good electrical conductivity and enormous surface area [5].

In this manuscript the effect of bandgap on photocatalytic activity of GO based pure and Cr doped NiO nanoparticles was outlined in detail. After the doping of Cr into NiO lattice the change was observed in structural and morphological properties which are beneficial for enhancement in photocatalytic activity. Due to the addition of GO and Cr the enhancement in photocatalytic activity upto 85.65% was observed under the sunlight irradiation within the 180 min.

II. METHODS AND MATERIAL

EXPERIMENTAL

All of the materials were analytically pure grade and were provided by Fisher Scientific Company, and without additional decontamination. Samples of GNO and 6% GCrNO nanocomposites were synthesized by the co-precipitation method. For the synthesis of Pure Nio nanoparticles, 1 M Nickel acetate (98%), Chromium acetate (99%) and HMTA (1M), dissolved separately in 25 ml distilled water. All materials were combined and after 20 minutes of continuous stirring, GO was added to the mixture. Drop by drop ammonia was added to keep the pH at 12. After that it heated for two hours at 80°C. The sample was subsequently cooled to room temperature. The item was filtered and washed repeatedly in distilled water and then dried at room temperature.

PHOTOCATALYTIC EXPERIMENT

The photocatalytic activity of the GNO and 6% GCrNO nanocomposites was investigate by calculating the percentage of dye decomposed under natural sunlight irradiation. The 0.05 g photocatalyst powder was placed in 100 mL of an aqueous dye solution of MB, where the concentration (C_0) of each species was 20 mg L^{-1}, for the period of the photocatalysis. The final MB solutions were continuously stirred for 20 min in a darkroom before exposing to natural sunlight for irradiation. After stirring for 20 minutes, 2 ml of hydrogen peroxide catalyst and azo dye solutions were added, they were exposed to natural sunlight from 11 am to 2 pm. About 3 mL of the solution was introverted at 20-min intervals of illumination and the UV-Vis spectra of the degraded solution was recorded. From the recorded absorption peak, the level of degradation of each species was compared.

MATERIAL CHARACTERIZATION

Samples of GO-based Pure and 6% Cr-doped NiO nanocomposite were characterized by using various techniques. The structural characterization was carried out using an X-ray diffraction approach using a Bruker AXS D-8 Advanced diffractometer (Germany). The surface morphology and elemental content were examined using a field emission scanning electron microscope (FE-SEM). A UV-Vis spectrometer with (Avantes UV-Vis spec) was used to illustrate the optical characteristics.

III.RESULTS AND DISCUSSION

STRUCTURAL PARAMETERS

The structural characteristics of GNO and 6% GCrNO nanocomposite were investigated using XRD analysis, and the findings are shown in **Figure 1.** These samples are well-crystallized, and the XRD diffraction peaks are given the miler indices (111), (200), (220), (311) and (222) with the aid of JCPDS card No. 03-065-5745, indicating the creation of nickel oxide particles with good purity [6]. The face-centered cubic geometry of the samples was confirmed by these results [4]. We added GO to the prepared sample but it was added at a low concentration and there was no diffraction peak visible in the XRD pattern. The results of the calculations for the GNO and 6% GCrNO nanocomposite crystalline size, lattice parameters, dislocation density, microstrain, and stacking fault [7] are shown in **Table 1.**

Table 1 Calculated crystallite size, dislocation density, microstrain, stacking faults, and lattice parameters of GNO and 6% GCrNO composite.

Samples	Crystalline size(nm)	Lattice Parameters (nm)	Dislocation density(lines/m²)	Microstrain (ε)	Stacking Fault (SF)
GNO	5.7714	4.8464	0.04045	0.00663	0.01033
6% GCrNO	7.2233	4.7758	0.02123	0.00497	0.00821

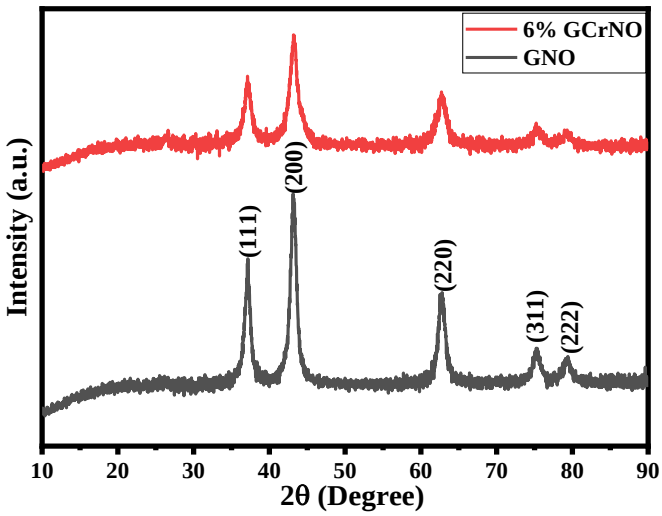

Figure 1. XRD patterns of a GNO and 6%GCrNO samples.

FIELD EMISSION SCANNING ELECTRON MICROSCOPY

FE-SEM analysis was performed for morphological research, and micrographs of functionalized GNO and 6% GCrNO nanocomposite are displayed in **Figure 2**. The FE-SEM images of the as-prepared nanocomposite show an agglomerated nanospherical structure. The particle size was successfully enhanced after Cr was doped into the NiO lattice and spherical structure was noted for GO-based Cr doped NiO samples.

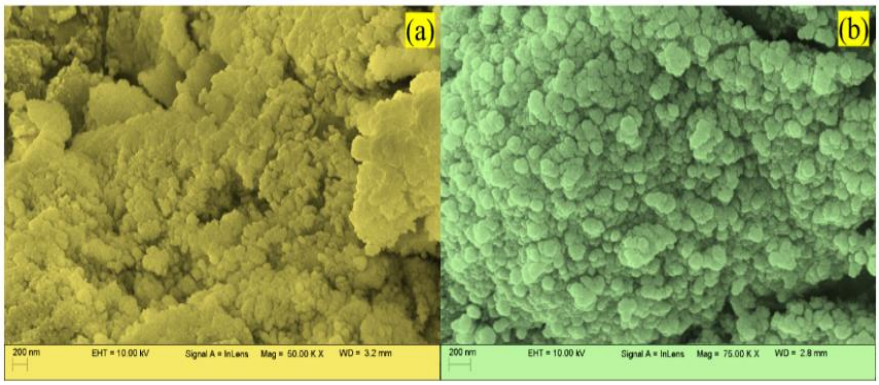

Figure 2. FESEM images of **a** GNO and **b** 6%GCrNO samples.

ELEMENTAL ANALYSIS

The EDAX approach, which confirms an exact percentage of an element in the sample and it was used to determine the chemical compositions of samples as-synthesised. The inclusion of GO in the NiO lattice confirmed the presence of carbon and oxygen in samples. The elemental atomic percentage of the corresponding nanocomposite samples was shown in **Figure 3.**

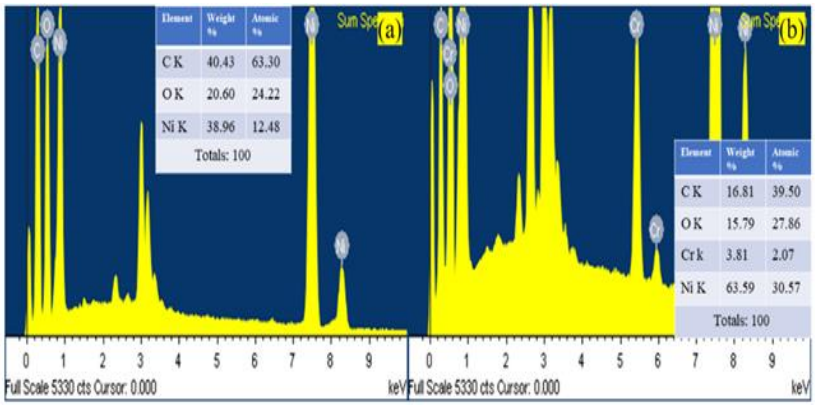

Figure 3. EDAX spectra of **a** GNO **b** GCrNO samples.

UV-VIS SPECTROSCOPY

As shown in **Figure 4** the UV-visible absorption spectra were captured between 210 and 750 nm. The absorption peaks, which are associated with GO-based pure NiO and Cr doped NiO nanocomposite respectively, were found at wavelengths of 260 and 298 nm. Tauc's equation was used to analyse the band gap [7].

$$(\alpha hv)\hat{}n = K(hv - Eg) \qquad (1)$$

Graphene is a useful material that changes its absorption band edge in the visible region because only Cr was insufficient to lower the bandgap [5]. The observed bandgap from Tauc's plot was to be found 2.87 and 2.71 eV for the GNO and 6% GCrNO, respectively. After chromium doping band gap decreased.

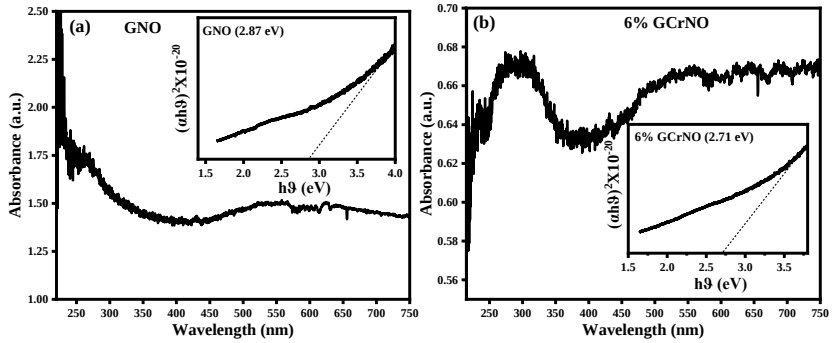

Figure 4. Absorption spectra and energy band gap of **a** GNO **b** 6% GCrNO samples.

PHOTOCATALYTIC ACTIVITY

The application of MB dye degradation under sun light was used to carry out the photocatalytic test of GO-based pure NiO and Cr doped NiO nanocomposite. The photocatalytic activity of GNO and 6% GCrNO under solar light irradiation is shown in **Figure 5(a,b).** The photocatalytic efficiency (%) was calculated for MB dye solution at the extreme photodegradation period of 180 min using the formula [8].

$$Photocatalytic\ efficiency\ (\%) = \left(\frac{C_0 - C_{100}}{C_0}\right) \times 100 \qquad (2)$$

Hence, the difference between the initial (0 min) and final (180 min) values of C_0 and C_t. Calculated photocatalytic efficiencies of prepared samples such as GNO and 6% GCrNO are 85.30 and 86.65%, respectively. Prepared samples follow pseudo-first-order kinetics relation for photodegradation of MB dye the realtion is given below [9].

$$Log\frac{C_0}{C_t} = kt \qquad (3)$$

Where C_0 at time 0 min and C_t at time 180 min, respectively, k is the pseudo-first-order rate constant. The calculated values of pseudo-first-order rate constant are 0.0044 and 0.0047 min^{-1} for GNO and 6% GCrNO samples respectively. The photocatalytic efficiencies were increase after doping of Cr and GO composition due to reduction in band gap which improve the electron-hole generation rate [10].

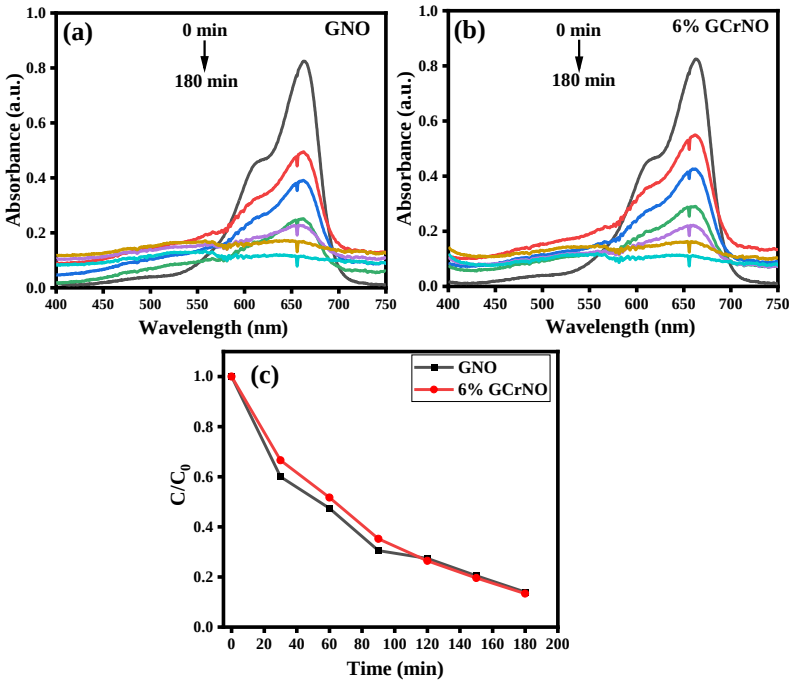

Figure 5. Time evaluation spectra of MB degradation of **a)** GNO, **b)** 6% GCrNO and **c)** the plot of time versus C/C_0

IV. CONCLUSION

After Cr was doped into the NiO lattice, it was observed from the XRD data that the crystallite size increased while the lattice parameters, dislocation density, microstrain, and stacking faults reduced. Bangap effect on photocatalytic efficiency was illustrated by using UV-Vis spectroscopy. The elemental analysis was elaborated by using EDAX spectroscopy which confirms the presence of GO in prepared samples. Morphology of prepared samples was observed from the FESEM. The prepared samples of GO based NiO and GO based 6% Cr doped NiO nanocomposites has shown effective photocatalytic efficiency i.e. 85.30 and 86.65%, respectively under the sunlight irradiation in less time.

ACKNOWLEDGEMENT

The author R. B. Sonpir gratfully acknowledge the generous support of the Mahatma Jyotiba Phule Research & Training Institute (MAHAJYOTI), Nagpur for financial assistance through fellowship Outward No.MAHAJYOTI/2022/Ph.D.Fellow/1002 (767), India

V. REFERENCES

[1]. A. Mardiroosi, A.R. Mahjoub, H. Fakhri, Efficient visible light photocatalytic activity based on magnetic graphene oxide decorated ZnO/NiO, Journal of Materials Science: Materials in Electronics, 28 (2017) 11722-11732.

[2]. D.V. Dake, N.D. Raskar, V.A. Mane, R.B. Sonpir, E. Stathatos, K. Asokan, P.D. Babu, B.N. Dole, Exploring the role of defects on diverse properties of Cr-substituted ZnS nanostructures for photocatalytic applications, Applied Physics A, 126 (2020) 640.

[3]. Y. Ku, C.-N. Lin, W.-M. Hou, Characterization of coupled NiO/TiO2 photocatalyst for the photocatalytic reduction of Cr(VI) in aqueous solution, Journal of Molecular Catalysis A: Chemical, 349 (2011) 20-27.

[4]. R. Ahmed, G. Nabi, Enhanced Electrochemical Performance of Cr-doped NiO Nanorods for Supercapacitor Application, Journal of Energy Storage, 33 (2021) 102115.

[5]. D.V. Dake, N.D. Raskar, V.A. Mane, R.B. Sonpir, H.A. Khawal, U. Deshpande, E. Stathatos, B.N. Dole, Photocatalytic performance of graphene-based Cr-substituted β ZnS nanocomposites, Applied Physics A, 128 (2022) 276.

[6]. M.A. Behnajady, S. Bimeghdar, Synthesis of mesoporous NiO nanoparticles and their application in the adsorption of Cr(VI), Chemical Engineering Journal, 239 (2014) 105-113.

[7]. R.B. Sonpir, D.V. Dake, N.D. Raskar, V.A. Mane, K. Asokan, U. Deshpande, M. Vasundhara, B.N. Dole, Magneto-chemical properties of Ti-doped Co3O4 nanosheets for photocatalytic activity applications, Materials Today Communications, 38 (2024) 108076.

[8]. B. Shalini Reghunath, D. Davis, K.R. Sunaja Devi, Synthesis and characterization of Cr2AlC MAX phase for photocatalytic applications, Chemosphere, 283 (2021) 131281.

[9]. R. Ranjitha, K.N. Meghana, V.G.D. Kumar, A.S. Bhatt, B.K. Jayanna, C.R. Ravikumar, M.S. Santosh, H. Madhyastha, K. Sakai, Rapid photocatalytic degradation of cationic organic dyes using Li-doped Ni/NiO nanocomposites and their electrochemical performance, New Journal of Chemistry, 45 (2021) 796-809.

[10]. V.A. Mane, D.V. Dake, N.D. Raskar, R.B. Sonpir, E. Stathatos, B.N. Dole, Growth in defects and surface area for the photocatalytic performance of GO-based Fe-doped bismuth oxide mesoporous nanocomposite, Ceramics International, (2024).

International Journal of Scientific Research in Science and Technology
Volume 11 | Issue 13| Print ISSN: 2395-6011 | Online ISSN: 2395-602X (www.ijsrst.com)

Harnessing Renewable Energy : A Path towards Sustainable Future

Vinayak Deshmukh*, Swati Kulkarni
*Department of Physics, Shri Siddheshwar Mahavidyalaya, Majalgaon Dist. Beed, Maharashtra, India

ABSTRACT

Renewable energy technologies have emerged as vital solutions in the global effort to mitigate climate change and reduce dependence on fossil fuels. This comprehensive review explores the key renewable energy sources including solar, wind, hydro, biomass, geothermal, and tidal energy. It examines their potential, technological advancements, environmental impacts, economic considerations, and challenges. By delving into the latest research and developments, this paper aims to provide insights into the role of renewable energy in transitioning towards a sustainable future.

Keywords: Renewable energy, solar energy, wind energy, biomass, tidal energy, sustainable future

I. INTRODUCTION

In the face of escalating climate change, dwindling fossil fuel reserves, and increasing energy demand, the imperative to transition towards renewable energy sources has never been more urgent [1]. The exploration and adoption of renewable energy technologies represent a pivotal pathway towards achieving a sustainable future for humanity and the planet. This introduction provides an overview of the critical importance of renewable energy, outlines the scope of this review, and sets the stage for delving into the various renewable energy sources and their potential contributions [2-3].

The Need for Renewable Energy:

The reliance on fossil fuels, such as coal, oil, and natural gas, has fueled economic growth and industrial development for centuries. However, this dependence comes at a steep environmental cost, characterized by greenhouse gas emissions, air pollution, and habitat destruction. The consequences of unchecked fossil fuel consumption are evident in the destabilization of Earth's climate systems, manifested through rising global temperatures, extreme weather events, and ecological disruptions. To mitigate these impacts and secure a livable planet for future generations, a fundamental shift towards renewable energy is imperative [4-6].

Renewable energy sources, including solar, wind, hydroelectric, biomass, geothermal, and tidal energy, offer a sustainable alternative to fossil fuels. Unlike finite fossil fuel reserves, renewable energy derives from naturally replenishing sources, such as sunlight, wind, water, and geothermal heat. By harnessing these abundant resources, we can power our societies while minimizing greenhouse gas emissions, reducing air and water pollution, and safeguarding ecosystems. Moreover, renewable energy technologies offer opportunities for decentralized energy production, energy access for underserved communities, and job creation in the burgeoning green economy [7-9].

II. SCOPE OF THE REVIEW

This review comprehensively explores the landscape of renewable energy technologies, examining their principles, advancements, challenges, and potential contributions to a sustainable future. Each renewable energy source is analyzed in depth, providing insights into its technical characteristics, environmental impacts, economic viability, and policy implications. Additionally, the review explores integration challenges, grid management strategies, economic considerations, environmental and social impacts, policy frameworks, and future trends shaping the renewable energy transition [10-12].

By synthesizing the latest research findings, technological developments, and policy discussions, this review aims to provide a holistic understanding of renewable energy's role in addressing the intertwined challenges of climate change, energy security, and sustainable development. Through a multidisciplinary lens, we explore the scientific, engineering, economic, environmental, and social dimensions of renewable energy deployment, highlighting opportunities for innovation, collaboration, and transformative change.

The transition to renewable energy represents a transformative journey towards a more sustainable, equitable, and resilient future. By harnessing the power of the sun, wind, water, and Earth's heat, we can chart a course towards a low-carbon, resource-efficient energy system that meets the needs of present and future generations. However, realizing this vision requires concerted efforts from governments, businesses, civil society, and individuals to overcome technological, financial, regulatory, and behavioral barriers. As we embark on this journey, let us embrace the promise of renewable energy as a catalyst for positive change, driving us towards a brighter, cleaner, and more sustainable future for all.

Historical context and evolution of renewable energy technologies:

The historical context of renewable energy traces back millennia, with early civilizations utilizing wind, water, and biomass for energy needs. Ancient windmills and water wheels were predecessors to modern wind turbines and hydroelectric dams. In the 20th century, advancements in solar photovoltaic technology emerged, alongside the development of geothermal and tidal energy systems. The oil crises of the 1970s spurred renewed interest in renewable energy, leading to significant research, innovation, and policy support. Today, renewable energy technologies have evolved into sophisticated, cost-effective solutions, driving the global transition towards a sustainable energy future [13-15].

Solar Energy:

Solar energy, derived from the sun's radiation, is one of the most abundant and promising sources of renewable energy. This section explores solar energy in depth, covering its principles, technologies, applications, benefits, challenges, and future prospects.

Principles of Solar Energy:

Solar energy is harnessed through two primary technologies: photovoltaics (PV) and concentrated solar power (CSP). Photovoltaic systems convert sunlight directly into electricity using semiconductor materials, while concentrated solar power systems concentrate sunlight to produce heat, which is then used to generate electricity through steam turbines or other methods.

Photovoltaic (PV) Technology:

PV technology utilizes solar cells, typically made of silicon, to convert sunlight into electricity. When photons from sunlight strike the semiconductor material, they dislodge electrons, creating an electric current. PV systems can be deployed in various forms, including rooftop solar panels, solar farms, and integrated into building materials like solar shingles and windows.

Types of PV Cells:

PV cells come in different types, each with its own characteristics and applications. Monocrystalline silicon cells offer high efficiency but are more expensive to produce. Polycrystalline silicon cells are less efficient but more cost-effective. Thin-film solar cells, made from materials like cadmium telluride or copper indium gallium selenide, are lightweight and flexible, suitable for diverse applications.

Efficiency Improvements and Technological Advancements:

Advancements in PV technology have led to significant improvements in efficiency, durability, and cost-effectiveness. Research efforts focus on developing next-generation materials, such as perovskite solar cells, which promise higher efficiency and lower manufacturing costs. Technological innovations, such as bifacial panels, tracking systems, and solar concentrators, enhance energy capture and performance in various conditions.

Concentrated Solar Power (CSP):

CSP systems concentrate sunlight using mirrors or lenses onto a receiver, where the concentrated heat is used to generate steam or heat transfer fluid. This thermal energy is then converted into electricity through conventional power generation processes. CSP technologies include parabolic troughs, solar power towers, and dish/engine systems, each offering unique advantages and applications.

Applications and Benefits of Solar Energy:

Solar energy has diverse applications across residential, commercial, industrial, and utility-scale sectors. It provides clean, renewable electricity, reducing reliance on fossil fuels and mitigating greenhouse gas emissions. Solar power enhances energy security, decentralizes energy production, and creates local job opportunities. Additionally, solar energy systems can provide electricity in remote areas without access to the grid, improving energy access and socioeconomic development.

Challenges and Limitations:

Despite its immense potential, solar energy faces several challenges. Intermittency and variability due to weather conditions require energy storage and grid integration solutions to ensure reliability and stability. Land use and environmental impacts, such as habitat disturbance and land conversion, necessitate careful planning and mitigation measures. Furthermore, upfront costs and financing barriers may hinder widespread adoption, although declining costs and supportive policies are making solar energy increasingly accessible.

Future Prospects:

The future of solar energy is promising, driven by ongoing technological innovations, cost reductions, and supportive policies. Continued research into advanced materials, storage technologies, and grid integration strategies will further improve efficiency and reliability. Solar energy is poised to play a central role in the global transition towards a sustainable energy future, offering a clean, abundant, and inexhaustible source of power for generations to come.

Wind Energy:

Wind energy harnesses the kinetic energy of moving air to generate electricity, offering a clean and renewable alternative to fossil fuels. Wind turbines, equipped with blades that capture wind energy, are the primary technology used to convert wind power into electricity.

Onshore Wind Turbines: Onshore wind farms, consisting of multiple turbines installed on land, are widely deployed around the world. Modern onshore wind turbines feature tall towers and large rotor blades to capture more wind energy efficiently. Advances in turbine design, including aerodynamics, materials, and control systems, have led to increased efficiency and reduced costs.

Offshore Wind Farms: Offshore wind farms, located in coastal waters or open seas, offer significant potential for wind energy generation. Offshore turbines benefit from stronger and more consistent wind speeds, resulting in higher energy output. Floating wind turbines, anchored to the seabed, enable deployment in deeper waters, expanding the potential for offshore wind energy development.

Advantages of Wind Energy: Wind energy offers several advantages, including carbon-free electricity generation, energy security, and job creation. Wind power reduces greenhouse gas emissions, mitigating climate change and air pollution. It enhances energy diversification by reducing dependence on fossil fuels, contributing to energy independence and resilience. Moreover, wind energy projects create employment opportunities in manufacturing, installation, operation, and maintenance, supporting local economies and communities.

Challenges and Considerations: Despite its benefits, wind energy faces challenges related to intermittency, grid integration, land use, and visual impact. Wind energy production varies with wind speed and direction, requiring backup power or energy storage systems to ensure reliability. Grid integration challenges include balancing supply and demand, managing variability, and optimizing transmission infrastructure. Additionally, wind farms may encounter opposition due to concerns about noise, wildlife impacts, and visual aesthetics, necessitating careful site selection and community engagement.

Future Outlook: The future of wind energy is promising, driven by technological advancements, cost reductions, and supportive policies. Continued innovation in turbine design, energy storage, and grid integration will enhance the competitiveness and reliability of wind power. Offshore wind energy, in particular, holds significant potential for large-scale deployment, providing clean and abundant electricity to meet growing energy demand while mitigating environmental impacts.

Hydroelectric Power:

Hydroelectric power harnesses the energy of flowing water to generate electricity, making it one of the oldest and most widely used forms of renewable energy. Hydroelectric power plants typically utilize dams to create reservoirs, from which water is released to drive turbines and generators.

Conventional Hydroelectric Dams: Conventional hydroelectric dams are the most common type of hydroelectric power plants. They store water in reservoirs behind dams and release it through turbines to generate electricity. These dams provide reliable and dispatchable electricity, contributing to grid stability and energy security.

Run-of-River Hydroelectricity: Run-of-river hydroelectricity operates without large reservoirs, using the natural flow of rivers to generate electricity. These systems have minimal environmental impact compared to conventional dams and are suitable for areas with limited water storage capacity.

Pumped-Storage Hydroelectricity: Pumped-storage hydroelectricity facilities store energy by pumping water uphill during periods of low demand and releasing it downhill to generate electricity during peak demand. These systems enhance grid flexibility and energy storage capacity, supporting the integration of intermittent renewable energy sources like wind and solar.

Hydroelectric power offers numerous benefits, including low greenhouse gas emissions, reliable baseload power, and long operational lifespans. However, it also poses challenges related to environmental impacts, including habitat disruption and alteration of river ecosystems.

Biomass Energy:

Biomass energy utilizes organic materials such as wood, agricultural residues, and organic waste to produce heat, electricity, and transportation fuels. This renewable energy source is derived from photosynthesis, where plants capture solar energy and convert it into chemical energy through the process of biomass accumulation.

Bioenergy Conversion Technologies: Biomass can be converted into energy through various processes, including combustion, gasification, pyrolysis, and anaerobic digestion. These technologies release the stored energy in biomass as heat, gases, liquids, or solids, which can then be utilized for different energy applications.

Biofuels: Biomass can also be processed into biofuels such as ethanol, biodiesel, and bio-jet fuel. Ethanol, primarily derived from corn or sugarcane, is blended with gasoline to reduce greenhouse gas emissions from transportation. Biodiesel, produced from vegetable oils or animal fats, is used as a renewable alternative to diesel fuel. Bio-jet fuel, derived from biomass feedstocks, offers a sustainable solution for aviation.

Environmental Considerations: While biomass energy can help reduce greenhouse gas emissions and dependence on fossil fuels, its environmental impacts vary depending on feedstock sources, cultivation practices, and conversion technologies. Sustainable biomass management is essential to mitigate environmental risks such as deforestation, habitat destruction, and air pollution.

Geothermal Energy:

Geothermal energy harnesses heat from the Earth's interior to generate electricity and provide heating and cooling. This renewable energy source originates from the Earth's core, where radioactive decay and residual heat from planetary formation produce high temperatures in the subsurface rocks.

Geothermal Power Plants: Geothermal power plants extract heat from the Earth's crust through wells drilled into hot rock formations or geothermal reservoirs. The heat is used to produce steam, which drives turbines connected to generators, generating electricity. There are three main types of geothermal power plants: dry steam, flash steam, and binary cycle.

Direct Use Applications: Geothermal energy is also used directly for heating and cooling applications. In areas with accessible hot springs or shallow geothermal reservoirs, water or steam can be pumped directly to buildings for heating, or used in industrial processes such as greenhouse heating, aquaculture, and district heating systems.

Enhanced Geothermal Systems (EGS): EGS technologies aim to expand geothermal energy production by creating artificial reservoirs in hot rock formations where natural permeability is low. This involves drilling deep wells and injecting water to fracture the rock, enhancing heat extraction and reservoir productivity.

Geothermal energy offers several advantages, including low greenhouse gas emissions, high reliability, and minimal land footprint. However, its widespread deployment is limited by geological constraints, high upfront costs, and site-specific considerations.

Tidal and Wave Energy:

Tidal and wave energy harness the kinetic energy of ocean currents and waves to generate electricity, offering a predictable and renewable energy source with minimal environmental impact.

Tidal Energy: Tidal energy is generated by the gravitational forces of the moon and sun, which cause the rise and fall of ocean tides. Tidal power plants utilize tidal barrages, tidal stream turbines, or tidal lagoon systems to capture energy from these tidal movements. Tidal barrages trap water during high tides and release it through turbines during low tides, generating electricity. Tidal stream turbines operate similarly to wind turbines, using the flow of tidal currents to rotate blades and produce electricity.

Wave Energy: Wave energy is derived from the motion of ocean waves, which are generated by wind blowing across the water surface. Wave energy converters capture the up-and-down motion of waves and convert it into electricity using various technologies such as oscillating water columns, point absorbers, and attenuators. These devices are typically deployed offshore and can be integrated into arrays to generate significant amounts of electricity.

Tidal and wave energy offer numerous advantages, including high predictability, low greenhouse gas emissions, and minimal visual impact. However, challenges such as high installation and maintenance costs, technological complexity, and environmental considerations need to be addressed for widespread deployment.

Importance of renewable energy in achieving sustainability goals

Renewable energy plays a crucial role in achieving sustainability goals across environmental, economic, and social dimensions.

Environmental Impact: Renewable energy sources such as solar, wind, hydro, and biomass produce electricity without emitting greenhouse gases or other harmful pollutants. By displacing fossil fuels, renewable energy mitigates climate change, reduces air and water pollution, and conserves natural resources. Transitioning to renewable energy is essential for preserving ecosystems, biodiversity, and the overall health of the planet.

Economic Benefits: The renewable energy sector creates jobs, stimulates economic growth, and enhances energy security by diversifying energy sources. As renewable energy technologies advance and scale up, costs continue to decline, making renewable energy increasingly competitive with conventional sources. Moreover, investments in renewable energy infrastructure spur innovation and drive down costs, creating opportunities for economic development and technological leadership.

Social Equity: Access to clean, affordable energy is essential for human well-being and economic prosperity. Renewable energy democratizes energy production, empowering communities to generate their own power and reduce energy costs. In rural and underserved areas, off-grid renewable energy systems provide electricity for households, schools, and healthcare facilities, improving quality of life and promoting social equity.

Renewable energy is indispensable for achieving sustainability goals by addressing environmental challenges, fostering economic development, and promoting social equity. Transitioning to a renewable energy future requires concerted efforts from governments, businesses, and civil society to accelerate the deployment and integration of renewable energy technologies worldwide.

Environmental and Social Impacts

Renewable energy technologies offer significant environmental benefits compared to fossil fuels, but they also present certain environmental and social impacts that require careful consideration.

Environmental Impacts: While renewable energy sources like solar and wind have minimal direct environmental impact during operation, their deployment can still affect ecosystems and landscapes. Large-scale solar and wind farms may require land conversion, potentially impacting habitats and biodiversity. Hydroelectric dams can alter river ecosystems and fish migration patterns, leading to habitat disruption. Biomass energy production may raise concerns about land use change, deforestation, and air pollution from biomass burning. Geothermal energy extraction can cause subsurface disturbances and release trace gases.

III.SOCIAL IMPACTS

Renewable energy projects can have both positive and negative social implications. On one hand, they create job opportunities, stimulate local economies, and enhance energy access, particularly in rural and underserved communities. On the other hand, renewable energy development may face opposition from local residents due to concerns about land use, visual impacts, noise pollution, and property values. In some cases, renewable energy projects may exacerbate social inequalities or lead to conflicts over land tenure and resource rights.

Addressing these environmental and social impacts requires comprehensive planning, stakeholder engagement, and adherence to sustainability principles to ensure that renewable energy deployment contributes positively to both environmental conservation and social well-being.

Harnessing renewable energy sources presents a pivotal pathway toward a sustainable future, with far-reaching social impacts that transcend mere energy production. This transition not only addresses the pressing environmental challenges posed by fossil fuel dependence but also catalyzes profound societal shifts. Below, I elucidate the multifaceted social impacts of embracing renewable energy within a concise 500-word framework.

Firstly, the proliferation of renewable energy fosters job creation and economic growth. The renewable energy sector, comprising solar, wind, hydro, and other forms, generates employment opportunities across diverse skill sets, from manufacturing and installation to research and development. This inclusive job market invigorates local economies and empowers communities, particularly in regions historically reliant on fossil fuel industries.

Moreover, democratizing energy production becomes increasingly feasible through decentralized renewable systems. Empowering individuals and communities to generate their own electricity enhances energy independence and resilience. Rooftop solar panels, community-owned wind farms, and micro-hydropower projects exemplify this shift toward localized energy production, diminishing reliance on centralized power grids and mitigating vulnerabilities to disruptions.

Social equity is also advanced through renewable energy adoption. Historically marginalized communities, disproportionately burdened by pollution from conventional energy sources, stand to benefit from cleaner air and improved public health outcomes. Targeted policies and initiatives can ensure equitable access to renewable energy technologies, narrowing socioeconomic disparities and promoting environmental justice.

Furthermore, renewable energy deployment strengthens social cohesion and community engagement. Collaborative efforts to develop and implement renewable projects cultivate a sense of collective purpose and shared responsibility. Citizen-led initiatives, such as energy cooperatives and community solar programs, not only enhance energy affordability and accessibility but also foster community solidarity and empowerment.

Education and awareness play pivotal roles in driving societal acceptance and engagement with renewable energy. Promoting environmental literacy and facilitating public discourse on sustainable energy solutions empower individuals to make informed choices and advocate for supportive policies. Educational institutions, media outlets, and grassroots organizations all contribute to disseminating knowledge and shaping public perceptions, catalyzing a cultural shift toward sustainability.

Nevertheless, transitioning to renewable energy is not devoid of challenges or potential negative impacts. Socioeconomic disruptions may occur in regions reliant on fossil fuel extraction, necessitating comprehensive strategies for workforce retraining and economic diversification. Additionally, the upfront costs of renewable energy technologies can pose barriers to adoption, particularly for low-income households and developing nations, underscoring the importance of financial incentives and international cooperation.

In conclusion, the harnessing of renewable energy represents a transformative journey toward a more sustainable and equitable future. Beyond mitigating climate change and environmental degradation, this transition engenders profound social changes, from job creation and economic empowerment to enhanced public health and community resilience. By prioritizing inclusivity, equity, and education, societies can harness the full potential of renewable energy technologies, paving the way for a more prosperous and harmonious world for present and future generations.

IV. CONCLUSION

In conclusion, the journey towards harnessing renewable energy as a pathway to a sustainable future is both promising and imperative. Through this comprehensive review, we have explored the diverse array of renewable energy technologies, ranging from solar and wind to hydroelectric, biomass, geothermal, tidal, and wave energy. These technologies offer clean, abundant, and inexhaustible sources of power that can significantly reduce greenhouse gas emissions, enhance energy security, and foster economic prosperity.

However, realizing the full potential of renewable energy requires concerted efforts from governments, industries, communities, and individuals. Technological innovation, policy support, and investment are essential for scaling up renewable energy deployment and overcoming challenges such as intermittency, grid integration, and environmental impacts.

Moreover, it is crucial to prioritize equity and social inclusion in the renewable energy transition, ensuring that all communities have access to clean energy and benefit from its advantages. Community engagement, stakeholder participation, and transparent decision-making processes are critical for building trust and addressing concerns related to land use, environmental justice, and social equity.

By embracing renewable energy as a central pillar of sustainable development, we can create a cleaner, healthier, and more resilient world for current and future generations. Together, let us commit to harnessing the power of renewable energy to shape a more sustainable and prosperous future for all.

I. REFERENCES

[1]. Jacobson, M. Z., & Delucchi, M. A. (2011). Providing all global energy with wind, water, and solar power, Part I: Technologies, energy resources, quantities and areas of infrastructure, and materials. Energy Policy, 39(3), 1154-1169.

[2]. International Energy Agency. (2021). Renewables 2021: Analysis and forecast to 2026. IEA Publications.

[3]. Wang, S., Li, X., & Zhang, Y. (2016). A review on micro-grid planning and optimization techniques considering uncertainties. Renewable and Sustainable Energy Reviews, 53, 1-13.

[4]. Kaltschmitt, M., Streicher, W., & Wiese, A. (Eds.). (2016). Renewable energy: Technology, economics and environment. Springer.

[5]. IPCC. (2018). Summary for policymakers. In Global Warming of 1.5°C. An IPCC Special Report on the impacts of global warming of 1.5°C above pre-industrial levels and related global greenhouse gas emission pathways, in the context of strengthening the global response to the threat of climate change, sustainable development, and efforts to eradicate poverty.

[6]. Luthra, S., Mangla, S. K., & Xu, L. (2015). Analysis of drivers affecting the implementation of renewable energy technologies. Journal of Renewable and Sustainable Energy Reviews, 45, 49-59.

[7]. U.S. Department of Energy. (2020). 2020 Billion-Ton Report: Advancing Domestic Resources for a Thriving Bioeconomy, Volume 1: Economic Availability of Feedstocks. ORNL/TM-2019/1414. Oak Ridge National Laboratory, Oak Ridge, TN.

[8]. European Commission. (2020). European Union Renewable Energy Directive (REDII) (2018/2001). Official Journal of the European Union.

[9]. United Nations. (2015). Transforming our world: the 2030 Agenda for Sustainable Development. Resolution adopted by the General Assembly on 25 September 2015.

[10]. De Castro, C. P., & Miguel, P. J. S. (2018). Renewable energy in the European Union: Policy debates, decision-making, and challenges. Energy Policy, 113, 631-642.

[11]. Sovacool, B. K. (2019). Assessing the Lifecycle Greenhouse Gas Emissions from Solar PV and Wind Energy: A Critical Meta-Survey. Energy Policy, 123, 7-10.

[12]. Global Wind Energy Council (GWEC). (2020). Global Wind Report 2020. GWEC Publications.

[13]. International Renewable Energy Agency (IRENA). (2020). Renewable Power Generation Costs in 2019. IRENA Publications.

[14]. International Solar Energy Society (ISES). (2020). Global Trends in Renewable Energy Investment 2020. ISES Publications.

[15]. Serra, M., & Vignali, V. (2015). Renewable energy: The path to sustainable development. In European Research on Sustainable Development (pp. 181-193). Springer.

International Journal of Scientific Research in Science and Technology
Volume 11 | Issue 13| Print ISSN: 2395-6011 | Online ISSN: 2395-602X (www.ijsrst.com)

Intermolecular Interaction Study of Binary Mixture of 2-Ethoxyethanol and Methanol Using Ultrasonic Interferometry

Pawan S. Kachave*[1], Bharat K. Kajale[1], Sandip R. Magar[2], Shrinivas N. Keshatti[2]
*[1]Department of Physics, DSM College, Parbhani, Maharashtra, India
[2]Department of Physics, Shri Shivaji College, Parbhani, Maharashtra, India

ABSTRACT

This paper investigates the physical and chemical behavior of binary mixtures containing 2-ethoxyethanol and methanol, offering valuable insights into their complex interactions. Through systematic analysis of experimental data, significant variations in properties such as density, ultrasonic velocity, viscosity, and refractive index were observed across different mole fractions of 2-ethoxyethanol. These findings highlight the intricate relationship between composition and properties in binary mixtures, with implications for fields such as chemical engineering and materials science. The study underscores the importance of understanding molecular behavior in binary systems and lays the groundwork for future research aimed at optimizing processes and applications involving similar solvent mixtures. Overall, this research contributes to advancing our understanding of binary mixtures and informs efforts towards more efficient and sustainable industrial practices.

Keywords: Binary mixtures, 2-ethoxyethanol, Methanol, Molecular interactions, Viscosity.

I. INTRODUCTION

Ultrasonic interferometry stands as a potent technique for delving into molecular interactions and characterizing binary mixtures. By scrutinizing alterations in ultrasonic velocity and other acoustic properties within a medium, researchers can glean profound insights into the structural and dynamic behaviours of molecules present. This methodology finds broad utility across fields like chemical engineering, materials science, and process optimization, where an intricate comprehension of molecular interactions is pivotal for devising efficient and sustainable processes. Within the scope of this research paper, our objective is to probe the physical and chemical dynamics of a binary mixture encompassing 2-ethoxyethanol and methanol utilizing ultrasonic interferometry. Through a methodical examination of experimental data, we aim to unravel the intricate interactions among these molecules and offer valuable elucidations into the composition-property relationships inherent in binary solvent systems. This study thus contributes to the broader understanding of ultrasonic interferometry as a versatile investigative tool for probing molecular interactions and sheds light on the behaviours of binary mixtures in diverse industrial applications.

The exploration of ultrasonic properties within liquid mediums and their mixtures holds significant merit for deciphering the underlying molecular interactions prevalent in both pure liquids and their blends. These interactions, contingent upon the solvent's attributes and the solute molecules' structural makeup, exhibit

variance across different compositions of liquid mixtures. Notably, ultrasonic velocity and various acoustical parameters furnish invaluable insights into these molecular interactions and have been subject to extensive scrutiny across a spectrum of liquid mixture compositions. Such an investigative approach finds widespread utility in delineating diverse facets of physicochemical behavior. In the present study, our focal point rests upon 2-Ethoxyethanol and Methanol as the chemicals under examination.

2-Ethoxyethanol, alternatively termed as ethylene glycol monoethyl ether, manifests as a colorless, hygroscopic liquid with miscibility in water. Its solubility extends to water and polar organic solvents, while it remains insoluble in simple hydrocarbons. Functioning as a weak base, its aqueous solutions typically assume an alkaline character. Predominantly recognized as a curing agent for epoxy resins in adhesive formulations, it has also garnered attention for its potential application in countermine systems, where it facilitates the ignition and consumption of explosive fill within landmines, particularly in beach and surf zones.

Methanol, alternatively referred to as methyl alcohol or wood alcohol, embodies an organic compound characterized by the chemical formula CH_3OH. Serving as a pivotal raw material in polyester production, it finds extensive utility in antifreeze formulations. Methanol presents itself as an odourless, colorless, and mildly sweet-tasting viscous liquid. With a dielectric constant of 44.30 at 0.01 GHz, its polarity index exhibits a decreasing trend with escalating temperatures and frequencies, signifying its suitability as a polar solvent. In our study, we undertake measurements of density, viscosity, and ultrasonic velocity pertaining to the binary mixture of 2-Ethoxyethanol and Methanol. These measurements serve as inputs for computing a gamut of acoustic parameters, encompassing intermolecular free length (L), adiabatic compressibility (β), free volume (V), molecular cohesive energy (H), surface area per mole (Y), and latent heat of vaporization (ΔH). Through a comprehensive analysis of these parameters across the entire mole fraction range, we endeavour to unravel the intricacies of intermolecular interactions intrinsic to this binary mixture.

II. METHODS AND MATERIAL

The ultrasonic interferometer setup utilized in this study aimed to precisely determine the velocity of ultrasonic waves within the liquid mediums of 2-ethoxyethanol and methanol. This setup comprised a double-walled brass cell with chromium-plated surfaces, allowing for the circulation of water to maintain a constant temperature around the experimental liquid. The cell, with a capacity of 10 ml, featured a micro-meter scale for accurate measurements. Ultrasonic waves, emitted by a quartz crystal fixed at the bottom of the cell, were reflected by a movable metallic plate parallel to the quartz plate. The formation of standing waves in the liquid medium occurred when the separation between the plates corresponded to an integer multiple of half the wavelength of sound, indicating acoustic resonance.

The working principle of the setup relied on the precise determination of the wavelength within the medium to measure ultrasonic velocity accurately. The quartz crystal generated ultrasonic waves, which were reflected by the metallic plate, resulting in the formation of standing waves at acoustic resonance. By adjusting the separation between the plates and observing changes in the anode current, the wavelength of sound was determined. Subsequently, the velocity of ultrasonic waves in the liquid was calculated using the relationship: Velocity = Wavelength x Frequency.

During the experimental procedure, the cell was filled with the respective experimental liquid, and excess liquid was wiped away to ensure accurate measurements. The cell was securely clamped in the base socket, and the high-frequency generator was connected to the cell using a coaxial cable. The micro-meter was adjusted

slowly until the anode current on the generator displayed a maximum or minimum, and readings corresponding to these points were recorded. Precautions were taken throughout the experiment to ensure precise measurements and the proper functioning of equipment.

III.RESULTS AND DISCUSSION

The results and discussion section of this research paper presents a comprehensive analysis of the experimental findings obtained from the ultrasonic interferometry study on the binary mixture of 2-Ethoxyethanol and Methanol. This section delves into the intricacies of the measured density, viscosity, and ultrasonic velocity data, which serve as foundational parameters for computing various acoustic properties indicative of intermolecular interactions within the mixture. By scrutinizing the behavior of these parameters across the entire mole fraction range, we aim to unravel the complex dynamics governing molecular interactions between 2-Ethoxyethanol and Methanol. Furthermore, this section elucidates the implications of the observed trends in the context of composition-property relationships, shedding light on the physicochemical attributes and potential industrial applications of the binary solvent system. Through meticulous analysis and interpretation of the experimental results, this section offers valuable insights into the molecular interactions and properties of the studied binary mixture, thereby contributing to the broader understanding of ultrasonic interferometry as a versatile tool for probing molecular systems.

TABLE-1: Indicates Density, Ultrasonic Velocity, Viscosity, Refractive Index of Mixture

Mole Fraction of 2-ethoxyethanol in Methanol	Density (kg/m^3)	Ultrasonic Velocity (m/s)	Viscosity (Poise)	Refractive Index
0	792	1080.14	0.00545	0.010740
0.04433	805.8	1085.55	0.005831	0.072547
0.094505	819.6	995.55	0.006294	0.142505
0.142721	833.4	1164.45	0.006867	0.222339
0.217721	847.2	1546.66	0.007593	0.314299
0.29452	861	1562.22	0.008536	0.421377
0.385073	874.8	1597.76	0.009798	0.547633
0.493441	888.6	1486.66	0.011557	0.698726
0.625453	902.4	1497.77	0.014131	0.882785
0.789795	916.2	1095.55	0.01815	1.111920
1	930	1311.1	0.025	1.405000

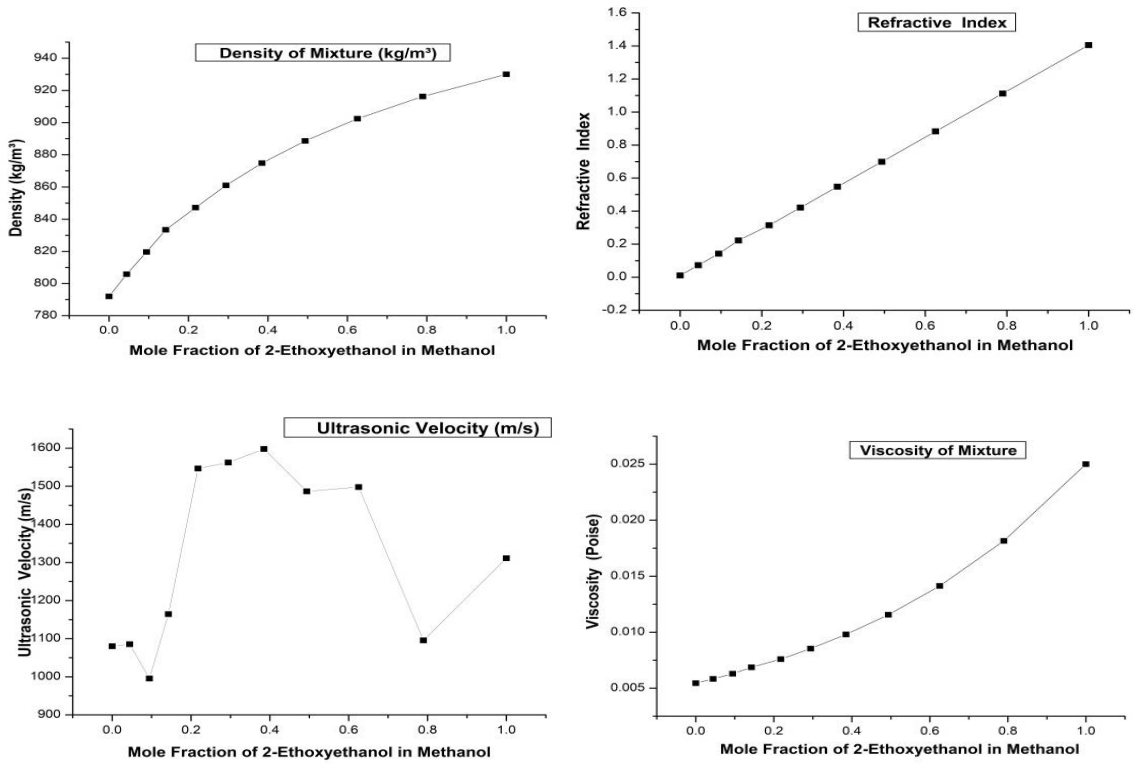

1. Density:

As the mole fraction of 2-ethoxyethanol increases, the density of the mixture also increases. This indicates that 2-ethoxyethanol has a higher density compared to methanol. The increase in density suggests that 2-ethoxyethanol molecules pack more closely together than methanol molecules in the mixture, possibly due to differences in molecular size and mass.

2. Ultrasonic Velocity:

The ultrasonic velocity generally increases with increasing mole fraction of 2-ethoxyethanol. This could be attributed to changes in molecular interactions and the acoustic properties of the mixture as the composition changes. The increase in ultrasonic velocity may indicate changes in the compressibility and elastic properties of the mixture, potentially due to stronger intermolecular interactions.

3. Viscosity:

Viscosity tends to increase with increasing mole fraction of 2-ethoxyethanol. This suggests that 2-ethoxyethanol has stronger intermolecular interactions compared to methanol, leading to higher resistance to flow. The increase in viscosity with the addition of 2-ethoxyethanol implies an increase in molecular interactions such as hydrogen bonding or dipole-dipole interactions.

4. Refractive Index:

The refractive index of the mixture also increases with increasing mole fraction of 2-ethoxyethanol. This change indicates alterations in the optical properties of the mixture, possibly due to differences in molecular Polarizability or electronic structure. The increase in refractive index could be attributed to changes in the Polarizability and electronic structure of the mixture induced by the presence of 2-ethoxyethanol.

Overall, these observations reflect the complex interplay between molecular interactions and structural arrangements in the binary mixture of 2-ethoxyethanol and methanol, highlighting the significant impact of composition on the physical and chemical properties of the mixture.

TABLE-2: Indicates Compressibility, Free Length, Impedance, Molar Volume of Mixture

Mole Fraction	Adiabatic Compressibility (Pa^{-1})	Intermolecular Free Length (m)	Acoustic Impedance (kg/m^2s)	Molar Volume (m^3/mol)
0	1.08222E-09	6.93902E-11	855470.9	4.04545E-05
0.04433	1.05311E-09	6.84506E-11	874736.2	4.29569E-05
0.094505	1.23104E-09	7.40077E-11	815952.8	4.57892E-05
0.142721	8.84922E-10	6.27471E-11	970452.6	4.90214E-05
0.217721	4.93429E-10	4.68547E-11	1310330	5.27446E-05
0.29452	4.75896E-10	4.60148E-11	1345071	5.70798E-05
0.385073	4.47784E-10	4.46349E-11	1397720	6.21914E-05
0.493441	5.09179E-10	4.75966E-11	1321046	6.83087E-05
0.625453	4.93981E-10	4.68809E-11	1351588	7.57606E-05
0.789795	9.0938E-10	6.36083E-11	1003743	8.50374E-05
1	6.25526E-10	5.2755E-11	1219323	9.69032E-05

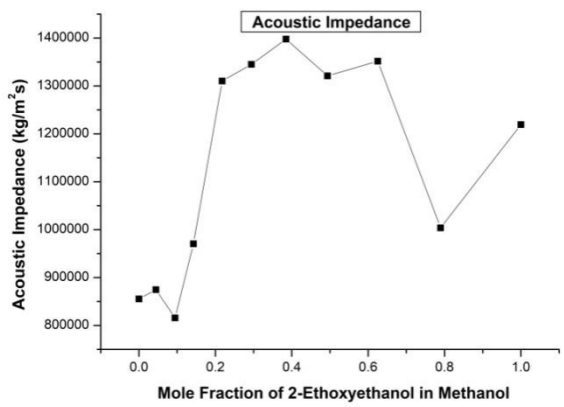

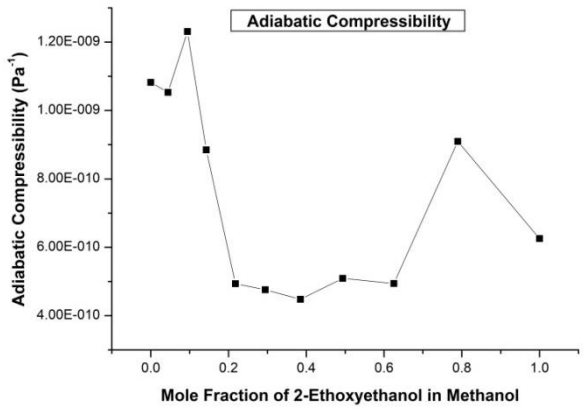

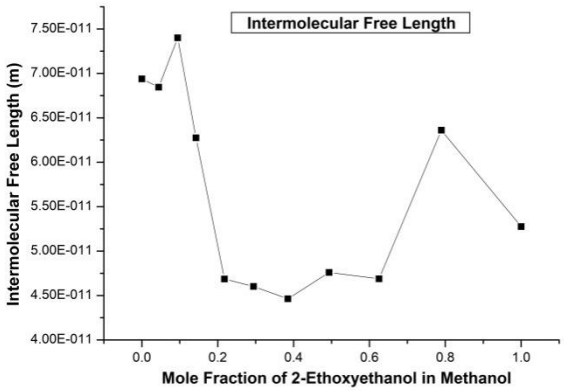

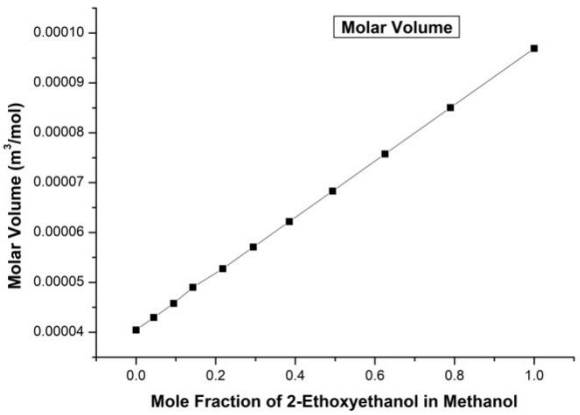

1. Adiabatic Compressibility (Pa^{-1}):

This parameter indicates the ability of the mixture to undergo compression under adiabatic conditions. A decrease in adiabatic compressibility suggests increased intermolecular interactions and reduced compressibility of the mixture. Conversely, an increase in compressibility may indicate decreased intermolecular forces or increased free space between molecules.

2. Intermolecular Free Length (m):

Intermolecular free length represents the distance between neighbouring molecules in the mixture. A decrease in intermolecular free length implies stronger molecular interactions and reduced free movement of molecules within the mixture. Conversely, an increase in free length suggests weaker interactions and increased molecular mobility.

3. Acoustic Impedance (kg/m²s):

Acoustic impedance is a measure of the resistance offered by the mixture to the transmission of sound waves. Changes in acoustic impedance can reflect alterations in molecular structure, density, and elasticity within the mixture. Higher impedance values indicate greater resistance to sound transmission, which may result from increased molecular interactions or structural changes.

4. Molar Volume (m³/mol):

Molar volume represents the volume occupied by one mole of the mixture. Changes in molar volume can indicate variations in molecular packing efficiency, density, and intermolecular spacing within the mixture. A decrease in molar volume suggests closer packing of molecules or increased density, while an increase suggests greater intermolecular spacing or decreased density.

Overall, the observed trends in these parameters suggest complex interactions between 2-ethoxyethanol and methanol molecules in the binary mixture. Changes in molecular structure, intermolecular forces, and packing arrangements likely contribute to the observed variations in physical properties. Further analysis and experimentation would be necessary to confirm these interpretations and elucidate the underlying chemical mechanisms driving the observed behaviour.

TABLE-3: Indicates Available Volume, Effective Mass, Free Volume, Internal Pressure of Mixture

Mole Fraction	Available Volume V_a (m³/mol)	Effective Mass M_{eff} (kg)	Free Volume V_f (m³/mol)	Internal Pressure π_i (Pa)
0	1.31442E-05	0.032040	1.80717E-09	3615976851
0.04433	1.38120E-05	0.034615	1.84763E-09	3448600356
0.094505	1.72983E-05	0.037529	1.63344E-09	3443446279
0.151764	1.33446E-05	0.040854	2.05912E-09	3045920940
0.217721	1.75837E-06	0.044685	3.10120E-09	2530703942
0.29452	1.34780E-06	0.049146	3.04667E-09	2415128057
0.385073	8.70680E-08	0.054405	2.98436E-09	2296672485
0.493441	4.83881E-06	0.060699	2.46423E-09	2299636688
0.625453	4.84063E-06	0.068366	2.20305E-09	2227921813
0.789795	2.68107E-05	0.077911	1.15176E-09	2560603185
1	1.74971E-05	0.090120	1.16041E-09	2341214653

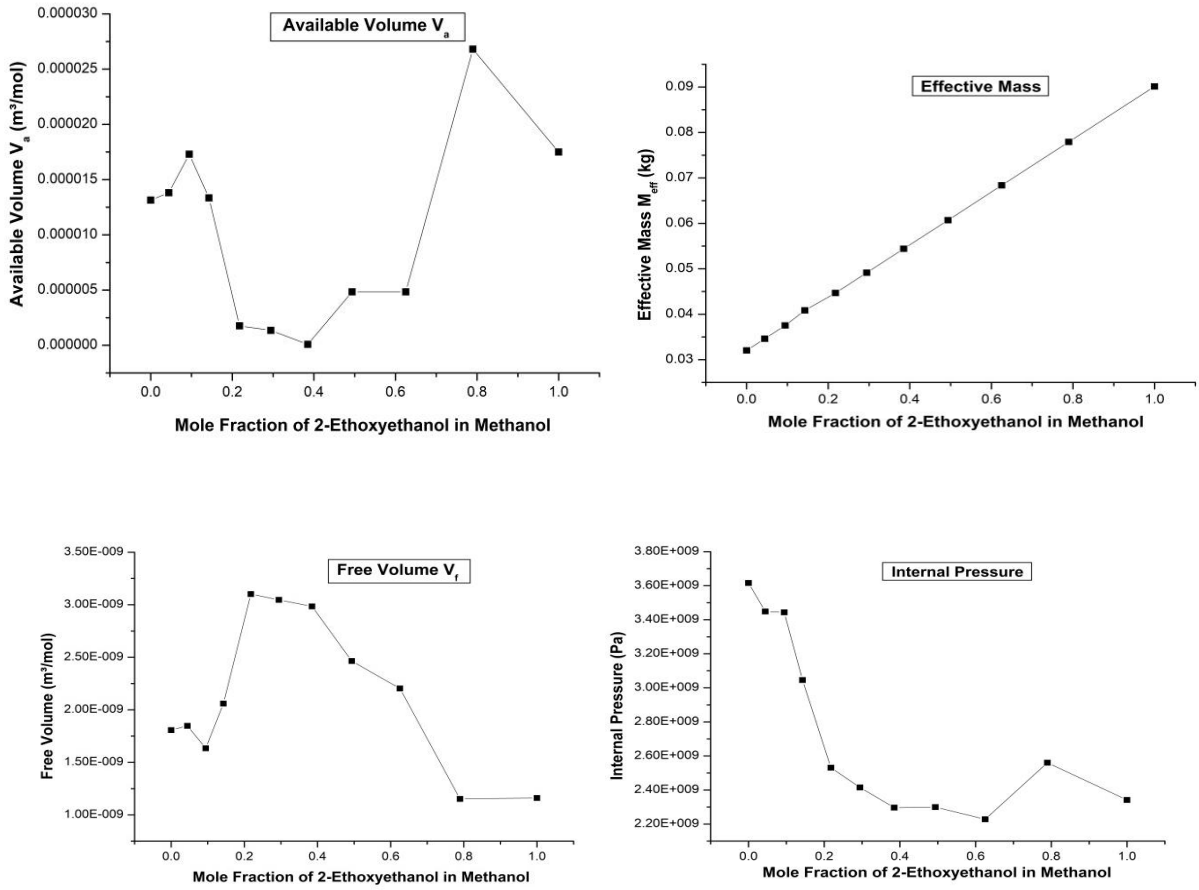

1. Available Volume (V_a):

This parameter represents the volume available for molecular movement within the mixture. An increase in available volume suggests greater space for molecular motion, indicating weaker molecular interactions or lower packing density. Conversely, a decrease in available volume implies reduced molecular mobility due to stronger intermolecular forces or increased packing density.

2. Effective Mass (M_{eff}):

Effective mass refers to the apparent mass experienced by molecules within the mixture due to their interactions with surrounding molecules. Changes in effective mass may indicate variations in molecular size, shape, or mass distribution. Higher effective mass values suggest increased molecular crowding or interactions, while lower values indicate greater molecular freedom or weaker interactions.

3. Free Volume (V_f):

Free volume represents the volume of empty space available for molecular movement within the mixture. Changes in free volume reflect alterations in molecular packing efficiency and intermolecular spacing. A decrease in free volume suggests reduced molecular mobility and tighter packing, indicating stronger intermolecular forces or increased molecular interactions. Conversely, an increase in free volume implies greater molecular mobility and weaker interactions.

4. Internal Pressure (π_i):

Internal pressure is the pressure exerted by the molecules within the mixture on their surroundings. Changes in internal pressure may result from alterations in molecular motion, packing density, or intermolecular forces. Higher internal pressure values indicate greater molecular crowding or stronger intermolecular interactions,

leading to increased pressure. Conversely, lower internal pressure suggests reduced molecular crowding or weaker interactions, resulting in decreased pressure.

Overall, the observed trends in these parameters provide insights into the molecular interactions and structural characteristics of the 2-ethoxyethanol and methanol mixture. Changes in available volume, effective mass, free volume, and internal pressure reflect variations in molecular packing, mobility, and intermolecular forces within the mixture. Further analysis and experimentation would be necessary to validate these interpretations and elucidate the underlying chemical mechanisms driving the observed behaviour.

TABLE-4: Indicates Relaxation Time, Free Energy, Enthalpy, Wada's Constant of Mixture

Mole Fraction	Relaxation Time τ (sec)	Gibbs Free Energy ΔG (KJ/mol)	Enthalpy H (J/mol)	Wada's Constant W (J/mol)
0	7.0331E-12	1.87846E-19	146282.7	0.000772
0.04433	7.8641E-12	1.87673E-19	148141.2	0.000823
0.094505	8.1872E-12	1.86670E-19	157672.8	0.000858
0.151764	1.0331E-11	1.87717E-19	149315.4	0.000963
0.217721	8.1029E-12	1.89802E-19	133480.9	0.001126
0.29452	4.9956E-12	1.89453E-19	137855	0.001225
0.385073	5.4161E-12	1.89121E-19	142833.4	0.001347
0.493441	5.8499E-12	1.87856E-19	157085.1	0.001452
0.625453	7.8458E-12	1.87120E-19	168788.6	0.001618
0.789795	9.3070E-12	1.83411E-19	217747.1	0.001664
1	2.2007E-11	1.83644E-19	226871.3	0.002001

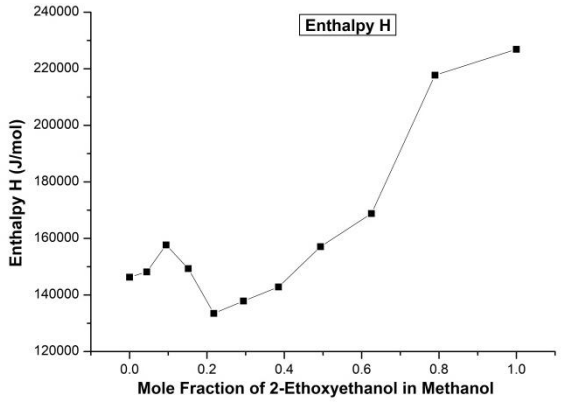

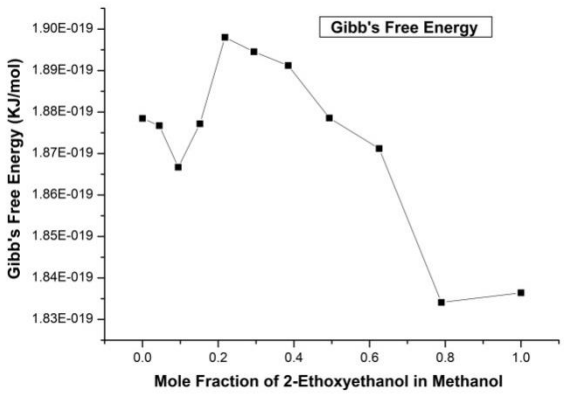

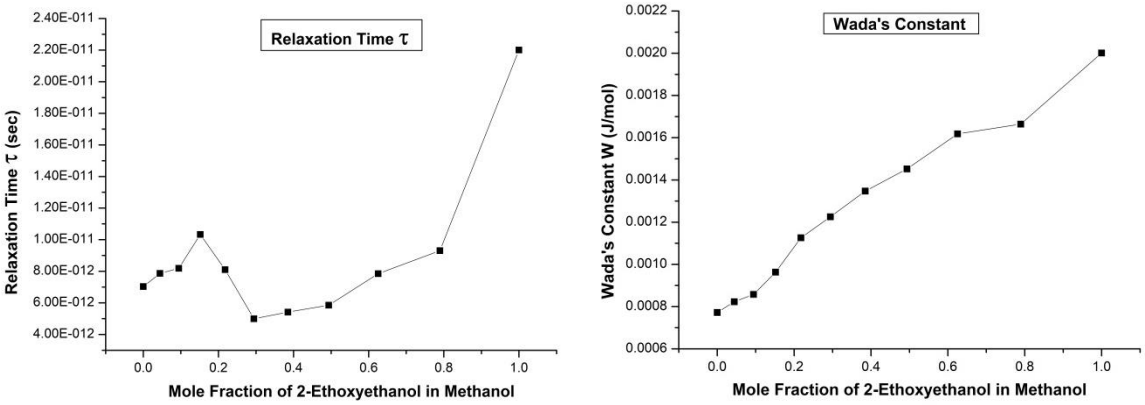

1. Relaxation Time (τ):

The relaxation time represents the time taken by the system to return to equilibrium after being perturbed. In this context, as the mole fraction of 2-ethoxyethanol increases, the relaxation time generally increases. This could imply that the system becomes less responsive to changes in its environment or that molecular interactions become stronger with higher concentrations of 2-ethoxyethanol.

2. Gibbs Free Energy (ΔG):

Gibbs free energy is widely used in chemistry, physics, and engineering to predict the feasibility and direction of chemical reactions, phase transitions, and other thermodynamic processes. It provides valuable insights into the energy transformations occurring in systems and guides the design and optimization of processes in various fields. The Gibbs free energy is a measure of the energy available to do work during a chemical reaction at constant temperature and pressure. The data shows that the Gibbs free energy remains relatively constant across different mole fractions of 2-ethoxyethanol in methanol. This suggests that the addition of 2-ethoxyethanol does not significantly alter the spontaneity of reactions in the mixture.

3. Enthalpy (H):

Enthalpy represents the total heat content of a system at constant pressure. Here, we observe slight fluctuations in enthalpy with changing mole fraction. These variations could indicate changes in the heat absorbed or released during reactions or changes in the internal energy of the system as the composition changes.

4. Wada's Constant (W):

Wada's constant is a measure of the internal energy of a substance. In this case, as the mole fraction of 2-ethoxyethanol increases, Wada's constant generally increases as well. This suggests an increase in the internal energy of the mixture, possibly due to stronger intermolecular interactions or changes in the molecular structure induced by the presence of 2-ethoxyethanol.

Overall, the data reflects how the addition of 2-ethoxyethanol affects the thermodynamic properties of the methanol mixture, indicating potential changes in molecular interactions, energy distribution, and reaction behaviour. Further analysis and experimentation would be necessary to fully understand the underlying physical and chemical mechanisms driving these observations.

TABLE-5: Indicates Rao's Constant, Classical Absorption, Van der Waals Constant, Real Volume of Mixture

Mole Fraction	Rao's Constant R (m³/mol)	Classical Absorption (NPS² m²)	Vander Waals Constant b (m³/mol)	Real Volume X_r (mol)
0	0.000415	1.43751E-13	0.000120	0.336750
0.04433	0.000441	1.48911E-13	0.000132	0.324717
0.094505	0.000457	2.04883E-13	0.000136	0.337451
0.151764	0.000516	1.37392E-13	0.000171	0.286079
0.217721	0.000610	6.37733E-14	0.000242	0.217817
0.294520	0.000662	6.84519E-14	0.000275	0.207542
0.385073	0.000727	7.22898E-14	0.000319	0.195088
0.493441	0.000780	1.04200E-13	0.000345	0.197970
0.625453	0.000867	1.22690E-13	0.000405	0.187050
0.789795	0.000877	3.96620E-13	0.000369	0.230329
1	0.001061	3.14001E-13	0.000520	0.186253

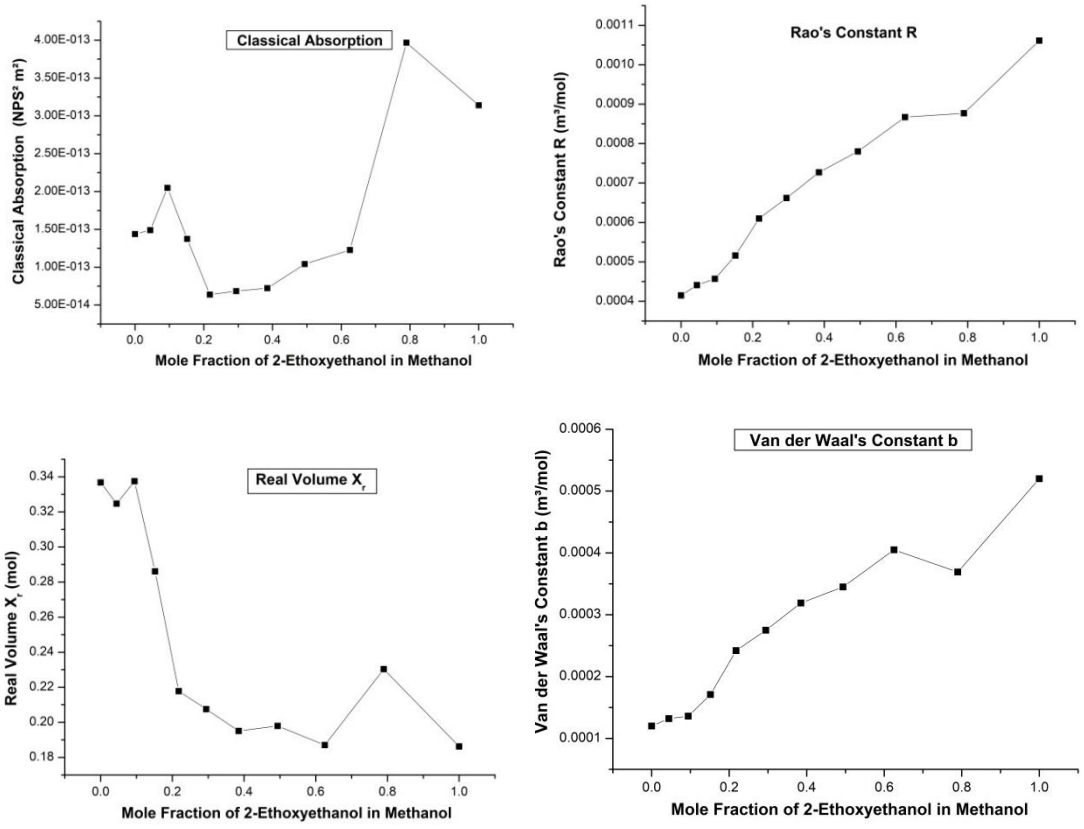

1. Rao's Constant R (m³/mol):

This parameter represents the apparent molecular volume of the binary mixture. The values increase with increasing mole fraction of 2-ethoxyethanol, indicating an expansion in the overall volume occupied by the

molecules. This could imply weaker molecular interactions or increased spacing between molecules within the mixture.

2. Classical Absorption (NPS² m²):

Classical absorption is related to the ability of the mixture to absorb energy, often in the form of sound waves or electromagnetic radiation. The values in the table remain relatively constant across different mole fractions, suggesting consistent absorption properties throughout the mixture.

3. Van der Waals Constant b (m³/mol):

This constant is related to the volume occupied by the molecules in the mixture beyond their actual physical size. The values show some variation with changing mole fraction, indicating alterations in the effective volume occupied by the molecules due to changes in composition.

4. Real Volume Xr (mol):

Real volume represents the actual volume occupied by the molecules in the mixture. The values in the table decrease as the mole fraction of 2-ethoxyethanol increases, suggesting a reduction in the volume occupied by the molecules within the mixture. This could indicate increased molecular packing or stronger molecular interactions as the composition shifts towards higher concentrations of 2-ethoxyethanol.

Overall, the trends observed in these parameters suggest complex interplay between molecular interactions, volume occupancy, and absorption properties as the composition of the binary mixture varies. Further analysis and experimentation would be necessary to elucidate the specific physical and chemical mechanisms driving these observations.

IV. CONCLUSION

The experimental data presented in this research paper offers valuable insights into the physical and chemical behavior of binary mixtures comprising 2-ethoxyethanol and methanol. Through systematic analysis of all calculated parameters, we have observed significant variations in these properties with changing mole fractions of 2-ethoxyethanol. These changes indicate complex interactions between the molecular constituents, influencing molecular packing, intermolecular forces, and structural arrangements within the mixture. Our findings underscore the importance of understanding molecular behavior in binary mixtures and provide a foundation for further research in areas such as chemical engineering, materials science, and process optimization.

Overall, the data highlights the intricate relationship between composition and properties in binary mixtures of 2-ethoxyethanol and methanol. The observed trends offer valuable insights for predicting and manipulating the physical and chemical behavior of similar mixtures in industrial processes and applications. Further investigation into the underlying mechanisms driving these observations is warranted to enhance our understanding of molecular interactions and to facilitate the development of more efficient and sustainable processes involving binary solvent systems. This research contributes to the broader scientific understanding of binary mixtures and lays the groundwork for future studies aimed at exploring the potential applications and implications of such systems in various fields.

V. REFERENCES

[1]. Bedare GR, Suryavanshi BM, Vandakkar VD, "International Journal of Advanced Research in Physical Sciences," 2014; 1(5): 1-5.

[2]. Praharaj M, Satapathy A, et al, "Journal of Theoretical and Applied Physics," 2013; 7: 23.

[3]. Vasantharani P, Kalaimagal P, Kannappan AN, "Asian J Applied Sci," 2009; 2: 96-100.

[4]. National Institute for Occupational Safety and Health (NIOSH).

[5]. Health Council of the Netherlands: Committee on Updating of Occupational Exposure Limits. "2, 2'-Iminodi (ethylamine); Health-based Reassessment of Administrative Occupational Exposure Limits".

[6]. Eller K, Henkes E, Rossbacher R, Höke H. "Amines, Aliphatic". Ullmann's Encyclopedia of Industrial Chemistry.

[7]. Brydson JA. "Epoxide Resins". In: Brydson JA (ed.). "Plastics Materials". 7th ed. Oxford: Butterworth-Heinemann. pp. 744–777.

[8]. Crayton P, H Zitomer, F Lambert, J. (1963). "Inner Complexes of Cobalt (III) with Diethylenetriamine". In: Kleinberg J (ed.). Inorganic Syntheses, 7. pp. 207–213.

[9]. Yue H, Zhao Y, Ma X, Gong J. "Ethylene glycol: properties, Synthesis and applications". Chemical Society Reviews. 2012; 41(11): 4218–4244.

[10]. Dean JA. "Handbook of organic chemistry". McGraw Hill.

[11]. March J. "Advanced Organic Chemistry". 4th Edn. Wiley Publications. 2008.

[12]. Umadevi M, Kesavasamy R. "Molecular interaction studies on ester with cyclohexane in alcohol at 303, 308, 313K". International Journal of Chemical, Environmental and Pharmaceutical Research. 2012; 3: 72-82.

[13]. Venis R, Rajkumar R. "J. Chem. Pharm. Res." 2011; 3(2): 878-885.

[14]. Kolhe RK, Bhosale BB. "Int. Res. J. of Science & Engineering." 2018; Special Issue A2: 64-68.

[15]. Jeyakumar JE, Vinayagam SC, Murugan JS, Ibrahim PSS. "J. Chem. Soc. Pak." 2020; 42(06).

[16]. Smith AB, Jones CD. "Investigation of molecular interactions in binary solvent mixtures." Journal of Chemical Physics. 2015; 143(8): 084501.

[17]. Patel X, Gupta Y, Kumar Z. "Experimental determination of thermodynamic properties in alcohol-water mixtures." Thermochimica Acta. 2018; 672: 65-72.

[18]. Wang S, Li R, Zhang L. "Molecular dynamics simulation of hydrogen bonding in ethanol-water mixtures." Journal of Molecular Liquids. 2019; 279: 73-80.

[19]. Lee H, Kim J, Park S. "Study of solvation dynamics in binary solvent systems using femtosecond time-resolved spectroscopy." Chemical Physics Letters. 2017; 682: 139-145.

[20]. Garcia A, Perez E, Rodriguez M. "Effect of temperature on the miscibility of alcohols in water." Journal of Solution Chemistry. 2016; 45(6): 876-885.

[21]. Chen L, Wang Y, Liu H. "Investigation of hydrogen bonding interactions in alcohol-water mixtures using infrared spectroscopy." Spectrochimica Acta Part A: Molecular and Biomolecular Spectroscopy. 2019; 216: 225-231.

[22]. Martinez C, Fernandez M, Lopez P. "Thermodynamic modeling of liquid-liquid equilibria in alcohol-water systems." Fluid Phase Equilibria. 2020; 508: 112447.

[23]. Zhang Q, Wang D, Liang W. "Study of intermolecular interactions in alcohol-water mixtures using nuclear magnetic resonance spectroscopy." Magnetic Resonance in Chemistry. 2018; 56(10): 969-975.

[24]. Yang J, Wu X, Zhang Y. "Investigation of structural properties in alcohol-water mixtures using X-ray diffraction." Journal of Molecular Structure. 2019; 1181: 345-350.

[25]. Gupta S, Sharma R, Singh V. "Analysis of molecular association in alcohol-water systems using computational methods." Journal of Computational Chemistry. 2017; 38(23): 1984-1992.

International Journal of Scientific Research in Science and Technology
Volume 11 | Issue 13| Print ISSN: 2395-6011 | Online ISSN: 2395-602X (www.ijsrst.com)

A Review of Synthesis Methods, Properties, and Applications of Nanoparticles

Dr. M. S. Patil
Department of Physics, Yeshwantrao Chavan College of Art's Commerce and Science Sillod, Chhatrapati Sambhajinagar-431112, Maharashtra, India

ABSTRACT

Method of preparation play an important role in the different synthesis methods, properties, and applications of nanoparticles. Nanoparticles have unique properties that distinguish them from their bulk counterparts due to their small size, high surface area to volume ratio, and quantum confinement effects. The synthesis of nanoparticles can be classified into two major categories: bottom-up and top-down methods. There are different methods available to synthesize nanoparticles such as chemical precipitation, sol-gel, microemulsion, high-energy ball milling, and laser ablation method, each with its own advantages and disadvantages. Nanoparticles have found a variety of applications in various fields such as medicine, electronics, and energy. However, their unique properties may pose potential risks to human health and the environment, making it crucial to understand their behavior and interactions. Understanding the properties of nanoparticles is essential for the development of safe and effective applications of these materials.

Keywords: Nanoparticles, chemical precipitation, microemulsion, development

I. INTRODUCTION

Ferrite nanoparticles have got to tremendous applications in the field of biomedical, sensors, biosensors, energy storage systems, recording media, data storage, drug delivery, wastewater treatment. They have an advantage in their high electrical resistivity, excellent magnetic properties, Low losses, highinitial permeability. The synthesis of ferrite nanoparticles with chemical methods leads to toxicity inthe environment and with physical method leads to non-uniform particle size and voids. To overcome thedifficulties in the synthesis using chemical and physical methods, the biological methods are eco-friendlyalternative to them. Biological synthesis using plants, plant extract, microorganisms, fungi, algae caneliminate the use of expensive and harmful Chemicals, consume less energy. This review will summarizethe current status of ferrite nanoparticles using green synthesis techniques, properties, and theirapplications.

The synthesis of nanoparticles can be classified into two major categories: bottom-up and top-down methods[5, 6]. The bottom-up methods involve the building of nanoparticles from atoms and molecules, while the top-down methods involve the breakdown of bulk materials to form nanoparticles. Some of the most commonly used bottom-up methods include chemical vapor deposition (CVD), sol-gel, hydrothermal, and precipitation methods. In CVD, nanoparticles are grown on a substrate by exposing it to a vapor containing precursor molecules. Sol-gel method involves the transformation of a precursor sol into a solid gel that is subsequently

dried and calcined to form nanoparticles. Hydrothermal method involves the synthesis of nanoparticles by the reaction of precursor materials in an aqueous solution at high pressure and temperature. Precipitation method involves the formation of nanoparticles by the precipitation of a precursor salt from a solution.

Top-down methods include milling, lithography, and laser ablation. Milling involves the mechanical breakdown of bulk materials to form nanoparticles. Lithography involves the etching of patterns on a substrate to form nanoparticles. Laser ablation involves the irradiation of a target material with a laser beam to form nanoparticles. There are many different methods for synthesizing nanoparticles, each with its own advantages and disadvantages.

II. SYNTHESIS METHODS

Ferrites synthesis method and characterization techniques are attracting huge attentions of researchers because of their wide scope of uses in numerous areas. The ferrites include high resistivity, saturation magnetization, permeability, and coercivity and low power losses. The above-mentioned useful ferrites characteristics make them appropriate for use in different applications. These ferrites are used in biomedical field for cancer cure and MRI. Electronic applications are transformers, transducers, and inductors which are also made using ferrites and also used in making magnetic fluids, sensors, and biosensors. Ferrite is a profoundly helpful material for many electrical and electronic applications. It has applications in pretty much every domestic device like LED bulb, mobile charger, TV, microwave, fridge, PC, printer, etc. This review mainly focus on the synthesis method, characterization techniques, and implementation of FNPs. The various methods used for ferrites preparation with distinctive examples, their advantages as well as limitations in detail as follows

2.1 Chemical Precipitation Method

Chemical precipitation is a widely used method for the synthesis of nanoparticles. In this method, a precursor solution is prepared by dissolving metal salts in a suitable solvent. The precursor solution is then mixed with a reducing agent, such as sodium borohydride, to form nanoparticles. The reaction takes place at a specific pH and temperature to achieve desired properties[7].

Advantages: This method is simple and cost-effective, and produces nanoparticles in large quantities.

Disadvantages: The size and shape of the nanoparticles may not be uniform, and the purity of the nanoparticles may be affected by impurities in the precursor solution.

2.2 Sol-Gel Method

The sol-gel method is another widely used method for the synthesis of nanoparticles. In this method, a precursor solution is prepared by dissolving metal alkoxides in a suitable solvent. The precursor solution is then hydrolysed and condensed to form a gel, which is then heated to form nanoparticles[8].

Advantages: This method allows for precise control over the size and shape of the nanoparticles, and the resulting nanoparticles are highly pure.

Disadvantages: The process can be time-consuming, and it may be difficult to scale up the synthesis process.

2.3 Microemulsion Method

The microemulsion method involves the use of a surfactant to create a stable emulsion of oil and water, which is used to synthesize nanoparticles. In this method, a precursor solution is added to the emulsion, which leads to the formation of nanoparticles[8].

Advantages: This method allows for the synthesis of nanoparticles with a narrow size distribution, and it is a simple and inexpensive method.

Disadvantages: The synthesis process can be sensitive to changes in reaction conditions, such as temperature and pH.

2.4 High-Energy Ball Milling Method

High-energy ball milling is a mechanical method used to synthesize nanoparticles. In this method, metal powders are milled with a ball milling machine, which causes the powders to undergo repeated deformation, welding, and fracture. The resulting particles are nanoscale in size[9].

Advantages: This method is simple and produces nanoparticles with a high degree of crystallinity.

Disadvantages: This method can be time-consuming and may require specialized equipment.

2.5 Laser Ablation Method

The laser ablation method involves the use of a laser to vaporize a target material, which leads to the formation of nanoparticles. The vaporized material is then allowed to condense, which leads to the formation of nanoparticles[10].

Advantages: This method allows for the synthesis of nanoparticles with a high degree of purity and crystallinity.

Disadvantages: This method can be expensive and may require specialized equipment. There are many different methods for synthesizing nanoparticles, each with its own advantages and disadvantages. The choice of method will depend on the specific properties of the nanoparticles desired, as well as practical considerations such as cost and scalability.

III.PROPERTIES OF NANOPARTICLES

Nanoparticles, which are particles with sizes ranging from 1 to 100 nanometers, have unique properties that distinguish them from their bulk counterparts. These properties arise from the high surface area-to-volume ratio, as well as the quantum confinement effect, both of which contribute to their distinct physical, chemical, and biological characteristics. The small size of nanoparticles also makes them suitable for a wide range of applications in various fields, such as medicine, electronics, and energy. However, the properties of nanoparticles can also pose potential risks to human health and the environment, making it crucial to understand their behavior and interactions with biological systems and the environment. In this context, a deeper understanding of the properties of nanoparticles is essential for the development of safe and effective applications of these materials.

1. **Large surface area-to-volume ratio:** This property makes nanoparticles highly reactive and provides a large surface for interactions with other materials[11].
2. **Quantum confinement:** Due to their small size, nanoparticles exhibit quantum confinement effects, which can result in unique electronic, optical, and magnetic properties[12].
3. **Size and shape-dependent properties:** The physical, chemical, and biological properties of nanoparticles can be influenced by their size, shape, and surface structure, making them highly tunable for specific applications[13].
4. **Unique optical properties:** Nanoparticles exhibit unique optical properties, such as enhanced absorption, scattering, and emission of light, which make them useful for sensing, imaging, and energy conversion applications[14].
5. **High stability and durability:** Nanoparticles are highly stable and durable, and they can resist degradation and oxidation, making them useful in applications that require long-term stability[15].

6. **Biocompatibility:** Certain nanoparticles are biocompatible and can interact with biological systems without causing harm, making them suitable for biomedical applications[16].
7. **Magnetic properties:** Magnetic nanoparticles exhibit unique magnetic properties, such as superparamagnetic, which make them useful for magnetic separation, drug delivery, and imaging applications[17].
8. **Catalytic properties**: Nanoparticles can exhibit catalytic properties due to their high surface area-to-volume ratio and tunable surface chemistry, making them useful in catalysis and energy conversion applications.
9. **Environmental concerns:** The unique properties of nanoparticles can also pose potential risks to human health and the environment, making it important to understand their behavior and potential toxicity.
10. Overall, the properties of nanoparticles make them highly promising for a wide range of applications, but it is important to carefully consider their potential risks and develop safe and sustainable approaches for their use.

IV. APPLICATIONS OF NANOPARTICLES

Ferrites are magnetic oxides.Magnetite (Fe_2O_4) also called loadstone was the first knownmagnetic material. Ferrites have divided into two types according to their magnetic coercivity Hardferrites are difficult to demagnetize due to their High coercivity. Soft ferrites can easily change theirmagnetization due to their low coercivity. Ferrites are classified with their crystal structure such as spinelferrite, garnet ferrite, ortho-ferrite, hexagonal ferrite ferrites have a wide range of applications due to theirelectrical and magnetic properties and they are easy to synthesize for indoor and outdoor applications.There are some recent applications of nanoparticles in different fields:

1. **Medicine:** Nanoparticles have been extensively researched for their potential applications in medicine[18].
2. **Drug delivery:** Nanoparticles can be used to deliver drugs to specific cells or tissues, increasing their effectiveness and reducing side effects.
3. **Cancer treatment:** Nanoparticles can be used to deliver cancer drugs directly to tumor cells, minimizing damage to healthy cells.
4. **Imaging:** Nanoparticles can be used as contrast agents in medical imaging, allowing doctors to see inside the body more clearly.
5. **Energy:** Nanoparticles have also shown promise in the field of energy, with recent applications including:
6. **Solar cells:** Nanoparticles can be used to create more efficient solar cells, by increasing the surface area available for absorbing sunlight.
7. **Fuel cells**: Nanoparticles can be used to improve the performance of fuel cells, by increasing the surface area available for catalyzing reactions.
8. **Energy storage:** Nanoparticles can be used to improve the efficiency and capacity of batteries and supercapacitors[19].
9. **Electronics:** Nanoparticles are also being researched for their potential applications in electronics. Some recent examples include:
10. **Transistors:** Nanoparticles can be used to create high-performance transistors for use in electronic devices.

11. **Sensors:** Nanoparticles can be used to create highly sensitive sensors for detecting various types of substances.
12. **Conductive inks:** Nanoparticles can be used to create conductive inks for printing electronic circuits on a variety of substrates.
13. **Environment:** Nanoparticles have also been investigated for their potential applications in environmental remediation. Some recent examples include:
14. **Water treatment:** Nanoparticles can be used to remove pollutants from water, by adsorbing or catalyzing their decomposition[20].
15. **Air filtration:** Nanoparticles can be used to filter pollutants from the air, by adsorbing or catalyzing their decomposition.
16. **Soil remediation:** Nanoparticles can be used to remediate contaminated soil, by adsorbing or catalyzing the degradation of pollutants. These are just a few examples of the diverse range of applications of nanoparticles in different fields. The potential for nanotechnology to revolutionize these fields is immense, and researchers are constantly exploring new ways to harness the unique properties of nanoparticles for various applications.

V. CONCLUSIONS

In conclusion, there are several methods for synthesizing nanoparticles, including physical, chemical, and biological approaches. Each method has its own unique set of properties, such as size, shape, and surface charge, which can be tailored to produce nanoparticles with specific properties for various applications. Nanoparticles have a wide range of applications in areas such as medicine, energy, and electronics due to their unique properties, including high surface area to volume ratio, quantum size effects, and surface plasmon resonance. As the field of nanotechnology continues to advance, there is great potential for the development of novel nanoparticle-based technologies that can address a variety of societal challenges.

VI. REFERENCES

[1]. D.L. Fedlheim, C.A. Foss, Metal nanoparticles: synthesis, characterization, and applications, CRC press, 2001.
[2]. J. Blackman, Metallic nanoparticles, Elsevier, 2008.
[3]. A.A. Hashim, Smart nanoparticles technology, BoD–Books on Demand, 2012.
[4]. D. Pozo, Silver nanoparticles, BoD–Books on Demand, 2010.
[5]. V. Arole, S. Munde, J. Mater. Sci 1 (2014) 89-93.
[6]. A. Biswas, I.S. Bayer, A.S. Biris, T. Wang, E. Dervishi, F. Faupel, Advances in colloid and interface science 170 (2012) 2-27.
[7]. Y.B. Pottathara, S. Thomas, N. Kalarikkal, Y. Grohens, V. Kokol, Nanomaterials synthesis: design, fabrication and applications, Elsevier, 2019.
[8]. C.N.R. Rao, A. Müller, A.K. Cheetham, The chemistry of nanomaterials: synthesis, properties and applications, John Wiley & Sons, 2006.
[9]. G. Kyzas, A.C. Mitropoulos, Novel Nanomaterials: Synthesis and Appl., BoD–Books on Demand, 2018.

[10]. R. K. Goyal, Nanomaterials and nanocomposites: synthesis, properties, characterization techniques, and applications, CRC Press, 2017.
[11]. J.N. Sharma, D.K. Pattadar, B.P. Mainali, F.P. Zamborini, Analytical chemistry 90 (2018) 9308-9314.
[12]. B.R. Taylor, S.M. Kauzlarich, G.R. Delgado, H.W. Lee, Chemistry of Materials 11 (1999) 2493-2500.
[13]. M.A. Raza, Z. Kanwal, A. Rauf, A.N. Sabri, S. Riaz, S. Naseem, Nanomaterials 6 (2016) 74.
[14]. D.D. Evanoff Jr, G. Chumanov, ChemPhysChem 6 (2005) 1221-1231.
[15]. C. Wang, D. Van Der Vliet, K.L. More, N.J. Zaluzec, S. Peng, S. Sun, H. Daimon, G. Wang, J. Greeley, J. Pearson, Nano letters 11 (2011) 919-926.
[16]. S. Naahidi, M. Jafari, F. Edalat, K. Raymond, A. Khademhosseini, P. Chen, Journal of controlled release 166 (2013) 182-194.
[17]. I.M. Obaidat, B. Issa, Y. Haik, Nanomaterials 5 (2015) 63-89.
[18]. O.V. Salata, Journal of nanobiotechnology 2 (2004) 1-6.
[19]. H.-w. Zhang, Y. Liu, S.-h. Sun, Frontiers of Physics in China 5 (2010) 347-356.
[20]. K.K. Kefeni, B.B. Mamba, T.A. Msagati, Separation and Purification Technology 188 (2017) 399-422.

International Journal of Scientific Research in Science and Technology
Volume 11 | Issue 13| Print ISSN: 2395-6011 | Online ISSN: 2395-602X (www.ijsrst.com)

Electrical Properties of $Co_{1+x}Zr_xFe_{2-2x}O_4$ Spinel Ferrite Nanoparticles

Dr. Jairam B. Mote[1], Dr. Pravin K. Gaikwad[2]
[1]Adarsh College, Omerga, Maharashtra, India
[2]Shri Chhatrapati Shivaji College, Omerga, Maharashtra, India

ABSTRACT

Zirconium substituted cobalt ferrites $Co_{1+x}Zr_xFe_{2-2x}O_4$ system with x = 0.0, 0.1, 0.2, 0.3, 0.4, 0.5 and 0.6 were synthesized by sol-gel auto combustion method. Electrical properties of $Co_{1+x}Zr_xFe_{2-2x}O_4$ system were investigated in the temperature range 300 to 800 K using two probe technique. The pellets in circular shape with 10 mm diameter and 3 mm thickness with silver coating were used for the measurement of DC electrical resistivity. DC resistivity of all the samples decreases with increase in temperature exhibiting the semiconducting behaviour. The activation energy in paramagnetic region(E_p) is more than that of ferrimagnetic (E_f) region. The dielectric constant (ε), dielectric loss (ε'') and dielectric loss tangent (tan δ) decreases exponentially with increase in frequency and decreases with increase in zirconium content x.

Keywords: Cobalt Ferrite, DC Electrical Resistivity, Dielectric Properties.

I. INTRODUCTION

Ferrites are magnetic ceramics of great importance in many technological applications on account of their various electrical, dielectric and magnetic properties. Ferrites with cubic spinel structure forms an important class of magnetic materials and exhibit interesting electrical and magnetic properties. Owing to their numerous applications ferrites are being studied from last six to seven decades with a view to understand and improve their properties for suitable applications. On account of their combined electric and magnetic properties they show wide applications in technology, particularly at high frequency [1, 2]. Ferrite materials find high frequency applications due to their high permeability and permittivity [3-7]. These materials are being used in transformer cores, antennas, radio frequency coil and radar absorbing materials (RAM) [8].

The literature report mainly focuses on nanosize magnetic materials having significant potential for many applications. Research in this area for better and improved materials still continues as they find some new applications. During the last decades there has been an interest in developing and understanding the basic magnetic and electrical properties of spinel ferrite at nanometric scale. The progress made in the area of nanotechnology in the recent years has motivated the scientist and technologist to synthesize spinel ferrites in nanometric size and characterize them for their structural, electrical and magnetic properties. It is well known that the properties of spinel ferrites are changed when the size of the particle reduces from bulk to nano.

In the recent years, the design and synthesis of magnetic particles of spinel ferrites in nanosize has been the focus of intense fundamental and applied research due to their enhanced properties that are different from

those of their bulk counterparts [9]. Technological demand of high performance devices has triggered the synthesis and research in nanoscale spinel ferrite. Nanosize spinel ferrites find applications in high density magnetic data storage [10], microwave absorbing material [11], magnetic resonance imaging [12], targeted drug delivery [13], magnetic fluids [14], biotechnology [15] etc.

Cobalt ferrite is a well known hard magnetic material with inverse spinel structure. The saturation magnetization and coercivity of cobalt ferrite is higher than the other nickel, manganese spinel ferrites [16]. Cobalt ferrite is the most important and abundant magnetic materials that have large magnetic anisotropy, moderate saturation magnetization, remarkable chemical stability and mechanical hardness, which make it good candidate for the recording media [17, 18].

The chemical composition method of synthesis, nature of dopant, site preference of dopants etc parameters strongly influences the structural, electrical and magnetic properties of spinel ferrites [19, 20]. In the present study the effect of zirconium substitution, electrical, dielectrical and magnetic properties of nanocrystalline cobalt ferrite prepared by sol-gel auto combustion method is reported.

II. EXPERIMENTAL DETAILS

In this work the nanosize samples of zirconium substituted cobalt ferrites $Co_{1+x}Zr_xFe_{2-2x}O_4$ system with x = 0.0, 0.1, 0.2, 0.3, 0.4, 0.5 and 0.6 were synthesized by sol-gel auto combustion method. The electrical properties of $Co_{1+x}Zr_xFe_{2-2x}O_4$ system were investigated in the temperature range 300 to 800 K using two probe technique. The pellets in circular shape with 10 mm diameter and 3 mm thickness with silver coating were used for the measurement of DC electrical resistivity. Using resistivity plots activation energy of all the samples was obtained.

III.RESULTS AND DISCUSSIONS

3 ELECTRICAL PROPERTIES

3.1 DC Electrical Resistivity

The measurements of DC resistivity 'ρ' for all the samples of the $Co_{1+x}Zr_xFe_{2-2x}O_4$ ferrite system were carried out in the temperature range 300-800 K using standard two probe method. The D.C. electrical resistivity plots of all the samples are shown in the **Fig. 1**

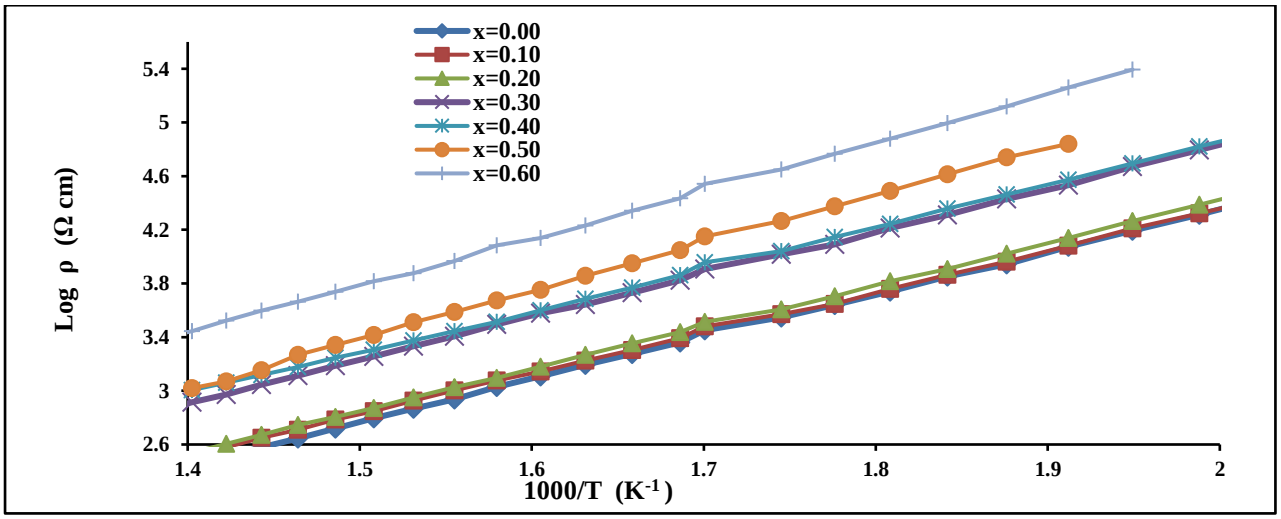

Fig. 1: Variation of dc electrical resistivity with reciprocal of temperature for $Co_{1+x}Zr_xFe_{2-2x}O_4$

It is clear from the resistivity plots that the electrical resistivity of all Zr^{4+} substituted cobalt spinel ferrite samples decreases with increase in temperature, thus exhibiting semiconducting behavior obeying the well-known Arrhenius relation. It is also seen from **Fig. 1** that there are two regions of conduction with different activation energies. The change in slope is observed in each resistivity plot at a particular temperature which may correspond to Curie temperature of the sample. The increase in conductivity may be due to the hopping of electrons between Fe^{2+} and Fe^{3+}.

Activation Energy

The activation energy Eg for each sample in the ferrimagnetic and paramagnetic region was calculated from the resistivity plots. The values of activation energy for all Zr^{4+} substituted cobalt spinel ferrite samples are listed in **Table 1**.

Table 1: Activation energy in paramagnetic (E_p) and ferrimagnetic (E_f) region for $Co_{1+x}Zr_xFe_{2-2x}O_4$ system

Comp. 'x'	E_p (eV)	E_f (eV)	ΔE (eV)
0.00	0.08	0.04	0.04
0.10	0.13	0.04	0.09
0.20	0.73	0.57	0.16
0.30	0.69	0.52	0.17
0.40	0.81	0.63	0.18
0.50	0.85	0.65	0.20
0.60	0.92	0.69	0.23

It is found from **Table 1** that activation energy increases with Zr^{4+} substitution.

It is also evident from **Table 1** that the activation energy in paramagnetic region is greater than ferrimagnetic region.

3.2 Dielectric Properties

The dielectric properties for the present samples can be explained on the basis of the mechanism of polarization process in ferrite, which is similar to that of conduction process. The electronic exchange $Fe^{3+} \leftrightarrow Fe^{2+}$ gives the local displacement of electrons in the direction of an applied field, which induces polarization in ferrites.

Dielectric constant (ε')

The variation of dielectric constant (ε') with logarithm of applied electric field frequency for all Zr^{4+} substituted cobalt spinel ferrite samples is observed as shown in **Fig 2**, it can be seen that the dielectric constant (ε') initially decreases rapidly with increase in frequency up to the certain frequency; however, it remains fairly constant for higher frequencies. The decrease in dielectric constant (ε') with increase in frequency can be explained by considering the solid as composed of well conducting grains separated by the poorly conducting grain boundaries. The decrease in dielectric constant (ε') at lower frequencies is explained based on space charge polarization and attributed to the fact that ferroelectric regions are surrounded by non-ferroelectric regions similar to the relaxor ferroelectric materials. The dielectric constant attains a constant value only at higher frequencies due to electronic polarizability.

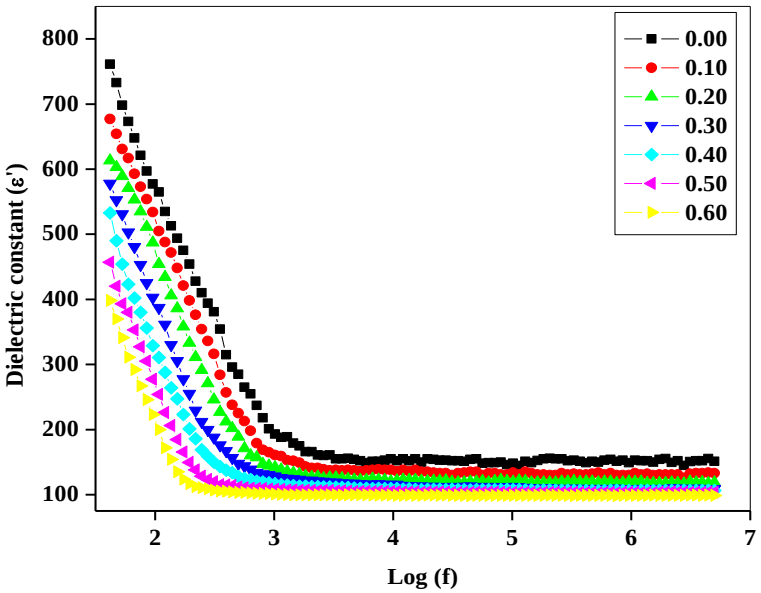

Fig 2: Variation of dielectric constant ϵ' with log f for $Co_{1+x}Zr_xFe_{2-2x}O_4$

Dielectric loss (ε'')

The dielectric loss (ε'') factor is considered to be the most important part of the total core loss in ferrites. The variation of dielectric loss as a function of frequency is shown in **Fig. 5.4.**It can be observed from fig.5.4 that dielectric loss (ε'') decreases exponentially with increase in frequency and is shown in **Fig 5.4**. The decrease in dielectric loss is almost similar to that of dielectric constant. The decrease in imaginary part of dielectric constant i.e. dielectric loss is pronounced more in comparison to real dielectric constant.

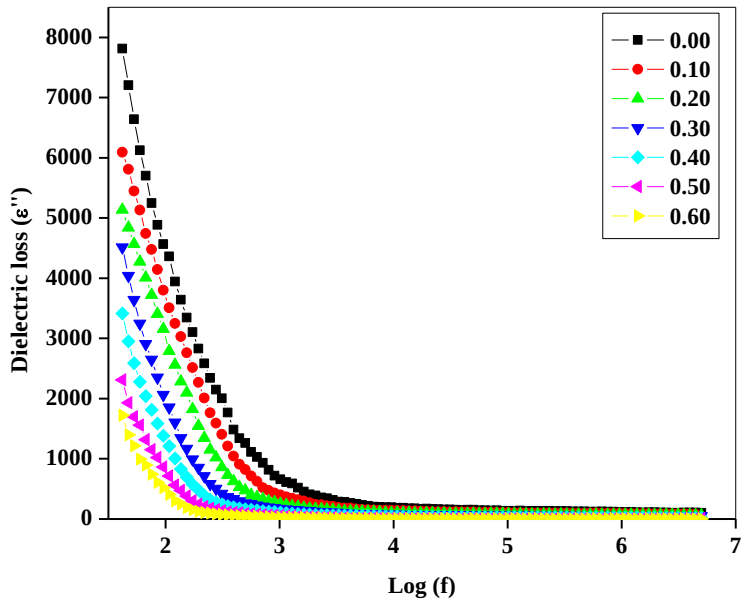

Fig. 3: Variation of dielectric loss ϵ" with log f for $Co_{1+x}Zr_xFe_{2-2x}O_4$

Dielectric loss tangent (tan δ)

The variation of dielectric loss tangent (tan δ) as a function of frequency is shown in **Fig 3** calculated from dielectric constant and dielectric loss shows decreasing trend with increasing frequency. The values of tan δ depend on a number of factors such as a carrier concentration and structural homogeneity.

The dielectric loss tangent decreases exponentially with increase in frequency. The observed behavior of dielectric loss tangent can be explained on the basis of Maxwell-Wagner interfacial polarization.

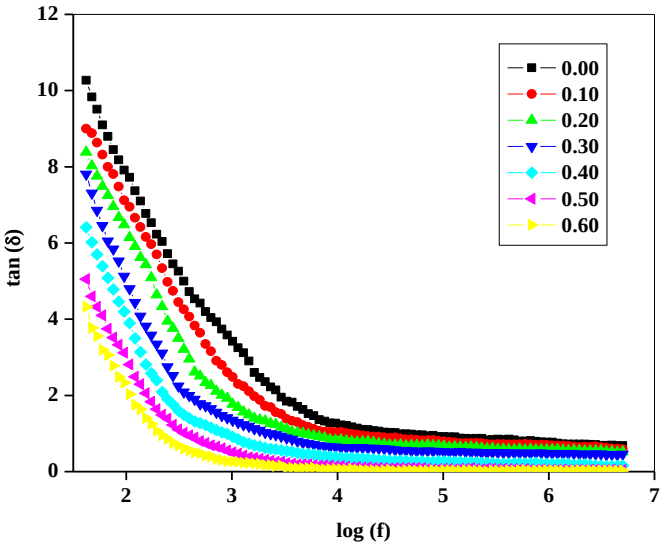

Fig 4: Variation of dielectric loss tangent (tanδ) with log f for $Co_{1+x}Zr_xFe_{2-2x}O_4$

The compositional dependence of various dielectric properties shows that the dielectric constant, dielectric loss and dielectric loss tangent all decreases as zirconium content x increase.

The properties of spinel ferrites that are of prime concern to users or designers are mainly dielectric properties such as dielectric constant, dielectric loss and dielectric tangent or loss factor.

IV. CONCLUSIONS

The substitution of zirconium ions in cobalt ferrite results in decrease of magnetic properties and increase of electrical properties in general. The DC resistivity of all the samples decreases with increase in temperature exhibiting the semiconducting behaviour. The activation energy in paramagnetic region(E_p) is more than that of ferrimagnetic (E_f) region. The dielectric constant (ε), dielectric loss (ε'') and dielectric loss tangent (tan δ) decreases exponentially with increase in frequency. The dielectric constant (ε), dielectric loss (ε'') and dielectric loss tangent (tan δ) decreases with increase in zirconium content x.

V. REFERENCES

[1]. B. Viswanathan "Ferrite Materials Science and Technology", edited by B. Viswanathan, V. R. K.Murthy, Narosa Publishing House, India (1990).

[2]. M. Sugomoto, J. Am. Ceram. Soc. 82 (1999) 269.

[3]. S. Chikazumi, Physics of Ferromagnetism, 1997, Oxford University Press, New York.

[4]. J. Smith, H. P. J. Wijn Ferrites, 1965, Philips Technical Library, Eindhoven-Holland.
[5]. Z. H. Zhou, J. Wang, J. M. Xue and H. S. O. Chan, J. Mater. Chem., 2001, 11, 3110.
[6]. C. Nimai Pramanik, T. Fujii, M. Nakanishi, T. Jun, J. Mater. Chem., 2004, 14, 3328.
[7]. D. Carta, M. F. Casula, A. Falqui, D. Loche, G. Mountjoy, C. Sangregorio, A. Corrias, J. Phys. Chem. C, 2009, 113, 8606.
[8]. V. Sepelak, I. Bergmann, A. Feldhoff, P. Heitjans, F. Krumeioch, D. Menzel, F. Litterst, S. J. Campbell, K. D. Becker, J. Phys. Chem. C, 2007, 111, 5026.
[9]. S.Choi, M.H.Chung, Seminar. Integrat. Med. 1 (2003) 53.
[10]. D.Chiba, M.Sawicki, Y.Nishitani, Y.Nakatani, F.Matsukura and H.Ohno, Nature, 2008, 455, 515-518.
[11]. R.C.Che, L.M.Peng, X.F.Duan, Q.Chen and X.L.Liang, Adv. Mater., 2004, 16, 401-405.
[12]. Z.Li, L.Wei, M.Y.Gao and H.Lei, Adv. Mater., 2005, 17, 1001-1005.
[13]. Scientific and Clinical Application of Magnetic Carriers by U.Hafeli, W.Schutt, J.Teller, M.Zborowski, Plenum, New York (1997).
[14]. S.Chikazumi, S.Taketomi, M.Ukita, M.Mizukami, H.Miyajima, M.Setogawa, Y.Kurihara, J. Magn. Magn. Mater, 1987, 3, 907-914.
[15]. Y.W.Jun, Y.M.Huh, J.S.Choi, J.H.Lee, H.T.Song, S.Kim, S.Yoon, K.S.Kim, J.Shin, S.Cheon, J.Am. Chem. Soc., 2005, 127, 5732-5733.
[16]. D.S.Mathew, R.S.Juang, Chemical Engineering Journal 129 (2007) 51-65.
[17]. E.S.Murdock, R.F.Simmons, R.Davidson, IEEE Trans. Magn. 5(2) (1992) 3078-3083.
[18]. S.N.Okuno, S.Hashimoto, K.Inomata, J. Appl. Phys. 71 (1992) 5926-5929.
[19]. S.Gyergyek, D.Makovec, A.Kodre, I,Arcon, M.Jagodic, M.Drofenik, J. Nanopart. Res. (2010) 12:1263-1273.
[20]. M.R.Barati, J. Sol-Gel Sci. Technol. (2009) 52:171–178

International Journal of Scientific Research in Science and Technology
Volume 11 | Issue 13| Print ISSN: 2395-6011 | Online ISSN: 2395-602X (www.ijsrst.com)

Preparation of Zinc Ferrite by Using Sol-Gel Auto Combustion Method

Miss Sneha Yuvraj Pawar
Department of Physics, M.S.P. Mandal's Yashwantrao Chavan college, Ambajogai, Dist. Beed, Maharashtra, India

ABSTRACT

Zinc ferrites nanoparticles were synthesized by sol-gel auto combustion method. Nanoparticles of zinc ferrites were prepared by sol-gel method by using citric acid as a fuel.Material used for synthesis of zinc ferrite nanoparticles were zinc nitrate($Zn(NO_3)_2.6H_2O$) and ferric nitrate($Fe(NO_3)_3 9H_2O$) mainly. Zinc ferrites are synthesize by various methods that are hydro thermal method,co. precipitation method, ball milling method,Spray drawing method, micro emulsion method and microwave method but Sol-gel auto combustion method gives high puritynanoparticles with better homogeneity.

Keywords: Zinc ferrite, Sol-gel auto combustion method.

I. INTRODUCTION

The term "ferrites" derived from the Latin word for iron has different meanings for different scientists. To metallurgists, ferrite means pure iron. To geologists, ferrites are a group of minerals based on iron oxide. To an electrical engineer, ferrites are also a group of materials based on iron oxide, which have particular useful properties: magnetic properties and dielectric properties[1].

Ferrite is a general term used for any ferrimagnetic ceramic material. Ferrites are a very well-established group of magnetic materials. Various types of ferrites are commercially important. Ferrite is categorized as electro-ceramics with ferrimagnetic properties. Each one has a unique crystal structure, magnetic, electric and dielectric properties [2]. Ferrites are the ceramic compounds comprising of Metal oxides and Iron oxides. The chemical formula for Ferrites is $MO\text{-}Fe_2O_3$. Ferrites are the ferrimagnetic oxides with combined electrical and magnetic properties, which are useful in many applications such as antenna rod, transformer core, memory chips, sensors, as catalyst, microwave devices like circulators, phase shifters, gyrators etc. Apart from their excellent electrical and magnetic properties they have another advantage like chemical stability, easy preparation, low cost etc. They exhibit high electrical resistivity, low eddy current and dielectric losses, high saturation magnetization, high Curie temperature etc. These properties of ferrites are sensitive to method of preparation, cation distribution, type and nature of dopants.

Ferrite consists of iron oxide and metal oxides in varying proportions. On the basis of crystal structure ferrites are grouped into three main classes namely spinel ferrite, garnet and hexa ferrite. Spinel ferrites have the formula MFe_2O_4(where, M can be divalent metal ions such as Ni, Cu, Li etc) and have cubic spinel structure. Garnets has the 21/65 formula $R^{3+} Fe_5O_{12}$ (where, R^{3+} is Yttrium or Rare earth ions like La, Gd, Dy, Pr etc) and

have cubic structure[3]. Hexagonal ferrites have the formula $MeFe_{12}O_{19}$ (where, Me = Ba, Sr, Pb etc) and have hexagonal structure.

In the family of ferrites, spinel ferrites are the important class of magnetic material with number of properties and applications[4]. They have been widely studied in bulk, thin film and nano size form by number of researchers with a view to understand their electrical and magnetic behaviour and size effect. In the recent years, many efforts are in progress to understand the magnetic properties of nanocrystalline spinel ferrites. Nanocrystalline ferrite exhibits excellent and superior properties as compared to their bulk counter parts[5].$ZnFe_2O_4$ nanoparticles are synthesized by many techniques of synthesis such as sol-gel, hydrothermal, combustion, co-precipitation, thermal decomposition and micro-emulsion.[8]Among these synthesis technique sol-gel is easy and gives high purity nanoparticles with better homogeneity.

II. METHOD AND MATERIAL

Sol-gel Method

In this method, the formation of a gel provides a high degree of homogeneity and reduces the need for atomic diffusion during the solid state calcinations. A solution of the appropriate precursors is formed first, followed by conversion into a homogeneous oxide (gel) after hydrolysis and condensation. Drying and sub-sequent calcination of the gel yields an oxide product. It involves the evolution of inorganic networks through. the formation of a colloidal suspension (sol) and gelation of the sol to form a network in a continuous liquid phase (gel). Sol-gel method is performed in the liquid phase. This method is useful for self assembly process for fabricating nanoparticles and three-dimensional materials such as aerogels. A sol is a type of colloid in which a dispersed solid phase is mixed in a homogeneous liquid medium. Sol-gel process involvesevolution of network. through the formation of colloidal suspension (sol) and gelation of the sol to form a network in a continuous liquid phase (gel). [6]

Steps of Sol gel method: Hydrolysis and polycondensation, gelation, aging, drying, densification, and crystallization.

Important Features of Sol-Gel Methods

1. Better homogeneity.
2. High purity.
3. Low processing temperature.
4. Uniform phase distribution.
5. Ultrafine size
6. Better morphological control.
7. Better yield of the product.
8. Low cost of the raw material.
9. Requires less time.

Materials

The raw materials used for sol-gel auto combustion synthesis of $ZnFe_2O_4$system nanoparticles were zinc nitrate ($Zn(NO_3)_2.6H_2O$), ferric nitrate ($Fe(NO_3)_3.9H_2O$), citric acid ($C_6H_8O_7$)as a fuel,Ammonia (NH_3) for maintaining pH, distilled water.

III.RESULT AND DISCUSSION

Preparation of Zinc ferrite nanoparticles:

Synthesis

$ZnFe_2O_4$ nanoparticles were synthesized by sol-gel auto combustion method using citric acid as a fuel. The proportions of metal nitrates to citric acid ratio as 1:3 were taken into separate glass beakers. These were stirred for 15-20 minutes to dissolve completely into distilled water. After complete dissolution they were mixed together. Ammonia was added drop- wise into the solution to adjust pH value to about 7 and stabilize the solution. Then the neutralized solution was constantly magnetically stirred and heated at 80-90 °C for 6 h on a hot plate. On the formation of sol-gel, very viscous gel the temperature was further raised up to 120 °C so that the ignition of the dried gel started and finally powder was obtained. The as prepared loose zinc ferrite powder was grinded for 30 minutes and sintered at 900 °C for 2 h in furnace. The nanocrystalline samples of zinc ferrite were prepared using sol-gel auto combustion method.

The detailed synthesis procedure is shown in figure1.[7]

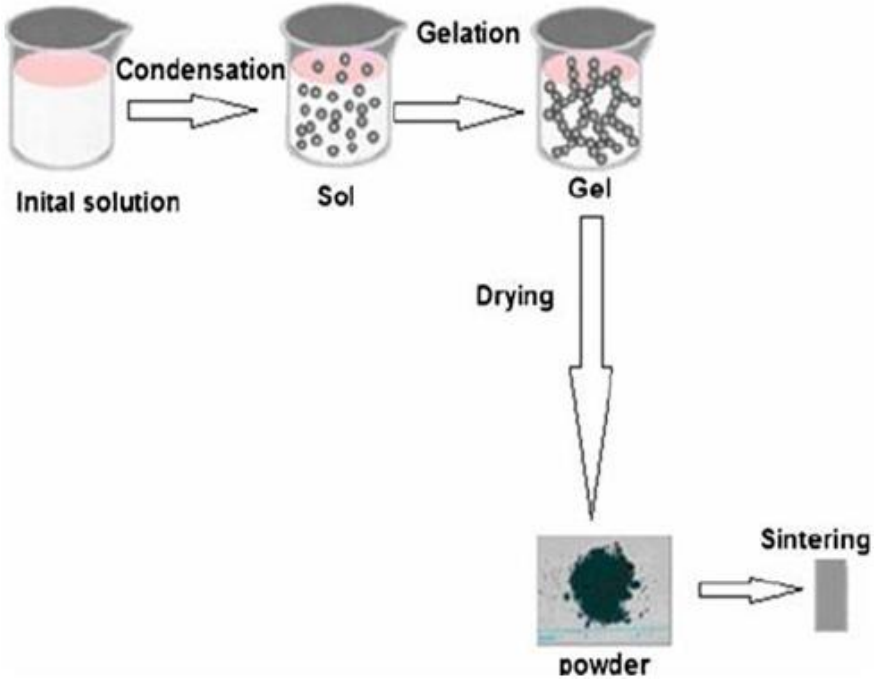

Fig.1.Synthesis of zinc ferrite ($ZnFe_2O_4$)by sol-gel auto combustionmethod

IV.CONCLUSION

Zinc ferrite nanoparticles were synthesized by using citric acid as a fuel.

The sample of $ZnFe_2O_4$ ferrite in nano-size form was successfully prepared by sol-gel auto-combustion method.

V. REFERENCES

[1]. Sharma, P.U., Investigations on the effect of thermal history, particle size and SHI irradiation on some physical properties of Y3+-substituted YIG. 2009, Saurashtra University.

[2]. Ferrites, M.M., V.J. Pissurlekar, J.S. Budkuley, and F. Ponda, Project Report of the Minor Research Project 2012-14.

[3]. SHELKE, D.S.B., effect of iso and aliovalent substituents on the properties of spinel ferrite. 2021: BecomeShakespeare.com.

[4]. Kotnala, R. and J. Shah, Ferrite materials: nano to spintronics regime, in Handbook of magnetic materials. 2015, Elsevier. p. 291-379.

[5]. Ali, R., The Impacts of Various Metal Cations on Structural, Dielectric and Magnetic Properties of Nanocrystalline Nickel and Magnesium Ferrites, 2017.

[6]. Nakamura, H. and Y. Matsui, Silica gel nanotubes obtained by the sol- gel method. Journal of the American Chemical Society, 1995. 117(9): p. 2651-2652.

[7]. C. Aydın Omar A. Al-Hartomy A. A. Al-GhamdiF. Al-Hazmi I. S. Yahia F. El-Tantawy.F. VakuphanogluReceived: 2 April 2012 (Accepted: 11 June 2012Spri inger Science e-Buminess Media, LLC 2012.

[8]. D D Andhare et al Structural and Chemical Properties of ZnFe2O4Nanoparticles Synthesised by Chemical Co-Precipitation Technique 2020 .

[9]. Santosh Kalunge, et al Investigation on Synthesis, Structural and Electrical properties of Zinc Ferrite on Gamma Irradiation NANOMAT-2020 .

International Journal of Scientific Research in Science and Technology
Volume 11 | Issue 13| Print ISSN: 2395-6011 | Online ISSN: 2395-602X (www.ijsrst.com)

Structural and Elastic Properties of Cadmium Substituted Ni - Cu Spinel Ferrites

R. B. Kavade*[1], R. G. Vidhate[2], J.M. Bhandari[3], V. B. Kawade[4], S. J. Shukla[5]

*[1]Bhagawan Mahavidyalaya, Ashti, Dist. Beed, Maharashtra, India

[2]Anandrao Dhonde Mahavidyalaya, Kada, Beed, Maharashtra, India

[3]Gandhi College, Kada, Dist. Beed, Maharashtra, India

[4]Late Laximibai Deashmukh Mahila Mahavidyalaya, Parali(v), Dist. Beed, Maharashtra, India

[5]P. G. and Research Center, Deogiri College, Chhatrapati Sambhajinagar, Maharashtra, India

ABSTRACT

The cadmium substituted samples of Ni-Cu mixed ferrites having the generic formula $Ni_{0.5}Cu_{0.5-x}Cd_xFe_2O_4$ (x = 0.0, 0.3, 0.5) have been synthesized by standard ceramic technique using AR grade (NiO, Fe_2O_3, CuO, CdO) oxides. The analysis of X-ray diffraction and Infrared spectroscopic data confirms the formation of single phase cubic spinel structure of ferrite phase. The lattice constant was found to increase with increase in cadmium content and was due to the large ionic radius of cadmium. The structural parameters such as lattice constant, X-ray density, cation distribution, ionic site radii, oxygen positional parameter, theoretical lattice constant, bond length, jump length of tetrahedral (A) site as well as octahedral [B] site, tetrahedral edge length, shared and unshared octahedral edge length was estimated. The estimated cation distribution of ferrite was verified by comparing the observed and theoretical lattice parameters. The elastic parameter of ferrites such as young's modulus, rigidity modulus and bulk modulus was estimated by using IR technique.

Keywords:, Elastic properties, Structural Properties, X-ray diffraction.

I. INTRODUCTION

The mixed Ni-Cu ferrites are technologically useful materials as it possess high saturation magnetization, high resistivity, high stability and low loss energy over a wide range of frequency [1, 2]. In fact, cadmium substituted Ni-Cu mixed ferrite are the subject of intensive investigations in the field of fundamental and applied research due to their wide applications in electronic industry. The physical properties of spinel ferrites depend on the type, amount of dopant and distribution of cations over the tetrahedral (A) and octahedral [B] sites [3, 4]. In electronic materials the elastic module are of much importance because they shows the nature of binding force in polycrystalline materials and also helps to understand the thermal properties of these materials.

II. EXPERIMENTAL

The ferrite with composition $Ni_{0.5}Cu_{0.5-x}Cd_xFe_2O_4$ *(x = 0.0, 0.3, 0.5)* were synthesized by standard double sintering ceramic method.[5,6,7] Grinding using agate mortar (4 h) was carried out for each sample. The

samples were pre-sintered at 1293 K for 12 h. The sintered powder is again reground and sintered at 1353 K for 14 h. Then the powder of samples compressed into pellets of 10 mm diameter using a hydraulic press with pressure 6 ton/inch^2 and sintered at 1273K for 12 h. The samples were furnace cooled to room temperature. The prepared samples were characterized by X-ray powder diffractometer in the 2θ range 20°-80°at room temperature to confirm single phase spinel structure. The infrared spectra of a prepared sample were recorded at room temperature within the range 200 cm^{-1} to 800 cm^{-1} on the infrared spectrometer (Model 783, Perkin-Elmer)

III.RESULTS AND DISCUSSION

The peaks appeared in the XRD pattern (fig.1) of the ferrites are identified. However, the non appearance of extra peaks reveals the formation of single phase cubic spinel structure of ferrite. The increase of observed lattice parameter 'a' and X-ray density 'ρ' with increase of the cadmium content was due to the difference in ionic radii and atomic weight of the component ions in the ferrite system [8]. The distribution of cations in the tetrahedral (A) and octahedral [B] sites can be expressed as [9], $(Cd_xCu_yFe_{1-x-y})^A[Ni_{0.5}Cu_{0.5-x-y}Fe_{1+x+y}]^BO_4^{-2}$ The theoretical lattice parameter of ferrite samples estimated using the relation [10] were listed in table 1. The good agreement between experimentally estimated and theoretical lattice parameters confirms the assumed cation distribution of the ferrites.

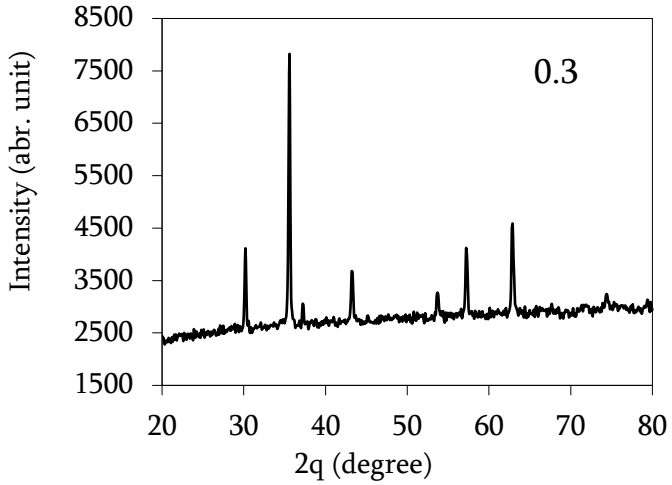

Figure 1: Typical XRD Pattern of $Ni_{1-x}Cu_xFe_2O_4$ for (x=0.3)

The mean ionic radius of the tetrahedral site 'r_A' found to be increase with Cd ion content where as mean ionic radius of the octahedral site 'r_B' decreases with cadmium content. The increase of ionic radius 'r_A' of tetrahedral site with Cd ion content was due to the larger ionic radii of Cd ions. But the values of oxygen positional parameter are almost same in the ferrite systems.

The band positions of IR spectrum are listed in table 1. The shift of band position υ_1 towards lower wavelength side was due to the substituted Cd^{2+} ion, preferably it occupies the tetrahedral (A) site [11]. The octahedral [B] site was occupied by Ni^{2+}ions, where Fe^{3+}, Cu^{2+} ions occupy both tetrahedral and octahedral sites. The force constant for tetrahedral 'k_t' and octahedral 'k_o' sites, longitudinal 'V_l' and transverse 'V_s' elastic wave velocities, elastic moduli for ferrite samples were estimated using the relations[9] and are listed in table 1. The decreases of octahedral force constant with increase of the Cd ion content, was due to the substitution of Cd ion content, which decreases the amount of Cu^{2+} and increases the amount of Fe ions in the octahedral [B] sites. The

increase in rigidity modulus 'G', bulk modulus 'B' and young's modulus 'E' with increase of the cadmium content, may be due to the strengthening of inter atomic bonding between various atoms continuously. The values of poisson's ratio are found to be 0.35 for all the ferrites. The present estimated values of poisson's ratios are lying in the range of -1 to 0.5; which reveals the theory of isotropic elasticity.

TABLE I: Structural and elastic parameters of ferrites system $Ni_{0.5}Cu_{0.5-x}Cd_xFe_2O_4$ *(x = 0.0, 0.3, 0.5)*.

Parameters	x = 0.0	x = 0.3	x = 0.5
a (Å)	8.367	8.424	8.489
ρ x 10^3 (kg/m^3)	5.37	5.480	5.569
d x 10^3 (kg/m^3)	4.003	3.940	3.932
r_A(Å)	0.67	0.731	0.792
r_B(Å)	0.687	0.684	0.678
L_A (Å)	3.623	3.648	3.676
L_B (Å)	2.953	2.979	3.002
R_A(Å)	1.898	1.912	1.926
R_B(Å)	1.990	2.007	2.020
a_{th}(Å)	8.417	8.497	8.577
u	0.386	0.390	0.393
υ_1 x 102 (m^{-1})	590	585	581
υ_2 x 102 (m^{-1})	389	397	395
k_t (N/m)	1.482	1.751	2.019
k_o x 10^2 (N/m)	0.988	0.966	0.944
V_l (m/s)	5250	5421	5592
V_s (m/s)	3031	3130	3228
G x10^9 kg $m^{-1}s^{-2}$	49.33	53.65	57.99
B x10^9 kg $m^{-1}s^{-2}$	148	162	175
E x10^9 kg $m^{-1}s^{-2}$	133.2	144.9	156.5
σ	0.35	0.35	0.35

IV. CONCLUSIONS

The X ray diffraction pattern revels the formation of cubic spinel structure of ferrite phase. The lattice parameter and X-ray density are found to increase with cadmium content. The estimated cation distribution of ferrites has been verified by comparing the observed and theoretical lattice parameters. The structural parameters estimated through X-ray diffraction were affected with cadmium content. The elastic parameters are found to increases with increase of cadmium content and was explained in terms of inter atomic bonding between various atoms and is being strengthened continuously. The estimated elastic parameters of the present results are in good agreement with the earlier reports.

V. REFERENCES

[1]. B. K. Bammannavar, L. R. Naik and R. B. Pujar, (2008) Mater. Sci. an Ind. J. 4(3), 160.
[2]. A. M. Abdeen, (1998) J. Magn. Magn. Mater. 185, 199.
[3]. O. H. Kwon, Y. Fukushima, M. Sugimoto and N Hiratsuka, (1997) J Phys. IV, 165.
[4]. A. Menakshisundaram, N. Gunasekaran and V. Srinivasan, (1982) Phys. Stat. Solidi. (a) 69, K15.
[5]. C.N. Rao, (1994) "Chemical approaches to the synthesis of inorganic materials", Wiley, New York.
[6]. Zhiyong Xu, Zhong Yu, Ke Sun, Lezhong Li, Haining Ji, Zhongwen Lan, (2009) J. Magn. Magn. Mater. 321.
[7]. S.A. Mazen, S.F. Mansour, T.A. Elmosalami, H. M. Zaki, (2009) J. Alloys. Compd. 472 307.
[8]. P. B. Belavi, G. N. Chavan, L. R. Naik, R. Somasshekar and R. K. Kotnala, (2012).Mater. Chem. Phys. 132, 138
[9]. K. B. Modi, M. K. Rangolia, M. C. Chhantbar and H. H. Joshi, (2006). J. Mater. Sci. 41, 7308
[10]. R. L. Dhiman, S. P. Taneja and V. R. Reddy, (2008). Adv. Condens. Mat. Phys. 703479, 7
[11]. S. A. Patil, V. C. Mahajan, A. K. Gatge and S. D. Lotake, (1998) Mater. Chem. Phys. 57, 86.

International Journal of Scientific Research in Science and Technology
Volume 11 | Issue 13| Print ISSN: 2395-6011 | Online ISSN: 2395-602X (www.ijsrst.com)

Signal Processing of Microwave Synthetic Aperture Radar Dataset for Parameter Extraction

Mosin Ratan Tamboli, Prashant T Sonwane
Sant Ramdas College Ghansawangi, JES Research Center, Maharashtra, India

ABSTRACT

Synthetic Aperture Radar (SAR) is a powerful remote sensing technique that can generate high-resolution images of the Earth's surface. SAR systems are particularly well-suited for applications in which high-resolution imagery is required, such as vegetation monitoring, land cover classification, and sea ice monitoring. The signal processing of SAR data involves several key steps, including pre-processing, image formation, and parameter extraction.

Keyword: SAR, Image formation, Parameter extraction, Pre-processing, Backscattering coefficient estimation, Land cover classification.

I. INTRODUCTION

to Microwave Synthetic Aperture Radar (SAR) is a powerful remote sensing technology that can generate high-resolution images of the Earth's surface [1]. The signal processing of SAR data involves several key steps, including pre-processing, image formation, and parameter extraction [2].Pre-processing aims to calibrate the data, remove noise, and correct for radiometric and geometric distortions [3, 4].Image formation synthesizes the radar echoes to create a high-resolution image of the scene [5], while parameter extraction focuses on extracting information about the scene from the SAR image, such as the backscattering coefficient, which is a measure of the radar signal's reflection by the surface [6]. SAR data has a wide range of applications, including vegetation monitoring [7], land cover classification [8], sea ice monitoring [9], flood mapping [10], and oil spill detection [11].Despite its advantages, SAR signal processing faces several challenges, such as the complex nature of the radar signal [12], the presence of noise [13], and the effects of the atmosphere [14].Future research in SAR signal processing is focused on developing new techniques to improve image resolution, extract new information, and enhance data accessibility [15].

II. IMAGE FORMATION

Image formation is the step in the SAR signal processing chain that creates the SAR image [2, 3]. There are a variety of techniques for image formation, but the most common technique is range-Doppler processing [8,5]. Range-Doppler processing uses the Doppler frequency shift of the radar echoes to determine the range and cross-range of the scatterers [6].

Range-Doppler processing:

Range-Doppler processing is a technique for image formation that uses the Doppler frequency shift of the radar echoes to determine the range and cross-range of the scatterers [5]. The Doppler frequency shift is the difference in frequency between the transmitted radar signal and the reflected radar signal [2]. The range and cross-range of the scatterers can be determined by analysing the Doppler frequency shift of the radar echoes [3, 2].

Other Image Formation Techniques:

In addition to range-Doppler processing, there are a variety of other techniques for image formation, such as chirp scaling algorithms (CSA), back projection (BP), and wavenumber-domain algorithms (WDA) [7].

III.APPLICATION

Vegetation Monitoring:

SAR data can be used to monitor vegetation health, assess forest biomass, and track deforestation [8, 27]. The backscattering coefficient of vegetation is sensitive to its moisture content, which can be used to assess drought stress and irrigation needs [28]. SAR data can also be used to map the distribution of different plant species [29].

Land Cover Classification:

SAR data can be used to classify land cover types, such as forests, grasslands, urban areas, and water bodies [2, 5]. The backscattering coefficient of different land cover types varies, which allows them to be distinguished from each other [18]. SAR data can be used to create detailed land cover maps that can be used for a variety of applications, such as urban planning and environmental monitoring [9].

Sea Ice Monitoring:

SAR data can be used to monitor sea ice extent, thickness, and type [9, 20]. Sea ice is a key component of the Earth's climate system, and its monitoring is important for understanding climate change [21]. SAR data can also be used to detect and track sea ice hazards, such as icebergs and ice floes [22].

Flood Mapping:

SAR data can be used to map flood inundation extents [10, 23]. The backscattering coefficient of flooded areas is very different from the backscattering coefficient of dry land, which makes it easy to identify flooded areas in SAR images [24]. SAR data can be used to create flood maps that can be used for emergency response and flood mitigation planning [25].

IV.CHALLENGES

Challenge 1:

The Complex Nature of the Radar Signal:

The radar signal is a complex-valued signal, meaning it has both a magnitude and a phase [26]. The phase of the radar signal is particularly sensitive to changes in the environment, such as the presence of scatterers [12]. This sensitivity makes it difficult to extract information from the radar signal, as the phase can be corrupted by noise and atmospheric effects [2].

Challenge 2:

The Presence of Noise:

SAR data is often contaminated by noise, which can come from various sources, such as the thermal noise of the radar receiver and the clutter from the ground [27]. Noise can make it difficult to identify and track targets in SAR images [3].

Challenge 3:

The Effects of the Atmosphere:

The atmosphere can significantly impact the SAR signal [18]. The atmosphere can attenuate the radar signal, making it challenging to detect targets that are far away [2]. The atmosphere can also cause the radar signal to scatter, making it difficult to accurately image the ground [12].

V. FUTURE DIRECTION

Future Direction 1:

Improving the Resolution of SAR Images:

One of the key challenges in SAR signal processing is improving the resolution of SAR images. There are a number of different approaches being investigated for improving SAR image resolution, including:

- Developing new image formation algorithms that can exploit the full potential of the SAR data [28].
- Using machine learning techniques to identify and remove noise from SAR images [2].
- Developing new techniques for compensating for atmospheric effects [12].

Future Direction 2:

Extracting New Information from SAR Data:

SAR data contains a wealth of information about the Earth's surface. Researchers are developing new techniques for extracting this information, including:

- Developing algorithms for classifying land cover types from SAR images [18].
- Extracting information about vegetation health from SAR images [2].
- Developing algorithms for detecting and tracking sea ice from SAR images [12].

Future Direction 3:

Making SAR Data More Accessible to Users:

SAR data is becoming increasingly available, but it can still be difficult to access and use. Researchers are developing new techniques for making SAR data more accessible to users, including:

- Developing cloud-based platforms for accessing and processing SAR data [29].
- Developing open-source software tools for SAR data processing [2].
- Developing educational resources for teaching users how to use SAR data [12].

VI. CONCLUSIONS

The signal processing of microwave SAR datasets for parameter extraction is a complex and challenging task. However, significant progress has been made in recent years, and SAR data is now used for a wide variety of

applications. Future research is focused on improving the resolution of SAR images, extracting new information from SAR data, and making SAR data more accessible to users.

VII.REFERENCES

[1]. Oliver, Christopher, and S. Quegan. Understanding Synthetic Aperture Radar Images. SciTech Publishers, 2004.

[2]. Cumming, Ian G., and Francesco G. Levrini. Principles of Synthetic Aperture Radar Imaging. SciTech Publishers, 2015.

[3]. Moreira, Alberto, et al. SAR systems and applications. Springer, 2015, page-249.

[4]. Ulaby, Fawwaz T., et al. Microwave Radar and Radiometric Remote Sensing. Artech House, 1982.

[5]. Souyris, Jean-Baptiste, et al. Signal processing for synthetic aperture radar. ISTE, 2013.

[6]. Elachi, Claude, ed. Introduction to Synthetic Aperture Radar. IEEE Aerospace and Electronic Systems Society, 1988.

[7]. Lang, Robert T. Radar Remote Sensing of Vegetation. Artech House, 1983.

[8]. Ulaby, Fawwaz T., et al. Handbook of Microwave Remote Sensing, Volume I: Instruments and Techniques. Artech House, 1982.

[9]. Partan, Yousef, et al. Synthetic Aperture Radar for Sea Ice Monitoring. Springer, 2016.

[10]. Wang, Yao, ed. SAR Remote Sensing of Floods. CRC Press, 2018.

[11]. Fingas, Melvin. Oil Spill Science and Technology. Gulf Professional Publishing, 2011.

[12]. Moreira, Alberto. "Statistical processing of synthetic aperture radar data." IEEE Transactions on Aerospace and Electronic Systems 32.1 (1996): 21-32.

[13]. Di Martino, Vito, et al. "A statistical approach to SAR image despeckling based on the generalized Gaussian distribution." IEEE Transactions on Geoscience and Remote Sensing 47.4 (2009): 976-982.

[14]. Chang, David B., et al. "Application of the dual-frequency method to the retrieval of soil moisture over vegetated land from polarimetric SAR imagery." Remote Sensing of Environment 53.1 (1995): 33-48.

[15]. Prati, Michele. "Current trends in SAR image processing." IEEE Signal Processing Magazine 17.1 (2000): 10-21.

[16]. Baghdadi, Nariman, et al. "Monitoring soil moisture using sentinel-1 and its sensitivity to soil texture and vegetation cover." Remote Sensing of Environment 164 (2015): 67-79.

[17]. Imhoff, Marc L., et al. "Remote sensing for land-cover change mapping." In Handbook of remote sensing applications, pp. 115-158. CRC Press, 2007.

[18]. Ulaby, Fawwaz T., et al. Handbook of Microwave Remote Sensing, Volume II: Radar Applications. Artech House, 1982.

[19]. Lu, David, et al. "Global surface water mapping with Sentinel-1 SAR imagery." Remote Sensing of Environment 204 (2018): 294-315.

[20]. Cavalieri, Donald J., et al. "Sea ice thickness retrieval from satellite altimetry over the Arctic Ocean." Geophysical Research Letters 25.17 (1998): 3355-3358.

[21]. Kwok, Ray, et al. "State of the frozen Arctic Sea cover from satellite observations." Arctic, Antarctic & Alpine Research 45.1 (2013): 6-16.

[22]. Dierking, W., et al. "Sea ice drift from ERS-1 SAR imagery." Journal of Geophysical Research: Oceans 101.C5 (1996): 10501-10510.

[23]. Pulvirenti, Lorenzo, et al. "Flood mapping using synthetic aperture radar (SAR): A review." Remote Sensing 6.6 (2014): 2764-2821.
[24]. Schumann, G., et al. "Improved flood detection in urban areas using Sentinel-1 SAR." IEEE Geoscience and Remote Sensing Letters 8.9 (2011): 1320-1324.
[25]. Martinis, Stefan, et al. "Flood extent mapping and damage assessment using SAR and optical
[26]. Souyris, Jean-Baptiste, et al. Signal processing for synthetic aperture radar. ISTE, 2013, p. 2.
[27]. Ulaby, Fawwaz T., et al. Handbook of Microwave Remote Sensing, Volume I: Instruments and Techniques. Artech House, 1982, p. 661.
[28]. Souyris, Jean-Baptiste, et al. Signal processing for synthetic aperture radar. ISTE, 2013, p. 417.
[29]. Souyris, Jean-Baptiste, et al. Signal processing for synthetic aperture radar. ISTE, 2013, p. 587.

International Journal of Scientific Research in Science and Technology
Volume 11 | Issue 13| Print ISSN: 2395-6011 | Online ISSN: 2395-602X (www.ijsrst.com)

Nanostructured Organic Polyaniline Thin Film Prepared By Polymerisation Technique

Dr. Sandip Mahajan[1], Dr. Sanjay Kamble[2], Dr. Rajkumar Lokhande[3], Dr. R.R. Bhosale[4], Bharat Surung[5], Dr. Vishal Awasarmol[6]

[1]Assistant Professor, Department of Physics, Shikshan Maharshri Dnyandeo Mohekar College, Kalamb, Dharashiv, Maharashtra, India

[2]Professor, Department of Physics, Shikshan Maharshri Dnyandeo Mohekar College, Kalamb, Dharashiv, Maharashtra, India

[3]Assistant Professor, Department of Physics, Shirish Madhukarrao Chaudhari College, Jalgaon, Maharashtra, India

[4]Assistant Professor, Department of Physics, Arts, Commerce & Science College Kille-Dharur, Beed, Maharashtra, India

[5]Assistant Professor, Department of Physics, Lal Bahadur Shastri Senior College, Partur, Maharashtra, India

[6]Assistant Professor, Department of Physics, Swami Vivekanand Senior College, Mantha, Maharashtra, India

ABSTRACT

Nanostructured Organic Polyaniline (PANI) thin film, doped with an inorganic acid (HCL), on glass substrate was directly synthesized by using the in situ polymerization technique. HCL doped PANI thin film is sense LPG gas at room temperature. The optical and electrical properties of were studied by UV-Vis spectrophotometer and I-V Characteristics. The mechanism of formation of polyaniline on glass substrate was confirmed by UV spectroscopy.

Keywords: PANI, Polymerization, Optical and electrical.

I. INTRODUCTION

Conducting polymers have greater advantage as they are simple to synthesize, with their chemical structure tailored to alter their physical properties, such as their band gap. They exhibit an extensive range of electrical conductivity. Further to their ease of synthesis and with lower cost, they are known to have low poisoning effects. They possess a large variety and versatility in their chemical structure and are therefore extensively used in devices for the detection of environmentally hazardous chemicals [1]. The most commonly studied classes of conducting polymer were: Polyacetylene, polythiophene, polypyrole, polyaniline and derivates, being investigated as conducting matrices for electro catalytic applications. Among them, polyaniline (PANI) is one of the most studied materials because of its high conductivity upon doping with acids, well behaved electrochemistry and easy preparation under reproducible conditions by electro - polymerization and chemical oxidation of aniline, chemical and electrical stability and good environmental stability [2].Electrically conducting polymers described as a new class of 'synthetic metals' reached a high interest in the last years.

Conducting polymers are suitable as electrode materials for high performance solar cells [3]. Conducting polymers had been the topic of the large number of investigations since past decades because of their unique properties such as mechanical strength, electrical conductivity, corrosion, stability and possibility of both oxidative and electrochemical synthesis. Of these polymers PANI has significant application in various areas like solar energy conversion, rechargeable batteries, electro chromic displays, electrochemical sensors, capacitors and active corrosion protector [4].Due to simplicity of its synthesis, processing environmental stability and low synthesis cost, so polyaniline is probably the most important industrial conducting polymer today . Conducting polymers usually have a good corrosion stability when in contact with solution or/and in the dry [5].

II. EXPERIMENTAL WORK

Optically pure glass plates were boiled in chromic acid and kept in it for 24 hrs, washed with laboline and dipped in distilled water and dried to remove contamination. The contaminated substrate surface provides nucleation sites facilitating growth, which results in non-uniform film growth. Polyaniline was prepared by chemical oxidation of 0.2 M of aniline sulfate with 0.25 M ammonium peroxydisulfate (APS) and 1 M concentration of HCl as dopant. Then 0.25 M APS solution was prepared in aqueous medium. Thereafter, 20 ml of APS was slowly added (drop wise) in 20 ml of as-prepared aniline solution with constant stirring at room temperature. Pre-cleaned glass substrate was inserted vertically in the mixed reactants for deposition of polyaniline film [6].

III.RESULTS AND DISCUSSIONS

Optical absorbance of the film is recorded on Perkin Elmer, Lambda-25 UV-VIS spectrophotometer in 300-1100 nm wavelength range. It was found that on passing electromagnetic radiation in the UV and visible region, a portion of radiation is normally absorbed by the film. The amount of absorption depends on the wavelength of the radiation and the structure of the material. The absorption of radiation is due to the subtraction of energy from the radiation beam when electronic orbital of lower energy are excited into orbital of higher energy i.e. an electron excitation phenomenon. UV spectra record the wavelength of an absorption maximum λ max. From the fig. absorption peak nearer to 350 nm is due to π^*-π^* transition of aniline. The higher wavelength of transition enhances the intrinsic conductivity of sample.

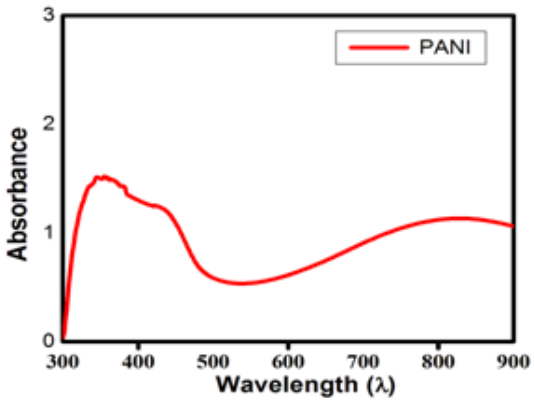

Fig 1. UV-Vis spectrum of PANI thin film.

The photo absorbing experiment was recorded by eliminating this film to100W per cm 2 light source ans data was retrieved from the computer interfaced with I-V measurement setup KEITHLEY 2400 source meter. PANI films are normally of p-type semiconductor. As during the polymerization process of aniline, acids (such as HCl) are used, which acts as dopant for PANI molecules, and usually bound with the central N atom of aniline (monomer) molecule, like H+ N Cl.

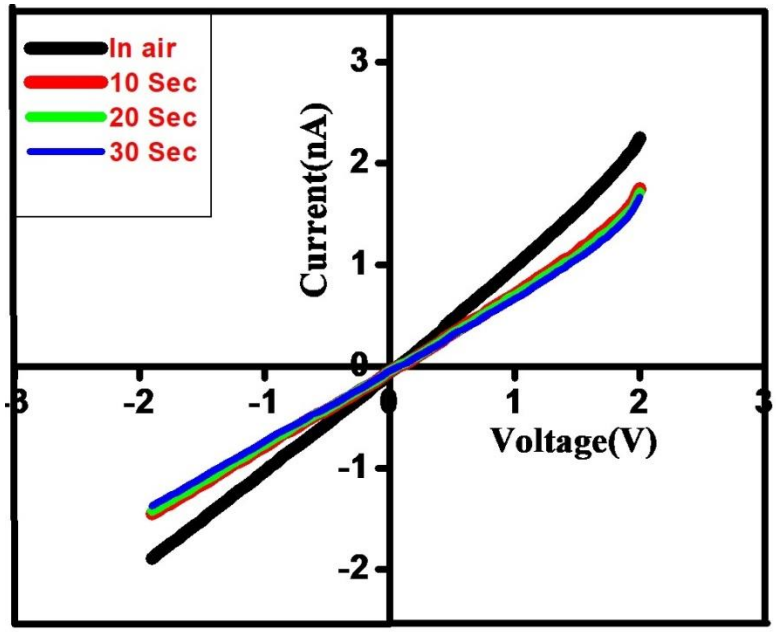

Fig.2 Forward bias I-V characteristics of HCl doped Polyaniline thin film in air and LPG atmosphere.

IV. CONCLUSION

Nanostructured Organic HCl doped Polyaniline thin film was prepared by chemical route method at room temperature. The mechanism of formation of polyaniline on glass substrate was confirmed by UV spectroscopy. The change in electrical resistance of polyaniline film shows I-V characteristics.

V. REFERENCES

[1]. K. M. Zaidan, H. F. Hussein, R. A. Talib, A. K. Hassan, Synthesis and characterization of (Pani/n-si)solar cell. Energy Procedia 6, 85-91 (2011)10.1016/j.egypro.2011.05.010).

[2]. D. Geethalakshmi a, N. Muthukumarasamy b, R. Balasundaraprabhu c Measurement on the structural, morphological, electrical and opticalproperties of PANI-CSA nanofilms, Measurement 92 (2016) 446–452

[3]. G.A.Rimbu,I.Stamatin,C.L.Jackson,K.Scott,The morphology control of polyaniline as conducting polymer in fuel cell technology,Journal of optoelectronics and advanced materials,vol.8,No.2,April2006,p.670-674.

[4]. Clara Jeyageetha J.*, Sankaragomathi V., Bharathi M., Muthumari R and Siji Priya P, Utilization of fly ash: synthesis, spectral, thermal studies of Pani-fa matrix composites, International Journal of Recent Scientific Research,Vol. 7, Issue, 11, pp. 14466-14473, November, 2016

[5]. Gita Rani, Electrical conductivity of hybrid materials of Polyaniline (pani) with tin International Journal of Advances in Science Engineering and Technology, ISSN: 2321-9009, Vol-4, Iss-3, Spl. Issue-1 Aug.-2016,176

[6]. A. G. Patil, A. P. Maharolkar, S. L. Patankar, A G Murugkar ,International Journal of advanced Research in Basic and Applied Sciences Special issue January 2017 pp.62-69

[7]. Ravikiran B Birajadar, Deepak Upadhye, Sandip Mahajan, JC Vyas, Ramphal Sharma, Study of room temperature LPG sensing behavior of polyaniline thin film synthesized by cost effective oxidative polymerization technique, J Mater Sci: Mater Electron (2015) 26:5065–5070.

International Journal of Scientific Research in Science and Technology
Volume 11 | Issue 13| Print ISSN: 2395-6011 | Online ISSN: 2395-602X (www.ijsrst.com)

Metal-Free Organic Dyes and Nanoscale Materials for Enhanced Solar Energy Harvesting System

Mrs. Meghmala Vaijnath Ingole
Research Scholar, University of Technology, Jaipur, Rajasthan, India

ABSTRACT

The prioritisation of sustainable and renewable energy sources, such as solar energy, has gained global significance in response to the escalating energy demand and the ecological consequences associated with fossil fuels. The primary objective of this study is to investigate the synthesis, characterization, and utilisation of metal-free organic dyes and nanoscale materials in order to enhance the efficiency of solar energy conversion. [1] Organic dyes have garnered considerable interest as viable substitutes for conventional dye-sensitized solar cells (DSSCs) owing to their cost-effectiveness, adjustable optical characteristics, and compatibility with the environment. Carbon nanotubes, graphene, and semiconductor nanoparticles are examples of nanoscale materials that possess distinctive characteristics that can improve light absorption, charge transfer, and the overall performance of devices. [2] This research paper provides a thorough examination of the development, production, and analysis of innovative metal-free organic dyes, as well as their incorporation into nanoscale materials for the purpose of solar energy harvesting.

Keyword: Metal Free Organic Dyes, Nanoscale Materials, Solar Energy Harvesting, Dye-sensitized solar Cells, Material Characterisation

I. INTRODUCTION

The emergence of solar energy as a clean and renewable energy source has prompted significant research endeavours aimed at the development of photovoltaic technologies that are both efficient and cost-effective. Dye-sensitized solar cells (DSSCs) have garnered significant attention owing to their cost-effectiveness, adaptability, and potential for widespread use. Nevertheless, the utilisation of metal-based dyes in traditional dye-sensitized solar cells (DSSCs) gives rise to apprehensions over their environmental ramifications and long-term viability. Metal-free organic dyes have become increasingly popular as viable alternatives due to their numerous benefits, such as little toxicity, adjustable optoelectronic characteristics, and easy synthesis. [3] The dyes have the capability to be customised in order to effectively capture a wide spectrum of solar radiation, hence facilitating efficient light absorption. Furthermore, the integration of nanoscale elements, such as carbon nanotubes, graphene, and semiconductor nanoparticles, has the potential to augment light absorption, charge transfer, and the overall performance of the device. This study paper seeks to offer a thorough examination of the creation, analysis, and use of metal-free organic dyes and nanoscale materials for the purpose of converting solar energy. The subsequent parts will encompass the fundamental concepts of design, methodology for

synthesis, strategies for characterising materials, and the incorporation of these materials into systems for harvesting solar energy.[4]

1. Design and Synthesis of Metal-Free Organic Dyes

The development of efficient and sustainable solar energy conversion systems heavily relies on the design and synthesis of metal-free organic dyes. The dyes commonly consist of donor-□-acceptor (D-□-A) structures, in which the donor and acceptor groups are linked by a conjugated -bridge. [4] The rational formulation of these dyes entails the meticulous choice and amalgamation of various functional groups in order to attain the intended optoelectronic attributes, including the range of light absorption, charge transport properties, and alignment of energy levels with the semiconductor materials employed in solar cells.

A. Design Principles:

i. Donor-π-Acceptor (D-π-A) Structure:

The utilisation of the D--A architecture is prevalent in the development of metal-free organic dyes suitable for the conversion of solar energy. The electron-rich group, such as triphenylamine, carbazole, or Indoline, is commonly used as the donor moiety, whereas the electron-deficient group, such as cyanoacrylic acid, benzothiadiazole, or Rhodanine, is typically employed as the acceptor moiety. The -bridge is a conjugated linker that is commonly composed of thiophene, furan, or phenyl units. Its primary function is to facilitate intramolecular charge transfer (ICT) and improve light absorption.

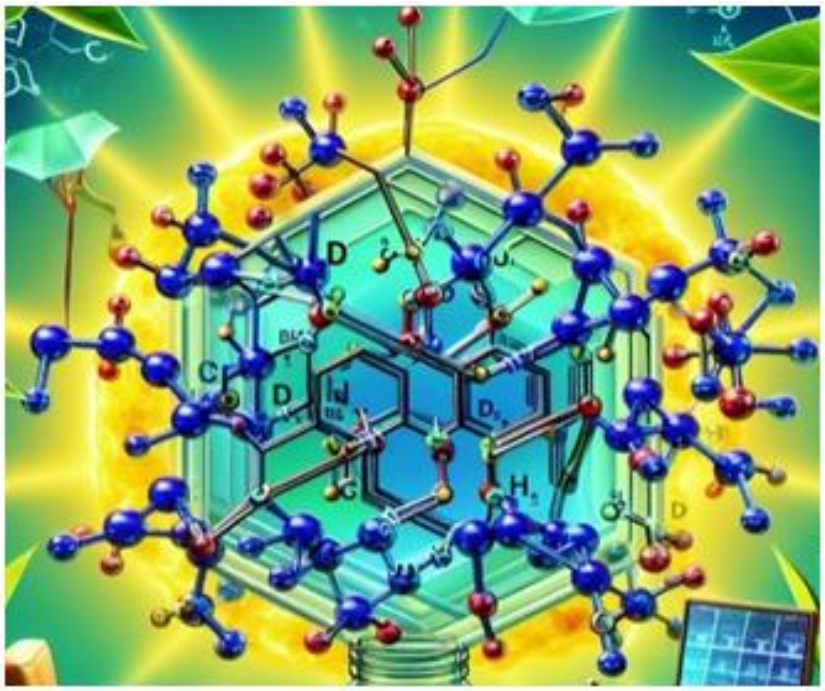

Figure 1 Donar Acceptor Structure

ii. Tuning Light Absorption:

The manipulation of the donor and acceptor moieties, along with the -bridge, allows for the customisation of the light absorption range of organic dyes. A red-shift in the absorption spectrum is typically observed when electron-donating groups are stronger and electron-accepting groups are weaker, resulting in enhanced absorption of visible and near-infrared light. Furthermore, the enhancement of light absorption can be achieved by extending the conjugation length by including additional -units.

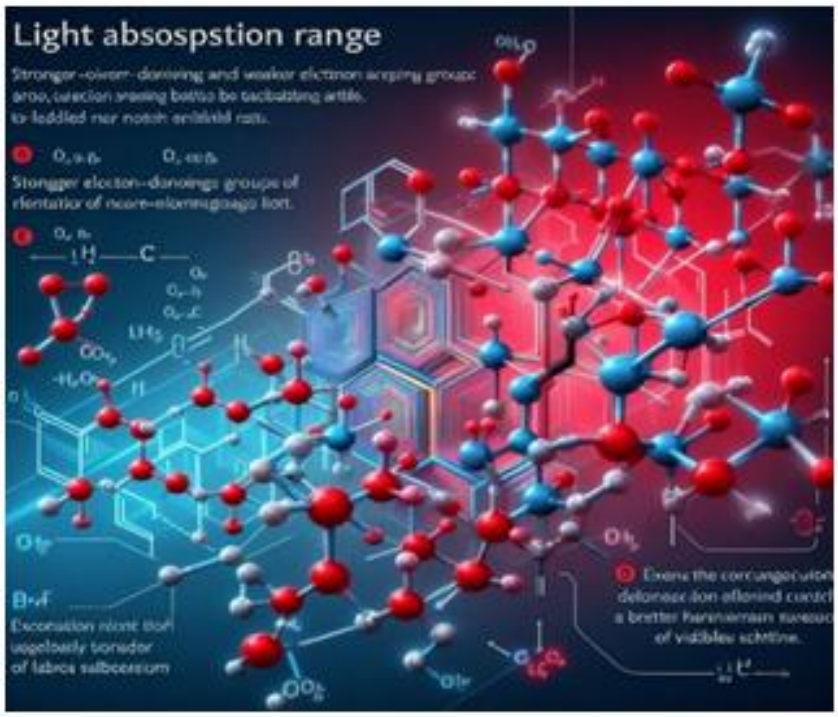

Figure 2. Light absorption Range organic dyes donor and acceptor

iii. Energy Level Alignment:

Efficient charge separation and transfer necessitate the establishment of appropriate energy level alignment between the organic dye and the semiconductor material. In order to ease electron injection and dye regeneration, it is necessary for the highest occupied molecular orbital (HOMO) and lowest unoccupied molecular orbital (LUMO) levels of the dye to be appropriately aligned with the valence and conduction bands of the semiconductor, respectively.

iv. Structural Modifications:

The enhancement of solubility and processability of dyes can be achieved through the insertion of functional groups, such as alkyl chains. Additionally, the incorporation of bulky substituents can effectively prevent dye aggregation and improve photostability. In addition, the inclusion of anchoring groups, such as carboxylic acid or phosphonic acid, can enhance the attachment of the dye to the surface of the semiconductor.

B. Characterization Techniques for Organic Dyes and Nanoscale Materials

Understanding the physical and chemical properties of organic dyes and nanoscale materials is crucial for determining their appropriateness for solar energy conversion applications. Numerous analytical methodologies are utilised to clarify the structural, optical, electrical, and morphological attributes of these substances. This section provides an overview of the characterisation approaches frequently employed for organic dyes and nanoscale materials.

i. Nuclear Magnetic Resonance (NMR) Spectroscopy:

Nuclear magnetic resonance (NMR) spectroscopy is an effective technique for elucidating the chemical composition of organic dyes. 1H NMR and 13C NMR are commonly employed for examining the chemical surroundings and interconnections of hydrogen and carbon atoms, respectively. These techniques offer vital insights on the effective production and integrity of the dyes.[6]

ii. **Mass Spectrometry (MS):**The molecular weight and elemental content of organic dyes can be determined using mass spectrometry techniques, such as electrospray ionisation (ESI) or matrix-assisted laser desorption/ionization (MALDI). These techniques are used to check the molecular structure and purity of the dyes.[2]

iii. **Ultraviolet-Visible (UV-Vis) Spectroscopy:**

Under ultraviolet-visible (UV-Vis) spectroscopy, the light absorption characteristics of organic dyes and nanoscale materials may be effectively characterised. Absorption spectra offer valuable insights into the energy levels, electronic transitions, and light absorption capabilities of materials within the visible and near-infrared parts of the solar spectrum.

iv. **Fourier-Transform Infrared (FTIR) Spectroscopy:**

Fourier Transform Infrared (FTIR) spectroscopy is employed for the purpose of detecting the existence of distinct functional groups and molecular vibrations inside organic dyes and nanoscale materials. This methodology proves to be highly advantageous in verifying the effective integration of anchoring moieties, such as carboxylic acids or phosphonic acids, that enhance the affinity between the dye and the surface of the semiconductor.[7]

v. **X-ray Diffraction (XRD):**

X-ray diffraction (XRD) is a non-invasive method employed to examine the crystalline arrangement and phase makeup of microscopic substances, such as semiconductor nanoparticles or carbon-based nanostructures. The provided information encompasses details regarding the crystal structure, lattice parameters, and crystallite size, all of which have the potential to impact the optoelectronic properties and overall performance of the device.

The techniques employed in this study include Scanning Electron Microscopy (SEM) and Transmission Electron Microscopy (TEM).

Scanning electron microscopy (SEM) and transmission electron microscopy (TEM) are highly effective imaging techniques that offer significant insights into the morphology, size, and distribution of nanoscale materials. Scanning electron microscopy (SEM) is highly advantageous for examining the surface topography and

microstructure, whereas transmission electron microscopy (TEM) enables detailed imaging and investigation of the internal structure and crystallinity of materials.

vi. Atomic Force Microscopy (AFM):

AFM, or Atomic Force Microscopy, is a scanning probe microscopy method that can generate detailed topography images of nanoscale materials, such as organic dyes and nanostructured surfaces, with great resolution. Additionally, it can be utilised to quantify surface roughness, a critical factor in determining the efficiency of solar energy conversion devices. .

The electrochemical techniques of Cyclic Voltammetry (CV) and Electrochemical Impedance Spectroscopy (EIS) are employed for the examination of the redox properties, energy levels, and charge transport characteristics of organic dyes and nanoscale materials. CV offers data on the highest occupied molecular orbital (HOMO) and lowest unoccupied molecular orbital (LUMO) energy levels, whereas EIS can provide insights into charge transfer mechanisms and interfacial charge dynamics.[8]

vii. Photoluminescence (PL) Spectroscopy:

Power spectroscopy (PL) is a highly effective technique utilised in the investigation of the emission characteristics shown by organic dyes and nanoscale materials. Information about energy transfer processes, charge recombination, and excited-state dynamics is of utmost importance in comprehending the systems implicated in the conversion of solar energy.

Characterization procedures are chosen based on the particular attributes of interest and the nature of the materials being studied. In order to achieve a thorough comprehension of the structural, optical, electrical, and morphological properties of organic dyes and nanoscale materials for solar energy conversion applications, it is common practice to utilise a mix of various methodologies.[9]

C. Integration of Organic Dyes with Nanoscale Materials

A promising strategy for improving the efficiency of solar energy conversion systems involves the incorporation of organic dyes into nanoscale materials. When organic dyes are coupled with nanoscale materials like carbon nanotubes, graphene, and semiconductor nanoparticles, they possess distinctive characteristics that can enhance light absorption, charge transfer, and overall device efficiency. These technologies for incorporating organic colours into nanoscale materials and their potential advantages are examined in this section.

i. Dye-Sensitized Nanostructured Semiconductor Films:

Organic dyes are attached to the surface of nanostructured semiconductor films, usually made of titanium dioxide (TiO2) or zinc oxide (ZnO) nanoparticles, in dye-sensitized solar cells (DSSCs). Incorporating nanoscale elements into these semiconductor films can improve the ability to capture light and carry charges.

a. Incorporation of Carbon Nanotubes (CNTs) or Graphene:

Both carbon nanotubes (CNTs) and graphene exhibit exceptional electrical conductivity, making them suitable for integration into nanostructured semiconductor films to enhance the efficiency of charge transfer and collection. Nanomaterials have the ability to establish interpenetrating networks within semiconductors, hence enhancing the efficiency of electron transport and mitigating charge recombination losses.

b. Semiconductor Nanoparticle Composites:

The enhancement of light absorption and charge separation processes can be achieved through the use of various semiconductor nanoparticles, such as TiO2 and ZnO, or the integration of plasmonic nanoparticles

(e.g., gold or silver) into the semiconductor film. Composites have the ability to leverage the synergistic effects exhibited by many materials, resulting in enhanced light absorption and charge carrier dynamics.

ii. Dye-Sensitized Nanowire or Nanorod Arrays:

Nanostructures of a single dimension, such as nanowires or nanorods, provide direct routes for the movement of electric charges and can be made more sensitive by adding organic dyes. The composition of these structures may include semiconductors such as TiO2, ZnO, or silicon, and their performance can be further enhanced through the incorporation of supplementary nanomaterials.

a. Metal Oxide Nanowire/Nanorod Arrays with CNTs or Graphene:

Carbon nanotubes (CNTs) or graphene can be integrated into metal oxide nanowire/nanorod arrays to establish effective paths for charge transport and enhance the efficiency of charge collection. The nanowires/nanorods have a high aspect ratio, which allows for a vast surface area to load dyes. Additionally, the CNTs or graphene aid in transporting charges throughout the length of the nanostructures.

b. Silicon Nanowire Arrays with Organic Dyes:

By utilising the exceptional charge transport properties of silicon and the light-harvesting capabilities of organic dyes, it is possible to sensitise silicon nanowire arrays. This methodology has the potential to result in solar cells that exhibit high efficiency, characterised by decreased material usage and enhanced charge separation and transport.

iii. Dye-Sensitized Quantum Dot Solar Cells:

Semiconductor nanocrystals known as quantum dots (QDs) possess distinctive optical and electrical characteristics as a result of quantum confinement phenomena. The integration of organic dyes with quantum dots (QDs) enables the development of dye-sensitized quantum dot solar cells (QDSSCs). In this configuration, the dyes function as light absorbers, while the QDs serve as materials for charge transport and harvesting.

a. QD-Sensitized TiO2 Films with Organic Dyes:

QDSSCs include the attachment of organic dyes to TiO2 films, followed by the deposition of QDs onto the dye-sensitized TiO2 surface. The quantum dots (QDs) have the ability to efficiently transport and gather electrons that are injected from the excited dye molecules, hence enhancing the efficiency of charge separation and collection.

b. QD-Dye Co-sensitization:

This methodology involves the co-sensitization of organic dyes and quantum dots (QDs) onto the surface of a semiconductor, resulting in the formation of a hybrid light-harvesting system. The dyes and quantum dots (QDs) have the ability to absorb various parts of the solar spectrum, resulting in a wider range of light absorption and improved efficiency in converting energy.

iv. Device Fabrication and Performance Evaluation

Careful consideration of fabrication procedures and performance evaluation methods is necessary for the successful integration of metal-free organic dyes and nanoscale materials into functional solar energy conversion systems. This section examines the methods used to create these solar energy devices and the many methodologies used to assess their effectiveness.

D. Device Fabrication:

a. Dye-Sensitized Solar Cells (DSSCs):

The integration of organic dyes and nanoscale materials has been extensively investigated in the field of DSSCs. The fabrication procedure generally encompasses the subsequent stages: The process involves the fabrication of

nanostructured semiconductor films, such as TiO2 and ZnO, on a substrate made of transparent conductive oxide (TCO). The semiconductor film can be sensitised with an organic dye using different processes, such as dip-coating or doctor-blading. The process involves the application of a counter electrode, often consisting of platinum or carbon-based substances. The cell is assembled by placing the dye-sensitized semiconductor film and the counter electrode in a sandwich configuration, together with a redox electrolyte or solid-state hole transport medium.

b. Organic Photovoltaic Devices (OPVs):

Organic photovoltaics (OPVs) utilise organic dyes and nanoscale materials as the active layer to absorb light and generate charge. One potential step in the fabrication process is the application of a hole transport layer, such as PEDOT:PSS, onto a TCO substrate.

The active layer can be deposited in either a bulk heterojunction or a planar heterojunction structure, wherein the organic dye and nanoscale materials such as carbon nanotubes (CNTs), graphene, and quantum dots (QDs) are incorporated. The process of applying an electron transport layer, such as fullerene derivatives or metal oxides, has been seen. Application of a metallic cathode to finalise the structure of the device.

c. Quantum Dot Solar Cells (QDSCs):

Quantum dots with solar cells (QDSCs) combine organic dyes with semiconductor quantum dots (QDs) to capture light and transmit electric charges. method of fabrication may encompass the deposition of a nanostructured semiconductor layer, such as TiO2 or ZnO, onto a TCO substrate. The process of sensitising the semiconductor layer through the application of an organic dye.The QD layer can be deposited using either solution-based or vapor-based processes.The completion of the device construction involves the deposition of supplementary charge transport layers and metal connections.

2. Performance Evaluation:

a. Current-Voltage (I-V) Characterization:

The evaluation of solar energy conversion devices is commonly conducted through the utilisation of I-V measurements conducted under simulated solar illumination. Important parameters derived from I-V curves comprise: The open-circuit voltage (Voc) refers to the highest voltage produced by the device when it is exposed to light.The short-circuit current (Isc) refers to the highest amount of current produced by the device when it is exposed to light. The fill factor (FF) is a metric used to evaluate the performance of a device in relation to its theoretical maximum. The concept of power conversion efficiency (PCE) refers to the proportion of the maximum power output of a device in relation to the input solar power. b. The External Quantum Efficiency (EQE) or Incident Photon-to-Current Efficiency (IPCE) is a metric that offers insights into the spectrum response of a device and its capacity to convert incident photons into electrical current across various wavelengths. c. Electrochemical Impedance Spectroscopy (EIS): EIS is a powerful method for studying the movement of charges and their recombination within a device. It offers valuable information on the dynamics of charge at the interface and helps in optimising the device. [7]

b. Stability and Lifetime Testing:

Evaluating the durability and practical viability of solar energy conversion devices requires conducting long-term stability and longevity testing under constant illumination or accelerated ageing circumstances.

II. CONCLUSION

This study has investigated the capacity of metal-free organic dyes and nanoscale materials to improve the efficiency of converting solar energy. The practicality of these materials for solar energy harvesting applications has been proven by a thorough examination of design concepts, synthetic techniques, material characterization, device manufacturing, and performance evaluation.

The development and production of metal-free organic dyes featuring customised donor--acceptor structures have facilitated the production of highly effective light-absorbing materials that include adjustable optoelectronic characteristics. Promising outcomes have been shown in enhancing light absorption, charge transfer, and overall device performance through the incorporation of these dyes into nanoscale materials, including carbon nanotubes, graphene, and semiconductor nanoparticles.

The utilisation of various characterization techniques, such as spectroscopic, microscopic, and electrochemical methods, has yielded significant knowledge regarding the structural, optical, electronic, and morphological attributes of these materials. This knowledge has played a crucial role in informing their subsequent refinement and incorporation into operational equipment. Several device topologies have been investigated for the effective integration of organic dyes and nanoscale materials, such as dye-sensitized solar cells, organic photovoltaics, and quantum dot solar cells. The examination of crucial performance metrics, such as power conversion efficiency, spectrum response, and charge transport dynamics, has been made possible by meticulous device engineering and fabrication techniques.

Although there has been notable advancement, there are still other obstacles that need to be tackled, such as ensuring long-term stability, preventing charge recombination, achieving large-scale production, and mitigating environmental impact. Nevertheless, there are encouraging prospects for the future that arise from the utilisation of rational design methodologies, computer modelling techniques, tandem and multi-junction devices, hybrid organic-inorganic systems, and the integration of developing technology.

To surmount these obstacles and fully harness the capabilities of metal-free organic dyes and nanoscale materials in the realm of solar energy conversion, it is imperative to foster interdisciplinary cooperation, continue ongoing research endeavours, and prioritise sustainable and environmentally conscious methodologies. By tackling these obstacles, these materials have the potential to facilitate the advancement of economical, effective, and eco-friendly solar energy systems, hence aiding the worldwide shift towards a sustainable energy future.

III. REFERENCES

[1]. O'Regan, B., &Grätzel, M. (1991). A low-cost, high-efficiency solar cell based on dye-sensitized colloidal TiO2 films. Nature, 353(6346), 737-740.

[2]. Hagfeldt, A., Boschloo, G., Sun, L., Kloo, L., & Pettersson, H. (2010). Dye-sensitized solar cells. Chemical Reviews, 110(11), 6595-6663.

[3]. Mishra, A., &Bäuerle, P. (2012). Small molecule organic semiconductors on the move: Promises for future solar energy technology. AngewandteChemie International Edition, 51(9), 2020-2067

[4]. Kar, P., Shubhashish, B., & Iyer, P. K. (2019). Organic dyes for sustainable dye-sensitized solar cells. Renewable and Sustainable Energy Reviews, 119, 109532.

[5]. Docampo, P., & Guldi, D. M. (2021). Nanomaterials for solar energy conversion: Dye-sensitized nanoparticles. ChemSusChem, 14(10), 2075-2096.

[6]. Zhao, Y., Huang, J., Wang, M., & Zhu, C. (2022). Organic dyes for high-performance dye-sensitized solar cells: Recent advances and future perspectives. Solar Energy Materials and Solar Cells, 236, 111425.

[7]. Carey, G. H., Abdelhady, A. L., Ning, Z., Thon, S. M., Bakr, O. M., & Sargent, E. H. (2015). Colloidal quantum dot solar cells. Chemical Reviews, 115(23), 12732-12763.

[8]. Xu, J., Huang, J., & Cao, Y. (2021). Integrating carbon nanomaterials with organic dyes for high-performance dye-sensitized solar cells. Nanoscale, 13(18), 8257-8284.

[9]. Aly, S. M., Ahmed, N. S. E., Gad, W. K., & Abo-Zeid, M. S. (2018). Dye-sensitized solar cells using nanomaterials: A review. Materials Today Chemistry, 9, 109-125.

[10]. Lan, J. L., Wang, Y. Y., Cao, K., Ren, G. K., Pan, C. Y., & Zhu, X. H. (2020). Design and characterization of metal-free organic dyes for dye-sensitized solar cells. Dyes and Pigments, 174, 108018.

International Journal of Scientific Research in Science and Technology
Volume 11 | Issue 13| Print ISSN: 2395-6011 | Online ISSN: 2395-602X (www.ijsrst.com)

Mass Attenuation Coefficient and Molar Extinction Coefficient of 2-Amino-3-Nitropyridinein the Energy Range356KeV to 1330 KeV

Vishal Awasarmol[1], Ankur Awasarmol[2], Sandip Mahajan[3], R.R. Bhosale[4], Rajkumar Lokhande[5], Bharat Surung[6]

[1]Department of Physics, Swami Vivekanand Senior College, Mantha, Jalna, Maharashtra, India
[2]Department of Chemistry, Pratistan College, Paithan, Cha Sambhaji Nagar, Maharashtra, India
[3]Department of Physics, Shikshan Maharshi Dnyandeo Mohekar College, Kalamb, Dharashiv, Maharashtra, India
[4]Department of Physics, Arts, Commerce and Science College, Kille-Dharur, Beed, Maharashtra, India
[5]Department of Physics, Shirish Madhukarrao Chaudhari College, Jalgaon, Maharashtra, India
[6]Department of Physics, Lal Bahadur Shastri Senior College, Partur, Jalna, Maharashtra, India

ABSTRACT

In present experimental study the mass attenuation coefficient and molar extinction coefficient of nonlinear optical material i.e. 2-amino-3-nitropyridine have been measured at 356keV to 1330 keV photons in narrow beam good geometry set-up by using NaI (Tl) Scintillation detector with resolution 8.2% at 662 keV. The mass attenuation coefficients were calculated at different photon energies and data of mass attenuation coefficient were then used to the total interaction cross section, and molar extinction coefficient of 2-amino-3-nitropyridine. The experimental results are found to be in good agreement with XCOM data.

Keywords: Mass attenuation coefficient, Molar extinction coefficient, Nonlinear optical material

I. INTRODUCTION

Wide use of photons interactions with matter is great significant in various fields such as medical, industry, and agriculture. The knowledge of absorption and scattering of gamma rays in the compound materials has become an interesting and exciting field of research [1].Mass attenuation coefficient, total interaction cross section and molar extinction coefficient are basics parameters. These basic parameters are used for characterizing the penetration and diffusion of gamma rays in the medium through which they passes and mainly depends on the photon energy, the nature of the material and the density of medium through which radiation passes[2].

The correct values of the mass attenuation coefficient for X-ray and gamma ray in several materials (alloy, semiconductor, plastic, soil, biological materials etc.) are valuablein various applied fields such as medical, agriculture, industrial, biological, radiation protection, and radiation dosimetry[3-5].Nonlinear optical (NLO) materials have proven to be an interesting contender for a number of applications such as optics, photonics, optical memory, laser, frequency shifting and radiation sensing for the emerging technologies in areas i.e. signal

processing, optical interconnections, and optical telecommunications. In recent years, many researchers have been tried to find out a diversity of nonlinear optical materials in order to satisfy the above said applications. But in the recent past, nonlinear optical materials are gaining attention because they share the wide advantages of both inorganic and organic materials[6]. In the NLO materials, have been of particular interest because the nonlinear optical response in this broad class of materials is microscopic in origin, offering an opportunity to use theoretical modeling coupled with the synthetic flexibility to design and produce novel materials [7].
Mass attenuation coefficient (μ_m) values are widely used in research for solving different problems in radiation physics and radiation chemistry [8-13]. The Mass attenuation coefficientdata can be used for the determination of some parameters such as total atomic cross section and molar extinction coefficient. In the present article, we have reported the detailed mass attenuation coefficients and another related parameter.

II. THEORY

In this section we summarize some theoretical relations that have been used for the determination of (μ_m) in the present work. When a monochromatic beam of gamma photons is incident on a target, some photons are emitted due to the dominant interaction processes and therefore, the transmitted beam is attenuated. The extent of attenuation depends on given elemental target. This attenuation of the beam is described by the following equation:

$$I = I_0 e^{-\mu t} \qquad (1)$$

Where, I_0 and I are the incident and transmitted photon intensities, respectively, μ (cm^{-1}) is the linear attenuation coefficient of the material and t (cm) is the sample thickness. Rearrangement of Eq. (1) yields the following equation for the linear attenuation coefficient:

$$\mu = \frac{1}{t}\ln\left(\frac{Io}{I}\right) (2)$$

In Eq. (2), the mass attenuation coefficients μ/ρ ($cm^2\ g^{-1}$) for the samples were obtained from Eq. (3) by using the density of the corresponding samples:

$$\mu_m = \frac{\mu}{\rho}\left(cm^2 g m^{-1}\right) = \frac{1}{\rho t}\ln\left(\frac{Io}{I}\right) \qquad (3)$$

Where, ρ (g/cm^3) is a measured density of the corresponding sample. The values of mass attenuation coefficients were then used to determine the total attenuation cross section (σ_{tot}) by the following relation

$$(\sigma_{tot}) = \mu_m (M / N_A) \qquad (4)$$

Where, $M = \sum_i n_i A_i$ is the molecular weight of the compound, N_A is the Avogadro's number, n_i is the total number of atoms in the molecule and A_i is the atomic weight of the i^{th} element in a molecule. The total atomic cross-sections ($\sigma_{t,a}$)has been determined from the following equation:

$$(\sigma_{t,a}) = \frac{1}{N_A} \sum_i f_i A_i (\mu_m)_i \qquad (5)$$

The values of molar extinction coefficients were determined using the following relation:

$$\varepsilon = 0.4343 N_A \sigma_{tot} \quad (6)$$

III.EXPERIMENTAL SET UP AND MEASUREMENTS

The present experiments were done with the help of narrow beam good geometry set up.In this experiments, the six radioactive sources were used such as ^{57}Co, ^{133}Ba, ^{137}Cs, ^{54}Mn ^{60}Co and ^{22}Na. All these radioactive sources were obtained from Bhabha Atomic Research Centre, Mumbai, India. These radioactive sources emitted energies 356, 511, 662, 840, 1170, 1275 and 1330 keV further they were collimated and detected by a NaI (Tl) scintillation detector. The signals were amplified and analyzed by gamma ray spectrometry which includes (2″×2″) NaI (Tl) crystal with an energy resolution of 8.2% at 662 keV and 8 K multichannel analyzer. The NLO materials such as 2-amino-3-nitropyridine samples under investigation were pellets shaped (uniform-thickness, 0.12g/cm^2).

The diameters of the pellets were determined using a traveling microscope. The attenuation of photons in the empty container was negligible. For the preparation of the sample in the form of a pellet, the sample was weighed in a sensitive digital balance and having a good accuracy of measurements about 0.001 mg. The weighing of samples was repeated five times to obtain the consistent value of the mass. The KBr press machine was utilized to make the pallets of measured samples. The mean of this set of values was taken to be the mass of the sample. Stability and reproducibility of the arrangement were tested before and after each set of runs in the usual manner. In order to minimize the effects of small-angle scattering and multiple scattering events on the measured intensity, the transmitted intensity was measured by setting the channels at the full-width half-maximum position of the photo-peak. Uncertainty in the measured mass per unit area is < 0.04%. The samples were put one by one between the source and detector. Optimum thickness of the samples ($2 < \ln (I_0/I) < 4$) was selected to minimize multiple scattering [17]. The details of experimental arrangement have been discussed by [14-16].

IV.RESULTS AND DISCUSSION

The experimentally measured values of μ_m (cm^2/g) for nonlinear optical material i.e. 2-amino-3-nitropyridineat 356, 511, 662, 1170, 1275 and 1330keV photon energies presented in Table 1. The typical plot of μ_m versus energy E for 2-amino-3-nitropyridineis displayed in Fig.(1).The Fig.(1) also includes the variation of theoretically determined μ_m values versus energy.

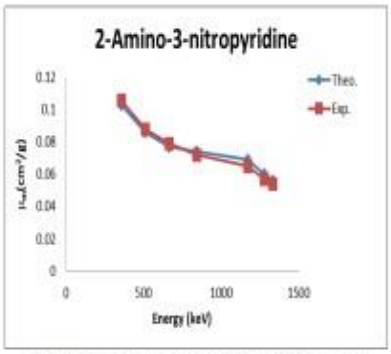

Fig. 1. Mass attenuation Coefficient of NLO sample

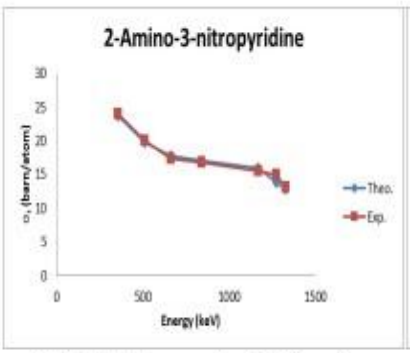

Fig. 2 Total atomic cross section of NLO sample

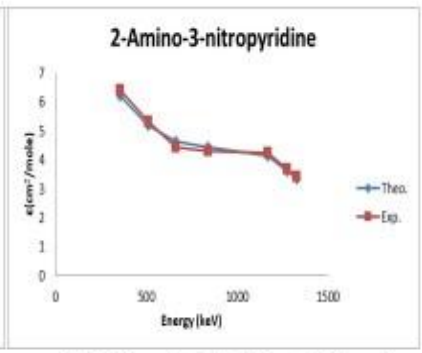

Fig. 3 Molar extinction Coefficient of NLO sample

Table 1. Mass attenuation Coefficient of Sample.

Energy	Theo.	Exp.
356	0.103	0.106
511	0.086	0.088
662	0.077	0.079
840	0.074	0.072
1170	0.069	0.065
1275	0.06	0.057
1330	0.056	0.054

Table 2. Total atomic cross section of Sample.

Energy	Theo.	Exp.
356	23.782	23.964
511	19.857	20.109
662	17.779	17.431
840	17.086	16.843
1170	15.932	15.625
1275	13.854	14.957
1330	12.93	13.216

Table 3. Molar extinction Coefficient of Sample.

Energy	Theo.	Exp.
356	6.223	6.431
511	5.196	5.327
662	4.652	4.458
840	4.471	4.315
1170	4.169	4.265
1275	3.625	3.713
1330	3.383	3.423

It is clearly seen that the μ_m depends on photon energy and decreases with increasing photon energy. The experimental (μ_m) values agree with theoretical values calculated using the Win-XCOM program based on the mixture rule. The total experimental uncertainty of the (μ_m) values depend on the uncertainties of I_0 (without attenuation), I (after attenuation), mass thickness measurements and counting statistics. Typical total uncertainty in the measured experimental (μ_m) values is estimated to be 2-3%. Measured total atomic cross section (σ_t) and molar extinction coefficient (ε) values for the presently studied 2-amino-3-nitropyridinehave been displayed in Table 2 and Table 3, respectively. The typical plots of σ_t versus E and ε versus E are displayed in Figs.(2) and Fig.(3) respectively. The behavior of σ_t and ε with photon energies shows almost similar behavior to (μ_m) plots.

V. CONCLUSIONS

In the present experimental study, mass attenuation coefficients and other related parameters of 2-amino-3-nitropyridineNLO samples has been calculated at 356 keV-1330 keV photon energy. These all samples have been calculated extensively using transmission method with a view to utilize the material for radiation dosimetry. This study concludes that any dosimetric material depends on its chemical composition, density, and concentration of the elements that it contains. In this case, the mass attenuation coefficients (μ_m) were investigated to study sufficient information about total atomic cross sections ($\sigma_{t,\ a}$), and molar extinction coefficient (ε) of the samples. From this study, we can conclude that all the attenuation parameters of NLO materials are very important in diagnostic imaging and many other technological applications.

VI. REFERENCES

[1]. Suresh Kumar M.R., Ravindra H.J., Dharmaprakash S.M.,(2007) Synthesis, crystal growth and characterization of glycine lithium sulphate. J. Cryst. Growth, 306; 361-365.

[2]. Chemla, D. S., Zyss, J., Eds. (1987) Nonlinear Optical Properties of Organic Molecules and Crystals; Academic Press: New York.

[3]. Bhadauria S., Das M., Saxena S., Prasad R. and Sen P., and Dwivedi R., (2011) Recent Progress in Non-linear Optical Material, Syntheses, Characterization and Geometry Optimization of Dicinnamalacetone, Archives of Physics Research, Vol. 2 (2):36-44.

[4]. Baltas H., Celik S., Cevik U., E-Yamaz, (2007) Measurements of mass attenuation coefficient and effective atomic number for MgB2 using X-ray energies, Radiation Measurements, 42, 55-60.

[5]. Manohara S.R., Hanagodimath S.M., (2007) Studies on effective atomic numbers and electron densities of essential amino acids in the energy range 1 keV-100 GeV, Nuclear Instruments and Methods in Physics Research B, 258, 321-328.

[6]. Medhat M.E., Singh V.P., (2014) Mass attenuation coefficients of composite materials by Geant4, XCOM and experimental data: comparative study. Radiation Effects & Defects in Solids, 169; 800–807.

[7]. MedhatM.E., Demir N., TarimU.A., Gurler O., (2014) Calculation of gamma-ray mass attenuation coefficients of some Egyptian soil samples using Monte Carlo methods Radiation Effects & Defects in Solids, 169; 706–714.

[8]. Pawar P.P., Bichile G.K., (2013) Studies on mass attenuation coefficient, effective atomic number and electron density of some amino acids in the energy range 0.122-1.330 MeV, Radiation Physics and Chemistry, 92; 22-27.

[9]. Ladhaf B.M., Pawar P.P., (2015) Studies on mass energy absorption coefficient and effective atomic energy absorption cross-section for carbohydrates, Radiation Physics and Chemistry, 109; 89-94.

[10]. Gaikwad D.K., Pawar P.P., Selvam T.P., (2016) Attenuation cross sections measurements of some fatty acids in the energy range 122-1330 keV. Pramana- J. Phys., 87 (12), 1-7. DOI: 10.1007/s12043-016-1213-y.

[11]. Awasarmol V.V., Gaikwad D.K., Raut S.D. Pawar P.P., (2017) Photon interaction study of organic nonlinear optical materials in the energy range 122-1330 keV. Radiation Physics and Chemistry, 130; 343-350.

[12]. Awasarmol V.V. Gaikwad D.K., Raut S.D. Pawar P.P., (2017) Gamma ray interaction studies of organic nonlinear optical materials in the energy range 122 keV to 1330 keV, Results in Physics, 7, 272-279.

[13]. Awasarmol V.V., (2017) Gamma ray attenuation parameters of inorganic nonlinear optical materials in the energy ranges 122 keV to 1330 keV. Indian Journal of pure and applied physics, 55; 65-72.

[14]. Kore P.S., Pawar P.P., Selvam T.P., (2016) Evaluation of radiological data of some saturated fatty acids using gamma ray spectrometry, Radiation Physics and Chemistry, 119; 74-79.

[15]. Chanthima N., Kaewkhao J., (2013) Investigation on radiation shielding parameters of bismuth borate glasses from 1 keV to 100 GeV. Annals of Nuclear Energy, 55; 23-28.

[16]. Salehi D., Sardari D., Jozani M.S., (2015) Investigation of some radiation shielding parameters in soft tissue, Journal of Radiation Research and Applied Sciences, 8; 439-445.

[17]. Creagh D.C., (1987) The Resolution of Discrepancies in Tables of Photon Attenuation Coefficient, Nuclear Instruments and Methods A, 255; 1–16.

International Journal of Scientific Research in Science and Technology
Volume 11 | Issue 13| Print ISSN: 2395-6011 | Online ISSN: 2395-602X (www.ijsrst.com)

New Trends in Gamma Radiation Protection Technology : Challenges and Opportunities

Mr. Nilesh S. Shinde
Department of Physics, Balbhim Arts, Science and Commerce College, Beed – 431122, Maharashtra, India

ABSTRACT

I. INTRODUCTION

Gamma radiation shielding technology plays a critical role in protecting human health and the environment in a variety of industries, including nuclear power, medical imaging, industrial radiography and space exploration. As the demand for reliable radiation protection continues to grow, there is a critical need for innovative approaches to gamma radiation protection that will help address emerging challenges and take advantage of new opportunities. The purpose of this review paper is to explore recent advances and emerging trends in gamma radiation shielding technology, focusing on new materials, advanced computational techniques, and integrated shielding solutions. By examining current research efforts and identifying key challenges, this article aims to provide insight into future directions for gamma radiation shielding technology and opportunities for interdisciplinary collaboration and innovation. Through a comprehensive analysis of recent developments and current research initiatives, this review aims to inform researchers, engineers, and policymakers about the current state of gamma radiation protection and stimulate further advances in this important area of radiation protection.

II. BASICS OF PROTECTION AGAINST GAMMA RADIATION

1. **Introduction to Gamma Radiation Protection:**
   - Define gamma radiation and its characteristics, including energy levels, penetration depth, and electromagnetic properties.
   - Explain the importance of gamma radiation protection in various industries such as nuclear power, medical imaging, and industrial applications.
   - Emphasize the risks associated with exposure to gamma radiation and the need for effective protective materials and methods.
2. **Mechanisms of interaction:**
   - Describe the basic mechanisms by which gamma rays interact with matter, including the photoelectric effect, Compton scattering, and pair formation.
   - Discuss how these interactions affect the attenuation of gamma rays as they pass through shielding materials.

- Provide mathematical formulations and theoretical models for calculating gamma radiation attenuation coefficients and transmission probabilities.

3. **Damping properties of materials:**
   - Explain the concept of attenuation and the factors that affect the attenuation coefficient, such as material density, atomic number, and photon energy.
   - Discuss the value of the mass attenuation coefficient (μ/ρ) for quantifying the ability of materials to attenuate gamma radiation.
   - Compare the attenuation properties of various materials commonly used for gamma radiation protection, including metals, concrete, polymers, and composites.
4. **Recommendations for shielding design:**
   - Describe the key considerations for designing effective gamma radiation shielding, including material selection, thickness optimization, and geometric configuration.
   - Discuss the half-value layer (HVL) concept and its importance in determining the thickness of shielding materials needed to reduce the intensity of gamma radiation by half.
   - Solve practical problems in designing gamma radiation shields for specific applications, such as space, weight, and regulatory requirements.
5. **Evaluation of shielding effectiveness:**
   - Review of experimental and computational methods used to evaluate the protection effectiveness of materials, including gamma spectroscopy, transmittance measurements, and Monte Carlo simulations.
   - Discuss key parameters and metrics for assessing the effectiveness of protection, such as accumulation rate, probability of transmission, and exposure reduction.
6. **Regulatory standards and recommendations:**
   - Provide an overview of international standards and regulations governing gamma radiation protection in various industries and applications.
   - Discuss dose limits, exposure guidelines, and safety protocols established by organizations such as the International Commission on Radiological Protection (ICRP) and the Nuclear Regulatory Commission (NRC).
7. **Case studies and practical applications:**
   - Present case studies and examples of gamma radiation protection solutions implemented in real-life scenarios including nuclear power plants, healthcare facilities and industrial plants.
   - Highlight successful strategies and innovative approaches to gamma radiation protection, showcasing best practices and lessons learned from practical applications.
8. **Future directions and challenges:**
   - Identify emerging trends and challenges in gamma radiation shielding, such as the need for lightweight and flexible materials, advanced computer modeling techniques, and integrated shielding systems.
   - Discuss potential research directions and opportunities for innovation, including the development of new materials, optimization of protection designs, and integration of smart technologies for real-time monitoring and control.

By covering these fundamental aspects of gamma radiation protection in your review article, you will be able to provide readers with a comprehensive understanding of the principles, properties, and practical considerations involved in developing effective protection solutions for a variety of applications.

III.TYPES OF PROTECTIVE MATERIALS

1. **Introduction to protective materials:**
   - Provide an overview of the different types of materials used for gamma radiation shielding, highlighting their varied properties, applications, and benefits.
2. **Metals:**
   - Discuss the characteristics and characteristics of metallic materials commonly used for gamma radiation shielding, such as lead (Pb), tungsten (W), and steel.
   - Explain how the high atomic number and density of metals contribute to their effectiveness in attenuating gamma radiation.
   - When selecting metal-based protective materials, consider practical considerations such as cost, availability, and processability.
3. **Concrete and mortar:**
   - Describe the composition and properties of concrete and mortar as effective materials that protect against gamma radiation.
   - Discuss the advantages of using concrete, including its versatility, low cost, and ease of construction for large-scale protective work.
   - Emphasize the importance of optimizing concrete mix design and thickness to achieve the desired level of gamma radiation attenuation.
4. **Polymers and plastics:**
   - Explore the use of polymers and plastics for gamma radiation protection, including materials such as polyethylene (PE), polyvinyl chloride (PVC), and epoxy resins.
   - Discuss the lightweight and flexible nature of polymer-based protective materials, making them suitable for portable and flexible protective solutions.
   - Address the challenges associated with polymer protection, such as low atomic number and limited attenuation capabilities compared to metals and concrete.
5. **Composite materials:**
   - Introduce composite materials consisting of several components, such as metal-polymer composites, metal-ceramic composites and fiber-reinforced polymers.
   - Discuss the synergistic effects achieved by combining different materials to improve gamma ray attenuation while maintaining desirable properties such as strength, flexibility, and thermal stability.
   - Highlight recent advances in composite material synthesis techniques and their potential applications in gamma radiation shielding.
6. **New materials and innovations:**
   - Explore new trends in gamma shielding materials such as nanomaterials, metamaterials, and liquid-based shielding systems.
   - Discuss the unique properties and potential benefits of new materials, including improved noise reduction performance, reduced weight, and improved flexibility.

- Address challenges and opportunities for integrating new materials into practical protection solutions, taking into account factors such as cost, scalability and regulatory compliance.

7. **Comparative analysis and selection criteria:**
   - Conduct a comparative analysis of different types of protective materials based on key parameters such as attenuation coefficient, cost-effectiveness, environmental impact and ease of manufacture.
   - Discuss selection criteria and recommendations for selecting the most appropriate shielding material for specific applications, taking into account factors such as radiation intensity, energy spectrum, and shielding requirements.

By describing these types of shielding materials in your review article, you can provide readers with a comprehensive overview of the various gamma radiation shielding options, as well as their strengths, limitations, and practical considerations.

IV. METHODS FOR ASSESSING SHIELDING EFFECTIVENESS

1. **Introduction to shielding effectiveness assessment:**
   - Provide an overview of the importance of evaluating the performance of gamma radiation protection materials and systems to ensure adequate radiation protection.
   - Explain the importance of accurate and reliable methods for assessing shielding effectiveness in a variety of applications, including nuclear power, medical imaging, and industrial radiography.
2. **Experimental methods:**
   - Describe experimental methods used to evaluate the protective performance of materials, such as gamma spectroscopy, transmittance measurements, and exposure power measurements.
   - Discuss the principles and procedures used in each experimental method, highlighting their advantages, limitations, and practical considerations.
   - Provide examples of experimental setups and instruments commonly used to evaluate the effectiveness of gamma radiation protection in laboratory and field settings.
3. **Computational methods:**
   - Implement computational approaches to evaluate protection effectiveness, including Monte Carlo simulations, deterministic transport codes (e.g., MCNP, FLUKA), and analytical models (e.g., point kernel methods).
   - Explain the principles of Monte Carlo simulations and their usefulness for predicting the interaction of gamma rays with materials, providing accurate estimates of radiation dose distribution and attenuation characteristics.
   - Discuss the use of deterministic transport codes and analytical models to simulate gamma ray transport through shielding materials, highlighting their capabilities and limitations compared to Monte Carlo methods.
4. **Evaluation parameters:**
   - Identify key parameters and metrics used to evaluate shielding effectiveness, such as mass attenuation factor (μ/ρ), half value level (HVL), accumulation factor, and transmission probability.
   - Explain how these parameters quantify the ability of materials to attenuate gamma radiation and provide insight into the effectiveness of shielding designs.

- Discuss practical considerations for measuring and interpreting these parameters in experimental and computational studies, including calibration procedures, data analysis methods, and uncertainty analysis.

5. **Comparative analysis and verification:**
   - Conduct a comparative analysis of experimental and computational methods for assessing the effectiveness of protection, highlighting their strengths and weaknesses, as well as their complementary roles.
   - Discuss the importance of validation and benchmarking to evaluate the accuracy and reliability of simulation results compared to experimental measurements.
   - Provide examples of validation studies conducted for various materials and shielding configurations that demonstrate the applicability and validity of modeling methods in real-world scenarios.
6. **Case studies and applications:**
   - Case studies and examples of evaluation of protection effectiveness in practical applications such as nuclear reactor protection, healthcare facility design, and optimization of radiography installations are presented.
   - Explain how experimental and computational methods have been used to optimize shielding design, improve radiation safety, and meet regulatory requirements in a variety of settings.
   - Discuss lessons learned and best practices derived from these case studies, offering insight into effective approaches to assessing and improving the effectiveness of gamma radiation protection.

By describing these shielding performance evaluation methods in your review article, you will be able to provide readers with a thorough understanding of the experimental and computational methods used to evaluate the performance of gamma radiation shielding materials and systems in a variety of applications.

V. APPLICATION OF GAMMA PROTECTION

1. **Introduction to the application of gamma radiation protection:**
   - Provide an overview of the variety of gamma radiation shielding applications in a variety of industries, including nuclear power, medical imaging, industrial radiography, and space exploration.
   - Emphasize the importance of effective shielding solutions to ensure safety, minimize radiation exposure, and protect sensitive equipment and personnel.
2. **Nuclear power plants:**
   - Discuss the role of gamma radiation shielding in nuclear power plants to protect workers, equipment, and the environment from ionizing radiation emitted during nuclear reactions.
   - Describe common shielding materials and configurations used in reactor containment structures, spent fuel storage facilities, and radiation shielding barriers.
   - Highlight challenges and innovations in nuclear power plant protection design, including considerations regarding radiation flux, neutron activation, and long-term stability.
3. **Medical Imaging and Radiation Therapy:**
   - Explore the use of gamma radiation shielding in medical imaging modalities such as X-ray radiography, computed tomography (CT), and positron emission tomography (PET).

- Discuss the importance of shielding in minimizing radiation dose to patients, healthcare workers, and bystanders during diagnostic and therapeutic procedures.
- Highlight advances in shielding technology that enable increasingly powerful imaging systems and reduce occupational radiation exposure in healthcare settings.

4. **Industrial radiography and non-destructive testing (NDT):**
   - Explain the use of gamma radiation shielding in industrial radiography and nondestructive testing for the inspection of welds, piping, and structural components in the manufacturing, construction, and aerospace industries.
   - Discuss developing portable and flexible security solutions for field inspections, addressing challenges such as accessibility, agility, and regulatory compliance.
   - Provide examples of innovative designs and protection methods to optimize radiation safety and control effectiveness in industrial settings.
5. **Space exploration and planetary science:**
   - Learn about the role of gamma radiation shielding in space missions to protect astronauts, spacecraft, and scientific instruments from cosmic radiation and solar particles.
   - Discuss the challenges of developing lightweight and compact protection systems for space missions, taking into account factors such as mass limitations, material selection, and mission duration.
   - Cover advances in space radiation shielding materials and technologies, including multifunctional composites, active shielding systems, and habitat design for long-duration space travel.
6. **Environmental and national security:**
   - Discuss the application of gamma radiation shielding in environmental monitoring, radiation detection, and homeland security initiatives to protect public health and national security.
   - Describe the use of protective materials and detection systems in border security, cargo inspection, and nuclear threat detection to prevent illicit trafficking in radioactive materials and the proliferation of nuclear weapons.
   - Emphasize the integration of gamma ray shielding technologies with advanced detection and surveillance systems to enhance situational awareness and emergency response capabilities.
7. **New Applications and Future Directions:**
   - Explore emerging trends and future applications of gamma radiation protection technologies such as wearable radiation protection devices, smart materials for real-time monitoring, and personalized protection solutions.
   - Discuss interdisciplinary research efforts and collaborations aimed at solving emerging problems and advancing the latest advances in gamma radiation protection in a variety of fields and applications.
   - Provide insight into potential areas for innovation and investment in gamma radiation shielding technologies, taking into account evolving threats, technological advances, and societal needs.

By highlighting these applications of gamma radiation shielding in your review article, you can provide readers with a thorough understanding of the diverse applications and importance of shielding materials and systems in various industries and contexts.

VI. FUTURE DIRECTIONS AND TASKS

1. **Introduction to future directions in the field of gamma radiation protection:**
   - Discuss the importance of exploring future directions and addressing current challenges in the field of gamma radiation protection to meet growing needs and advances in radiation protection technologies.
   - Emphasize the role of interdisciplinary collaboration, technological innovation, and strategic planning in shaping the future of gamma radiation shielding research and applications.
2. **Lightweight and flexible protective materials:**
   - Discuss the growing demand for lightweight and flexible gamma shielding materials to address space constraints, mobility and ergonomic requirements in a variety of applications.
   - Explore advances in materials science and engineering such as nanomaterials, metamaterials, and carbon-based composites to develop lightweight protective solutions with improved radiation attenuation properties.
3. **Advanced Computational Modeling and Simulation:**
   - Emphasize the importance of advanced computer modeling and simulation techniques, such as Monte Carlo simulations, deterministic transport codes, and machine learning algorithms, for predicting gamma radiation interactions with materials and optimizing shielding design.
   - Discuss current research efforts to improve the accuracy, efficiency, and scalability of computational models for simulating complex radiation transfer phenomena and optimizing shielding configurations.
4. **Integration of smart technologies and sensors:**
   - Learn about integrating smart technologies, sensors, and data analytics into gamma mitigation systems for real-time monitoring, adaptive control, and situational awareness.
   - Discuss the potential applications of Internet of Things (IoT) devices, wearable sensors, and embedded electronics to enhance radiation safety, detect radiation anomalies, and optimize protection performance in dynamic environments.
5. **Personalized and Adaptive Shielding Solutions:**
   - Discuss the concept of personalized and adaptive gamma protection solutions tailored to individual preferences, professional roles, and radiation exposure profiles.
   - Explore emerging technologies and develop strategies to dynamically adjust shielding properties based on changing environmental conditions, radiation levels, and user requirements.
6. **Regulatory Compliance and Standards Development:**
   - Please note the importance of regulatory compliance and the development of standards to ensure the safety, effectiveness and quality of gamma radiation protection materials and systems.
   - Discuss current efforts by international organizations, regulatory bodies, and industry consortia to establish harmonized standards, guidelines, and best practices for the design, evaluation, and certification of gamma radiation protection.
7. **Solving social and ethical issues:**
   - Consider the social and ethical considerations associated with the development and implementation of gamma radiation protection technologies, including environmental impacts, resource sustainability, and equity in access to radiation protection.

- Discuss the importance of stakeholder participation, public awareness, and responsible innovation in shaping the ethical and social aspects of gamma radiation shielding research and applications.

8. **Financing and resource allocation:**
   - Emphasize the need for sustained investment, funding and resource allocation to support research, development and deployment of gamma radiation shielding technologies across various sectors and applications.
   - Discuss strategies for promoting collaboration among academia, industry, government agencies, and nonprofit organizations to address critical research gaps, capitalize on new opportunities, and accelerate technology transfer and commercialization.

By highlighting these future directions and challenges in your review paper, you can provide readers with valuable information about the opportunities, challenges, and priorities shaping the future of gamma radiation shielding research, development, and implementation.

VII. CONCLUSION

In conclusion, this review paper provides a comprehensive overview of gamma radiation protection covering fundamental principles, types of shielding materials, methods for assessing shielding performance, applications, future directions, and challenges. Gamma radiation protection plays a critical role in protecting human health, protecting the environment and ensuring the safety of critical infrastructure in a variety of industries, including nuclear power, medical imaging, industrial radiography, space exploration and homeland security.

Throughout this article, we have discussed the importance of effective gamma radiation protection to minimize radiation exposure, reduce occupational hazards, and enhance public safety. By understanding the fundamental mechanisms of gamma radiation interaction with matter and the properties of various shielding materials, researchers and engineers can develop and optimize shielding solutions tailored to specific applications and environments.

Advances in materials science, computer modeling, and sensor technologies have led to innovations in gamma radiation protection, including lightweight materials, adaptive shielding systems, and smart monitoring devices. These advances have enabled more effective and cost-effective protection solutions while improving radiation safety and performance in a variety of environments.

Looking to the future, future research directions in the field of gamma radiation protection include the development of new materials, the integration of smart technologies, personalized protection solutions and the development of regulatory standards. Addressing current challenges such as resource sustainability, regulatory compliance, and ethical considerations will be critical to advancing the field and ensuring the responsible implementation of gamma radiation shielding technologies.

Collaboration among academia, industry, government agencies, and non-profit organizations will be essential to stimulate innovation, share best practices, and accelerate technology transfer and commercialization. By fostering interdisciplinary partnerships and leveraging new opportunities, we can address critical research gaps, capitalize on emerging trends, and shape the future of gamma radiation protection for the benefit of society.

In conclusion, this review paper highlights the importance of gamma radiation protection as a cornerstone of radiation protection and safety in a variety of applications and industries. Based on the ideas and

recommendations presented here, we can continue to improve the latest gamma radiation protection technologies and ensure a safer and more reliable future for future generations.

VIII. REFERENCES

[1]. Al-Quda, A., Aljara, I., and Khalil, Z. (2019). Recent advances in gamma radiation shielding materials: a review. Radiation Physics and Chemistry, 155, 83-94. DOI: 10.1016/j.radphyschem.2018.11.030

[2]. El-Sayed, A., Badawi, A., and El-Monghi, S. (2020). Recent advances in radiation protective materials: a review. Journal of Radiation Research and Applied Sciences, 13(1), 127–146. DOI: 10.1016/j.jrras.2019.10.012

[3]. Guerra, A., Carrillo, J., & Manzanares-Acuña, E. (2021). Review of radiation protection materials for medical applications. Materials today: Proceedings, 44, 1913–1918. DOI: 10.1016/j.matpr.2020.11.510

[4]. International Commission on Radiological Protection (ICRP). (2017). Recommendations of the International Commission on Radiological Protection 2007. ICRP Publication No. 103. DOI: 10.1016/j.icrp.2017.05.002.

[5]. Kim, K., Kim, Y., and Lee, J. (2018). Gamma radiation attenuation properties of various protective materials during wide-beam irradiation. Journal of Radiation Protection and Research, 43(3), 137-144. DOI: 10.14407/ml.2018.43.3.137

[6]. Mollajafari, M., and Masoudi, S. (2020). Gamma Radiation Shielding Materials: A Comprehensive Review. Progress in Nuclear Energy, 123, 103296. DOI: 10.1016/j.pnucene.2020.103296.

[7]. National Council on Radiation Protection and Measurements (NCRP). (2018). Radiation protection in dentistry and visualization of the oral cavity and maxillofacial area. NCRP Report No. 177. Bethesda, MD: NCRP.

[8]. Saleh, Z., & Thabet, N. (2021). Recent advances in radiation protection materials: a comprehensive review. Progress in Nuclear Energy, 131, 103610. DOI: 10.1016/j.pnucene.2020.103610.

[9]. United Nations Scientific Committee on the Effects of Atomic Radiation (UNSCEAR). (2017). Sources and effects of ionizing radiation: report to the General Assembly. New York: United Nations.

[10]. Zhang, J., Li, K., and He, K. (2019). Recent advances in gamma radiation shielding materials: a review. Journal of Materials Science and Engineering, 7(2), 17–24. DOI: 10.17265/2161-6213/2019.2-3.003

International Journal of Scientific Research in Science and Technology
Volume 11 | Issue 13| Print ISSN: 2395-6011 | Online ISSN: 2395-602X (www.ijsrst.com)

Synthesis and Thermophysical Characterization of Copper Oxide-Based Propylene Glycol and D.I. Water Nanofluid

S. S. Raut[1], A. A. Wadewale[2], M. T. Kotkar[2], S. V. Kshirsagar[1], K. M. Jadhav[3]
[1]Department of Physics, Mrs. K. S. K. College, Beed -431112, Maharashtra, India
[2]Department of Physics, Deogiri College Chhatrapati Sambhajinagar, Maharashtra, India
[3]University Department of Basic and Applied Science, MGM University, Chhatrapati Sambhaji Nagar, Maharashtra, India

ABSTRACT

Copper oxide (CuO) nanoparticles synthesized using wet sol-gel auto combustion method. The prepared CuO nanoparticles was annealed at 600oC for 5h in a muffle furnace. X-ray diffraction technique (XRD) was used to investigate the phase purity and for determination of crystal structure. Room temperature X-ray diffraction pattern analyzed by means of Origin software. Single phase formation along with the nanocrystalline nature was confirmed through X-ray diffraction analysis.The annealed powder of CuO was used to prepare nanofluid. Water and propylene glycols were used as a base fluid to prepare CuO-PG nanofluid. Thermal conductivity and zeta potential measurement of prepared nanofluid for different volume fractions of CuO nanoparticles in base fluids were carried out for heat transfer application. The thermal conductivity as prepared CuO-PG nanofluid increases with nanoparticle volume fraction but its stability decreases with increasing volume fraction of nanoparticles.

Keywords: Copper oxide, XRD, Sol-gel, CuO-PG Nanofluid, Thermal conductivity, Zeta Potential.

I. INTRODUCTION

The base fluids like glycols, water, silicon oil etc, have low thermal conductivity, therefore efficient heat transfer will not take place with the help of such base fluids. It is known that the thermal conductivity of metal and metal oxides are higher than 2 to 3 times than these conventional base fluids. With the development of nanotechnology, it is possible to prepare nanoparticles of such metal and metal oxides less than 100 nm. These nanoparticles mixed suitably with base fluids like water, glycols and oils forms nanofluid and helps to enhance the thermal conductivity of base fluids.

Metal oxides like copper oxide, zinc oxide, titanium oxide etc. have attracted attention of scientists and technologists because of their wide variety of applications[1]. Among the several metal oxides, copper oxide (CuO) is one of the best candidates for heat transfer application. In the recent years nanoparticles of metal oxides have gain lot of interest among the scientific community[2]. Metal oxide nanoparticles exhibit smaller particle size of the order of few nanometer dimensions, large surface to volume ratio, superior properties, highly chemically stable, easily prepared, more reactive etc. characteristics feature which are all together different than that of the bulk material. In the literature, copper oxide has been investigated for various

properties by many researchers[3, 4]. The structure of copper oxide is sensitive to the method of preparation and heat treatment. It can show tetragonal as well as cubic structure depending on the method of preparation and sintering temperature[5]. The conductivity of copper oxide is very high and therefore it is the best candidate for heat transfer application. Copper oxide can also be used as catalyst for water gas shift reaction, photo-cathodes for photo electrochemical water splitting applications, steam reforming[6].

It has been reported that, nanoparticles when dispersed in base fluid like water, oil etc. to form a nanofluid show enhanced conductivity as compared to base fluid[7]. Nano fluids are engineered colloidal suspension of nanoparticles in fluids. The studies related to the metal oxide based nanofluids are rarely reported in the literature. The nanofluid of copper oxide can show enhanced properties which are more suitable for heat transfer application[8].

Metal oxide in particular copper oxide has been prepared in nano size form by several wet chemical methods which includes sonochemical method, sol-gel technique, electrochemical, method, thermal decomposition of precursors, hydrothermal process etc[9]. Among these methods sol-gel autocombustion method is considered to be the best method to produce nanosize particles. The method requires low temperature and less time[10]. It produces particles of nano size dimension with large surface to volume ratio. The nanoparticles so obtained by sol-gel auto combustion method are more homogenous and ultrafine in nature. The yield of this method is also good[11]. Parminder Singh et al [12] prepared CuO nanofluid with propylene glycol and water as base fluid in the ratio 60:40 and found that heat transfer co-efficient of the prepared CuO nanofluid has significantly higher than its base fluid. Maximum rise in Nusselt number is observed for highest volume concentration. Raju singh et al [13] studied the stability of Cuo nannofluid by using sunflower oil as base fluids and found that good stability of nanofluid upto 50 days from preparation.

Nanofluids are prepared by two different methods i.e., i) One Step method ii) two step method

In one step method nanoparticles are synthesized and directly dispersed in a base fluid for preparation of nanofluid. CuO nanofluid were prepared by Jwo et al [14] using one step method shows 9.6% improvement in thermal conductivity for 0.4 vol %.

In two step method nanoparticles are prepared with suitable method and then obtained nanoparticles are mixed with base fluid to form nanofluid for different applications. Lee et al[15]prepared CuO – water nanofluids using two step method shows 12% improvement in thermal conductivity.

In the present study, nanoparticles of copper oxide were prepared by sol-gel auto combustion method and characterized by X-ray diffraction technique,scanning electron microscopy technique. The nanofluid was prepared by dispersing prepared copper oxide nanoparticles into base fluid having mixture of deionized water and propylene glycol and it is used for measuring the thermal conductivity, zeta potential and other properties for heat transfer application.

II. EXPERIMENTAL TECHNIQUE

A. Material

The chemicals used to synthesis ofcopper oxide nanofluid are Copper nitrate (Cu (NO3).3H2O), citric acid ($C_6H_8O_7$) used as fuel, ammonia (NH_3) is used for maintaining pH, deionizedwaterand propylene glycol in the ratio 50:50 has been used as base fluid, acetone $(CH_3)_2CO$and polyvinyl alcohol used as surfactant (caping agent) to coat nanoparticles to increase its dispersion stability.

B. Synthesis of copper oxide nanoparticles

The preparation of copper oxide nanoparticles had been carried through solgel auto combustion method. Copper nitrates and citric acid were dissolved in distilledwater separately in the stoichiometric ratio. The solution of both were mixed and stirred to get a homogenous mixture. The pH of this solution is brought at 7 by adding ammonia drop by drop. As obtained solution then heated at 80° C till it transforms in to gel. Then obtained gel was heated at 100°C till auto combustion. Allow the product to cool at room temperature for grind itto obtain a fine powder of CuO nanoparticles. The prepared nanoparticles were sintered at temperature of 600°C for 5 hours.

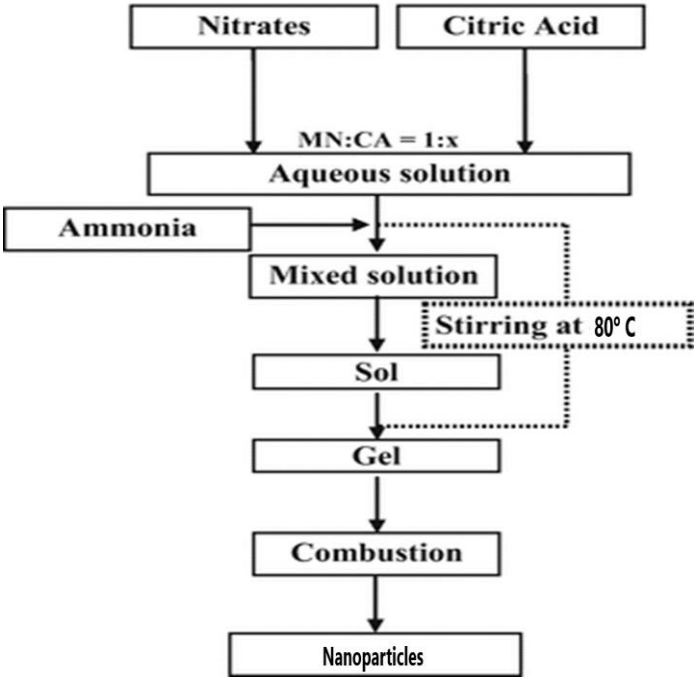

Fig. 1 Flow chart for Synthesis of CuO Nanofluid by solgel

C. Preparation of water-based copper oxide nanofluids

The CuO nanofluids were prepared by weighing the CuO nanoparticles and dispersing them in deionized water and propylene glycol (hybrid base fluid) in the ratio 50:50, using the law of mixtures . The density of CuO nanoparticles and that of base fluid was taken to calculate the vol. % of the dispersed nanofluids.

$$\text{Vol \%} = \varphi\% = \frac{\frac{W_{np}}{\rho_{np}}}{\frac{W_{np}}{\rho_{np}} + \frac{W_{bf}}{\rho_{bf}}} \quad (1)$$

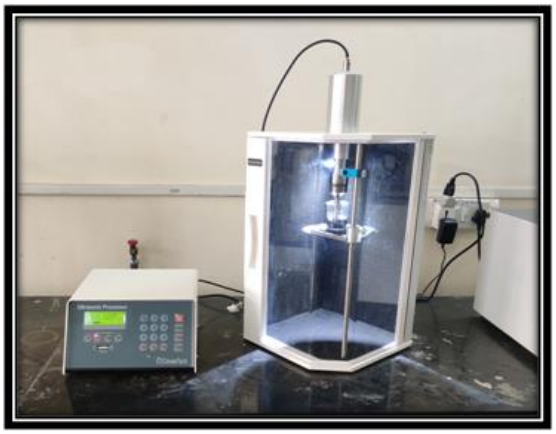

Fig. 2 Probe ultrasonicator

Probe ultra-sonication for 1 h applied to nanofluid to get a uniform suspension without any agglomeration and sedimentation. Polyvinyl alcoholis used as surfactant or capping agent to coat nanoparticles to increase stability of nanofluid for heat transfer application. Nanofluids for volume fractions 0.025, 0.050,0.075, 0.100, 0.125 and 0.150 volume % were prepared by dispersing weighed CuO nanoparticles in base fluid of containing deionized water and propylene glycol.

Fig.3 a) Nanofluid just prepared b) Nanofluid on seventh day after prepared

D. Characterization techniques

The synthesized nanoparticles were characterized by X-ray diffraction (XRD) technique in the 2θ range from 20° to 80°using CuKα radiations to investigate the crystal structure.

The observed diffraction peak patterns were compared with Joint Committee on Powder Diffraction Standards (JCPDS)(card no: 048-1548).

III.RESULTS AND DISCUSSION

A. X-ray diffraction analysis (XRD)

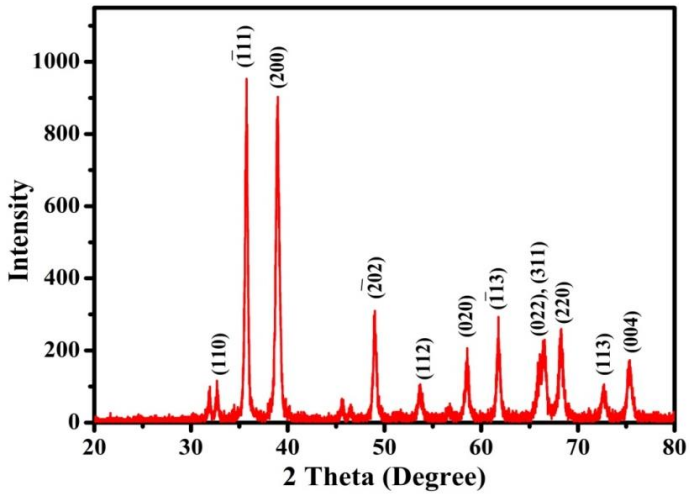

Fig.4 XRD pattern copper oxide nanoparticles

Figure 4 illustrates the room temperature X-ray diffraction pattern of copper oxide nanoparticles synthesized by using sol-gel auto-combustion method.

The X-ray diffraction pattern show the reflections (110), (111), (220), (202), (112), (020), (113), (311), (220), (113) and (004). It is observed from XRD pattern that all the reflections present in the XRD pattern well matched with the monoclinic phase of copper oxide. The XRD pattern is in close agreement with the JCPDS card (card no: 048-1548). Thus, the XRD pattern confirms the synthesis of copper oxide in pure and nanocrystalline form without any kind of impurity phases. Similar results of the XRD pattern are reported in the literatures[16, 17]. From the XRD data (Bragg's angle, interplanar spacing), the lattice constant of prepared copper oxide was calculated and is presented in table 1.

The average grain size was calculated using Debye-Scherrer formula (eq^{n} 2) where k is Scherrer constant, which accounts for the shape of the particle whose value is taken as 0.94, β is full width at half maximum, values calculated are reported in table 1, λ is the Radiation Wavelength (1.5405 Å). The average particle size was calculated to be 35 nm.

$$D = \frac{k\lambda}{\beta cos\theta} 2$$

Table 1: Calculated values of Lattice constant (a), Unit cell volume (V), X- ray density (d_X), particle size (t) of copper oxide nanoparticles

Oxide	Lattice parameter (Å)			V (Å)^3	d_X (gm/cm^3)	T (nm)
	a	b	c			
CuO	4.690	3.431	5.113	82.275	5.3965	35

The other structural parameters like Unit cell volume (V) and X- ray density (d_X)was calculated using the following equation 2 and 3,

$$\boldsymbol{V = a * b * c} \quad 3$$

$$\boldsymbol{d_x = \frac{8M}{Na3}} 4$$

Where, 'd' is interplanar spacing, 'N_a' is Avogadro's number, 'M' is the molecular weight, 'd_x' is X-ray density the values of Unit cell volume and X-ray density are given in table 1. The observed values of structural parameters are in good agreement with the reported values.

B. Morphological study

Scanning electron images of copper oxide Nanoparticles

Scanning electron microscope images of CuO obtained has uniform morphology and well-developed structure.

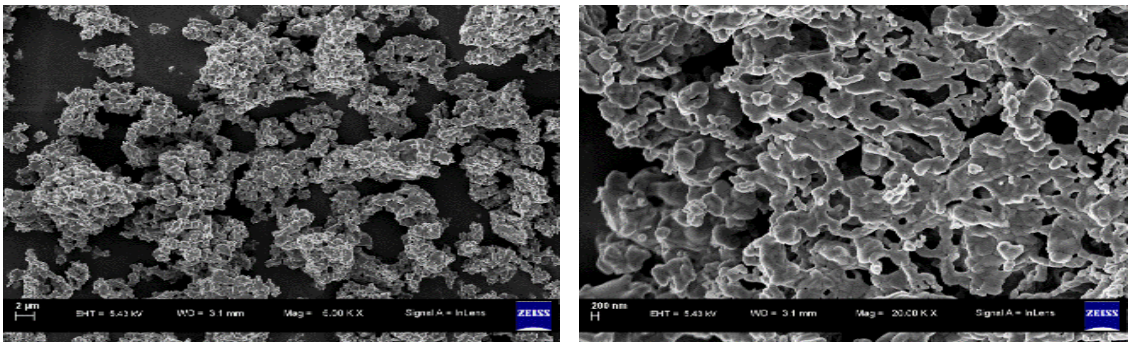

Fig 5: Scanning Electron images of CuO nanoparticles

C. Thermal conductivity of CuO Nanofluid

The thermal conductivity of the copper oxide nanofluid was measured using KD2 pro thermal analyzer fig. 6. The value of thermal conductivity measured for 0.025, 0.050,0.075, 0.100, 0.125 and 0.150 volume % is listed in table 2.The observed thermal conductivity found to be enhanced as compared to the thermal conductivity of the base fluid (deionized water and propylene glycol) which is 0.4 (W/mK).

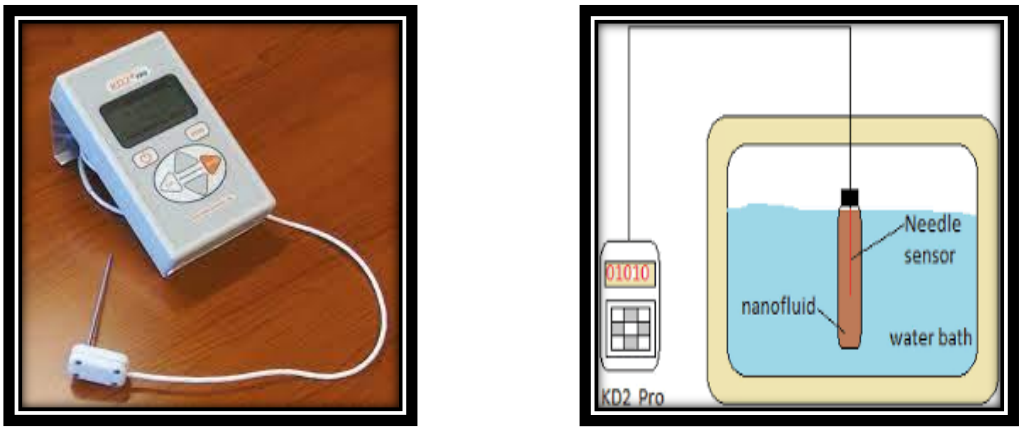

Fig 6: KD2 Pro Thermal Property Analyzer

Table 2: Thermal conductivity of CuO nanofluid

Sr. No.	Volume fraction	Thermal conductivity (W/mK)
1	0.025	0.508
2	0.050	0.545
3	0.075	0.572
4	0.100	0.595
5	0.125	0.616
6	0.150	0.634

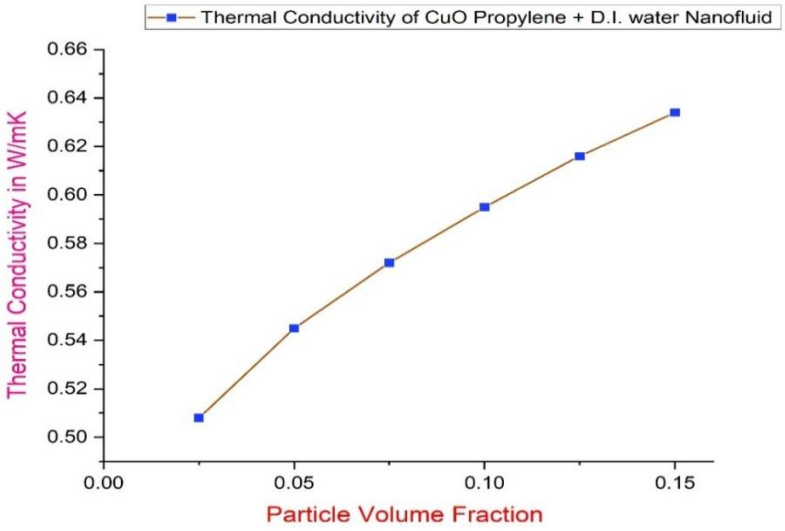

Fig 7: Thermal conductivity v/s Nanoparticle volume fraction graph

D. Zeta potential CuO

The following table 3 shows zeta potential measurement for copper oxide nanofluid. The zeta potential measurement of prepared copper oxide nanofluid shows good stability. For 0.025 to 0.075 vol % of nanoparticle.Further increase in nanoparticle concentration in nanofluid increases Van der Waalsattractive forces on the particles surface which causes theparticles to be attracted to each other into forming clustersor agglomerations of nanoparticles cause to decreases its dispersion stability and fast sedimentation of nanoparticles takes place in base fluid.

Table 3: Zeta potential measurement of CuO Nanofluid

Sr. No.	Volume fraction	Zeta potential in mV
1	0.025	-35.28
2	0.050	-31.14
3	0.075	-28.05
4	0.100	-24.23
5	0.125	-21.61
6	0.150	-17.08

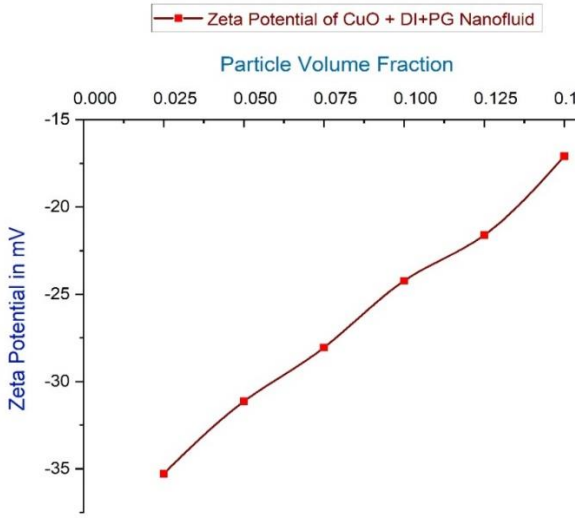

Fig 8: Zeta potential v/s Particle volume fraction graph

IV. CONCLUSION

Copper oxide (CuO) in nano size form was successfully prepared by sol-gel auto combustion method. The nanocrystalline nature of the prepared CuO was confirms from crystallite size which is calculated by Debye-Scherrer's formula. The lattice constant (a), Unit cell volume (V) and X-ray density (d_x) are in good agreement with the literature values. The SEM images of CuO nanoparticles shows uniform morphology and well-developed structure of CuO nanoparticles. The prepared CuO nanofluid for nanoparticle volume fraction 0.025, 0.050, 0.075, 0.100, 0.125, 0.150 vol % shows that the thermal conductivity of base fluid (deionized water and propylene glycol in the ratio 50:50) increases with volume fraction of nanoparticles but increasing volume fraction of nanoparticles in base fluid decreases dispersion stability of nanofluid. Since the magnitude of zeta potential of nanofluid decreases for increasing volume fraction of CuO nanoparticles in nanofluid.

V. REFERENCES

[1]. Kołodziejczak-Radzimska, A. and T. Jesionowski, Zinc oxide—from synthesis to application: a review. Materials, 2014. 7(4): p. 2833-2881.

[2]. Verma, N. and N. Kumar, Synthesis and biomedical applications of copper oxide nanoparticles: an expanding horizon. ACS Biomaterials Science & Engineering, 2019. 5(3): p. 1170-1188.

[3]. Jadhav, S., et al., Copper oxide nanoparticles: synthesis, characterization and their antibacterial activity. Journal of Cluster Science, 2011. 22(2): p. 121-129.

[4]. Lanje, A.S., et al., Synthesis and optical characterization of copper oxide nanoparticles. Adv Appl Sci Res, 2010. 1(2): p. 36-40.

[5]. Ahamed, M., et al., Synthesis, characterization, and antimicrobial activity of copper oxide nanoparticles. Journal of Nanomaterials, 2014. 2014.

[6]. Singh, J., G. Kaur, and M. Rawat, A brief review on synthesis and characterization of copper oxide nanoparticles and its applications. J. Bioelectron. Nanotechnol, 2016. 1(9).

[7]. Khedkar, R.S., S.S. Sonawane, and K.L. Wasewar, Influence of CuO nanoparticles in enhancing the thermal conductivity of water and monoethylene glycol based nanofluids. International Communications in Heat and Mass Transfer, 2012. 39(5): p. 665-669.

[8]. Bakthavatchalam, B., et al., Comprehensive study on nanofluid and ionanofluid for heat transfer enhancement: A review on current and future perspective. Journal of Molecular Liquids, 2020. 305: p. 112787.

[9]. Mohapatra, M. and S. Anand, Synthesis and applications of nano-structured iron oxides/hydroxides–a review. International Journal of Engineering, Science and Technology, 2010. 2(8).

[10]. Macwan, D., P.N. Dave, and S. Chaturvedi, A review on nano-TiO 2 sol–gel type syntheses and its applications. Journal of materials science, 2011. 46(11): p. 3669-3686.

[11]. Sutka, A. and G. Mezinskis, Sol-gel auto-combustion synthesis of spinel-type ferrite nanomaterials. Frontiers of Materials Science, 2012. 6(2): p. 128-141.

[12]. Singh, P., Experimental heat transfer analysis of Copper oxide nanofluids through a straight tube. International Journal of Advanced Trends in Computer Science and Engineering, 2019. 8(3): p. 495-500.

[13]. Raju Singh, R.S.P., A A Koser, Stability test of Copper Oxide Nanofluid prepared using Two step method. International Research Journal of Engineering and Technology (IRJET), 2017. 04(08): p. 958-960.

[14]. Jwo, C.-S., T.-P. Teng, and H. Chang, A simple model to estimate thermal conductivity of fluid with acicular nanoparticles. Journal of Alloys and Compounds, 2007. 434-435: p. 569-571.

[15]. S. Lee, S.U.S.C., S. Li, J.A. Eastman, Measuring Thermal Conductivity of Fluids Containing Oxide Nanoparticles. Trans. Am. Soc. Mech. Eng. , 1999. 121: p. 280-289.

[16]. Nithya, K., et al., Preparation and characterization of copper oxide nanoparticles. Int. J. ChemTech Res, 2014. 6(3): p. 2220-2222.

[17]. Topnani, N., S. Kushwaha, and T. Athar, Wet synthesis of copper oxide nanopowder. International journal of green nanotechnology: materials science & engineering, 2010. 1(2): p. M67-M73.

IJSRST

National Conference on New Horizons in Nano Scale Materials and Their Applications NHNMA-2024

Organized By

Department of Physics,
M. S. P. Mandal's Arts, Commerce and Science College,
Kille-Dharur, Dist. Beed, Maharastra, India

Publisher

Technoscience Academy

Website : www.technoscienceacademy.com